ÉCOLE POLYTECHNIQUE DE BRUXELLES
UNIVERSITÉ LIBRE DE BRUXELLES

Quantitative methods to evaluate the radioprotection and shielding activation impacts of industrial and medical applications using particle accelerators

Thesis presented by Robin TESSE
in fulfilment of the requirements of the
PhD Degree in Engineering Sciences and Technology
("Docteur en Sciences de l'Ingénieur et Technologie")
Academic year 2018-2019

Supervisor: Professor Alain DUBUS
Co-supervisors: Professors Nicolas PAULY
and Gilles DE LENTDECKER
Nuclear Metrology

Thesis jury:

Jean-Marc SPARENBERG (Université libre de Bruxelles, Chair)
Pierre-Etienne LABEAU (Université libre de Bruxelles, Secretary)
Nicolas PAULY (Université libre de Bruxelles)
Gilles DE LENTDECKER (Université libre de Bruxelles)
Frédéric STICHELBAUT (Ion Beam Applications)
Cédric HERNALSTEENS (Ion Beam Applications)
Francesco CERUTTI (CERN)

AVN

iba

Remerciements

Quatre années de recherche. Quatre années d'efforts. Quatre années d'échanges. Quatre années d'émotions. Et au bout cette thèse. Un challenge qui n'aurait pu être relevé sans les nombreuses personnes avec qui j'ai travaillé, qui ont su me conseiller, me soutenir et m'orienter. La route fut longue mais passionnante. Je souhaite ici remercier tous ceux et celles qui ont participé d'une manière ou d'une autre à l'aboutissement de ce travail.

Je tiens tout d'abord à remercier Alain Dubus et Nicolas Pauly, mes promoteur et co-promoteur. Ils sont à l'initiative de ce projet de recherche, indispensable premier pas qui m'a permis d'approfondir un sujet dans un domaine qui me tenait particulièrement à cœur. Tout au long de cette thèse, ils m'ont consacré de leur temps et m'ont prodigué leurs conseils avisés. Je leur suis redevable de la prise d'autonomie progressive du jeune ingénieur diplômé que j'étais voici 4 ans. Malheureusement le professeur Alain Dubus n'aura pas pu voir le résultat final de ce travail à la suite de sa disparition tragique.

Frédéric Stichelbaut et Cédric Hernalsteens, mes deux superviseurs industriels chez Ion Beam Applications (IBA), ont également beaucoup compté dans la réussite de ce projet.

Merci à Frédéric pour son support. En prenant le temps de répondre à mes nombreuses interrogations, il aura été un acteur majeur dans le lancement de ma recherche. Grâce à son expertise dans le domaine de la protonthérapie et sa grande connaissance des installations chez IBA, il a su nourrir mes réflexions. Son feedback constructif m'aura permis d'approfondir mes recherches et d'affiner mes résultats.

D'autre part, ce projet de recherche n'aurait pu être mené à bien sans l'aide de Cédric. Je le remercie chaleureusement pour l'intérêt qu'il a porté à mon travail et pour son accompagnement lors de ces deux dernières années. J'ai beaucoup appris à ses côtés, j'ai pu apprécier son enthousiasme et sa sympathie. Son regard critique et ses nombreux retours auront été pour moi une aide précieuse lors de la rédaction finale de ma thèse et m'auront poussé à me dépasser. Je lui suis aussi reconnaissant pour l'opportunité qui m'a été donnée de participer aux conférences internationales de l'IPAC (International Particle Accelerator Conference) et de l'ICAP (International Computational Accelerator Physics Conference), de suivre les cours à l'USPAS sur les accélérateurs de particules ainsi que d'aller au CERN.

Ce travail n'aurait pas été possible sans l'Association Vinçotte Nuclear et leur financement. Je les remercie pour la confiance qu'ils ont accordée à mon projet et qui a permis de me consacrer pleinement à ma recherche. Je désire en outre remercier l'entreprise Ion Beam Applications (IBA) avec qui j'ai eu la chance de collaborer. Elle m'a donné le support technique, l'accès aux informations et toute l'aide nécessaire pour arriver à ces résultats. Elle m'a également offert l'opportunité d'aller sur site, ce qui fut très instructif. Je tiens à saluer toutes les personnes travaillant chez IBA, en particulier au service engineering que j'ai pu régulièrement côtoyer ces dernières années. Sans oublier, Baptiste et Kevin avec qui j'ai pu échanger et discuter de mes résultats.

Mes remerciements s'adressent aussi à tous les membres du service de Métrologie Nucléaire: Artem, Bernard, Eustache, Gamze, Iaroslav, Idriss, Jonathan, Juan, Julien, Julio, Laëtitia, Nicolas S., Raphaël, Pierre-Étienne, Pierre-Loïc, Sander, Vasiliki et Yvan; qui auront enrichi tant humainement qu'intellectuellement mon parcours. J'espère continuer encore un peu avec eux dans le cadre d'un post-doctorat.

Je tiens également à remercier Adrien, doctorant au Beams et ami infatigable, sans qui mes pauses n'auraient pas eu la même saveur.

Mes remerciements vont aussi à ma famille, à ma belle-famille et à mes amis. Tout particulièrement à mes parents, à mon frère et grands-parents qui même s'ils ne comprennent pas tous les détails de mon travail m'ont apporté un soutien sans faille tout au long de cette thèse. Leurs nombreux encouragements et leur soutien moral, auront été pour moi un vrai moteur. Merci à tous ceux qui ont pris le temps de relire, tout ou en partie, mon travail pour leurs remarques constructives, je sais que cela a parfois été fastidieux. Un grand merci en particuler à Marie-Claire qui eu le courage de relire l'ensemble de ce document pour corriger les nombreuses fautes d'anglais.

Finalement, un grand merci à ma compagne, Céline, pour son soutien quotidien et ses encouragements dans les bons comme dans les moments de doute. Elle a eu le courage de relire cette thèse et de me motiver sans cesse pour améliorer ce manuscrit. Pour tout cela je la remercie du fond du coeur.

A Céline

Abstract

Proton therapy facilities, as other industrial applications using ionizing radiations, are confronted to radioprotection problems and seek to mitigate the undesirable effects. The aim of this thesis is to study the *IBA* compact proton therapy center, the Proteus®One in this radioprotection context. The compactness of this system implies important radioprotection issues, mainly the concrete shielding activation where a model allowing to predict and characterize the impact of secondary radiations on the system is required. Numerical simulations using Monte Carlo methods are used and in particular, a benchmark between different existing software has been carried out to validate the use of the *Geant4* software in this work. The first part of this thesis focuses on the design of the structural shielding taking into account neutron sources in the model. In particular, the concept of neutron-equivalent source is introduced. In this framework, the quantity and the localization of the generated nuclear waste in concrete are determined. The second part of the work investigates the beam properties and its interactions with matter along the transport beamline. After the analysis of the existing system, a new degrader, which is one of the critical elements for the emission of secondary radiations and for the performances of the device, is proposed. Comparisons between existing (aluminium, graphite, beryllium) and novel (boron carbide and diamond) degrader materials are provided and evaluated against semi-analytical models of multiple Coulomb scattering. The use of diamond with a geometry adaptation allows beam emittance reduction and beam transmission increase. The third part of this thesis considers a complete 3D model of the Proteus®One system. It contributes to acquire a detailed knowledge of the beam properties inside the beamline. This model is validated with experimental data and the assumption of neutron-equivalent source is verified. Finally, maps of proton and neutron interactions are generated to provide a complete mapping of the secondary radiations in the system. These maps can be used to determine dosimetric or radioprotection quantities.

Scientific Contributions

1. **R. Tesse, F. Stichelbaut, N. Pauly, A. Dubus and J. Derrien**
   GEANT4 benchmark with MCNPX and PHITS for activation of concrete
   Nuclear Instrumentation and Methods in Physics Research, Section B **416** (2018), pp. 68-72
   doi: 10.1016/j.nimb.2017.12.006

2. **R. Tesse, A. Dubus, N. Pauly, C. Hernalsteens, W. Kleeven and F. Stichelbaut**
   Numerical Simulations to Evaluate and Compare the Performances of Existing and Novel Degrader Materials for Proton Therapy
   9th International Particle Accelerator Conference, Vancouver, Canada, 2018
   doi: 10.1088/1742-6596/1067/9/092001

3. **R. Tesse, C. Hernalsteens, A. Dubus, E. Gnacadja, N. Pauly, L. Nevay, W. Shields and S. Boogert**
   Seamless beam and radiation transport simulations of IBA Proteus systems using BDSIM
   13th International Computational Accelerator Physics Conference, Key West, USA, 2018

4. **C. Hernalsteens, R. Tesse, K. André, V. Collignon, Q. Flandroy, B. Herregod, R. Jungers and Z. Wang**
   Optimization of hadron therapy beamlines using a novel fast tracking code for beam transport and beam-matter interactions
   13th International Computational Accelerator Physics Conference, Key West, USA, 2018

Contents

List of Figures

List of Tables

Introduction

Motivation and problem statement

The growth and increased availability for the general public of industrial and medical systems using particle accelerators pose new challenges in term of radioprotection and subsequent shielding activation. Indeed, facilities producing ionizing radiations are confronted to radioprotection issues and seek to mitigate the undesirable effects. To limit the exposure to such radiations, concrete shieldings are routinely used. They contribute to a large fraction of the total cost of ownership for medical and industrial facilities. In particular, the activated concrete of the shielding must be dealt with in accordance with international requirements for nuclear waste management during the decommissioning of the installation. Improving the computational methods used for the design of the shieldings allows to reduce the uncertainty margin and to estimate with better accuracy the fraction of activated concrete.

In this thesis, we develop two novel methods to tackle those challenges: a method based on neutron-equivalent sources is developed and integrated with Monte Carlo simulations and a new approach is proposed to realize a single-pass simulation of a complete installation, considering both the accelerated beam modelling and the subsequent beam-matter interactions leading to the activation of the shielding within a single simulation.

Those methods are specifically applied and validated for the case of compact proton-therapy systems. Indeed, those systems reveal key challenges in this context, while at the same time, have important economic and social impacts. Radiotherapy is largely used for the cure of cancer (50% of patient undergoing cancer treatment are prescribed with radiotherapy, in addition to other techniques [1]). Among those patients, 1% will be treated with proton therapy but it is estimated that 20% of patients could benefit from received proton therapy treatments instead of X-ray radiotherapy [2]. Those reasons explain the rapid worldwide growth of proton therapy installations. Single-room compact proton therapy installations have been developed by different manufacturers and present an additional challenge in term of shielding design and nuclear waste management. Indeed, those installations are typically located within or next to existing hospitals or clinics. The global footprint of the installations can be minimized using improved shielding computations. In addition, the minimization of the generated nuclear waste is particularly important for the decommissioning phase whose tight schedule is intended to maximize the economic value for the care provider.

To apply the techniques and methods developed in this thesis, work has been carried out in collaboration with Ion Beam Applications (*IBA*), the world-leader in term of installed proton therapy solutions. In particular, the product Proteus®One, offering a compact proton therapy installation featuring a rotating gantry has been chosen for

our models and simulations. The collaboration with *IBA* allowed to validate our models with data collected in clinically-used installations and to compare our results with existing shielding and activation design computations performed by *IBA*.

Nuclear applications and shielding

Since end of Second World War, nuclear applications are constantly growing [3, 4, 5]: energy production, food sterilization, medical applications, nuclear research, quality control, ... The diverse studies in this area continue to open new possibilities and offer new industrial perspectives.

All these applications have in common the emission of energetic particles that may generate health or environmental problems. In this respect, the International Atomic Energy Agency (IAEA), promoting the safe, secure and peaceful use of nuclear technologies, defines different standards to protect people against undesirable exposure to radiations: transport of radioactive material, protection of workers, radioactive waste identification and management, ... [6]

Every nuclear installation must be equipped with a proper shielding depending on the application to attenuate and reduce external radiations. For most utilizations, concrete is considered as an excellent material given its properties and its attractive price [3, 4]. Different concrete compositions exist and they all have in common a mixture of light and heavy elements which permit a good attenuation of photons and neutrons.

The particles attenuation is done by interactions of incident particles (and their generated secondary particles) with the different elements in the material. The attenuation of the secondary radiations through a shielding wall have been intensively investigated in recent years by researchers [7, 8, 9, 10] focusing on the attenuation of particles through the wall.

However, ordinary concrete contains some impurities, like europium or cobalt [11, 5] in addition to its standard components. All these elements interact with the neutrons through different processes and produce radionuclides with a long half-life (^{22}Na, ^{152}Eu, ^{60}Co, ...). For each of these radioisotopes, different clearance levels are defined by the IAEA to determine if concrete must be considered as a nuclear waste or not.

The government and the industries are legally obliged to budget the dismantling costs of their installations. The quantity of nuclear waste depends on how the facilities have been used, how many times, etc. To properly model the different reactions, the secondary radiations and the type of produced radionuclides, the methods of Monte Carlo have become essential.

Cancer treatment and proton therapy

The World Health Organization classifies cancer as a noncommunicable disease which is the second cause of death worldwide. Cancer is a generic term for diseases that affect any part of the body and result in a rapid division of abnormal cells. If these cells spread to other organs, we speak of metastasizing which is the major cause of death from cancer. In 2012, in Belgium, cancer causes 29.600 deaths. Lung cancer and colorectal cancer are the most frequent with prostate cancer in men and breast cancer in women [12, 13].

Depending on the type of cancer different treatments may be considered:

- Surgery (Mechanical treatment)
- Chemotherapy (Chemical treatment)
- Radiotherapy (Physical treatment)
- Immunotherapy (Biological treatment)

The choice of the treatment is left to the discretion of the physician but for half of the patients, a treatment by radiotherapy is used. The treatment by radiotherapy consists in irradiating the tumour with particles to destroy them. More specifically, the particles transfer their energy to the electrons in the medium and these electrons interact with the DeoxyriboNucleic Acid (DNA) of the cell. These interactions cause the death of the cells.

In function of the type of particles used for the treatment, the radiotherapy may be subdivided in three categories:

1. Conventional radiotherapy: with electrons and photons
2. Hadrontherapy: with protons and carbon ions
3. Neutron therapy: with neutrons

These last years, the hadrontherapy has demonstrated its ability to treat some specific cancers as the ocular or prostate tumor [14, 15]. Indeed, as the particles are charged, it is easier to focus the beam on a specific position without irradiating healthy tissues. We illustrate in figure 1 the deposit dose for the treatment of a Hodgkin lymphoma with protons (on the left) and with photons (on the right) [16].

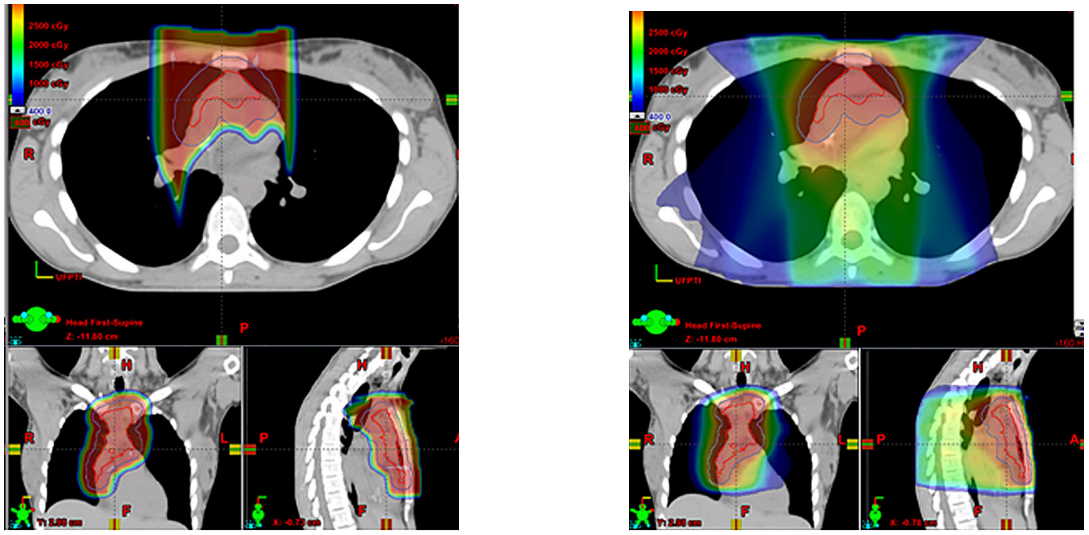

(a) protons. *(b) photons.*

Figure 1: A radiation treatment plans using protons (a) and photons (b). Reproduced from [16].

We remark that the normal tissues and sensitive organs (spinal cord, breast, hearth, lung) receive a lesser dose with a proton therapy treatment than with photons. This low

dose reduces the risk of late irradiation and thus the risk of secondary cancer caused by the treatment itself [17, 18]. Authors of [19] have shown different advantages of neutrons utilization but the main disadvantage of this technique is the clinical production of the neutron beam. We will focus our attention on the cancer treatment with proton therapy.

Different irradiation techniques exist but the most effective is pencil beam scanning (PBS) in which a few millimeters proton beam is moved by magnetic scanning [20]. This technique irradiates the tumor more accurately and has many advantages: improvement of the dose distribution and reduction of the delivery time. Moreover, this technique is particularly well adapted for the treatment of children. [21, 22]

As these treatments require hadron beam with energy up to hundreds of MeV, a proton therapy facility is a huge and expensive installation. A lot of efforts are made by the companies to reduce the cost and make the proton therapy accessible to everyone. In this perspective, *IBA* developed in 2014 a new concept of proton therapy center which is more compact with only one treatment room and consequently easier to finance : the Proteus®One.

As we said above, any facility dealing with nuclear radiations requires a shielding often made of concrete. Nevertheless, the compactness of the treatment room induce more interaction between the secondary radiations and the concrete shielding making the radioprotection study even more important [23].

Work structure

This thesis is divided in three parts: the quantification of nuclear waste produced in a medical installation using neutron-equivalent sources (replacement of proton beam/target by a punctual neutron source), the study of the degrader to reduce beam losses and finally, the complete installation modelling taking into account the beam transport and particles interactions.

Part 1: Activation study using neutron-equivalent sources

Chapter 1 introduces the key components required for the study of particles interactions with matter. Monte Carlo numerical methods and software used for that purpose are also described. We especially present *MCNPX*, *Geant4* and *Phits*.

In chapter 2, the Proteus®One shielding geometry has been modelled using *Geant4* to estimate the proportion of activated concrete produced after 20 years of clinical operation. After estimating the locations of neutrons production sources, we use the method of neutron-equivalent source which is developed in this work to improve computation efficiency. This method requires a validation of the hadronic models of *Geant4* with other softwares such as *MCNPX* and *Phits*. Theses models and the results are discussed in details. The utilization of *Geant4* for activation studies is quantitatively justified. The quantity of activated concrete for the Proteus®One shielding is evaluated with *Geant4* and is compared with that obtained by *IBA* with *MCNPX*. Two possible solutions are presented to reduce the proportions of nuclear waste. The first one consists in modifying the composition of the shielding. The second one, which is detailed in this thesis, is a proposition of a new degrader design to reduce the beam losses.

Part 2: Reduction of the neutrons production by the energy degrader

To limit secondary radiations, the comprehension and the model of the source terms are of primary importance. As the degrader is the one of major contributors to the produced neutrons, a complete study of the degrader in the *IBA* system is performed and compared to analytic models. Chapter 3 describes the Hamiltonian formalism for the transport of charged particles in electromagnetic fields. The important notions as the phase space and the emittance are introduced. Different beam transport software, MAD-X, Manzoni and BDSIM, are compared and validated for the *IBA* beam line.

We study in chapter 4 different materials to limit the harmful effects of radiations, by reducing the beam size and increasing the beam transmission. Comparisons between existing (aluminium, graphite, beryllium) and novel (boron carbide and diamond) degrader materials are provided and evaluated against semi-analytical models of multiple Coulomb scattering. The properties of the actual *IBA* degrader are studied in details and more specifically, the beam emittance. Finally, a proposal of geometry made in diamond is developed to decrease beam losses.

Part 3: Complete Proteus®One installation simulation using BDSIM

To study the impact of these optimizations at the system level, we proceed to a complete and detailed modelling of the proton beam dynamics in the beamline. This model allows to precisely quantify the beam losses distribution, knowing that this one strongly depends on the fine modelling of the degrader. In chapter 5, the complete Monte Carlo model of the Proteus®One system is presented. This model is based on BDSIM, based on *Geant4*. BDSIM combines both the transport of the proton beam in magnetic elements as well as the interactions between particles and matter. The model obtained is validated and discussed in details, in particular by means of experimental measurements collected along the beamline and at the isocenter of the Proteus®One installations currently in operation.

Finally, with this detailed knowledge of the system, we perform in chapter 6 a single-pass shielding study. Indeed, the detailed transport of the beam makes it possible to characterize the source terms and to determine the generation of neutrons in the same simulation. This study ensures consistency between beam physics and neutrons generation using the previously validated software BDSIM. This result is discussed in details and compared with the *IBA* study and our results based on loss estimates coupled with our neutron-equivalent sources method. This model also allows to generate 2D maps for the localization of protons and neutrons interactions that can be used for the establishment of ambient dose maps.

The conclusion summarizes the main results obtained in the different chapters and suggests future research directions for radioprotection and shielding design.

Part I

Activation study using neutron-equivalent sources

Chapter 1

Physics for shielding studies

Contents

In this work, we are particularly interested in the interactions between protons and neutrons with matter. Thus, in this chapter, we recall some prerequisites about the different processes occurring in matter. We introduce in section 1.1, the concept of particles collision and the cross section notion. The interaction of protons and neutrons with matter are described in section 1.2 and in section 1.3 respectively. In section 1.4, we detail a general reaction involving protons as well as neutrons which is called spallation. Different models of this reaction are also described. Finally, in section 1.5, we introduce the concept of Monte Carlo simulations which are the useful methods to treat and simulate the interactions of a large number of particles with matter.

1.1 General principles

1.1.1 Particles collision

In 1932, the first cyclotron is built in Berkeley and in 1957, a second one is built at CERN. The purpose of these equipments is to improve our understanding of matter. It

allows boosting particles to high energy (GeV, TeV) before colliding together or with stationary targets. In this thesis, we are more specially interested in the second type of experiment which consists in irradiating a target with a particle beam. This experiment allows observing and understand the kind of reactions inside the target as well as to study the ejected particles. Different analytical models which have been developed recently have been validated with these experimental results [24].

A schematic view of a collision experiment is represented in figure 1.1a. A particle beam hits a target, different reactions occurred and secondary particles are emitted. Detectors observe and record the results of these collisions. The type of incoming particles and the target material influence the beam deflection, the ionization of matter and the secondary particles emitted.

As example, figure 1.1b simulates with a Monte Carlo tool these effects on a lead target: incident protons (in blue) are diffused when passing through matter, neutrons are generated (in green).

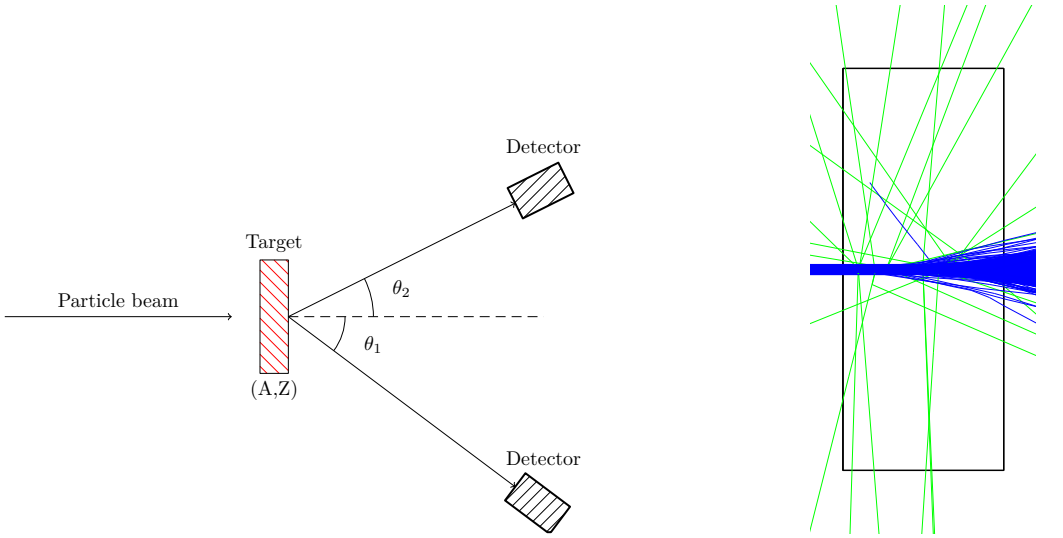

(a) Schematic view [25]. *(b) Monte Carlo model.*

Figure 1.1: Representation of a collision experiment.

1.1.2 Concept of cross section

We consider a particle entering a target as shown in figure 1.1a. There is a certain probability that this particle interacts with the nucleus if passing close enough. This probability is linked to the cross section σ. It has the dimension of a surface and is generally expressed in barn ($1barn = 10^{-24}cm^2$). It depends on the incident particles and on the characteristic of the target.

The total cross section can be expressed as the sum of the partial cross-sections corresponding to the different interactions. In this thesis, we focus our attention on the capture, the elastic, the inelastic and the non-elastic reactions because they are the most important in the energy range considered in this thesis [26, 27]. Consequently, we have:

$$\sigma_{tot} = \sigma_c + \sigma_{ele} + \sigma_{ine} + \sigma_{nonele} \,. \tag{1.1}$$

The figure 1.2 shows the different cross sections of a ^{235}U target irradiated by a neutron. From this figure, we see that the most probable effect is the fission.

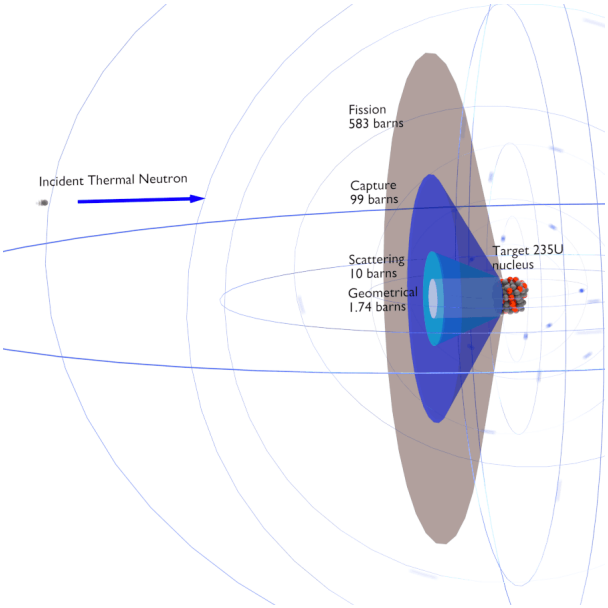

Figure 1.2: Cross-sections representation for a ^{235}U target irradiated by a thermal neutron. Reproduced from [28].

The macroscopic cross section Σ (in cm^{-1}) represents the probability of interaction by unit of length in the medium. Σ is derived from σ and the atomic density (N): [29]:

$$\Sigma = N\,\sigma. \tag{1.2}$$

The mean free path (in cm) of the particle is defined as the average distance between two successive collisions and is given by:

$$\lambda = \frac{1}{\Sigma}\,. \tag{1.3}$$

The cross section is related to the impact parameter b. This parameter corresponds to the distance between the target and the incident trajectory of the incoming particle (see figure 1.3). The relation between b and σ is given by [30].

$$d\sigma = 2\pi\, b\, db\,. \tag{1.4}$$

A particle with an energy E and an impact parameter b makes a collision with a target characterized by a cross section σ. This particle is deviated from its original trajectory with an angle θ and an energy after collision of E'. The aim of the different physical models is to predict the angle and the loss of energy as a function of b and σ.

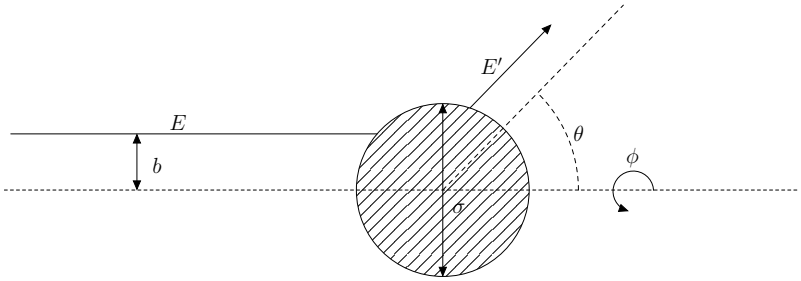

Figure 1.3: Impact parameter. Reproduced from [31].

The differential angular cross section $d\sigma/d\Omega$ is defined as the ratio between $d\sigma$ and the differential solid angle $d\Omega$ which is given by:

$$d\Omega = \sin(\theta)\ d\theta\, d\phi\,. \tag{1.5}$$

In the next sections, the different interactions are detailed. The International Commission on Radiation Units and Measurements (ICRU) classifies the nuclear interactions in three categories [27]:

elastic: *The term elastic denotes a reaction in which the incident projectile scatters off the target nucleus, with the total kinetic energy being conserved (the internal state of the target nucleus and of the projectile are unchanged by the reaction).*

non-elastic: *The term non-elastic is a general term referring to nuclear reactions that are not elastic (i.e. kinetic energy is not conserved). For instance, the target nucleus may undergo break-up, it may be excited into a higher quantum state, or a particle transfer reaction may occur.*

inelastic: *The term inelastic refers to a specific type of non-elastic reaction in which the kinetic energy is not conserved, but the final nucleus is the same as the bombarded nucleus.*

The section 1.2 focuses on the proton interactions and the section 1.3 on the neutron interactions. The section 1.4 treats of the non-elastic scattering σ_{nonele}, also called spallation reaction, common to both protons and neutrons.

1.2 Proton interactions

In matter, protons interact by nuclear interactions or with the atomic nuclei through the electromagnetic force (Coulomb interactions) [32]. These different processes are shown in figure 1.4. The spallation reaction will be described in section 1.4

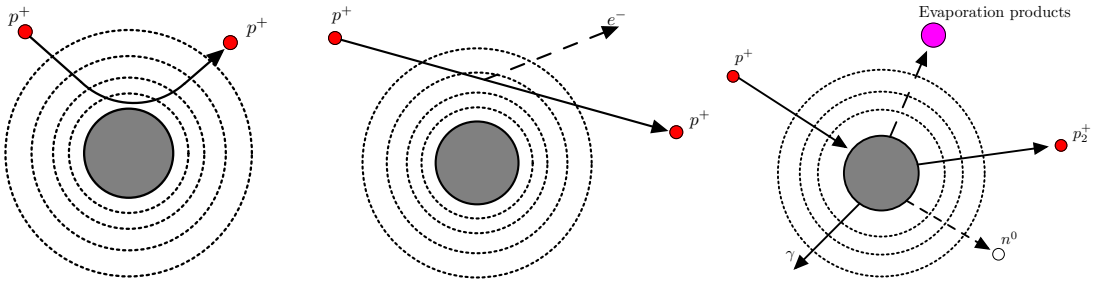

(a) Elastic scattering. *(b) Inelastic scattering.* *(c) Nuclear non elastic reaction.*

Figure 1.4: Interactions that protons may suffer in matter. Reproduced from [33].

Protons can be deflected without energy loss by the nucleus (elastic scattering) as shown in figure 1.4a. Protons energy is lost by inelastic scattering with the electrons (see case 1.4b) or by nuclear reactions with the nucleus (see case 1.4c). For a 240 MeV proton beam in water, the fraction of the energy lost by spallation interactions (case 1.4c) is about 20% [34]. This fraction of nuclear interaction will be computed in chapter 4. The elastic and inelastic scattering are described using three mathematical notions: the *Stopping Power* and the *Range*, for the energy losses and the *Scattering Power* for the angular deviation.

1.2.1 Stopping Power

The *Stopping Power* S is defined as the average loss of energy dE (MeV) of a charged particle with kinetic energy T per unit of length dx (cm) in a medium of atomic number Z [7, 35]. In the following, we develop equations for general ions. However, in the framework of this thesis, we focus on protons.

$$S \equiv -\left(\frac{dE}{dx}\right)_{T,Z} \frac{\text{MeV}}{\text{cm}} \,. \tag{1.6}$$

We often express the *Mass Stopping Power* S/ρ which is S divided by the density of the material.

$$\frac{S}{\rho} \equiv -\frac{1}{\rho}\left(\frac{dE}{dx}\right)_{T,Z} \quad \frac{\text{MeV}}{\text{g/cm}^2} \,. \tag{1.7}$$

As a function of the impact parameter b, described in section 1.1.2, two kinds of reaction can occur.

If b is greater or equal to the atomic radius, charged particles mainly lose their energy with atomic electrons (figure 1.4b), the stopping power is called *electronic stopping power* S_{elec} and is given by the Bethe-Bloch relation:

$$\left(\frac{S_{elec}}{\rho}\right) = \frac{1}{\rho}\frac{4\pi r_e^2 m_e c^2}{\beta^2} Z\, z^2 L(\beta) \,, \tag{1.8}$$

where r_e is the classical electron radius, m_e the mass of the electron, c the speed of light, β the reduced speed (v/c), z the charge of the particle (in multiples of the electron charge). For protons, z is equal to -1. The function $L(\beta)$ is the *stopping number* and take into account the details of the energy losses.

$$L(\beta) = L_0(\beta) + zL_1(\beta) + z^2 L_2(\beta) \,, \tag{1.9}$$

where $zL_1(\beta)$ and $z^2L_2(\beta)$ are the Barkas-Andersen correction and the Bloch correction [36].

If b is $\ll$ than the atomic radius, proton interacts with the atomic nucleus (hard collision) by elastic or inelastic reactions. For the elastic process, energy losses are negligible for high energy protons but increase when particles slow down. At 1keV, it is about 30%. Thus, even if this type of reaction is quite rare, radiations have harmful effects on solids materials and degrade their properties. These radiation damages are especially important for spacial applications [37, 29]. In [37], the *Nuclear Mass Stopping Power* is given by:

$$\left(\frac{S_{nucl}}{\rho}\right) = \frac{2\pi n_A \left(zZe^2\right)^2}{\rho} \frac{E^2}{p^2 M c^4} \left[\ln\left(\frac{1}{A_s}\right)\right] \,, \tag{1.10}$$

with n_A, the number of atom per unit of volume, ez (projectile) and eZ (target) are the charges of the nuclei, E and p are the total energy and the momentum of the incident particle, M is the mass of the target and A_s is a screening parameter (see equation 11 in [37]).

The *mass total stopping power* S_{tot}/ρ is simply the sum of the collision mass stopping power and the nuclear mass stopping power:

$$\frac{S_{tot}}{\rho} = \frac{S_{elec}}{\rho} + \frac{S_{nucl}}{\rho} \,. \tag{1.11}$$

The *Mass Stopping Power* is tabulated for different materials by the *National Institute of Standards and Technology* (NIST). We show in figure 1.5 the nuclear and the collision Stopping Power for water irradiated by protons. We observe that $\left(\frac{S_{nucl}}{\rho}\right)$ is quite negligible compared to $\left(\frac{S_{elec}}{\rho}\right)$.

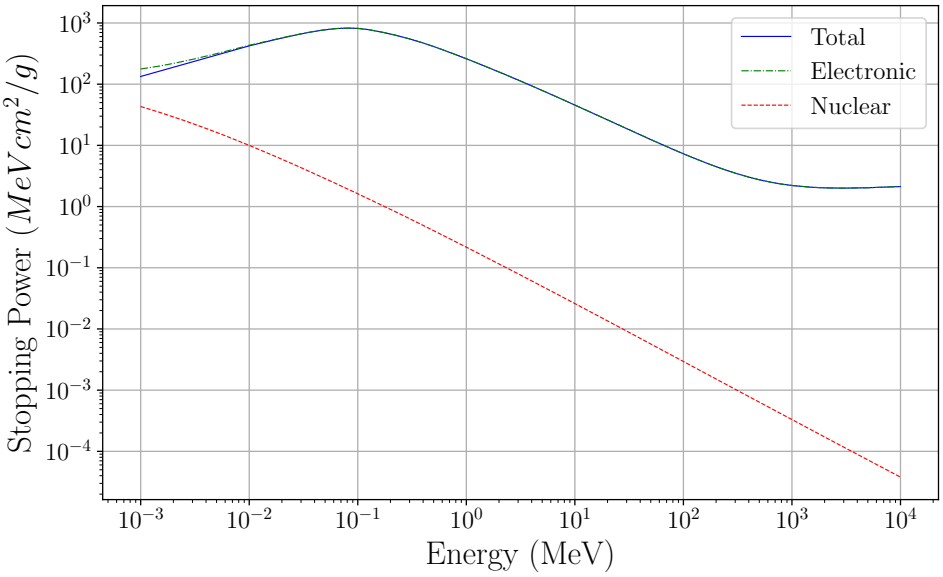

Figure 1.5: Proton Mass Stopping Power for Water. Data are taken from [38].

In figure 1.6, we show the total *Stopping Power* for various materials used later in this work. We observe that for incident proton beam with an energy larger than 10MeV, $\left(\frac{S}{\rho}\right)$ is similar for each material.

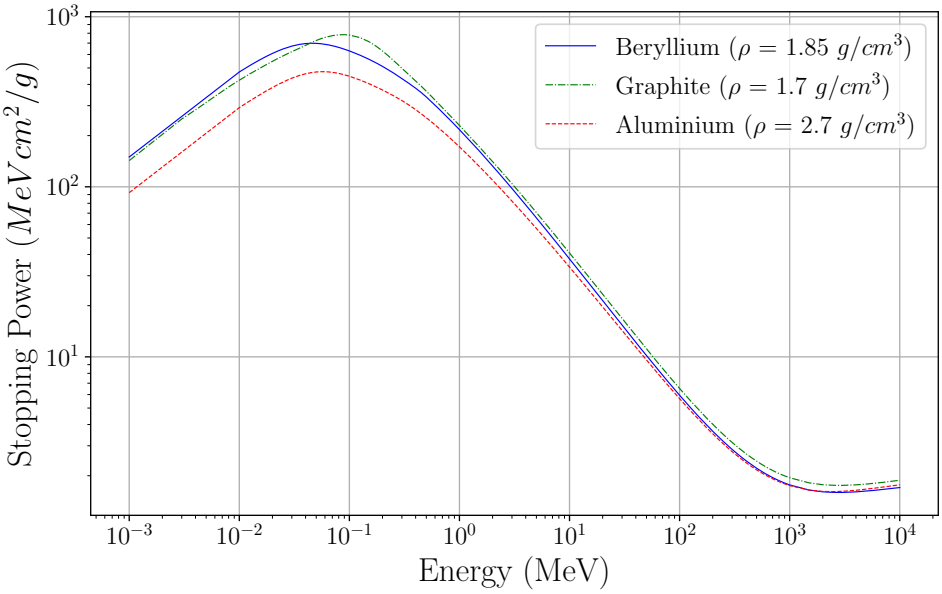

Figure 1.6: Proton Mass Stopping Power for various materials. All results are quite equal for each material for kinetic energy of the proton larger than 10 MeV.

1.2.2 Range

As defined by Attix [36]: *The range* $\mathbb{R}$ *of a charged particle of a given type and energy in a given medium is the expectation value of the path-length that it follows until it comes to rest (discounting thermal motion).* In common usage, fluctuations of energy losses are considered as negligible and then, the energy E of the projectile is a continuous function of the penetration depth x. This assumption is called *Continuous Slowing Down Approximation (CSDA).* With this approximation, the range of a charged particle with an initial energy E_0 is defined by:

$$\mathbb{R}_{CSDA} \equiv \frac{1}{\rho} \int_0^{E0} \frac{1}{\left(\frac{S_{tot}}{\rho}\right)(E)} dE \,. \tag{1.12}$$

The figure 1.7 shows the range for protons in water. To treat all common tumors in the body, which is composed by 65% of water, the protons must have a minimal energy of 40 MeV and a maximal energy around 230-250 MeV [39]. It corresponds to a range in water between 1.4 and 32.98-35 cm.

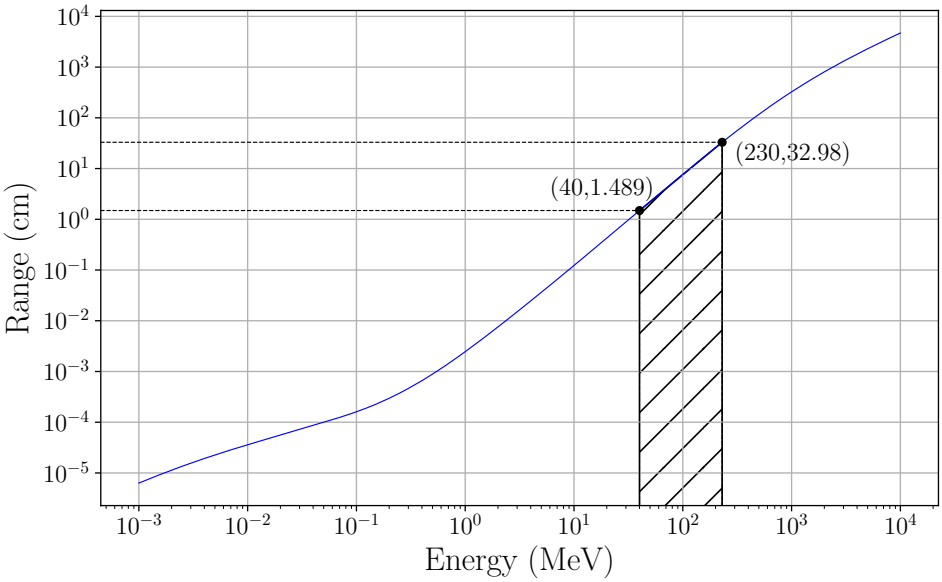

Figure 1.7: Range of protons in water. Data are taken from [38].

In proton therapy, it is convenient to characterize the penetration of proton respectively to the water. The Water Equivalent Thickness (WET) is defined by [40]:

$$t_w = t_m \frac{\rho_m}{\rho_w} \frac{\overline{S_m}}{\overline{S_w}} \,, \tag{1.13}$$

where t_w and t_m (resp. ρ_w and ρ_m) are the thickness (resp. the densities) of water and the considered material. $\overline{S_w}$ and $\overline{S_m}$ are the mean proton mass stopping power values for the water and the material, defined by:

$$\overline{S} = \frac{\int_E S \, dE}{\int_E dE} \,. \tag{1.14}$$

The figure 1.8 shows the concept of Water-Equivalent Thickness (WET). A proton with an energy E_i goes through a slice of matter m and has an energy E_f at the exit. The

thickness of water is calculated to have the same energy at the exit. The WET is used to characterize the beam penetration range, especially for treatment near critical structure [41].

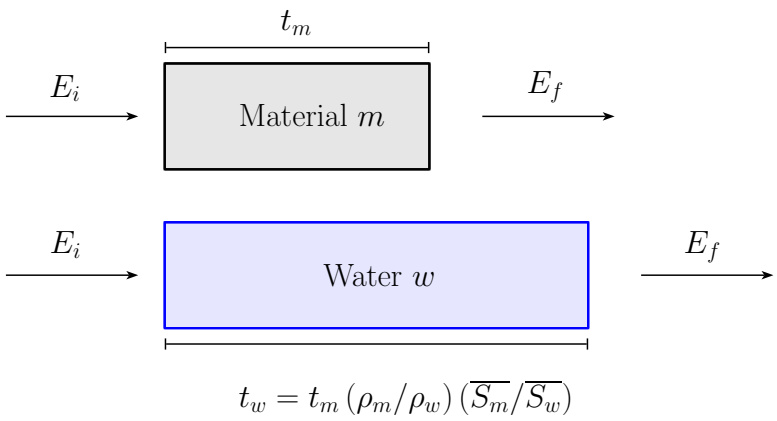

Figure 1.8: Schematic representation of the Water-Equivalent Thickness. Reproduced from [40].

1.2.2.1 Bragg peak

For radiotherapy treatment, it is very important to know the relation between the depth and the deposit dose, also called Bragg curve. If a proton with a kinetic energy E_0 enters into a medium for which the range is $\mathbb{R}$, the relation between $\mathbb{R}$ and E_0 is parameterized using p and α [42]:

$$\mathbb{R} = \alpha E_0^p\,. \tag{1.15}$$

For protons with energy between 10 and 200 MeV, p is equal to 1.8 and $\alpha = 0.0022$ [42, 43]. The remaining energy at any depth x in the medium is simply defined by:

$$E(x) = \left(\frac{\mathbb{R} - x}{\alpha}\right)^{1/p}\,. \tag{1.16}$$

If we combine equation (1.7) and (1.16) and assume that the deposit dose is proportional to S, we obtain:

$$D_{BP}(x) \propto \frac{1}{(\mathbb{R} - x)^{1-1/p}}\,. \tag{1.17}$$

This relationship shows a peak when proton is at a depth near the range. This peak is called Bragg-Peak and is the fundamental notion in proton therapy. Figure 1.9 shows a real Bragg curve with all effects described above.

The first part of the curve is called the build-up zone, it corresponds to establishment of the electronic equilibrium in the detector or is due to a low energy contamination. In the second part, interactions of protons occur with the target. The protons slow down and lose more and more energy, the *Stopping Power* is increasing and the maximum of the protons energy is lost at the end of its path (see figure 1.5). The width of this peak is related to the energy spread of the beam but also to the range straggling of protons. After the peak, there is no more protons interacting with the medium and thus, the dose is decreasing up to 0.

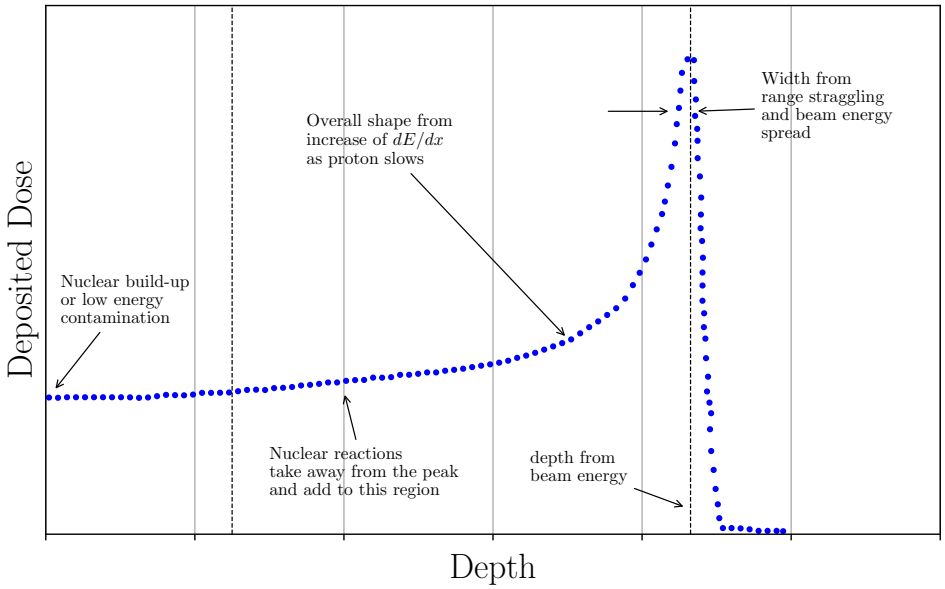

Figure 1.9: Representation of different effects on a Bragg peak in water. Reproduced from [32].

1.2.2.2 Spread Out Bragg Peak

During a medical treatment, it is essential to cover the entirety of a tumour. In practice, we use Bragg peak at different depths to create a *Spread Out Bragg Peak (SOBP)*, which is simply a superposition of weighted Bragg-curves with different input energies as shown in figure 1.10.

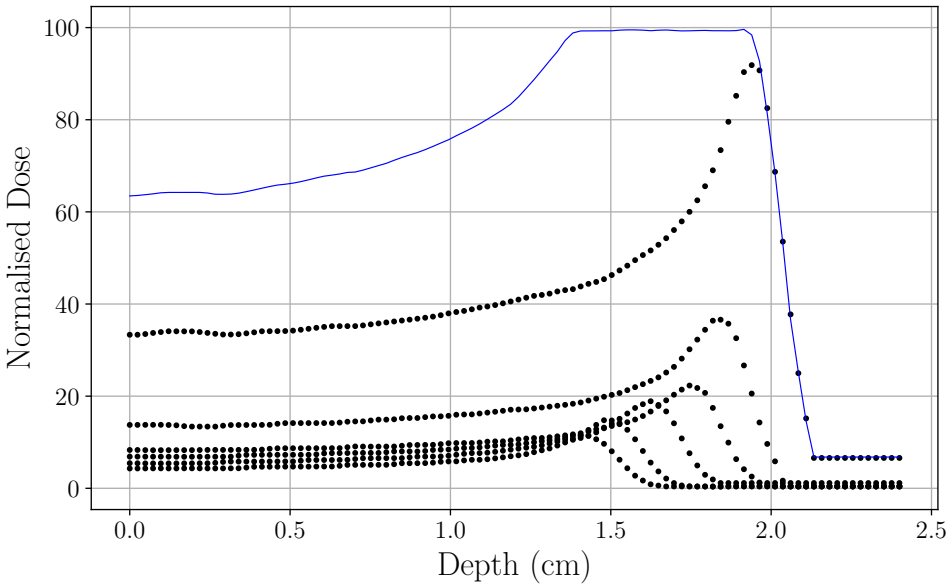

Figure 1.10: SOBP constituted by different weighted Bragg curves. Reproduced from [44]

1.2.3 Scattering Power

In the previous section, we have analysed the energy losses of a proton in a medium but when protons slow down they also scatter due to interactions with the atomic nuclei. As seen in section 1.2, the prevalent phenomenon is the interaction between the protons and the electrons of the atom (green curve in figure 1.5).

These collisions will produce, due to the mass difference, a small deviation of the protons [32]. The addition of these small angles has to be considered and thus, under the Central Limit Theorem, the angular distribution is Gaussian. In reality, this distribution is not totally Gaussian due to the electromagnetic interactions with the atomic nucleus which produce large angle deviation. The consequences are the apparition of tails in the angular distribution.

For a proton beam entering a slab of matter as shown in figure 1.11, different theories has been developed to predict the exact form of the angular distribution and the characteristic width (X_0) as a function of the entrance energy E and the target (thickness t and material).

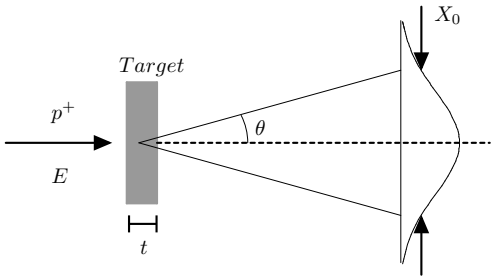

Figure 1.11: Scattering of protons in a slab. Reproduced from [32].

It is well-known that Molière's theory gives a definitive solution to the problem for thin target. We will describe the development made by Molière in 1948. We consider a target made of different elements (Z_i, A_i) with i the i^{th} constituent of the target. The aim of this theory is to find the θ distribution for a target thickness t with $t \ll \mathbb{R}$ (proton range). Molière gives a *characteristic multiple scattering angle* θ_M:

$$\theta_M = \frac{1}{\sqrt{2}} \left(\chi_c \sqrt{B} \right) . \tag{1.18}$$

χ_c is the characteristic single scattering angle (see equation 2.23 in [32]) and B, the reduced thickness which is the solution of:

$$B - \ln(B) = \ln \left(\frac{\chi_c^2}{1.167 \chi_a^2} \right) . \tag{1.19}$$

In this expression, χ_a is a cut-off angle related to the nuclear charge by the orbital electrons (see equation 2.25 in [32]). Molière approximates the desired distribution function $f(\theta)$ by a power series of $1/B$. Using a reduced angle variable $\theta' = \theta/(\chi_c \sqrt{B})$:

$$f(\theta) = \frac{1}{2\pi\theta_M^2} \frac{1}{2} \left\{ f^{(0)}(\theta') + \frac{f^{(1)}(\theta')}{B} + \frac{f^{(2)}(\theta')}{B^2} \right\} , \tag{1.20}$$

where the function f^n is given by:

$$f^n(\theta') = \frac{1}{n!}\int_0^\infty y\, J_0(\theta' y)\, e^{y^2/4}\left(\frac{y^2}{4}\ln\frac{y^2}{4}\right)^n dy\,, \tag{1.21}$$

with J_0, the Bessel function. $f^{(0)}$ is a Gaussian function:

$$f^{(0)}(\theta') = 2\, e^{-\theta'^2}\,. \tag{1.22}$$

We show in figure 1.12a results obtained by Molière. This figure also shows the comparison between experimental results and the results obtained from the Molière theory. We observe that the theory and the experience are in agreement. We also show the Molière angular distribution as a function of θ' (see 1.12b). The dashed line is the term $f^{(0)}(\theta')$ (Gaussian). Bethe and Molière give further tables for $f^{(1)}$ and $f^{(2)}$ [45]. Two remarks can be done about this result [46]:

1. This is a weak dependence of target thickness (in B term).
2. $f(\theta')$ for small θ' is nearly Gaussian but not completely as we can see in the inset of figure 1.12b.

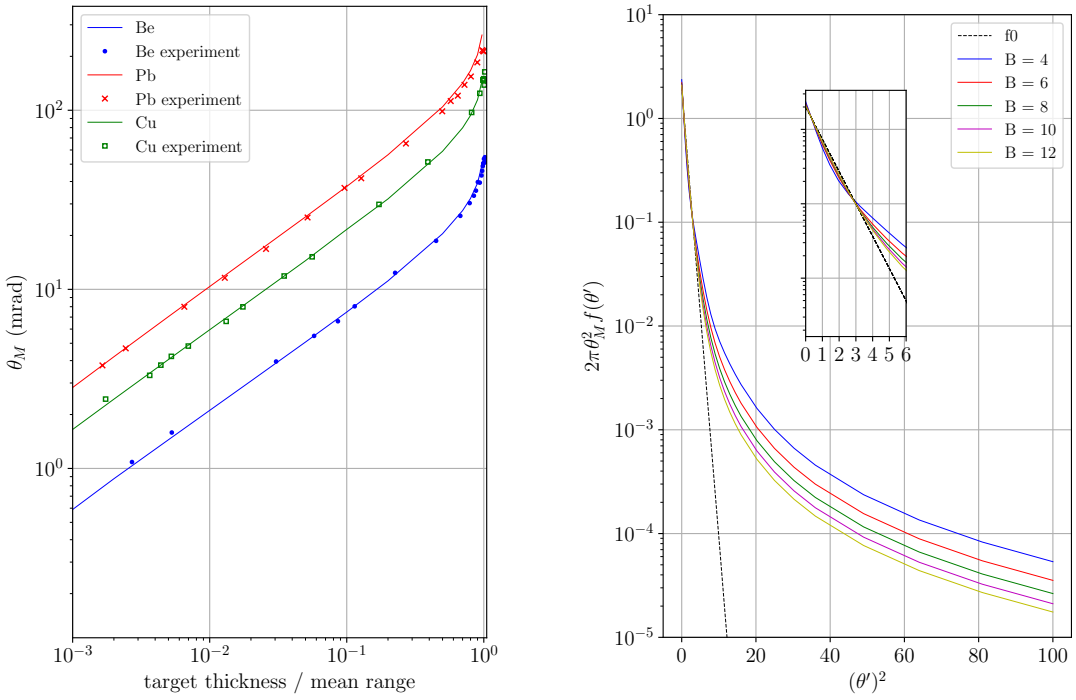

(a) Molière theory vs experiment for three metals.

(b) Molière angular distribution.

Figure 1.12: Representation of multiple scattering. Reproduced from [46].

For complex geometries, it is more convenient to find a differential relation $d\theta/dx$ as the result does not depend on the step size Δx. Therefore, it is possible to define a *Scattering Power*:

$$T \equiv \frac{\langle d\theta\rangle}{dx}\,\frac{\text{radian}}{\text{cm}}\,. \tag{1.23}$$

Integral over x for a homogeneous medium of arbitrary thickness give the θ angle in the Gaussian region. Different descriptions of $T(x)$ exist and are detailed in [47, 48]. In this report, two *Scattering Powers* are compared. The first one is described by Farley [48] and the second one by Gottschalk [32].

Farley
In 2004, Farley proposed a methodology to easily compute beam characteristics at the exit of a block of matter. Considering a material with a radiation length X_0, which is the path length covered by an electron before its energy is reduced by a factor e owing to radiation [49, 50], and a charged particle of atomic number Z with a momentum p and a reduced speed β (v/c), the particles suffer many small-angles elastic scattering. Assuming a Gaussian distribution, the Scattering Power T_F is given by:

$$T_F = \frac{200\, Z^2}{X_0 (p\beta)^2}\,. \tag{1.24}$$

Gottschalk
In 2014, a new scattering power is introduced by Gottschalk:

$$T_{dM} \equiv f_{dM}(pv, p_1v_1) \times \left(\frac{E_s}{pv}\right)^2 \frac{1}{X_S}\,. \tag{1.25}$$

where pv (resp. p_1v_1) is the kinematic quantity in the point of interest (resp. at the entrance of the slab). In this relation, X_S is the scattering length (analogous to the radiation length [32]), E_s is fixed at 15.0 MeV and f_{dM} is a correction factor which represents the non-locality, e.g the fact that the energy decreases as a function of the depth in the slab. These quantities are defined by the following relations:

$$\frac{1}{\rho X_S} \equiv \alpha N r_e^2 \frac{Z^2}{A}\left(2\log_{10}(33219(AZ)^{-1/3}) - 1\right)\,, \tag{1.26}$$

$$\begin{aligned} f_{dM} \equiv 0.5244 + 0.1975\log_{10}(1-(pv/p_1v_1)^2) + 0.2320\log_{10}(pv) - \\ 0.0098\log_{10}(pv)\log_{10}(1-(pv/p_1v_1)^2)\,, \end{aligned} \tag{1.27}$$

with α, N and r_e are respectively: the fine structure constant, the Avogadro's number and the electron radius.

These two Scattering Powers will be compared to numerical simulations in chapter 4.

1.3 Neutron interactions

Figure 1.13 illustrates different processes that may occur in a target for neutrons. The spallation process is the non-elastic reaction with high energy hadron-nucleus and is described in section 1.4

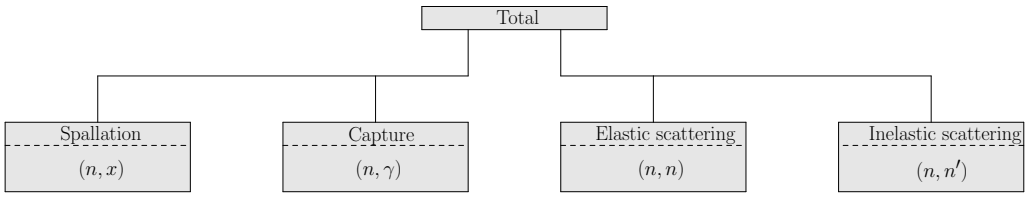

Figure 1.13: Summary of the different neutrons interactions. Adapted from [51].

Figure 1.14 shows an example of the different contributions of partial cross-section to the total cross section (see equation (1.1)). In the case of low neutron energy in an europium target, the capture is the most important process while around 1MeV incident energy, the elastic and inelastic cross sections have the same order of magnitude.

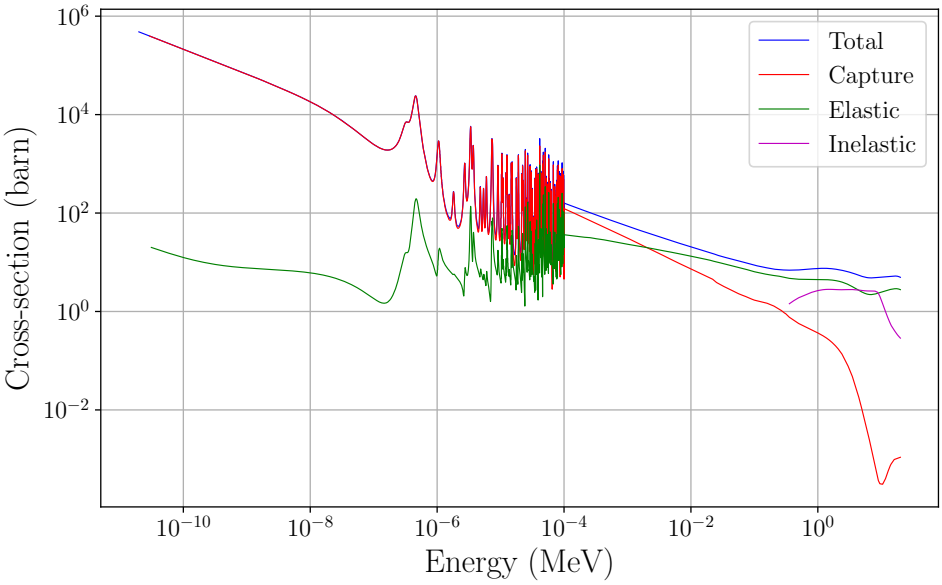

Figure 1.14: Partial cross section in function of the neutron energy. Data taken from [52].

As the spallation reaction has been described in section 1.4, we explain hereafter the other interactions: the capture, the elastic and the inelastic process [53].

1.3.1 Capture

The neutron is absorbed by the nucleus to form a heavier one. In many cases, the emission of a gamma follows the neutron absorption (radiative capture). The radiative capture is the main contribution to the total cross-section for neutrons with an energy below 0.5MeV [53].

$$n^0 + {}^{A}_{Z}X = {}^{A+1}_{Z}X^* \,. \tag{1.28}$$

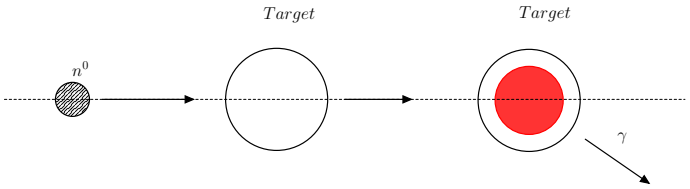

Figure 1.15: Radiative capture of a neutron and γ emission.

1.3.2 Elastic scattering

The elastic scattering is a collision between the neutron and the nucleus, where after reaction, the neutron is deviated from its trajectory with a transfer of kinetic energy and the nucleus is left in his ground state (see figure 1.16).

$$n^0 + {}^{A}_{Z}X = n^0 + {}^{A}_{Z}X \,. \tag{1.29}$$

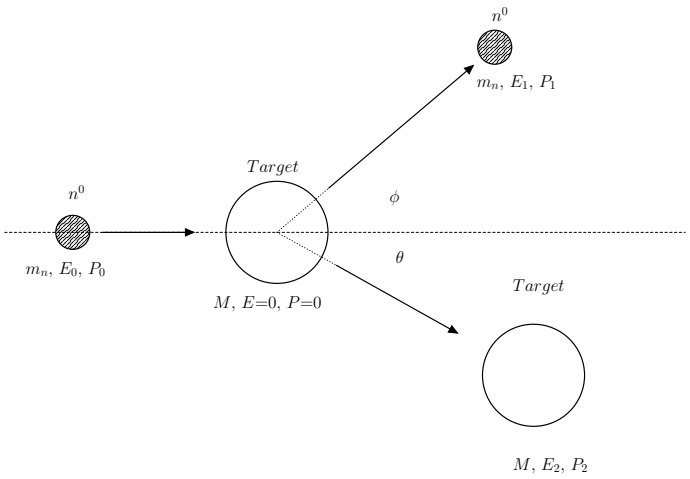

Figure 1.16: Elastic scattering.

Using the laws of the conservation of momentum P and energy E, we have:

$$\begin{cases} E_0 = E_1 + E_2\,, \\ P_0 = P_1 cos(\phi) + P_2 cos(\theta)\,, \\ P_1 sin(\phi) = P_2 sin(\theta)\,, \end{cases} \tag{1.30}$$

with $E = P^2/2m$ and m the mass of the particle. The energy of the particle after interaction is given by:

$$E_1 = E_0 \frac{1}{(A+1)^2}\left(cos(\phi) + \sqrt{cos^2(\phi) + A^2 - 1}\right)\,, \tag{1.31}$$

where $A = M/m_n$ is the ratio of the mass of the target to that of the neutron.

1.3.3 Inelastic

For inelastic interaction, a neutron is captured by the nucleus and then re-emitted in a different direction than the initial neutron with a lower energy as shown in figure 1.17. The resulting nucleus is in an excited state and therefore, it can de-excite by emission of a gamma particle.

$$n^0 + {}^A_Z X = n^0 + {}^A_Z X^*\,. \tag{1.32}$$

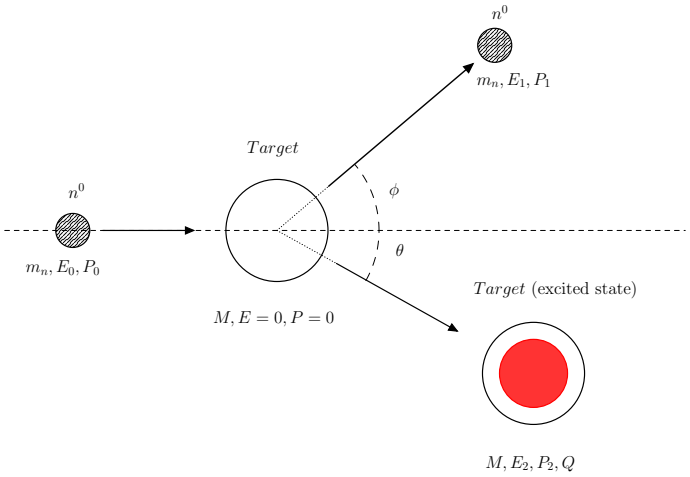

Figure 1.17: Inelastic scattering of neutron.

Q is defined as the excess of kinetic energy of the product particles over that of the original particles [53]. The energy of the neutron after collision is given by:

$$E_1 = \frac{1}{(1+A)^2}\left(cos^2(\phi)\sqrt{E_0} \pm \sqrt{E_0(cos(\phi)+A^2-1)+A(1+A)Q}\right)^2 . \tag{1.33}$$

There is a minimum energy above which the reaction is possible. This threshold is given when $cos(\phi) = 0$ and then (1.33) becomes [54]:

$$E_0 = -\frac{A+1}{A}Q . \tag{1.34}$$

As example, the first excited state of the ^{151}Eu is 150.919 keV which we observe on figure 1.14.

1.4 Spallation reaction

Spallation reaction refers to non-elastic reaction which occurs with high energy hadron-nucleus (p^+, n^0, π, etc.) in MeV to GeV energy range. This reaction produces many secondary particles, mainly neutrons. As example, figure 1.18 shows the cross section as a function of the number of emitted neutrons for a 1.2 GeV energy proton beam incident on a lead target [55]. We observe that for one incident proton, there is a large probability to create 15 neutrons (maximum of the cross section).

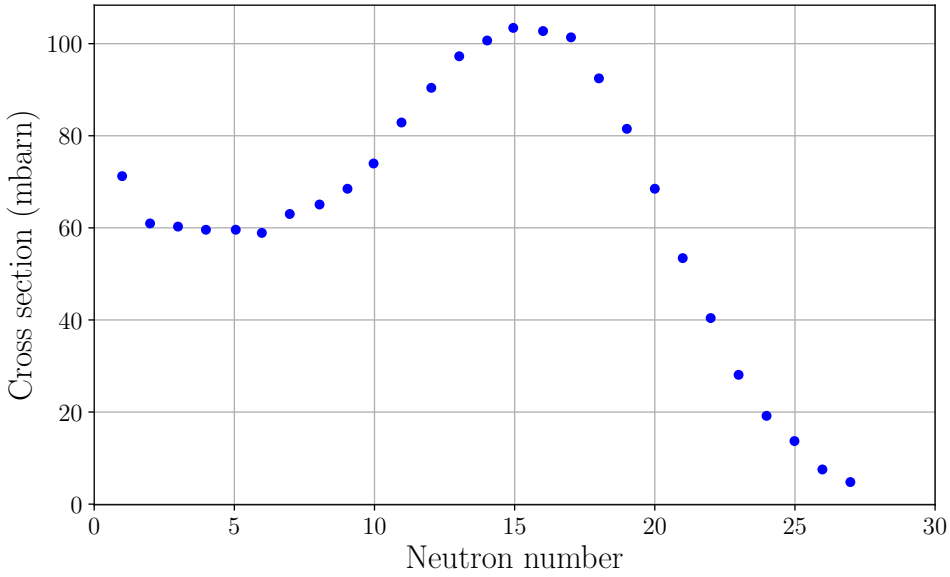

Figure 1.18: Neutron multiplicity cross section as function of the neutron number for a 1.2 GeV energy proton beam incident on lead. Reproduced from [55].

Unfortunately, up to now, this process is not characterized by cross section databases and has to be modeled [24]. In 1947, Serber [56] suggested that the spallation reaction could be separated into two stages. The first one, called the intranuclear cascade (INC), is very fast ($10^{-22}s$) and consists of a succession of interactions between the incident particle and the nucleons of the target. High energy particles (n^0, p^+, π) are emitted mainly in the direction of the incident particle during this step. The second stage, evaporation, is slower than the INC ($10^{-20}s$) and consists of an isotropic emission of low energy particles

or by fission of the remnant nucleus. The representation of a spallation reaction is shown in figure 1.19 [57]. The models used in this thesis are presented afterwards. As the Pauli exclusion principle is always applied, it implies that the collision products cannot be emitted in occupied states.

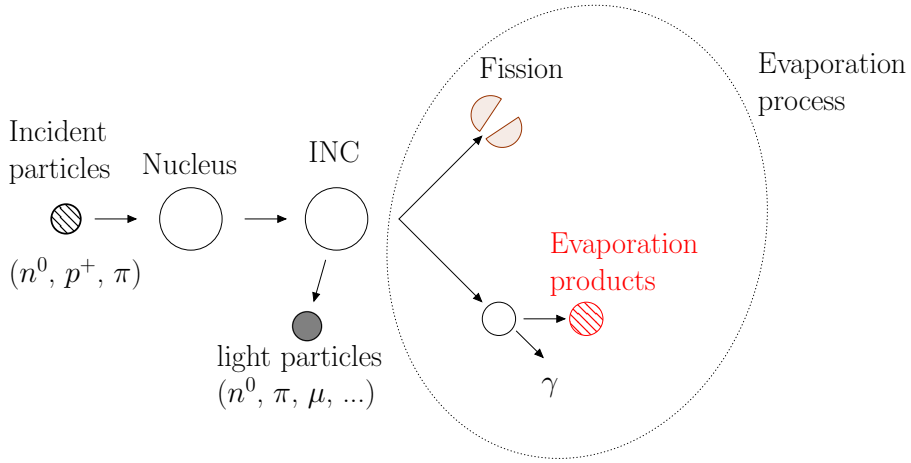

Figure 1.19: Scheme of a spallation reaction. A light particle collides with a nucleus producing an intranuclear cascade. This nucleus disintegrates by emission of particles (evaporation) or by fission. Reproduced from [57].

The figure 1.20 shows the neutron yield experimentally measured for a carbon target irradiated by a 113 MeV energy proton beam [58]. We observe that the high energy neutrons are produced preferably in the direction of the incident particle, corresponding to the INC. Low energy-neutrons are emitted isotropically around the target, this is due to evaporation.

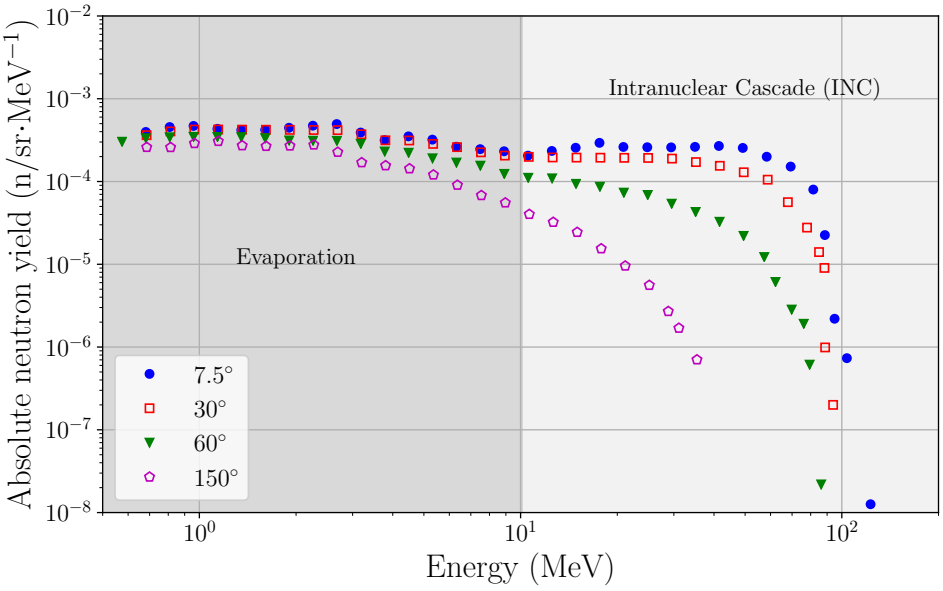

Figure 1.20: Experimental neutron yields. Irradiation of a carbon target by 113 MeV *energy protons. Extracted data from [58].*

1.4.1 Intranuclear cascade (INC)

Hereafter, the formalism of the intranuclear cascade (INC) is discussed as well as the condition of validity. Then, we describe the mathematical basis of the INC and the three models of the intranuclear cascade used in this thesis are explained: Bertini [59, 60, 61], Binary cascade (BIC) [62] and Liège model (INCL) [63, 64]. Each of them is implemented in the software mainly used in this work: *Geant4*.

1.4.1.1 Intranuclear cascade formalism

The intranuclear cascade describes the collision between a particle and a nucleus using a semi-classical microscopic description [65]. When the initial particle enters the nucleus, treated as a system of nucleons in a potential and a momentum, it may collide with one of these nucleons. Different particles are generated, collide also with the intranuclear nucleons and so on. A particle can leave the nucleus if it reaches its boundary and if its energy is sufficient. All transmitted particles are the product of the intranuclear cascade. Two assumptions are made to provide a mathematical formulation of the INC [65]:

1. The motion of the particles involved in the cascade follows the laws of the classical motion.

2. Any collision is instantaneous and localized in a point.

The principle of the intranuclear cascade is to consider the dominance of independent binary collisions [66]. This means that each collision can be considered independently. It is assumed that the particles move on a straight line without energy loss between collisions. This assumption is satisfied when the following condition is met [67, 64]:

$$\lambda_B << r_s < \lambda \leq d\,. \tag{1.35}$$

Where λ_B is the de Broglie wavelength[1], λ is the mean free path of the particle in the nucleus (see equation (1.3)), r_s is the maximal interaction distance between two nucleons and d is the average distance between nucleons. The first inequality ensures that the projectile see the nucleons of the target individually and legitimate the use of classical trajectories between collisions.

The energy range validity of the INC is graphically represented in figure 1.21, showing the mean free path of the particle comparatively to the quantities defined above. R is fixed as the radius of a typical heavy nucleus [67]. From this figure, we deduce that the condition is valid for a projectile with an energy higher than a few GeV. Experimentally, INC has been validated from an energy of 40 MeV [66].

Different models exist to treat the INC as the Vlasov-Uehling-Uhlenbeck (VUU) transport equations or the Quantum Molecular Dynamics (QMD). They describe both the collisions between the projectile and the target as well as the time evolution of the system before its thermalization.

[1]The de Broglie wavelength is defined as the ratio between the Planck constant and the relativistic momentum of the particle: $\lambda_B = h/p$

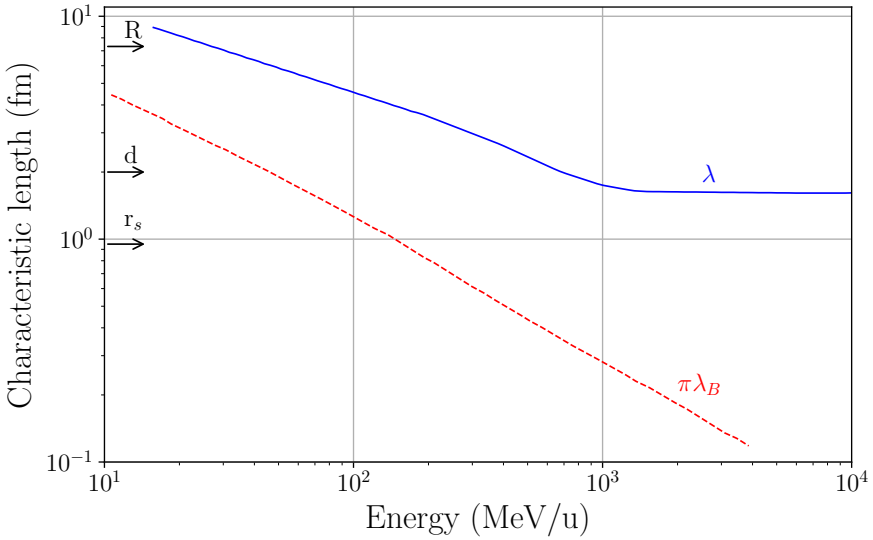

Figure 1.21: Energy range validity of the intranuclear cascade. Reproduced from [67].

1.4.1.2 Mathematical formulation of the intranuclear cascade

As the impact parameter, the position and the momentum of the nucleons in the nucleus are chosen randomly, we use a statistical approach to describe the INC. Let us consider a nucleus with Z protons and N neutrons. Each nucleon has a position $\mathbf{r}_i$ and a momentum $\mathbf{p}_i$.

Let us consider a dynamical system governed by a phase space distribution function $f(\mathbf{r}, \mathbf{p}, t)$ and a Hamiltonian $H(\mathbf{r}, \mathbf{p}, t)$ with $\mathbf{r}$, the position, $\mathbf{p}$, the momentum and t, the time. The Vlasov equation gives the time evolution of the phase space distribution in absence of collisions [68]:

$$D_t(f) = \frac{\partial f}{\partial t} + \nabla_{\mathbf{r}} f \, \nabla_{\mathbf{p}} H - \nabla_{\mathbf{p}} f \, \nabla_{\mathbf{r}} H = 0 \,. \tag{1.36}$$

If we consider an interaction between two particles, namely 1 and 2, given after the collision particles 3 and 4, equation (1.36) must be adapted to take into account the nucleus-nucleus collision. This is done using the Uehling-Uhlenbeck collision term which describes the evolution of the phase-space distribution induced by the residual interaction. We modify equation (1.36) taking into account the collision term:

$$D_t^{Coll}(f) = \int d\mathbf{r_2} \, I(\mathbf{r_1}, \mathbf{p_1}, \mathbf{r_2}; t) \,, \tag{1.37}$$

with:

$$I = \int\int\int d\mathbf{p_2} d\mathbf{p_3} d\mathbf{p_4} \delta(d\mathbf{p_1} + d\mathbf{p_2} - d\mathbf{p_3} - d\mathbf{p_4}) \delta(\epsilon_1 + \epsilon_2 - \epsilon_3 - \epsilon_4) \tag{1.38}$$
$$\left(\frac{d\sigma}{d\Omega}\right)_{NN}^{eff} \left[(1-\bar{f}_1)(1-\bar{f}_2) f_3 f_4 - (1-\bar{f}_3)((1-\bar{f}_4)) f_1 f_2\right] \,.$$

ϵ_i and $\mathbf{p}_i$ refer to the energy and the momentum of the i^{th} particle, f_i are the density distributions and $\bar{f}_i$ are the occupation probabilities. The nucleon-nucleon (NN) cross

section in the nuclear medium can be deduced from the free relative energy according to:

$$\left(\frac{d\sigma}{d\Omega}\right)^{eff}_{NN} = \left(\frac{d\sigma}{d\Omega}\right)^{free} (1 - Y(\rho)) \ . \tag{1.39}$$

$Y(\rho)$ is a density scaling factor, which takes into account the reduction of the cross section for increasing density. $Y(\rho)$ is expressed as the ratio between the square of the Brueckner matrix G and the free scattering matrix T [68, 69]. This Brueckner matrix is a correction of the potential and is the solution of the Bethe-Goldstone equation [70, 71]:

$$G = V + V\frac{Q_F}{E - H_{12}}G\,, \tag{1.40}$$

where V corresponds to the effective-interaction potential, Q_F is the Pauli operator forbidding occupied intermediate states and $(E - H_{12})$ shows the influence of the mean field between nucleons.

Considering the Hamiltonian of the form $H = \frac{p^2}{2m} + U(\mathbf{r}, \mathbf{p})$, equation (1.37) becomes:

$$D_t^{Coll}(f) = \frac{\partial f}{\partial t} + \frac{\mathbf{p}}{m}\nabla_{\mathbf{r}} f + \nabla_{\mathbf{p}} U \nabla_{\mathbf{r}} f - \nabla_{\mathbf{p}} f \nabla_{\mathbf{r}} U = \int d\mathbf{r_2}\, I(\mathbf{r_1}, \mathbf{p_1}, \mathbf{r_2}; t)\,. \tag{1.41}$$

To be valid, this equation needs to satisfy the following conditions [67]:

1. *Closure approximation*: the correlation between the particles in the collision term is negligible.
2. *Low gradient approximation*: the potential U is a smooth function of the spatial extension of f.
3. *Independence of collisions*: the particles lose memory after collision.

Bunakov et al. [72] have demonstrated that the resolution of equation (1.41) with Monte Carlo methods correspond to the intranuclear cascade algorithm as illustrated on figure 1.22 [61, 65, 73]. The different steps of the Monte Carlo simulation are given below.

(1) The different characteristics of the primary particle are calculated.

(2) An impact parameter is chosen randomly and a point on the surface of the target is defined.

(3) The particles are propagated until their remoteness is sufficient to have reaction. This minimal distance is calculated with the relation $d_{min} = \sqrt{(\sigma_{NN,tot}/\pi)}$, with $\sigma_{NN,tot}$, the total NN reaction cross section.

(4) The interaction point is determined from the mean free path.

(5) We check if the particles goes out of the nucleus without undergoing collisions.

(6) If the interaction point is inside the nucleus, the probability that the i^{th} reaction occurs is computed using the ratio σ_i/σ_{tot}.

(7) From the type of the interactions, the characteristics of all secondary particles are determined.

(8) If the collision is not allowed according to the Pauli principle, the reaction is prohibited and the simulation returns to step (4).

(9) The energy of the particle is compared with a cut-off energy (E_{cutoff}). Only particles with an energy higher than E_{cutoff} contribute to the INC and their characteristics are stored in (10) and the cascade calculation starts again from step (3).

(10) The particles with an energy lower than E_{cutoff} are supposed to be absorbed by the nucleus and contribute to the characteristics of the residual nucleus.

(11) The calculation is carried out until all secondary particles are absorbed or leave the nucleus. This step is made by block (10) and (11).

(12) After the intranuclear cascade, the characteristics of the residual nucleus are computed and the nucleus is de-excited in a second step (see section 1.4.2).

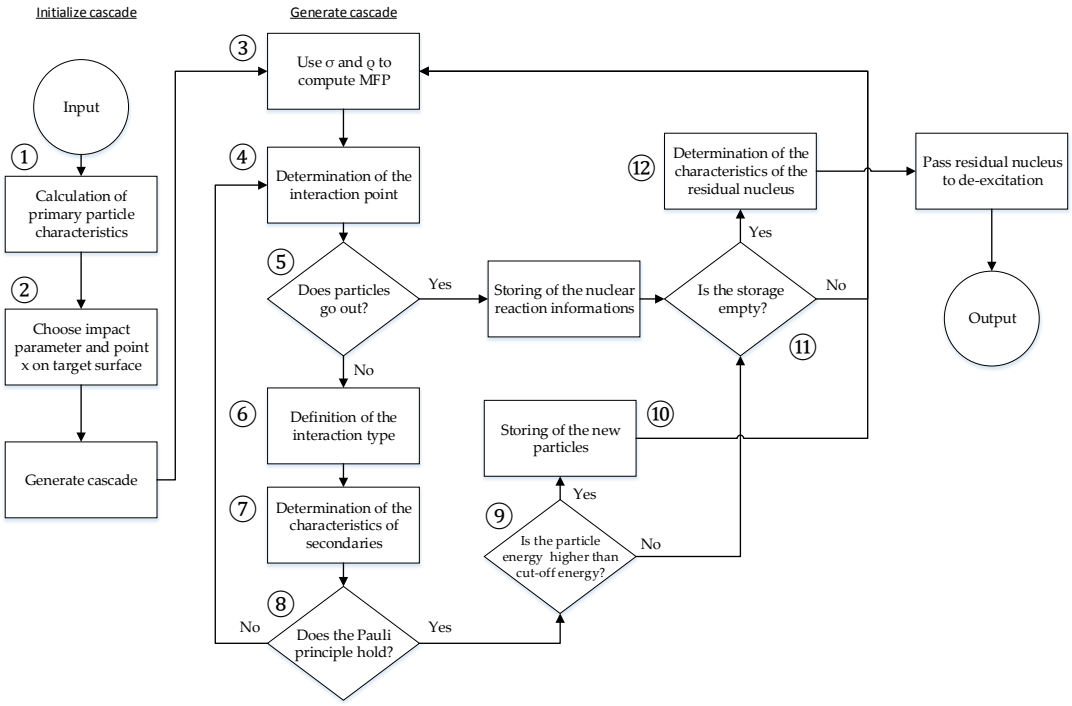

Figure 1.22: General algorithm of the intranuclear cascade as implemented in Geant4. *Reproduced from [61, 65].*

Different approaches exist to solve this algorithm. In this thesis, we give an overview of the Bertini, the Binary cascade (BIC) and the intranuclear cascade of Liège (INCL) models. The major differences between models are on the approximation of the nuclear charge distribution and on the potential.

1.4.1.3 Bertini Model

In 1963, Bertini writes his thesis about the Monte Carlo calculations on intranuclear cascade. The purpose was to develop a realistic model to describe the different steps of the cascade [60, 59, 61, 74]. Hereafter, we briefly summarize the different steps of the model.

Construction of the target We consider a target with an atomic number A and a nuclear charge distribution of the nucleons given by a Wood-Saxon distribution:

$$\rho(r) = \frac{\rho_0}{e^{(R-R_0)/a}+1}\,, \tag{1.42}$$

where ρ_0 is a normalization constant, $R_0 = 1.07A^{1/3} \times 10^{-13}$cm and $a = 0.545 \times 10^{-13}$cm. In this model, this continuous distribution is approximated with three concentric spheres. The density of each region is equal to the average value of the continuous distribution in that region. In function of A, nuclei models are different:

1. If $A = 1$ (hydrogen), a simple collision is performed.
2. If $1 < A < 4$, the nucleus model consists of one layer with radius of 8.0 fm.
3. If $4 < A < 11$, the nucleus model consists of three concentric spheres with radii:

$$r_i(\alpha_i) = \sqrt{C_1^2\left(1 - \frac{1}{A} + 6.4\sqrt{-\log(\alpha_i)}\right)}\,, \tag{1.43}$$

   with $\alpha_i = \{0.01, 0.3, 0.7\}$ and $C_1 = 3.3836A^{1/3}$.

4. If A > 11, the nucleus is also composed of three concentric spheres with radii:

$$r_i(\alpha_i) = C_2 * log\left(\frac{1 + e^{-\frac{C_1}{C_2}}}{\alpha_i} - 1\right) + C_1\,, \tag{1.44}$$

   with $\alpha_i = \{0.01, 0.3, 0.7\}$, $C_1 = 3.3836A^{1/3}$ and $C_2 = 1.7234$

In each region, the momentum distribution of the nucleus ($f(p)$) follows a Fermi distribution:

$$\int_0^{p_{F_i}(r_i)} f(p)dp = N_p \quad \text{or} \quad N_n\,, \tag{1.45}$$

where N_p (resp. N_n) is the number of protons (resp. neutrons). The Fermi momentum $p_{F_i}(r_i)$ is given by:

$$p_{F_i}(r_i) = \hbar\left(\frac{3\pi^2\rho(r_i)}{2}\right)^{1/3}\,. \tag{1.46}$$

The potential of nucleon N in the i^{th} zone is given by:

$$V_i = \frac{p_{F_i}(r_i)^2}{2m_N} + BE_N(A, Z)\,, \tag{1.47}$$

with m_N, the nucleon mass and BE_N the nucleon's binding energy.

Cross sections and cascade generation To determine the location of the interactions in the nucleus, the total hadron-nucleon cross-sections are used. They are tabulated using parametrizations described in [75, 76]. These parametrizations are obtained by fitting experimental results for different targets and energies and are available in the Evaluated Nuclear Data File (ENDF) database.

Some quantities as the path length of nucleons in the nucleus, the type of the interaction and the multiplicity of the secondaries, in the broad sense, are determined from the local density and the free nucleon cross-sections available in [77, 60]. The figure 1.23 shows the

cross-section for (p, p) reaction and (p, n) reaction. The (n, n) cross section is assumed to be equal to the (p, p) cross-sections [60].

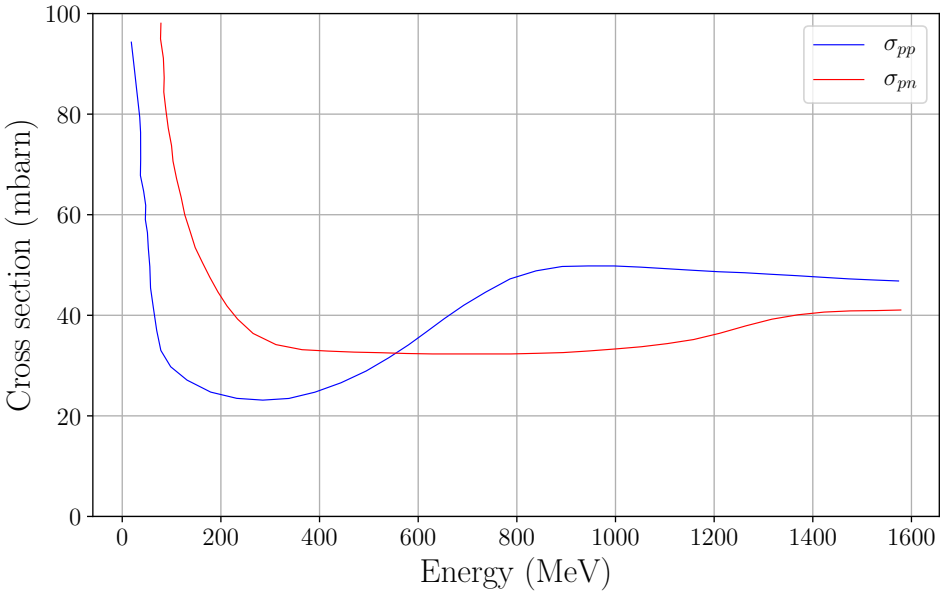

Figure 1.23: Proton-Proton (blue) and Neutron-Proton (red) total cross-section. Reproduced from [60].

Emissions angles after collisions are determined from experimental differential cross-sections. As an example, we show in figure 1.24, the angular distribution for (π^-, p) elastic scattering [78] for (π^-, p) at 350 MeV.

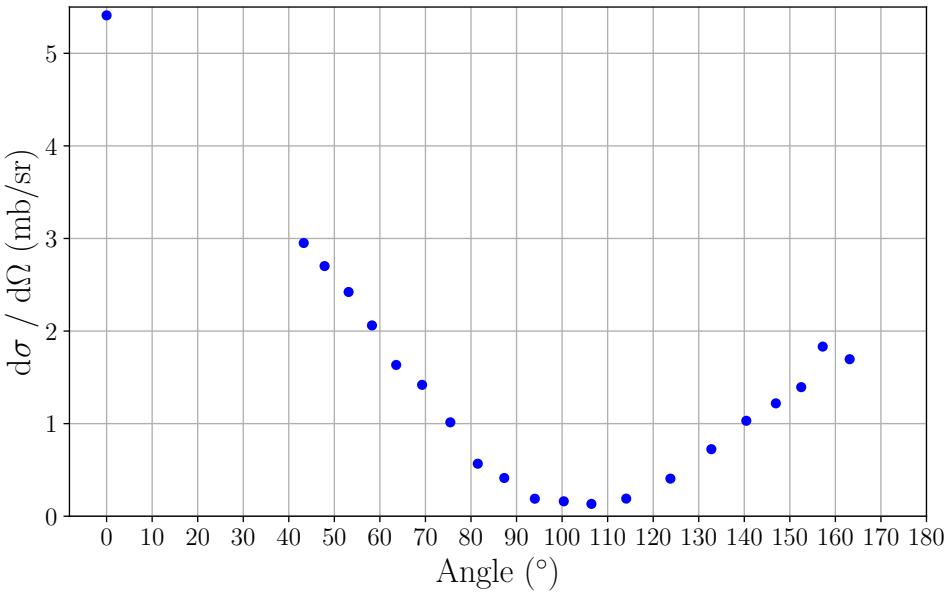

Figure 1.24: Differential cross section for (π^-, p) elastic scattering. Data extracted from [78].

Determination of the excitation energy In the Bertini model, the excitation energy of the resulting nucleus at the end of the cascade is calculated from the expression:

$$E^* = T_i - T_0 - 7(n-1)\,, \tag{1.48}$$

where T_i is the kinetic energy of the incident particle, T_0 is the sum of the kinetic energy of the outgoing particles, n is the number of emitted particles and 7 (MeV) is the binding energy of the most loosely bound nucleus which is assumed to be constant for all nuclei.

1.4.1.4 Binary Cascade Model

The Binary Cascade (BIC) is a model developed in 2004 and which proposes a new approach for the treatment of the intranuclear cascade [62, 79]. This model is a feature between a classical code and a quantum molecular dynamics model (QMD). Each participating nucleon is described as a Gaussian wave package:

$$\phi(x, q_i, p_i, t) = \frac{2}{(L\pi)^{3/4}} \exp\left(-2/L(x - q(t))^2 + ip_i(t)x\right)\,, \tag{1.49}$$

where x and t are the space and time coordinates, $L = 2.16$ fm and q_i (resp.p_i) describes the position (resp. the momentum) space of the nucleon i. A complete description of QMD is detailed by Niita et al. in [80]. During the cascade, this package is propagated in time and space and suffers collisions with nucleons in the nuclear medium. Only primary particles or secondary generated during the cascade (called participants) are propagated. The collisions between participants are not considered.

Construction of the target In the BIC model, the nucleon distribution is given by a harmonic-oscillator for light nuclei and by a Wood-Saxon distribution for target with $A > 16$. We have

1. if $A < 16$:
$$\rho(r) = \left(\pi R^2\right)^{-3/2} \exp\left(-\frac{r^2}{R^2}\right)\,, \tag{1.50}$$
where $R^2 = 0.8133\ A^{2/3}$ fm^2

2. For target with $A > 16$:
$$\rho(r) = \frac{\rho_0}{1 + \exp\left(\frac{r-R}{a}\right)}\,, \tag{1.51}$$
with ρ_0 given by:
$$\rho_0 = \frac{3}{4\pi R^3}\left(1 + \frac{a^2\pi^2}{R^2}\right)^{-1}\,. \tag{1.52}$$
Here, $a = 0.545$ fm, R $= r_0\ A^{1/3}$ fm with $r_0 = 1.16\ \left(1 - 1.16A^{-2/3}\right)$ fm

The nucleon position is chosen randomly according the nuclear density $\rho(r)$. To take the repulsive core into account, a minimum inter-nucleon distance of 0.8fm is fixed.

The momentum p_i of the nucleons is chosen randomly between 0 and the Fermi momentum $p_F^{max}(r_i)$. This latter one is obtained as a function of the nuclear density:

$$p_F^{max}(r) = \hbar c \left(3\pi^2\rho(r)\right)^{1/3}\,. \tag{1.53}$$

To ensure that the vector sum of the nucleon momenta is zero, the momentum of the last constructed nucleon is fixed to $p_{\text{rest}} = -\sum_{i=1}^{i=A-1} p_i$.

The Hamiltonian in the BIC model is calculated from time-independent optical potentials. When the beam particle is composed of protons or neutrons, the potential used is determined by the local Fermi momentum $p_F(r)$ as:

$$V(r) = \frac{p_F^2(r)}{2m}\,. \tag{1.54}$$

Cross sections and cascade generation Experimental data are used in the calculation of the total, inelastic and elastic cross sections. For hadron-nucleon scattering ((p,p) and (p,n) reactions), data are taken from the Particle Data Group for both elastic and inelastic collisions [81].

Determination of the excitation energy At the end of the cascade, the residual nucleus is characterized by its number of nucleons in the nucleus, its number of holes (difference between the number of nucleons in the incident particle and the number of nucleons in the pre-fragment), its number of excitons (nucleons captured in the residual nucleus). The excitation energy is given by the energy of the excitons in the residual nucleus.

1.4.1.5 Intranuclear Cascade of Liège

The Intranuclear cascade of Liège (INCL) model is the latest model introduced and it is still under development. The version described in this thesis is version 4 [82, 83]. In [84], an extension of the intranuclear cascade for irradiation by light nuclei is made but is out of the scope of this work.

Construction of the target Depending on the value of the atomic number A of the target, different distributions for the density are used [85]:

1. A $\leq$ 6: the distribution is Gaussian with a tabulated value for the standard deviation which is equal to $\sqrt{\frac{3}{5}}p_F$ [84].

2. 6 < A $\leq$ 28: A modified harmonic oscillator is used:

$$\rho(r) = \left(1 + R_0\left(\frac{r}{a}\right)^2\right)\exp\left(-\left(\frac{r}{a}\right)^2\right)\,, \tag{1.55}$$

   where $R_0 = (2.745\times10^{-4}A + 1.063)A^{1/3}$ fm and $a = 0.510 + 1.63^{-4}A$ fm.

3. A > 27: the radial density is given by a Wood-Saxon distribution, up to a maximum distance $R_{max} = R_0 + a$.

$$\rho(r) = \frac{1}{1+\exp\left(\frac{r-R_0}{a}\right)}\,. \tag{1.56}$$

The following relation must also be satisfied:

$$\int_0^{R_{max}} \rho(r)\vec{dr} = A\,. \tag{1.57}$$

The momentum of the nucleon is chosen randomly in the Fermi sphere with a maximum value of p_F (equation (1.53)). Nucleons with a large momentum are expected to reach a larger radial distance than a nucleon with a small momentum. It is thus assumed that the

number of nucleons with a momentum between p and $p + dp$ is the same as in a layer of density profile $\rho(R(p))$ and $\rho(R(p + dp))$ as shown in figure 1.25.

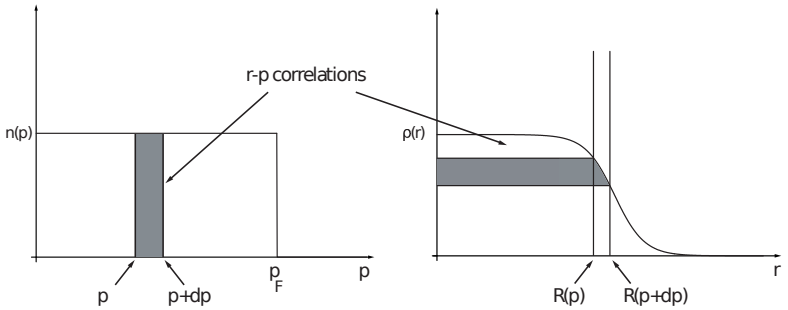

Figure 1.25: Illustration of the correlation between the position and the momentum. Reproduced from [82].

This implies:

$$A\frac{4\pi p^2 dp}{\frac{4\pi}{3}p_F^3} = \frac{4\pi}{3}R^3(p)dp\,. \tag{1.58}$$

The boundary conditions are set to $R(0) = 0$ and $R(p_F) = R_{max}$, which gives:

$$\left(\frac{p}{p_F}\right)^3 = \frac{4\pi}{3}\int_0^{R(p)} \frac{d\rho(r)}{dr}r^3 dr\,. \tag{1.59}$$

With this relation, the following algorithm is used to determine the position and the momentum of the nucleon:

1. $\vec{p}$ is chosen randomly in a sphere of radius p_F.
2. $R(p)$ is computed using the relation (1.59).
3. $\vec{r}$ is chosen at random in a sphere of radius $R(p)$.

In the nucleus, the mean field is described by an attractive square potential V_0 for all baryons with an extension equal to $R(p)$. To satisfy energy conservation law, the incident particle has an energy equal to $T_i + V_0$ when it enters the nucleus (at $r = R_{max}$).

Cross sections and cascade generation After the initialization of the projectile and the target, an impact parameter of the projectile is chosen randomly in a circle of radius R_{max}. Then, particles are propagated through the medium using relativistic kinematics and straight trajectories. A distinction is introduced between *participants* and *spectators*. The projectile is considered as a *participant*. Each particle that is collided with a *participant* (or is created during an inelastic reaction) becomes a *participant*, otherwise, particles are *spectators*. This distinction avoids interactions between *spectators*. When two particles are separated by a distance d_{min}, an impact parameter b_{min} is computed using the relation [82]:

$$b_{min}^2 = d_{min}^2 + \frac{(\vec{d}_{min}\cdot\vec{\beta}_{cm})^2}{1-\beta_{cm}^2}\,, \tag{1.60}$$

with $\vec{\beta}_{cm}$, the velocity of the center of mass in the laboratory data frame. The quantity πb_{min}^2 is compared to the cross section for the energy of center of mass ($\sqrt{s}$) of the two particles.

1. $\pi b_{min}^2 > \sigma(\sqrt{s})$, particles do not interact and propagate until the next collision.
2. $\pi b_{min}^2 < \sigma(\sqrt{s})$, a collision happens if the Pauli principle is satisfied.

In the INCL model, the experimental cross sections are used when data are available otherwise, different parameterisations may be used. These ones are summarized in [73]. Figure 1.26 illustrates the behaviour of the cascade, the incoming nucleon reaches the minimum distance d_{min} and undergoes elastic reaction or inelastic reaction (with production of Δ resonance). Such resonance decays in a pion and a nucleon which are transmitted through the nuclear surface.

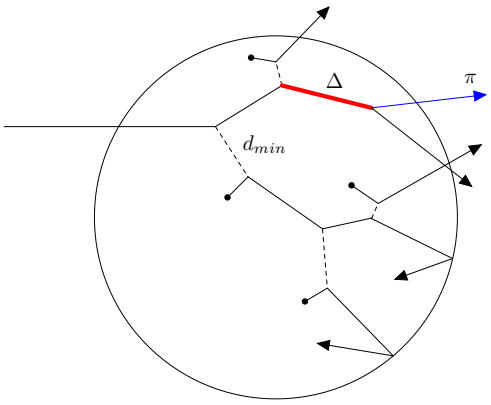

Figure 1.26: Representation of the intranuclear cascade in the Liège model. Reproduced from [82].

Transmission or reflection on the surface The INCL model introduces the concept of reflection and transmission on the nucleus surface. If a participant reaches the nuclear surface, a transmission probability is computed as a function of the kinetic energy T_i and of the nuclear mean field V_0 [86]:

$$T = \frac{4\sqrt{T_i(T_i - V_0)}}{2T_i - V_0 + 2\sqrt{T_i(T_i - V_0)}} e^{-2G}\,, \tag{1.61}$$

where G is the Gamow factor. If the energy of the particle is lower than a threshold, it is reflected. Otherwise, it is reflected on the target or transmitted with the probability T. For transmission, its final energy is given by $T_{end} = T_i - V_0$ and there is no change of direction.

Stopping time of the cascade The major difference between INCL and the other developed models is the time dependence in the cascade. This time, t_{stop} determines the boundary between the intranuclear cascade and evaporation model which is described in section 1.4.2. t_{stop} corresponds to:

$$t_{stop} = f_{stop}\, t_0 \left(\frac{A}{208}\right)^{0.16}\,, \tag{1.62}$$

where $t_0 = 70\text{fm}/c$ and $f_{stop} = 1$.

End of the cascade and excitation energy At t_{stop} or at the end of the cascade, the Δ resonances are forced to decay and with the conservation law for the energy, we write:

$$T_{lab} = K_{ej} + W_\pi + E_{rec} + E^* + S\,. \tag{1.63}$$

In this relation, K_{ej} is the kinetic energy of the emitted particles, W_π is the energy of pions, E_{rec} is the recoil energy of the nucleus, E^* is the excitation energy and S is the separation energy, i.e, the minimum energy to eject all pions and ejectiles from the nucleus in their ground state. E_{rec} and S are expressed as a function of the properties of the remnant nucleus [86]:

$$E_{rec} = \frac{\tilde{p}_{rem}^2}{2m_N A_{rem}}\,. \tag{1.64}$$

$$S = (A_T - A_{rem})\,(V_0 - T_F)\,. \tag{1.65}$$

This allows determining E^* which is used in a second time as input in evaporation model. All explanations about elementary collisions are described in [82].

1.4.2 Evaporation

Due to difference in time scale between the intranuclear cascade and evaporation (10^{-22}s vs 10^{-20}s), these processes are considered independently of each other. After the intranuclear cascade, the nucleus can be quite excited and then, may be de-excited through different channels in competition. In particular, emission of light particles (neutrons, protons, etc.), γ radiation, etc. can occur. Probability of emitting each type of particles is based on the assumption that the model reaches a statistical equilibrium after every evaporation step and on the principle of detailed balance [83, 87, 88].

Light particle emission The purpose of evaporation theory is to evaluate the probability of the emission of a particle ν with a mass m and an energy ϵ_ν. We consider an initial nucleus characterized by an excitation energy U_i and a total angular momentum J_i. This nucleus decays into a final nucleus (U_f, J_f) emitting a nucleon or a light nucleus ν with a kinetic energy ϵ_ν, spin s_ν and orbital angular momentum l. The decay width for this process can be calculated using [88]:

$$\Gamma\left(U_i, J_i; U_f, J_f, s_\nu\right) = \frac{2s_\nu + 1 k_f^2}{2\pi^2}\sigma_{fi}(U_i, J_i)\frac{(2J_f+1)\rho(U_f, J_f)}{(2J_i+1)\rho(U_i, J_i)}\,. \tag{1.66}$$

The energies U_i and U_f are related by $U_i = U_f + \epsilon_\nu + S_\nu + B_\nu$, where S_ν is the separation energy and B_ν the Coulomb barrier for the emitted particle. $\sigma_{fi}(U_i, J_i)$ is written in term of the transmission coefficients T as:

$$\sigma_{fi}(U_i, J_i) = \frac{\pi}{k_f^2}\frac{2J_i+1}{(2s_\nu+1)(2J_f+1)}\sum_{S=|J_f-s_\nu|}^{J_f+s_\nu}\sum_{l=|J_i-S|}^{J_i+S} T_\nu^l(\epsilon_\nu)\,, \tag{1.67}$$

with $S = J_f + s_\nu$ is the channel spin and T_ν^l incorporates the effects of the Coulomb and the centrifugal barrier together with the nuclear potential. By combining (1.66) and (1.67), the average decay rate R_ν of a nucleus emitting a particle ν is given by:

$$R_\nu = \frac{\Gamma_\nu}{\hbar} = \frac{1}{h}\frac{\rho(U_f, J_f)}{\rho(U_i, J_i)}\sum_{S=|J_f-s_\nu|}^{J_f+s_\nu}\sum_{l=|J_i-S|}^{J_i+S} T_\nu^l(\epsilon_\nu)\,. \tag{1.68}$$

Partial width of light particle emission process is obtained from summing over all possibilities of the angular momentum and integrating over all possible kinetic energy ϵ_ν of the emitted particle. It is thus expressed as:

$$\Gamma_\nu = \frac{1}{2\pi\rho(U_i)} \frac{4m_\nu R^2}{\hbar^2} T_f^2 \rho(U_i - S_\nu - B_\nu)\,, \tag{1.69}$$

with R the radius of the nucleus and T_f, the temperature of the final residue which is given by the relation [89]:

$$T_f = \sqrt{\frac{U_f}{c \cdot A}}\,. \tag{1.70}$$

γ emission The partial decay width for γ emission is parametrised by:

$$\Gamma_\gamma\left(\epsilon_\gamma\right) = 0.624 \cdot 10^{-9} \cdot A^{1.6} T^5 MeV\,. \tag{1.71}$$

Fission The fission decay width Γ_f may be calculated with:

$$\Gamma_f\left(U_i, J_i\right) = \frac{1}{2\pi\rho\left(U_i, J_i\right)} T_{sad}\rho\left(U_i - B_f\right)\,. \tag{1.72}$$

With B_f, the fission barrier and T_{sad}, the nuclear temperature at saddle.

Final probability for evaporation of the particle i is the branching ratio between the partial width and the sum of all evaporation possibilities:

$$P_i = \frac{\Gamma_i}{\sum_i \Gamma_i}\,. \tag{1.73}$$

1.5 Monte Carlo principle

In the previous section, we have described the different types of interactions between a particle and matter. In practice, we need to model a very large number of particles, all reactions are combined and the problem becomes impossible to solve analytically. This is the reason why Monte Carlo softwares have been developed. To attack complex problems like space computation of radiation levels in the International Space Station, shielding studies or medical applications, utilisation of Monte Carlo methods are mandatory. These methods were first introduced to solve the Boltzmann equation [54, 90] but with the development of computational power, more complicated problems could be solved in a reasonable time.

Lux and Koblinger [53] give a very comprehensive definition of a Monte Carlo simulation: *In all Monte Carlo applications, a stochastic model is constructed in which the expected value of a certain random variable is equivalent to the value of a physical quantity to be determined.*

In our application field, this is done using a pseudo random number generator which determines the probability distribution for scattering angle, track length, etc. These particles can obviously interact with the medium and create secondary particles which are added to the history of the incident particles. As said, the main purpose of particle

tracking is to evaluate the mean $\bar{x}$ of a certain quantity of interest (flux, number of created isotopes, etc.). For each particle, these quantities can be computed as well as their standard deviation (also noted σ). Then, the results of the simulation is given by:

$$\bar{x} = \frac{1}{N}\sum_{n=0}^{N} x_n \,, \tag{1.74}$$

$$\sigma(x) = \sqrt{\frac{1}{N-1}\sum_{n=0}^{N}(x_n - \bar{x})^2} \,, \tag{1.75}$$

with x_n, the contribution of the n^{th} history.

A standard criterion to evaluate the performance of a Monte Carlo simulation is the *Figure of Merit (FOM)* and is defined as the inverse of the product between the variance of the studied quantity and the time of the simulation (T):

$$FOM = \frac{1}{\sigma^2 T} \,. \tag{1.76}$$

A Monte Carlo simulation is efficient if the FOM is as large as possible. Reducing computing time using energy or time cutoffs is sometimes not sufficient and thus, for some complex problem as activation, variance reduction techniques must be applied. We can mention the *importance sampling*, the *exponential transformation* or the *forced collision* methods [54, 53]. In this work, the first one has been used and will be explained in section 1.5.2. The performance of a Monte Carlo simulation will be also analysed after the presentation of the Monte Carlo software.

1.5.1 Monte Carlo Software

Since 1950, many Monte Carlo softwares have been developed. In the field of shielding studies, detector design, space applications or medical physics, we may cite *Geant4*, *Phits* or *MCNPX* for example [91, 92, 93, 94, 95, 96]. In this work, version 10.03 of *Geant4*, version 2.7.0 of *MCNPX* and version 2.82 of *Phits* have been used and are briefly described. Fluka [97] is also a possibility but is not used in this thesis.

Geant4 *Geant4* (GEometry ANd Tracking) code is written in C++ and developed by the CERN and the High Energy Accelerator Research Organization from 1998. This software simulates the passage of particles, including exotic ones, through matter. Cross sections for different processes are taken from the existing database as ENDF [52]. The structure of a *Geant4* application defines the geometry, the type of incident particles, the magnetic field and the physics processes of interest. Many complex geometries can be imported through a GDML (Geometry Description Markup Language) module [98] and the analysis of the results can be done using the ROOT framework [99]. Moreover, users can implement their own functionalities to perform the simulation such as killing secondary particles for example.

MCNPX *MCNPX* (Monte Carlo N-Particles eXtended) code has been elaborated at Los Alamos National Laboratory 30 years ago. It uses standard evaluated nuclear data tables to transport protons and neutrons and physics models to transport neutrons, protons and other type of particles when no tabular data are available. Nuclear data and libraries up to 150 MeV are used [100]. This software is used in many applications and has been

validated for many cases. The user has to write a simple ASCII file as input which makes the program very quick when simple geometries have to be performed. A licence is needed to use *MCNPX*.

Phits The Particle and Heavy-Ion Transport code System (*Phits*) has been developed using the Fortran-77 code language in 2002 under the collaboration of Japan Atomic Energy Agency (JAEA), Research Organization for Information Science and Technology (RIST) and KEK [101]. *Phits* transports all particles in material over wide range of energy, using nuclear data libraries ans reaction models. Different packages may be used for the Stopping Power and for the angular straggling. The input file consists of an ASCII file, as in *MCNPX*, which describes the model used. This software can be used freely after a registration.

The principal aim of a radiation shielding is to protect peoples against radiations. However, at deeper zone of the concrete, the particles population is low and equation (1.76) could have a large variance and that implies that the *Figure of Merit* (*FOM*) of the simulation is low. To increase this quantity, some techniques of variance reduction must be implemented. In the next section, we explain the concept of the importance sampling.

1.5.2 Importance sampling

In shielding application, this method is used quite often because it reduces the error over any quantity in the deeper areas of the shielding. The shielding is divided into geometrical cells and an importance value is given to each one (see figure 1.27). If a particle crosses the boundary between two cells with importance I_a and I_b, the quantity $f = I_b/I_a$ is computed:

1. $f = 1$: no action, the particle continues
2. $f > 1$: the incident particle is replaced on average by f particles, each with a weight (w) equal to $1/f$ of the original particle's weight. This step is the splitting.
3. $f < 1$: the original particle is killed with a probability $1 - f$ (Russian roulette technique)

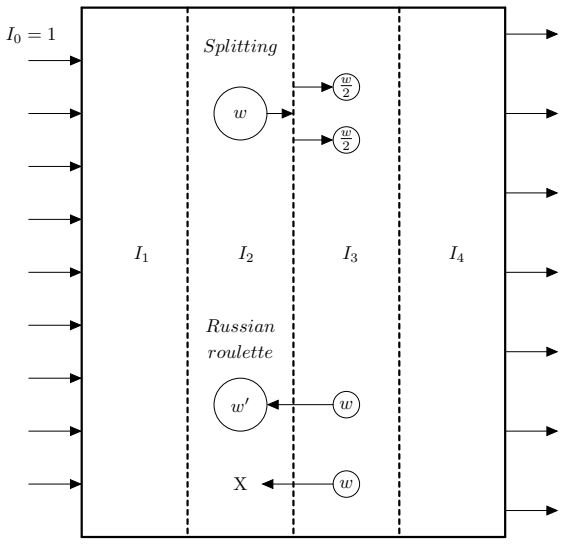

Figure 1.27: Importance sampling.

In figure 1.28, the importance sampling as implemented in *Geant4* is illustrated. It consists of 200 MeV neutrons crossing 1 meter of concrete (2.3 g/cm^3). The total thickness of concrete is divided in 8 cells and for each of them an importance is defined. In figure 1.28a, the importance of each cell is equal to 1 (analogue simulation). In case 1.28b, an importance of 2^n (with n the index of the cell) is assigned. We remark that at deeper areas of the shielding and with variance reduction technique, the number of simulated neutrons is more important. It implies that any quantity computed in case 1.28b will have a lower error.

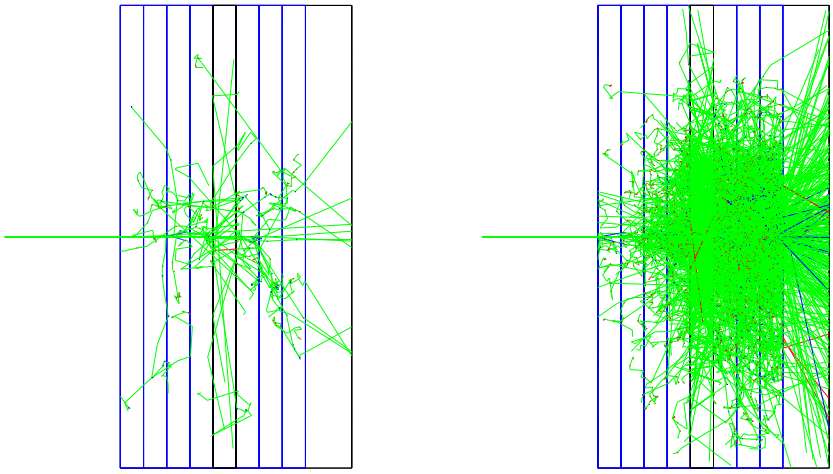

(a) Without importance sampling. *(b) With importance sampling.*

Figure 1.28: Importance sampling in Monte Carlo simulation. We observe that at deeper area of the shielding, the number of simulated neutrons is more important which allows to increase the FOM.

As example, we compute the neutron fluence and the simulated population in the last cell of the shielding and we compute the *FOM* related to these simulations. The results are summarized in table 1.1. We remark that the *FOM* and the variance (σ^2) are better when we use the importance sampling.

Quantities	No importance sampling	With importance sampling
Flux	15300.27	14626.16
Population (not weighted)	110.8	14199.2
σ^2	644.54	82.12
Time (ms)	1393.92	7246.23
FOM	1.11E^{-6}	1.68E^{-6}

Table 1.1: FOM computation for two Geant4 *simulations.*

It is important to note that the *FOM* is very dependent on computer performance, the software or the multithreading possibilities. In *Geant4*, some classes exist to quickly implement the importance sampling.

Chapter 2

Monte Carlo simulations for the activation of concrete shieldings

Contents

By the 1950s, particles accelerators are routinely used in nuclear physics research. Since then, the applications have grown and are now routinely used for the medical treatment of cancer as well. Clinical specifications require a proton energy in 40-230 MeV range corresponding to a range in water between 1.4 and 32.98 cm.

At these energies, the interactions of protons with matter will create energetic enough neutrons to produce radionuclides in shielding materials, like concrete. Interactions of neutrons with concrete will produce various radionuclides such as ^{22}Na, ^{54}Mn or ^{46}Sc (produced by high energy neutrons, greater than 1MeV or ^{152}Eu, ^{154}Eu, ^{60}Co, ^{134}Cs

(produced by low energy neutrons, lower than 1MeV) [102, 103]. These elements generate radiations which cause dangerous health effects, environmental problems [104] and waste management issues during the decommissioning phase.

In this chapter, we use Monte Carlo simulations to estimate the quantity of activated concrete in the shielding of a proton therapy system after its 20 years lifetime. Based on these simulations, we propose several ways to limit that quantity. These ones are explored and discussed in the next chapters.

The International Atomic Energy Agency defines criteria for protection against ionizing radiations [6]. It was created in 1957 in the context of the Cold War to accelerate and enlarge the development of atomic energy for peaceful applications, prosperity and health throughout the world [105].

The clearance levels, limit threshold for acceptable activity concentration, are part of these requirements and are used to determine if an irradiated material must be considered as a radioactive waste or not. Clearance levels are calculated so that the effective dose to individuals is lower or equal to 10µSv per year. For materials containing a mixture of radionuclides, the IAEA recommends to use the following criterion to identify whether the material is a nuclear waste or not. If the left side of equation (2.1) is greater or equal to one, the clearance level is exceeded and the material shall be considered a nuclear waste and must be treated adequately.

$$\sum_{i}^{n} \frac{A_i}{(CL)_i} \leq 1\,, \tag{2.1}$$

where A_i is the activity concentration (in Bq/g) of the ith radionuclide in the material, CL_i is the clearance level of the ith radionuclide and n is the number of radionuclides species present in the material. The clearance levels are tabulated as a function of the type of radionuclides [6].

In order to predict the activation level after operation for a given number of years, Monte Carlo radiation transport codes (e.g *MCNPX*, *Geant4*, *Phits*, ...) are used. Different models exist to characterize the interactions between high energy neutrons and the nucleus. We discuss and compare these models in section 2.3.

The structure of this chapter is as follows. In section 2.1, the different equations to determine the activity concentration are introduced. We present in section 2.2 the algorithm developed for general activation studies. In section 2.3, we use this new method on a simple case to compare different spallation models in Monte Carlo softwares. We model an entire compact proton therapy system in section 2.4 and we predict the quantity of activated concrete after 20 years of utilization and finally, we propose solutions to reduce the quantity of activated shielding and thus the quantity of nuclear waste.

2.1 Tools for the computation of activity concentration

2.1.1 Activation of materials

The activity concentration is defined by the following equation :

$$A = \lambda R\,, \tag{2.2}$$

where λ is the radioactive decay constant and R is the reaction rate, which corresponds to the number of created isotopes per unit of mass [54]. Two approaches may be envisaged to compute R.

The first one is simply counting the number of radioisotopes which are created. However, this method is not adapted when activation of trace elements (concentration in ppm[1]) must be calculated because the interaction probability is very low (see equation (1.2)) and consequently, the error and the computation time will be too large. The second approach is more suitable for Monte Carlo simulations. The reaction rate is computed as [54] :

$$R = N \int \phi(E)\sigma(E)dE\,, \tag{2.3}$$

where σ is the cross section for the considered reaction in cm^2, ϕ is the differential fluence in $\mathrm{MeV}^{-1}\,\mathrm{cm}^{-2}$ and N is the concentration of stable nuclides in g^{-1}.

The radioactive constant λ is given by $\ln(2)/T_{1/2}$ with $T_{1/2}$, the half life of the isotope. Then, equation 2.2 may be written as :

$$A = \lambda R = \frac{\ln(2)}{T_{1/2}} N \int \phi(E)\sigma(E)dE\,. \tag{2.4}$$

This equation gives the created activity concentration per incident particle. After the irradiation, this quantity decreases with time following an exponential decay. Thus, the resulting activity is given by:

$$A(t) = \frac{\ln(2)}{T_{1/2}} R\, exp\left(-\frac{t\,\ln(2)}{T_{1/2}}\right)\,. \tag{2.5}$$

To compute the reaction rate, three quantities need to be determined, from equation (2.3):

- The concentration of stable nuclides (N) which depends on the considered material.
- The neutronic fluence (ϕ).
- The cross-section which produces radionuclides (σ).

These notions are developed in the next three sections.

2.1.2 Concrete composition used for Monte Carlo simulation

The calculation of concrete activation requires some approximations on the composition of the concrete. *Williams et al.* [106] provide a compendium of material composition for radiation modelling. They describe the composition of different types of concrete including the Portland concrete which is one of the most common ones. This one is also described in the *National Institute of Standards and Technology* (NIST) database [38] and is available in *Geant4*.

The concentration of stable nuclides of this specific concrete is detailed in table 2.1 and is used in this work. Moreover, some impurities are also present in the cement or in the aggregates [107]. They will be taken into account given their impact on the activation.

Some of these impurities have a large capture cross section which produces radionuclides with a long decay time. Previous studies [107, 108, 102] revealed the presence of europium, cobalt and caesium in concrete material.

[1] parts per million

Element	Mass Fraction (%)
H	1
C	0.1
O	52.91
Na	1.6
Mg	0.2
Al	3.39
Si	33.7
K	1.3
Ca	4.4
Fe	1.4
Impurities	Concentration in ppm [2]

Table 2.1: Composition of standard concrete used in this work [38].

The total activation is due to two dominant phenomena (see section 1.4 and 1.3). On one hand, the spallation reactions which occur with the principal components of concrete and on the other hand, the neutronic capture, which is caused by the impurities present in concrete.

In this work, only the radionuclides with a half-life greater than 3 months are considered. Indeed, after exploitation of a proton therapy center, there is a period of rest before decommissioning. During this period, the activation decreases following the natural decay. In average, we assume that this period is three months.

Table 2.2 details the different radioisotopes that are considered in this work. The production method, the half-life, the clearance level and the parent element are specified. The last are the stable elements which will produce the radioactive elements after interactions with neutrons. The radionuclides produced by spallation depend on the composition of concrete and the parent element may not be identified clearly[3]. The clearance levels are tabulated in [6] and are needed to evaluate the quantity of radioactive waste (see equation (2.1)).

Element	Production method	Half life $T_{1/2}$ [years]	Clearance level (Bq/g)	Parent element
^{45}Ca	Spallation	0.445	100	"Concrete"
^{55}Fe	Spallation	2.744	100	"Concrete"
^{54}Mn	Spallation	0.855	0.1	"Concrete"
^{22}Na	Spallation	2.603	0.1	"Concrete"
^{35}S	Spallation	0.239	100	"Concrete"
^{46}Sc	Spallation	0.229	0.1	"Concrete"
^{152}Eu	Capture	13.33	0.1	^{151}Eu
^{154}Eu	Capture	8.8	0.1	^{153}Eu
^{60}Co	Capture	5.3	0.1	^{59}Co
^{134}Cs	Capture	2.06	0.1	^{133}Cs

Table 2.2: Radionuclides properties considered in this thesis.

[2] Depending on the composition of the considered concrete. See text for precise values.
[3] Different elements can give the same radionuclide.

2.1.3 Fluence computation and path-length estimator

The International Commission on Radiological Protection (ICRP) [109] defines the fluence (in m^{-2}) as : *the quotient of dN by dA, where dN is the number of particles incident on a sphere of cross-sectional area dA* :

$$\phi = \frac{dN}{dA}\,. \tag{2.6}$$

In Monte Carlo simulations, this definition is not directly applicable and it is more convenient to use the Path-Length estimator which is equivalent [54]. For the Path-Length estimator, we use the definition of *Lewis and Miller*: *The fluence is defined by the track length (L) of a particle inside a volume divided by the volume of this cell (V).* The track length is calculated from a summation of the step lengths (l) in the cell. Furthermore, if a variance reduction technique is used (see chapter 1.5.2), the fluence is multiplied by the weight of the particle. We thus have:

$$\phi = W \times \frac{L}{V} = W \times \frac{\sum l}{V}\,. \tag{2.7}$$

These two equations ((2.6) and (2.7)) are illustrated in figure 2.1. The fluence is equal in 2.1a to the number of particles (ΔN) passing through the surface (ΔA) into a sphere, while, in figure 2.1b, it corresponds to the sum of the paths of each particle (L) passing through the sphere divided by the volume V [110].

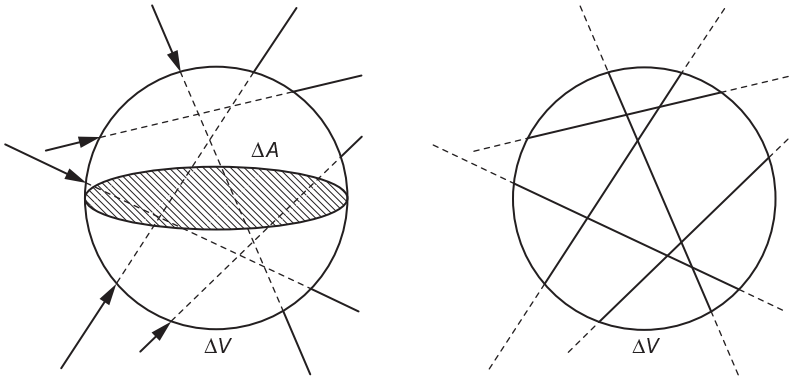

(a) Definition of the ICRP. *(b) Path Length estimator.*

Figure 2.1: Two interpretations of the fluence using the volume ΔV and the cross-sectionnal area ΔA. The interpretation b is more useful for Monte Carlo simulations. Reproduced from [110].

2.1.4 Cross section for radionuclides production

The last quantity to determine the reaction rate is the cross section for the production of radionuclides. As explained in chapter 1, neutron reactions that mainly produce radioisotopes are the capture and the spallation reactions. Hereafter, we describe the cross section for capture process and then, we discuss the spallation reaction.

2.1.4.1 Capture cross section

The capture cross-sections are tabulated for incident neutrons with kinetic energy from 10^{-11}MeV up to 20MeV in the *Evaluated Nuclear Data File* (ENDF) database [52]. For

each element that is produced by capture (^{152}Eu, ^{154}Eu, ^{60}Co and ^{134}Cs) the corresponding capture cross section of the parent element is presented in figure 2.2. We see that at low neutron energy, the capture cross section is more important. This means that the chance to capture the neutron is greater at low energy. Moreover, the cross section for the ^{151}Eu is about one thousand times greater than the others increasing its chance of interaction.

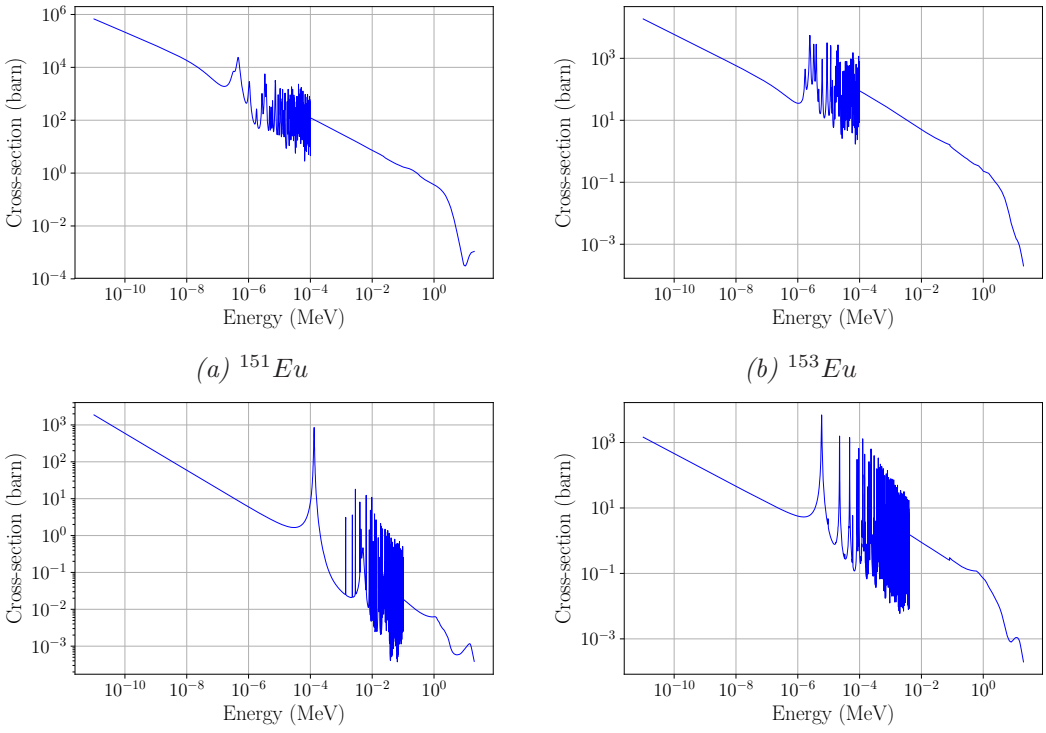

(a) ^{151}Eu (b) ^{153}Eu

(c) ^{59}Co (d) ^{133}Cs

Figure 2.2: Neutron capture cross section from the ENDF database [52].

Even if these elements are present as traces in the concrete shielding, the capture cross sections are non negligible for energies lower than 20MeV. For energies above 20MeV, we assume a cross section equal to 0. As the produced radionuclides are long-lived, it is important to take into account these isotopes for activation studies.

2.1.4.2 Spallation cross section

When neutrons interact with the concrete, they may produce some radionuclides by spallation. As we have seen in section 1.4, different models (Bertini, BIC and INCL) exist to describe this particular reaction. The cross section for the production of a specific radionuclides ($\sigma_{production}$) is given by [111, 26]:

$$\sigma_{production}(E) = \frac{N_{radionuclides}(Z,A)}{N_{neutrons}}\sigma_{tot}(E)\,, \tag{2.8}$$

where $N_{radionuclides}(Z,A)$ is the number of radionuclides with an atomic number Z and a nucleon number A produced by spallation, $N_{neutrons}$ is the total number of neutrons irradiating the concrete (input) and σ_{tot} is the total interaction cross section in the concrete.

These models must be compared to quantify the difference between them and thus, we perform simulations over a simple configuration. It consists of a target of concrete which is irradiated with neutrons at different energies. The thickness of the target is "infinite" to be sure that any primary neutron interacts in the medium.

First, the total cross section (σ_{tot}) is deduced from equation (1.3), where the mean free path is computed as the mean value of the track lengths of the incident particles. The results obtained with the different models from *Geant4* as well as the data given by the TALYS software (nuclear model code) [112] are presented in figure 2.3. We observe no major differences between them, the three *Geant4* models give the same results.

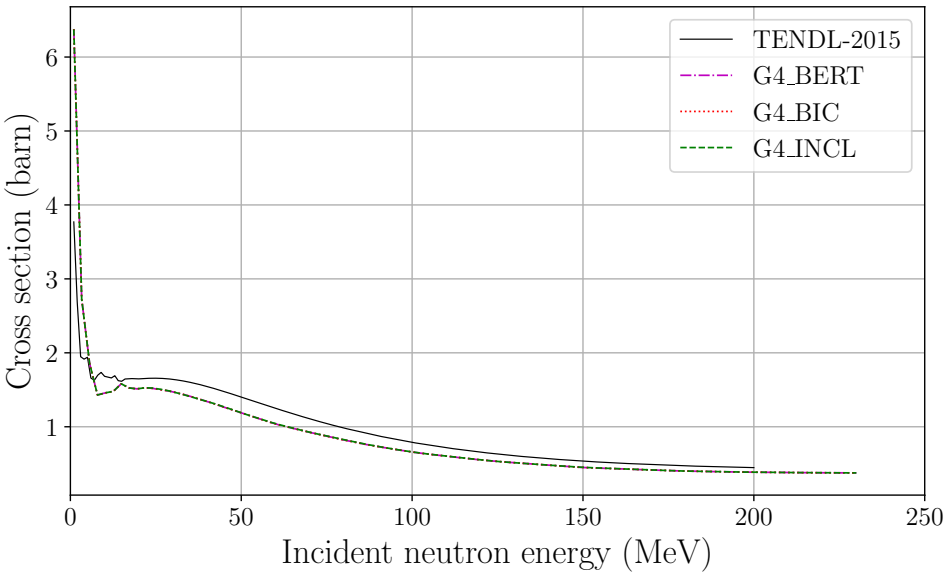

Figure 2.3: Neutron total cross section for concrete. The results obtained with the three Geant4 *models are superposed.*

Secondly, we compare the production cross section in concrete for the elements in table 2.2 with the different theoretical models (equation (2.8)). The results are illustrated for ^{22}Na (Z=11, A=22) in figure 2.4. The trends for the other elements are similar and presented in appendix A.

Starting from these results, some remarks must be made. First, we observe some differences between the production cross section while the total cross section is the same with the different models. We have seen in chapter 1 that the total cross section is a sum of partial cross sections (equation (1.1)). This means that the cross sections for other processes vary depending on the models. Second, the cross sections are only in the mb range. However, as the atomic density is important, the numbers of produced isotopes will be quite significant. Thirdly, the G4_BERT model underestimates the production of ^{22}Na while the other models give equivalent results. Finally, even if the description of the models relies on the same physics, differences are in the details of the implementation [113]. The differences between the models have been confirmed in previous studies (see [24] and [26]). Nevertheless, they have shown a global improvement of the reliability of the models over the past years.

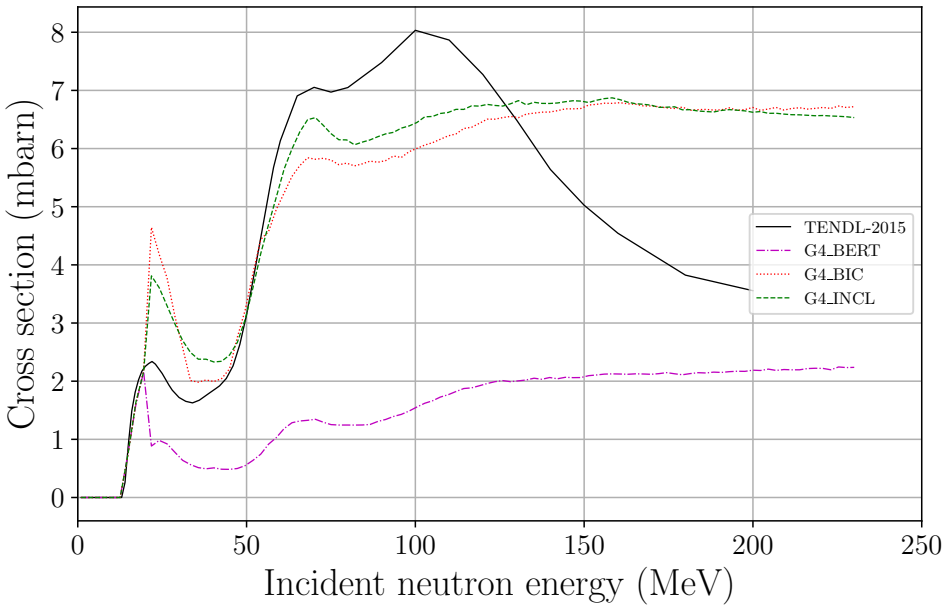

Figure 2.4: Production cross section of ^{22}Na in concrete.

2.2 Methodology to compute the activity concentration

We present in this section the approach introduced in this thesis to study the activation concentration in any materials and configurations. We describe in section 2.2.1 the method neutron-equivalent source, introduced to reduce the computation time. In section 2.2.2, we explain the algorithm developed in *Geant4* to compute the activation.

2.2.1 Neutron-equivalent source method

The neutron-equivalent source is a technique to reduce the computation time in case of low creation rate of secondary neutrons. For example, we consider a graphite target (1.7 g/cm^3) irradiated by protons and we analyse the properties of neutrons emitted by this target : multiplicity, energy, angle, etc. Figure 2.5 shows the neutron yields emitted by this target due to a 230 MeV proton beam for different degraded energies.

This figure illustrates clearly that the major part of the computational resources are not used to generate neutrons. Indeed, the number of created neutrons per incident proton is low. For instance, at 130 MeV at the target exit, approximately 20 neutrons are generated for 100 incident protons.

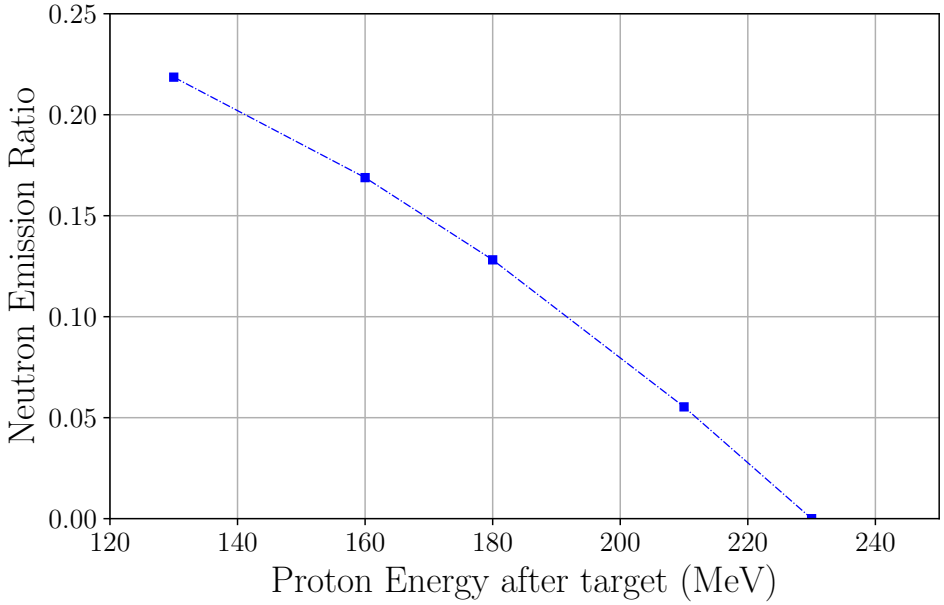

Figure 2.5: Neutron emission ratio for a graphite target irradiated by a 230 MeV *proton beam.*

A solution to improve the simulation efficiency and to avoid excessive computation time is to replace the set *beam-target* by a point neutron source having same energy and angle properties, θ and ϕ, as the set *beam-target* (see figure 2.6). This technique has been already used by F. Stichelbaut in a study of secondary X-Rays generated in a beam stop or by *Medaustron* for a study of the ambient dose in their facility [114, 115]. For our particular purpose, this method will be validated in section 2.3.2.

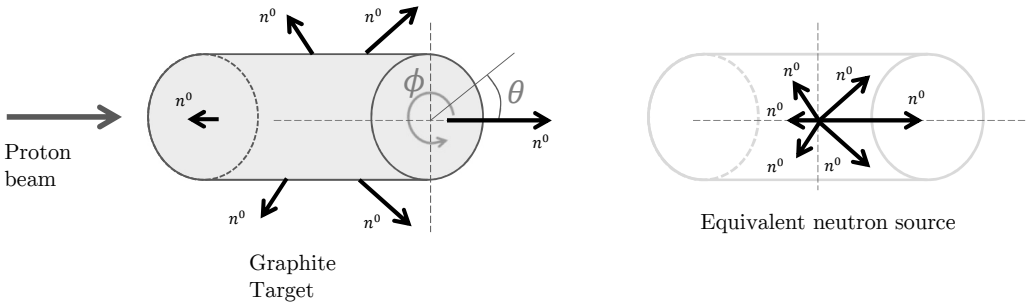

Figure 2.6: Replacement of the beam target by a point neutron source.

Figure 2.7 shows for example a histogram of the energy versus angle θ (in 2.7a) and the angle ϕ (in 2.7b) for a set proton beam target. The proton beam has an energy of 230 MeV and the energy at the target exit correspond to 130 MeV. We note that the distribution of θ is energy-dependent which means that we have a peak at small angles due to the spallation processes. For each neutron energy, number of emitted neutrons is constant whatever ϕ angle. This means that the high energy neutrons are emitted in the same direction as the incident beam.

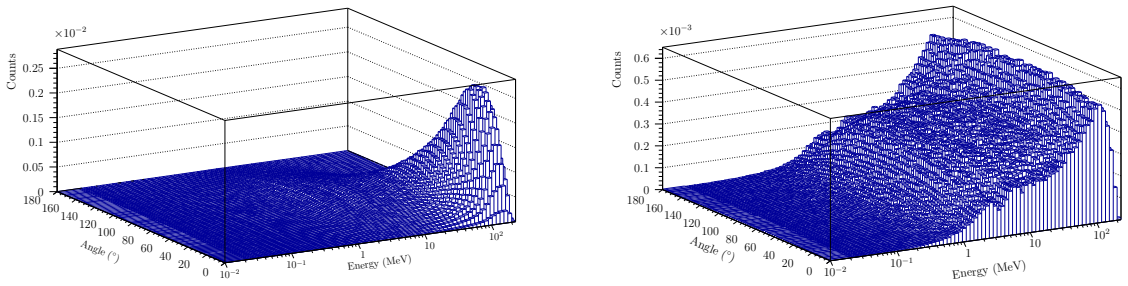

(a) θ angle. *(b) ϕ angle.*

Figure 2.7: Angle-Energy properties of emitted neutrons.

If the energy at the exit of the target increases, *i.e* the target is thinner, the shape of the distribution is similar but the maximum is shifted to the value of the exit energy.

2.2.2 *Geant4* class for general activation studies

We present here the algorithm developed in this thesis to evaluate the activation concentration which can be adapted as a function of the geometry and the material studied (input parameters). The algorithm is the following:

1. Generate the neutron spectrum for a radiation source to determine the neutron-equivalent source (hereafter a graphite target irradiated by protons) as in section 2.2.1.
2. Compute the cross section for the wanted effect in the studied configuration (hereafter a concrete shielding sphere) as in section 2.1.4.
3. Subdivide in cells the geometry configuration to study.
4. In each cell, implement the relation (2.4) to obtain the activation concentration.
5. In the post processing, take into account the decay of the produced radionuclides (equation (2.5)) to obtain the final values of the activity concentration.
6. Determine with equation (2.1) if the cell needs to be considered as a radioactive waste or not.

Step 4 is directly introduced in a C++ class based on *Primitive Scorer* in *Geant4* and is presented in appendix B. Before analysing the results for a Proteus®One(compact proton therapy center) system, we validated the method on a simple case and we selected the most appropriate model for the rest of this work.

2.3 Benchmarking of spallation models in Monte Carlo softwares

Geant4 has already been validated in previous studies like the neutron emission production and shielding studies [116]. The purpose of this section is to demonstrate that *Geant4* can also be used for activation studies. The following results have been published by the author in [117] and are discussed in details in the next sections. The following softwares have been compared : *Geant4*, *Phits* and *MCNPX*

In this benchmark, we focus our attention on the elements produced by capture and on the ^{22}Na which is produced by spallation. Indeed, this one has a small clearance level (0.1 Bq/g) and a significant half-life (2.6 years). The physical data for the considered isotopes are summarized in Table 2.3.

Isotope	Clearance level [Bq/g]	$T_{1/2}$ [years]	λ [s^{-1}]
^{152}Eu	0.1	13.33	$1.652e^{-9}$
^{154}Eu	0.1	8.8	$2.49e^{-9}$
^{60}Co	0.1	5.3	$4.14e^{-9}$
^{134}Cs	0.1	2.06	$1.06e^{-8}$
^{22}Na	0.1	2.6	$8.44e^{-9}$

Table 2.3: Characteristics of radionuclides studied in this benchmark.

2.3.1 Definition of the reference geometry

A simple geometry is built for the comparison of different softwares (see figure 2.8). It consists of a cylindrical beam-stop (target) made of graphite (density of 1.7g cm^{-3}) with a radius equal to 16.55 cm and a length of 30 cm designed in order to stop all protons. A 230 MeV pencil proton beam irradiates the target in the z direction. A concrete (density of 2.3 g/cm^3) shielding sphere surrounds the target with respectively an inner and an outer radius of 1 m and 3 m.

The sphere is divided into 20 radial slices in order to study activation along the radial direction. Moreover, 18 equivalent regions are defined in the polar direction to study polar activation (θ angle). This discretization gives cells where equation (2.5) is computed.

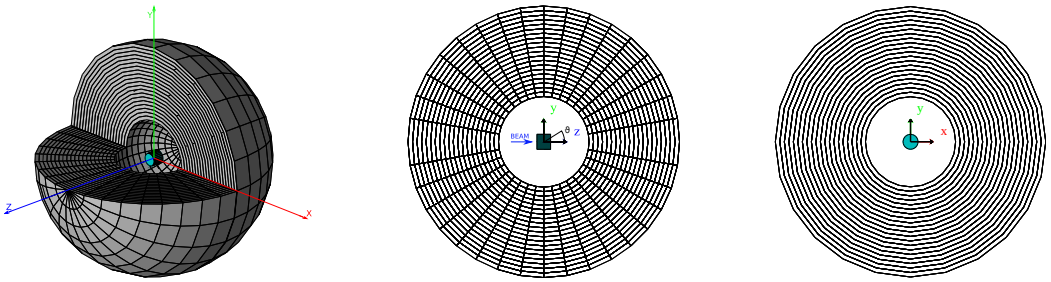

(a) *(b)* *(c)*

Figure 2.8: Spherical model used to study concrete activation.

2.3.2 Validation of a neutron-equivalent source

Before analysing the results, we verify that the concept of neutron-equivalent source introduced in section 2.2.1 is applicable in this case. We compute the activity concentration of the ^{152}Eu and the ^{22}Na on the first slice of our spherical shielding. On figure 2.9 and 2.10, the activity concentration is computed using a proton beam/target model (in red) and the corresponding neutron-equivalent source (in blue). For each case the relative error is also represented.

The two models are in good agreement for the expectation of the mean values for both kinds of sources (figure 2.9a and 2.10a), the patterns are similar however, the relative error

is lower for the neutron-equivalent source than for the proton beam/target model (figure 2.9b and 2.10b).

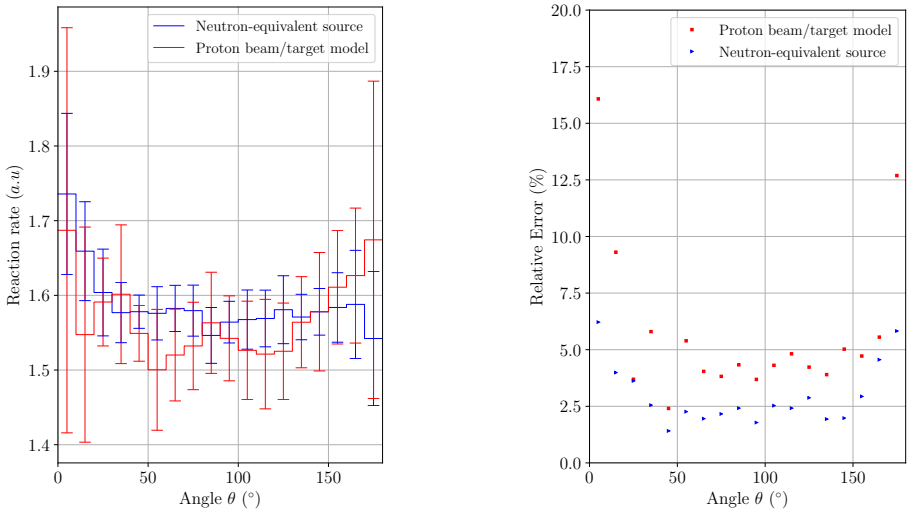

(a) Capture. *(b) Relative Error.*

Figure 2.9: Radionuclides produced by capture (protons or neutrons source).

For the spallation case, neutrons are mainly emitted in the direction of the incident beam. Consequently, there are only few high energy neutrons emitted backward. This explains why the relative error is important at large angle in this case. One advantage of the neutron-equivalent source is clearly visible in the spallation case where neutrons are emitted in the direction of the incident beam. Indeed, very few high energies neutrons are emitted backward in the proton beam/ target model while the neutron-equivalent source allows to provide a much larger statistics and thus to reduce the relative error.

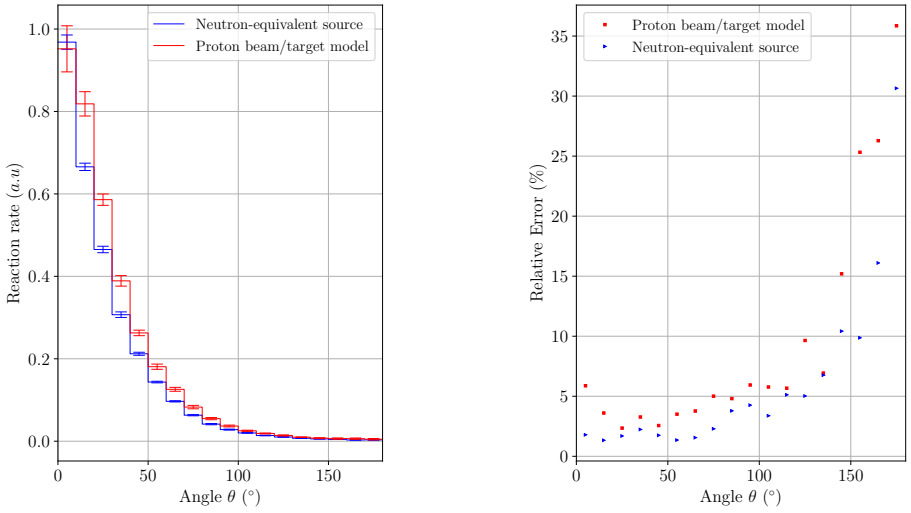

(a) Spallation. *(b) Relative Error.*

Figure 2.10: Radionuclides produced by spallation (protons or neutrons).

We conclude that the neutron-equivalent source allows reducing the relative error on the activation rate keeping the same number of primary particles (same computation time).

Thus, we artificially increase the *Figure Of Merit* (FOM) (equation (1.76)).

2.3.3 Simulation results

To compute the activity concentration of isotopes, it is assumed that the target is irradiated without dead-time during a period of 20 years. The energy of the proton beam is 230 MeV and the beam current is constant and equal to 0.6076 nA (*IBA* average value). The activity of each of the isotopes is computed during these 20 years taking into account the radioactive decay. Finally, the quantity (2.1) is computed and plotted for the various production methods of radionuclides: spallation in section 2.3.3.1 and capture in section 2.3.3.2. In the following, we display the obtained activity as a function of the sphere radius for an angle θ varying between 0 and 10° as well as the activity as a function of the polar angle θ for a radius in the 0-10 cm range.

2.3.3.1 Spallation Reaction

Figure 2.11 shows results for the production of ^{22}Na obtained with the considered softwares and models. *MCNPX* is used with the Bertini model (MCNPX_BERT) and INCL is used by default in *Phits* (PHITS_INCL). Results obtained from *MCNPX*, *Phits* and *Geant4* (G4_BIC and G4_INCL) are in agreement. Results obtained from G4_BERT underestimates the reaction rate but as shown in figure 2.4, cross section for ^{22}Na production for the Bertini model is lower than for the other models. Differences are also observed between G4_BERT and MCNPX_BERT. This is due to a different implementation in both softwares. Same comments can be made considering G4_INCL and PHITS_INCL. Finally, the use of the G4_BIC gives a reaction rate larger up to a factor two than the results obtained with the G4_INCL model (while cross sections for both models are equivalent, see figure 2.4). The exact reasons for these differences are not clear and it would be interesting to compare these results with experimental data.

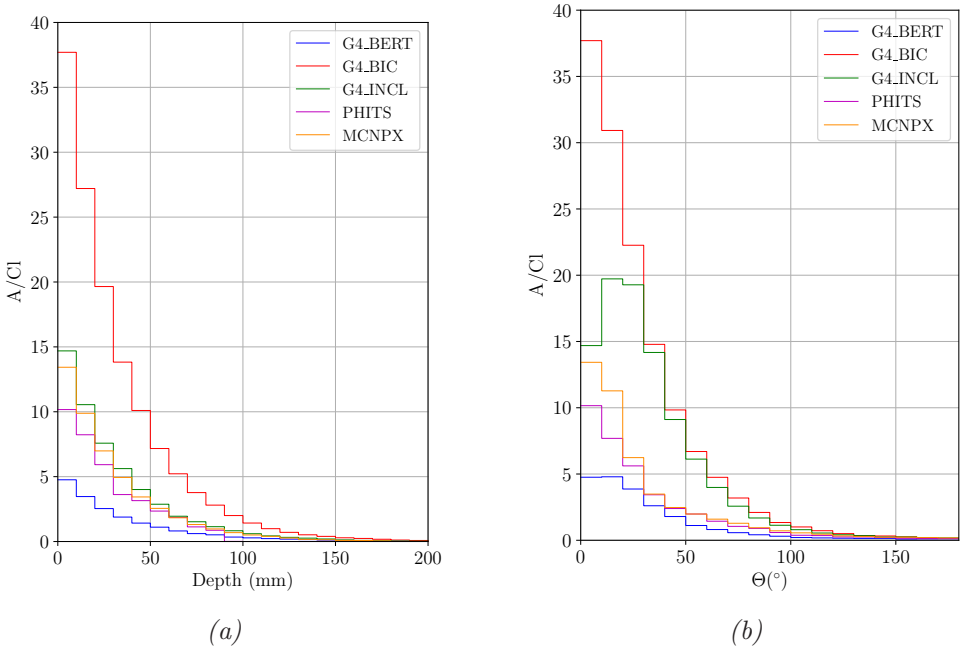

Figure 2.11: Activity concentration of ^{22}Na divided by the clearance index (for the spallation reaction) as a function of a the sphere radius for an angle between 0 and 10° and b the polar angle for a radius in the 0-10 cm *range.*

2.3.3.2 Neutron Capture

For the neutron capture reaction, the concentration of parent radionuclides in the concrete (N in equation (2.3)) is of primary importance. A small variation has important impacts on the results. As the aim of this section is to benchmark models implemented in different softwares, we have chosen the same database as *IBA*. Data are taken from L. Carroll in *Predicting Long-Lived, Neutron-Induced Activation of Concrete in a Cyclotron Vault* [108] (see table 2.4). Using these concentration values, we compute the clearance level ($\Sigma_i A_i/Cl_i$) due to neutron capture. The obtained results are shown in figure 2.12 as a function of depth and polar angle.

Isotopes	Concentration (N)
Eu-151	0.14 ppm
Eu-153	0.15 ppm
Co-59	2.5 ppm
Cs-133	1.5 ppm

Table 2.4: Concentration of radionuclides considered in the present section [108].

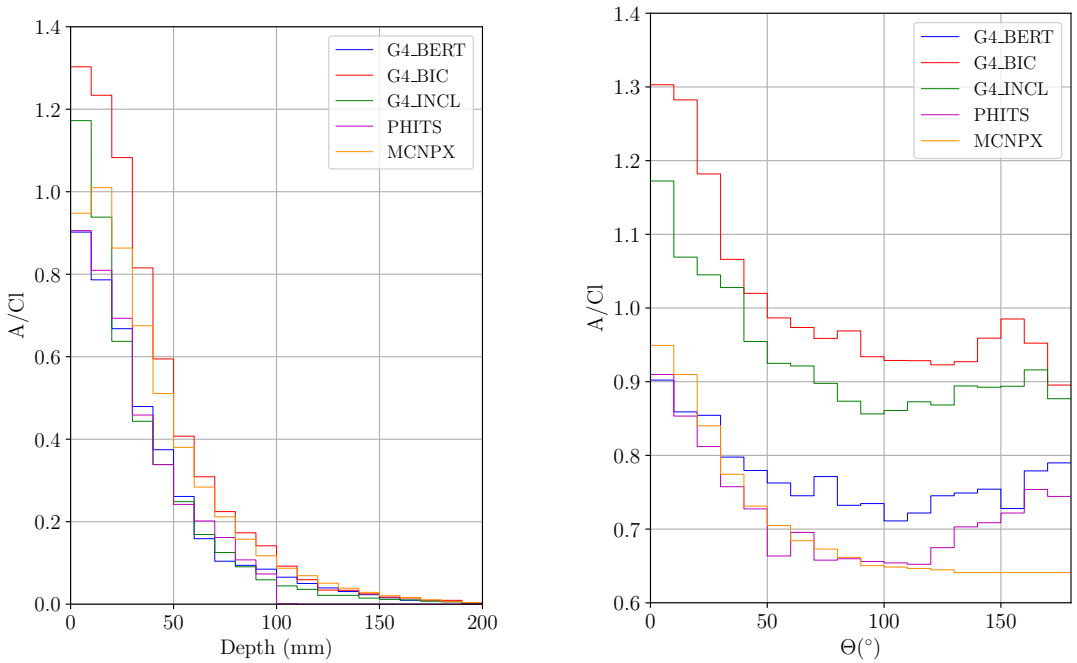

(a) *(b)*

Figure 2.12: Activity concentration divided by the Clearance index (for the capture reaction) as a function of a the sphere radius for an angle between 0 and 10° and b the polar angle for a radius in the 0-10 cm *range.*

Considering the same capture cross section, the only differences arise from the neutron spectrum emitted by the target. These minor discrepancies have already been identified in [104, 118, 7]. As example, figure 2.13 shows the differential energy spectrum of neutrons leaving the carbon target irradiated by a 230 MeV proton beam, calculated with the three models implemented in *Geant4* and with *Phits*. As in this figure, the scale is logarithmic, the differences are amplified and explain the results obtained in this section.

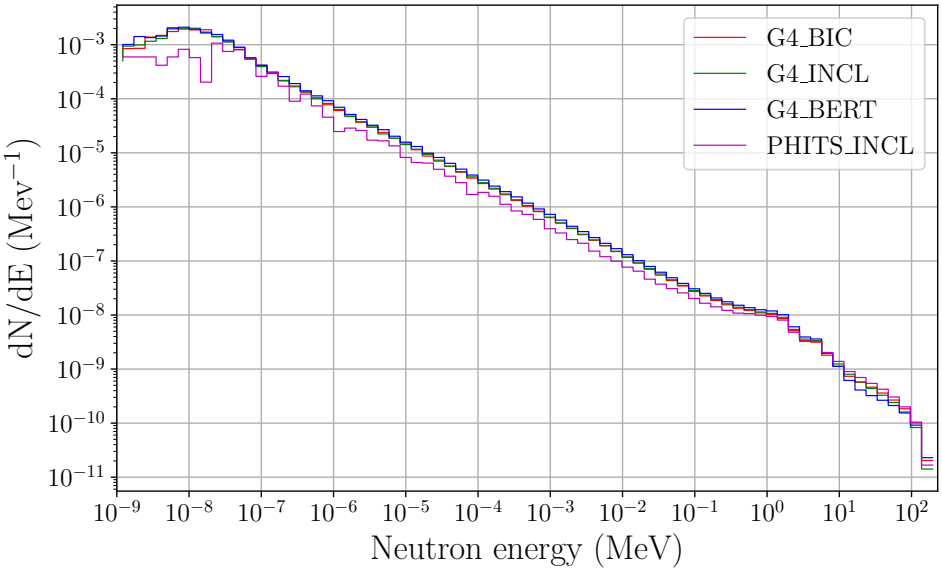

Figure 2.13: Neutron Spectrum of the target obtained with Geant4 *and* Phits *for different models.*

2.3.4 Validation and model selection

In this section, we have compared different softwares and models in order to simulate activation concentration in a concrete shielding. This activation is due to neutrons produced by a 230 MeV proton beam irradiating a carbon target. Trace elements contribute to activation of concrete via neutron capture phenomena while the spallation reactions produce ^{22}Na.

We conclude that *Geant4* is suitable to study activation of the concrete shielding. However precautions have to be taken according to the considered model for capture and spallation in the software. Using the radiation safety principle of *As Low As Reasonably Achievable (ALARA), the use of the G4_BIC or possibly G4_INCL model is recommended for a global activation study. The model G4_BERT underestimates the production of* ^{22}Na.

In the next section, a proton therapy center is modelled. The G4_BIC model is used in the rest of this thesis. Indeed, in the activation context, a conservative approach must be adopted. We can expect an overestimation of the quantity of activated concrete compared to the results with the other spallation models.

2.4 Activation computation of a Proteus One

The Proteus®One consists of a single treatment room with a proton accelerator (S2C2) as displayed in figure 2.14. Another product of *IBA*, a Proteus®Plus center with multi-rooms is also shown in comparison.

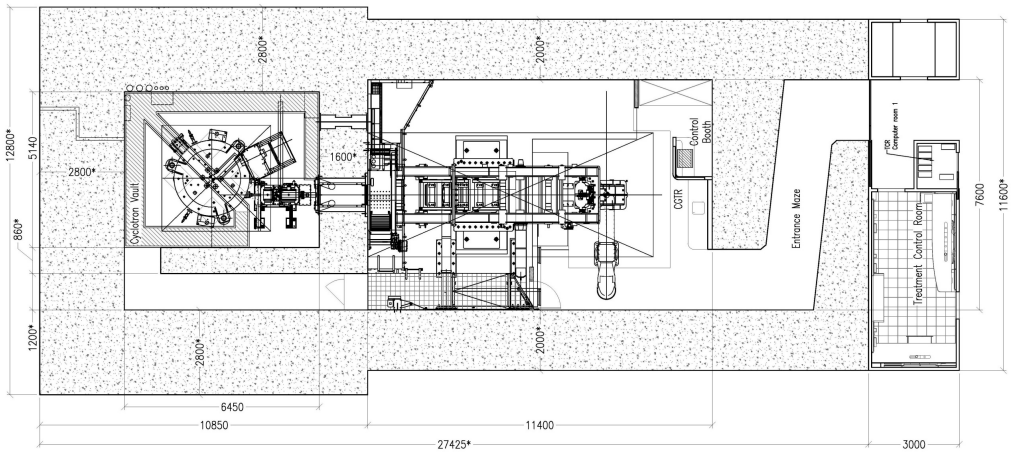

(a) Proteus® One center.

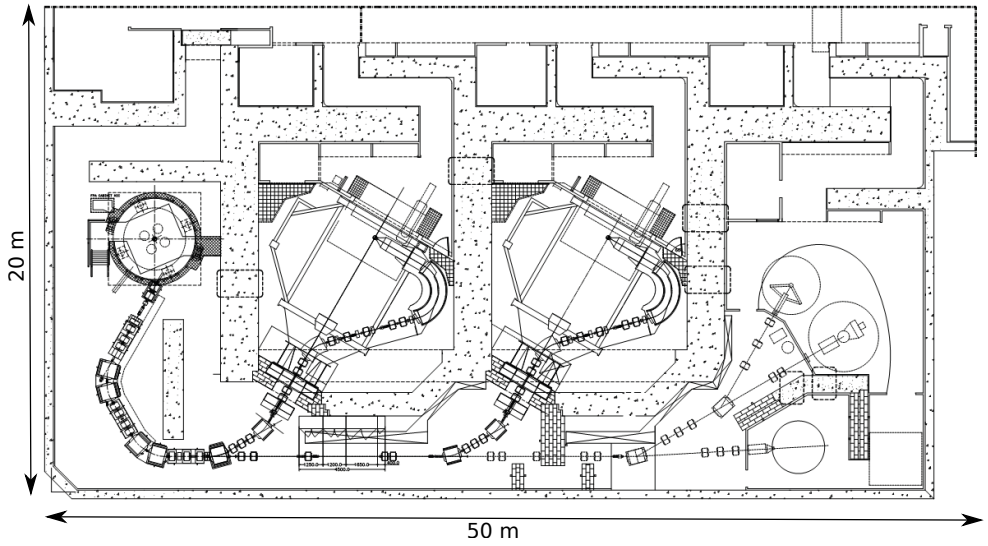

(b) Proteus® Plus center.

Figure 2.14: Representation of the two IBA *products. Reproduced from [119].*

As we observe in this figure, a Proteus® One is quite more compact than a Proteus® Plus. Consequently, the different radiation sources, such as the accelerator or the degrader, are close to each other. Moreover, they are located in the same are, *i.e* in the vault housing the accelerator. It means that the activation of the concrete shielding is more important than in a Proteus® Plus. The clearance levels defined by the IAEA for nuclear waste may thus be exceeded more quickly, involving a specific treatment for the decommissioning of the facilities and consequently additional costs.

To analyze the concrete activation of a Proteus® One, we first describe the modelisation of the compact proton therapy solution in section 2.4.1. Then, we present the different sources of radiation and the workload. The results obtained with *Geant4* are discussed in section 2.4.3. Finally, we introduce in section 2.5 two methods to reduce the quantity of nuclear waste.

2.4.1 Geometry modelisation of the Proteus One

For the *Geant4* simulation, we have subdivided the Proteus®One center into different walls as illustrated in figure 2.15. Only principle activation sources are shown, as the cyclotron (in yellow), the extraction quadrupole (in orange), the degrader (in green), the collimator (in magenta) and the patient (in blue). The entire beamline has not been modelled because in a normal case, the beam does not interact significantly with these elements and these effects are neglected in this chapter. The dimensions of each wall are summarized in table 2.5.

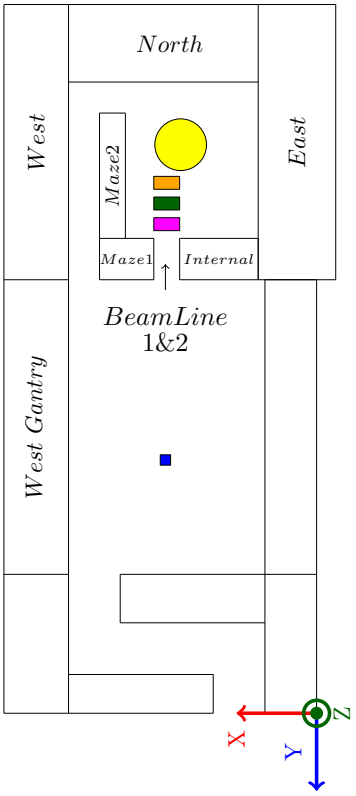

Figure 2.15: Model of the Proteus® One center.

	X (mm)	Y (mm)	Z (mm)
Beam Line 1	1000	1600	750
Beam Line 2	1000	1600	2050
Internal	3040	1600	3800
Maze 1	2100	1600	3800
Maze 2	1000	4850	3800
East	3000	10650	3800
West	2500	10650	3800
North	7340	3000	3800
Roof	12840	10650	3250
Floor	12840	10650	3000
West Gantry	2500	11400	5150

Table 2.5: Dimensions of each wall.

During a treatment, different irradiation angles are used to irradiate the tumour. *IBA* has estimated that, during a year, all treatments can be classified following three orientations with this distribution [120]:

- 50% following $1\vec{}_X$ direction
- 25% following -$1\vec{}_Z$ direction
- 25% following $1\vec{}_Z$ direction

Based on these percentages, we only analyse the wall in front of the patient in the treatment room (*West_Gantry* in figure 2.15) for which the beam is oriented in 50% of the case. If this one is not activated, the other walls will not be either.

In 2001, the authors of [107] have measured the concentration of stable isotopes for neutron capture in different types of concrete and like F.Stichelbaut, we also used the following concentration in parent elements (see table 2.6).

Isotopes	Concentration (N)
Eu-151	0.5162 ppm
Eu-153	0.5637 ppm
Co-59	21.9 ppm
Cs-133	3.21 ppm

Table 2.6: Concentration of stable nuclides. Data taken from [107].

2.4.2 Description of the radiation sources

In order to perform the study of the concrete shielding activation, we will first describe the various radiation sources considered in a Proteus® One. They correspond to the locations where the beam interacts with matter, namely inside the accelerator, the extraction quadrupoles, the degrader, the collimator and the patient. The beam losses have been estimated by R. Doyen and are summarized in [121]. To compute the clearance levels in each wall, we use a pencil beam[4] with different energies at the output of the degrader: 70, 86, 116, 160, 200 and 230 MeV. For these energies, the typical number of protons sent to the patient (modelled as a 40 cm water cube), called *workload*, is summarized in table 2.7 [122]. These values are related to the therapeutic doses given by medical physicists.

Energy (MeV)	Workload (nA·h) per year
70	65.6
86	74.056
116	89.911
160	113.65
200	128.53
230	145.48

Table 2.7: Proteus® One workload used in this work. Data taken from [122].

2.4.2.1 Accelerator

The S2C2, a super conducting proton synchrocyclotron, has been modeled using cylinders. Figure 2.16a shows the global view of the S2C2, the model in *Geant4* is shown in figure 2.16b. It consists of cylinders with different radii and made of iron. The internal cavity allows to accelerate the protons which are extracted when they have the correct energy.

This accelerator is able to generate a proton beam with a fixed energy of 230 MeV. As a conservative approach, we consider an extraction efficiency of 30 % [121]. The rest of the protons is lost in the accelerator for which we assume the following distribution:

- 25% of the losses are uniformly distributed along the circumference of the S2C2 with an energy of protons equal to 230 MeV.
- 45% of the losses occur at the extraction of the beam at 230 MeV.

[4] Ideal monoenergetic beam without spatial extension.

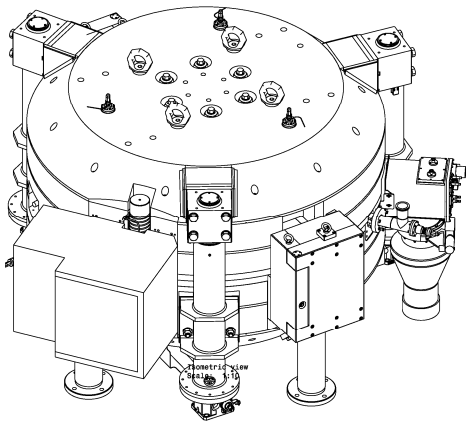

(a) Global view.

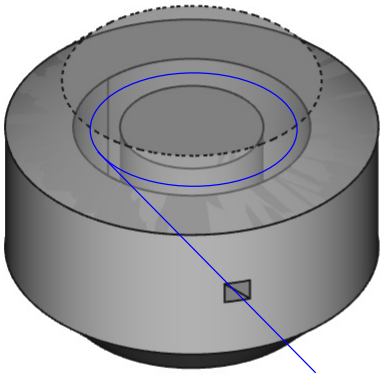

(b) Geant4 *model with protons in blue.*

Figure 2.16: S2C2 representation.

2.4.2.2 Degrader

The degrader allows to change the proton beam energy. It consists of a rotating wheel with blocks of variable thicknesses and materials as shown in figure 2.17.

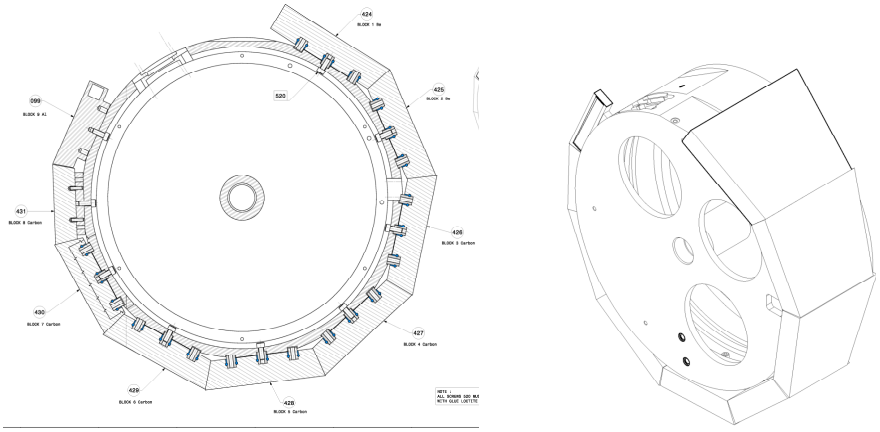

Figure 2.17: Details of the energy degrader.

As function of the desired energy, different materials are used. They are summarized in table 2.8:

Energy (MeV)	Material	Density (g/cm^3)
Lower than 130	beryllium	1.85
130-220	graphite	1.7
Greater than 220	aluminium	2.7

Table 2.8: Materials used as function of the exit energy.

As the beam used for these simulations is a pencil beam, the degrader is modelled as a simple block of matter with the correct thickness. It is adapted in the simulation as function of the energy desired at the output. The table 2.9 details the dimensions and the beam losses for each simulated energy. Note that for an energy of 230 MeV, there is no

need to reduce the energy, the degrader is in *pass-through* position[5].

Energy (MeV)	Material	Thickness (cm)	Beam losses (%)
70	Beryllium	19.137	34.4
86	Beryllium	17.933	33.73
116	Beryllium	15.196	29.16
160	Graphite	10.054	17.67
200	Graphite	4.599	8.88

Table 2.9: Material and thickness of the block as function of the transmitted energy. Data taken from [121].

The degrader will be studied in detail in chapter 4, especially the properties of the transmitted beam.

2.4.2.3 Collimator

The collimator is a tantalum cylinder with a 10 mm diameter hole in the centre. It is placed just after the degrader to reduce the angular divergence of the beam. Figure 2.18 shows the collimator used in the system by *IBA*.

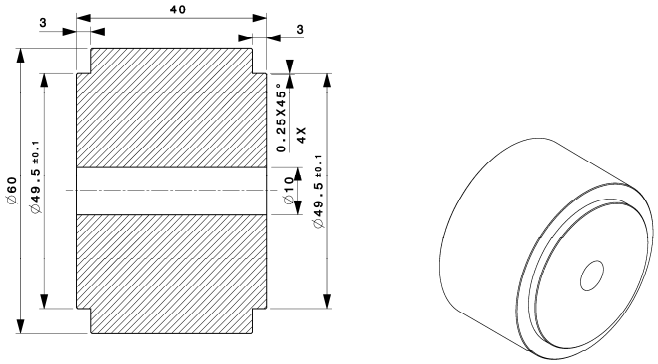

Figure 2.18: Detail of the collimator made of tantalum.

The following assumption is made to simulate the activation due to the collimator. At the exit face of the degrader, the beam has a large divergence. As the hole of the collimator is small, it is reasonable to suppose that the center of the beam goes through without interactions while the rest of the beam intercepts a block of tantalum (see figure 2.19). These interactions generate neutrons. Therefore, we use the concept of neutron-equivalent source [120].

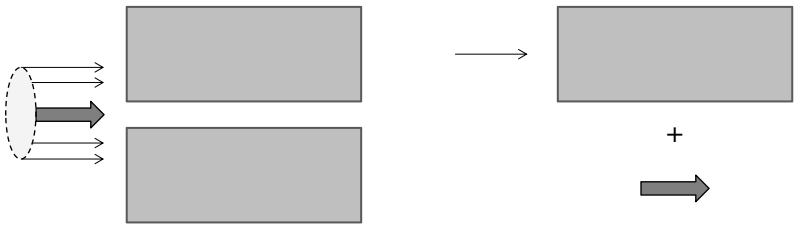

Figure 2.19: Model of the collimator in Geant4.

[5]In reality, a very small thickness of aluminium is used for a transmitted energy of 230 MeV but is neglected in this work.

The beam losses of the collimator are summarized in table 2.10 [121].

Energy	Beam losses (%)
70	41.69
86	42.93
116	44.66
160	48.19
200	44.02
230	36.32

Table 2.10: Beam losses of the collimator in function of the transmitted energy. Data taken from [121].

2.4.2.4 Quadrupoles

The quadrupoles are used to focus the beam extracted from the S2C2 up to the degrader. Indeed, we will see in chapter 5 the necessity of these quadrupoles, named Q1C and Q2C. They interact with the beam just at the exit of the accelerator (in orange in figure 2.15) and they intercept the beam with an energy of 230 MeV. The beam losses are fixed at 4.02% (resp. 14.01%) for Q1C (resp. Q2C) [121]. We use the same principle as for the collimator to generate the neutron spectrum.

2.4.2.5 Transmission efficiency

The workload defined in table 2.7 corresponds to the number of protons sent to the patient. To deduce the number of protons at the exit of the S2C2, we need to divide these values by the complete efficiency of the system, noted ϵ. ϵ is the fraction of extracted beam finally reaching the patient. These values have been estimated in 2012 by R. Doyen [123].

Energy (MeV)	ϵ(%)
70	0.21
86	0.27
116	0.8
160	1.82
200	4.96
230	12.07

Table 2.11: Beam losses along the CGTR in function of the transmitted energy. Data taken from [123].

2.4.3 Activation simulation results

In this section, we make the same assumption as in section 2.3, *i.e*, utilization of the Proteus®One center during 20 years without dead-time. The activity of each isotope summarized in table 2.2 is computed during this period taking into account the radioactive decay (see equation (2.5)).

In this section, we present the results that we have obtained with *Geant4* for the Proteus®One system. For the different walls of the system, we have computed the thickness of activated concrete depending on the position. We observe that the entire depth

needs to be considered as a nuclear waste for some walls while for others it is only the surface layer in the vault. Practically, it is too complex to remove different thicknesses from a same wall. Consequently, a constant thickness is considered in each wall corresponding to the maximum thickness where the concrete is activated.

We observe that the most activated places are those located near the radiation sources described in the last section especially those situated just in front of the quadrupoles, the degrader and the collimator, separating the vault and the treatment room (figure 2.20 and 2.21). The behaviour is similar for the Beam Line1, Beam Line2 and Maze1 walls. The walls are completely activated and must be considered as nuclear waste. The activation of the other walls (figure 2.22 to 2.24) in the vault is mainly due to the neutronic emission of the accelerator. The roof and the floor (figure 2.25) are impacted by all sources with a peak situated near the degrader and the collimator.

Finally, we find that the wall in the treatment room (named West Gantry) is not activated. It means that the activation of the rest of the treatment room is also lower than the IAEA standards. The treatment room is therefore considered as a non-nuclear waste.

Internal

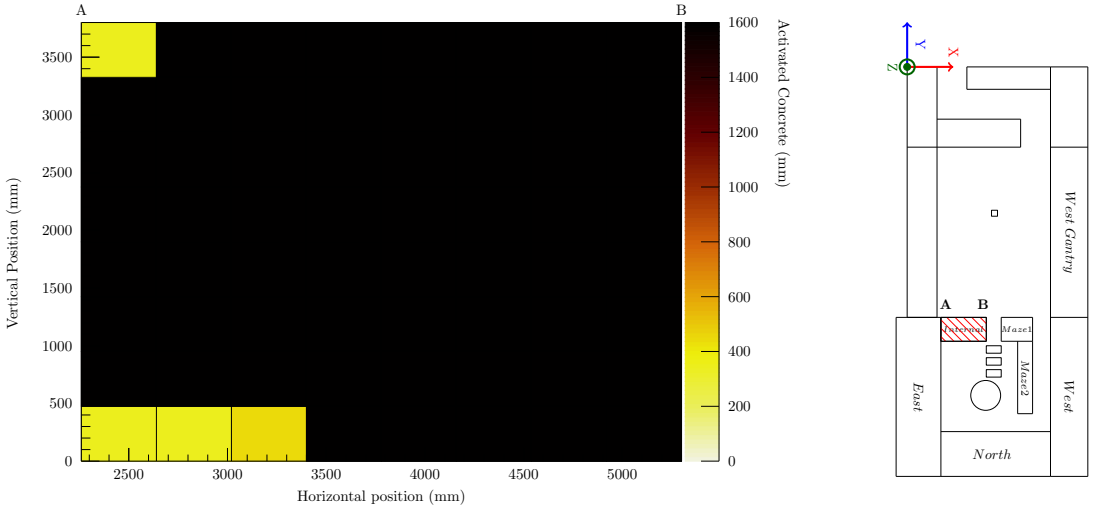

Figure 2.20: Quantity of activated concrete for the internal wall.

Maze 2

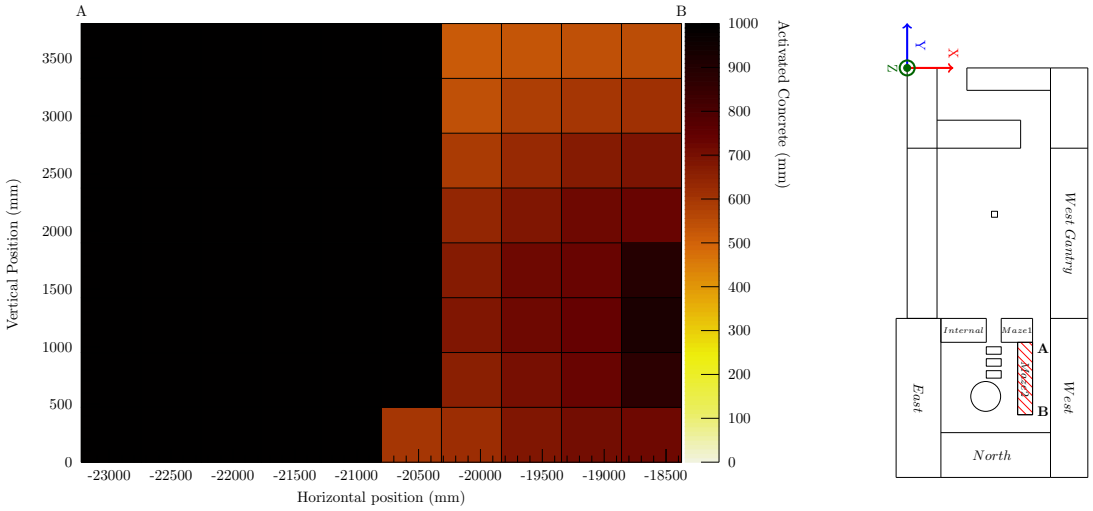

Figure 2.21: Quantity of activated concrete for the maze wall.

North

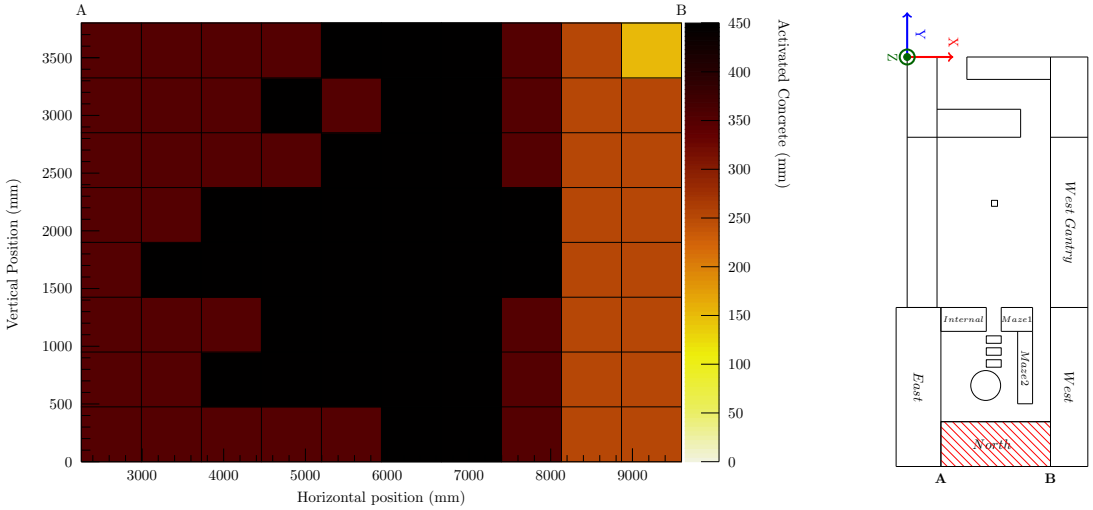

Figure 2.22: Quantity of activated concrete for the north wall.

East

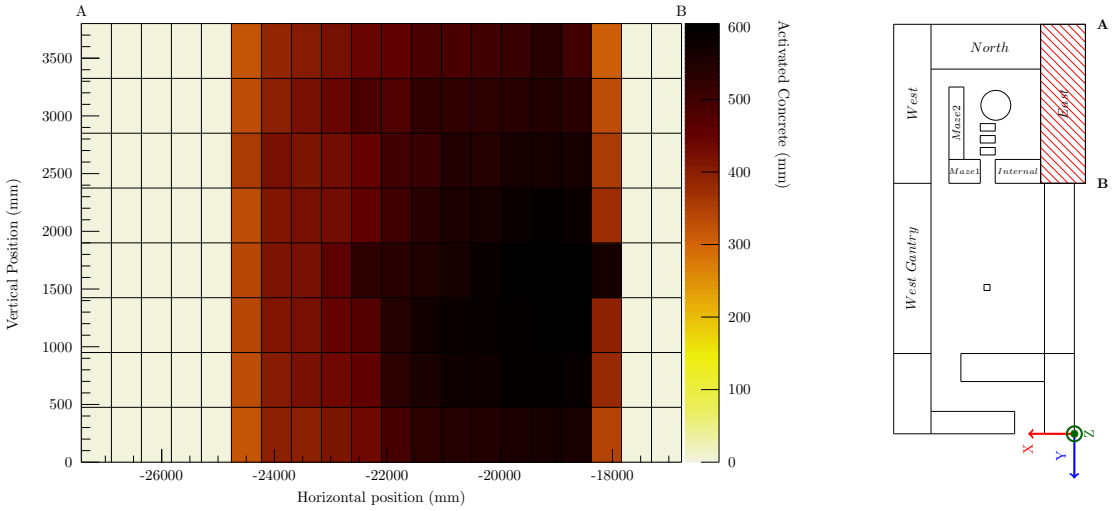

Figure 2.23: Quantity of activated concrete for the east wall.

West

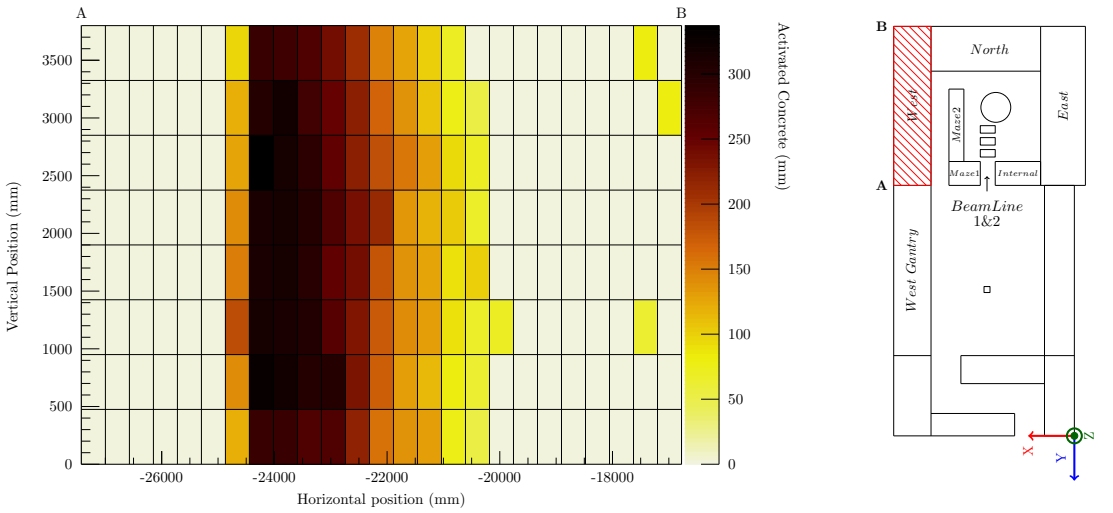

Figure 2.24: Quantity of activated concrete for the west wall.

Floor

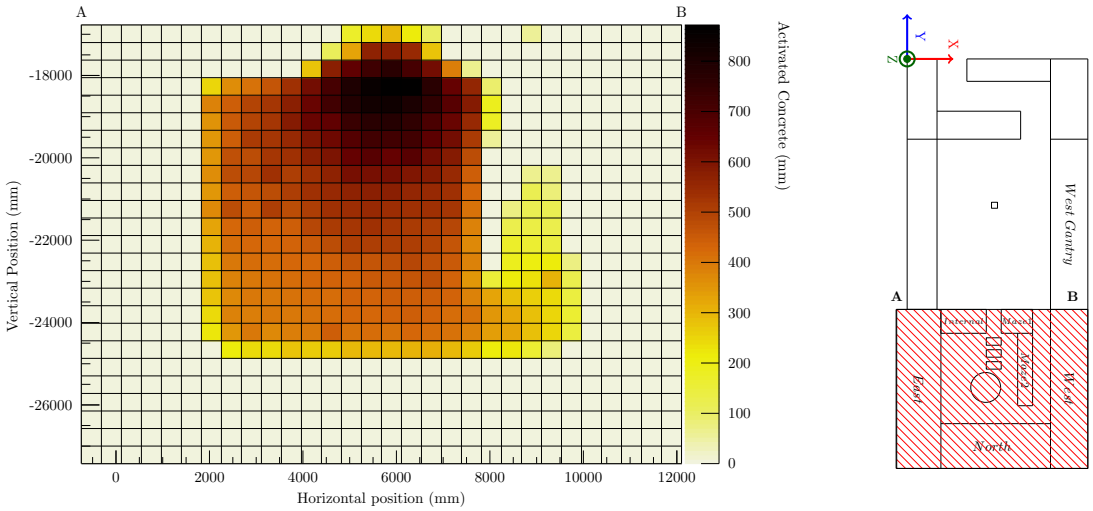

Figure 2.25: Quantity of activated concrete for the floor.

For each wall, the total thickness of concrete to remove is computed and results have been detailed in table 2.12. In this table, results obtained with *Geant4* are compared with those obtained by *IBA* with *MCNPX* [122]. Over a total of 437 m^3 of concrete, *IBA* finds a proportion of activated concrete equal to 22% while with *Geant4*, we obtain 30%.

	Geant4 (mm)	*MCNPX* (mm)
Beam Line 1	1600	1600
Beam Line 2	1600	1600
Internal	1600	1600
Maze 1	1600	1600
Maze 2	1000	500
East	600	400
West	300	200
North	500	400
Roof	700	500
Floor	800	500
West_Gantry	0	0

Table 2.12: Results obtained with Geant4 *and compared with those obtained by* IBA *with* MCNPX.

The results between *Geant4* and *MCNPX* are in good agreement. Differences can be explained from the discrepancies between models used in spallation computation (see figure 2.4 in section 2.1.4.2) or, to a lesser extent, the capture process via the neutron fluence. Figure 2.26 illustrates the areas where the activity concentration of concrete is above the limit for nuclear waste (in red).

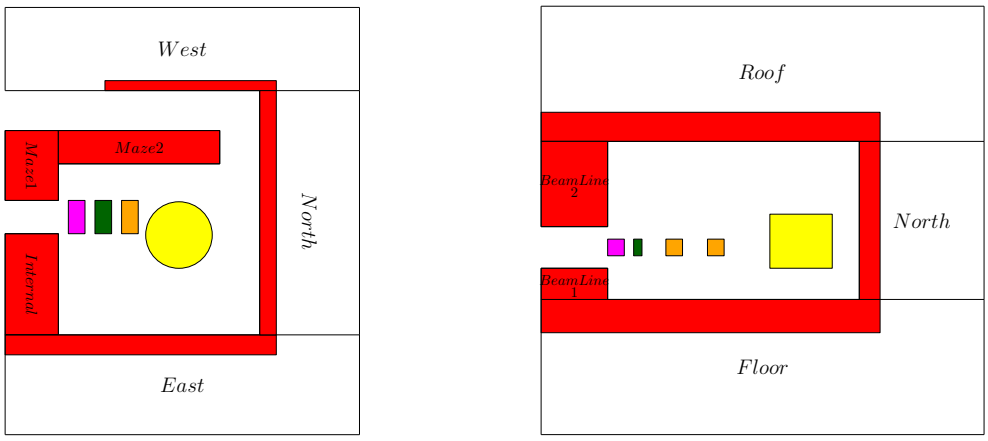

(a) Layout of the S2C2 vault (b) Transversal view of the S2C2 vault

Figure 2.26: Quantity of activated concrete in the Proteus® One room.

In Belgian legislation, there is a principle whereby a producer of radioactive waste needs to pay for the treatment of this waste. At the end of the operating period, the National Agency for Radioactive Waste and enriched Fissile Material analyzes the quantity of activated concrete. Based on [124], the cost for the treatment of nuclear waste is several M€. It is therefore essential to limit the generated waste. Two solutions are highlighted and described in the next section.

2.5 Reduction of activated concrete in a Proteus One

Various approaches have been explored to reduce the quantity of radioactive waste in industrial and medical applications [125, 126, 127, 128]. Two solutions can be investigated: the first one is to change the composition of the concrete to limit the neutronic capture and the second one is the improvement of the design of the elements interacting with the beam to limit the number of emitted neutrons. The composition of concrete has been studied in [125, 126], the conclusions of these works are summarized herebelow. The activation contribution of each element is presented in section 2.5.2.

2.5.1 Utilisation of Low-Activation Concrete

We explain here the possibilities to reduce the activation in shielding concrete by adapting its composition. Any concrete is composed of three major elements: cement, water and solid aggregates, in different proportions.

In the cement or in the aggregates, we can find nuclides such as europium, cobalt or caesium. As seen before, these elements are the parent elements of problematic radionuclides. Consequently, a low activation concrete needs to have a small percentage of these elements.

In 2015, *IBA* and the Scientific and Technical Center for Construction have developed two type of Low-Activation Concrete (LAC) while preserving the mechanical properties of a standard concrete. This LAC is composed of limestone aggregates with white cement (namely type EI) or with aluminous cement (namely type S1). The atomic composition of these concretes is summarized in table 2.13. Values for a standard concrete are also provided [23].

Element	Standard (%)	LAC EI (%)	LAC S1 (%)
H	1	0.72	0.75
C	0.1	8.91	8.72
O	52.91	47.77	49.21
Na	1.6	0.08	0.08
Mg	0.2	0.24	0.16
Al	3.39	0.27	6.77
Si	33.7	1.24	0.09
K	1.3	0.03	0.02
Ca	4.4	40.51	34.05
Fe	1.4	0.06	0.06
Eu(ppm)	1.08	0.023	0.0081
Co(ppm)	21.9	0.75	0.25
Cs(ppm)	3.21	0.052	0.010

Table 2.13: Atomic composition of standard and low-activation concretes. Data taken from [23]

With a LAC EI concrete, the quantity of nuclear waste can be reduced to 2 m^3. Moreover, the facility does not need to be dismantled directly after the end of its operation. *IBA* estimates a rest period of about 5 years to decrease the activity and therefore, the amount of remaining nuclear waste is further reduced to 0 m^3. This solution, low activation concrete, is already in use for the new Proteus®One center all around the world.

2.5.2 Contribution of each element to activation

In the following chapters of this thesis, we focus our attention on the second solution: the decrease of the generated neutrons. In figure 2.27, the activation concentration divided by the clearance level is shown as function of the depth in a wall. The contribution of each element interacting with the beam and responsible for activation is also presented.

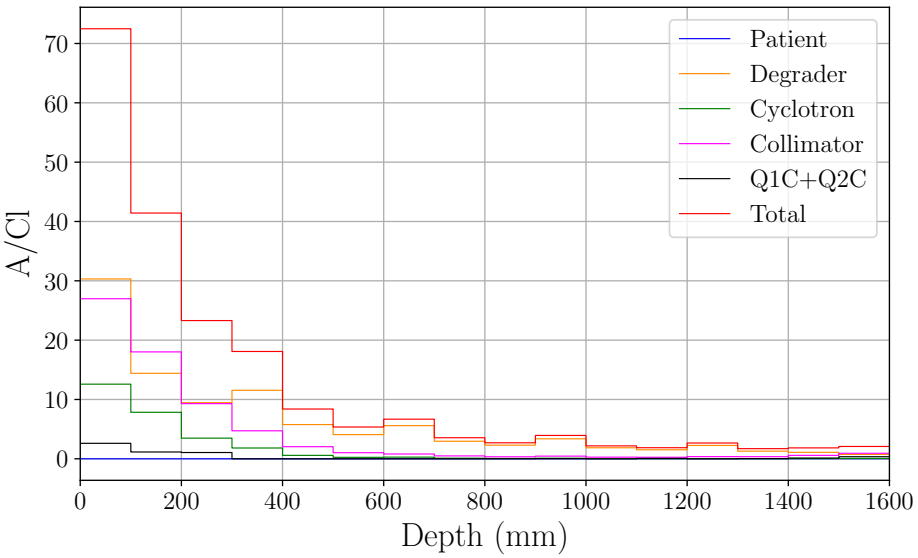

Figure 2.27: Contribution of the elements in the beamline to the concrete activation.

The patient does not create any activation contrarily to the cyclotron, the degrader and the collimator. The properties of the beam at the exit of the degrader and the collimator are detailed in chapter 4 where a new solution is proposed. In chapter 5, we will analyse the propagation of the extracted beam of the S2C2 inside the beamline.

2.6 Conclusion

The purpose of this chapter was to determine the proportion of activated concrete in a compact proton therapy center, a Proteus®One. To answer this problem, we have introduced the concept of equivalent-neutron source. This method allows increasing the number of primary particles while keeping the same computation time which reduce the relative error on the reaction rate. Then, we compared the different hadronic models of *Geant4* with *MCNPX* and *Phits*. This study showed that the reaction rate for isotopes produced by neutronic capture are the same for the different models, whereas the spallation reactions give a large difference. The Bertini model is not adapted for activation studies because the ^{22}Na production cross sections is underestimated. We conclude that the BIC model, as implemented in *Geant4*, can be used for activation studies in a conservative approach. After having detailed radiation sources, we simulate the amount of activated concrete in a Proteus®One center after 20 years of operation. We determined that 30 % of the shielding is considered as radioactive waste which requires specific actions during the decommissioning phase. Two solutions have been presented to minimize this quantity. The first, studied by *IBA* consists of a modification of the concrete composition. It shows that this quantity can be reduced to 0 m^3 if a rest period of 5 years is considered. The second solution, studied in this work proposes a new solution for the degrader to limit the neutron production. The estimations of the beam losses for each radiation source will be compared and confirmed with the results obtained using the complete model of the Proteus®One system in chapter 6.

Part II

Optimisation and reduction of the neutrons production by the energy degrader

Chapter 3

Beam dynamics and beam transport formalism

Contents

As we have seen in the previous chapter, a better knowledge of the radiation source terms is important to predict the activation level in concrete after several years of operation. Thus, to localize these production sources of secondary particles we need to model the beam at the exit of an accelerator and its propagation along the beamline. The latter consists of a succession of bending and quadrupole but other components may interact locally to monitor the beam for instance.

In this chapter, we first recall in section 3.1 some notions of classical mechanics for beam physics. We introduce, in section 3.2, the particle acceleration principle, *i.e.* the transverse motion formalism of particles in an electromagnetic field. In section 3.3, we introduce three codes developed to simulate the beam dynamics.

3.1 Elements of classical mechanics for beam physics

In this section, we recall the general concept of classical mechanics [129]. In section 3.1.1, we derive, from the Lagrangian equations, the Hamilton equations of motion. Section 3.1.2 deals with the notion of canonical transformations and the symplectic conditions.

3.1.1 Hamilton equations of motion

Let consider a dynamic system characterized by a Lagrangian L as defined in appendix C.

$$\frac{d}{dt}\left(\frac{\partial L}{\partial \dot{q}_i}\right) - \frac{\partial L}{\partial q_i} = 0\,, \tag{3.1}$$

where q_i and $\dot{q}_i$ are generalized variables and their time derivatives. We now derive, using the Lagrangian of the system as a starting point, the Hamilton equations of motion. The canonical momentum p_i is defined as :

$$p_i = \frac{\partial L\left(\boldsymbol{q}, \dot{\boldsymbol{q}}, t\right)}{\partial \dot{q}_i}\,. \tag{3.2}$$

Where $\boldsymbol{q} = (q_1, q_2, ..., q_N)$. The quantities $(p_i,\, q_i)$ are conjugated canonical variables. The transition from Lagrangian to Hamilton formulation corresponds to the use of variables $(q_i,\, p_i,\, t)$ instead of $(q_i,\, \dot{q}_i,\, t)$. The relation between H and L is of the form :

$$H(\boldsymbol{q}, \dot{\boldsymbol{q}}, t) = \sum_i \dot{q}_i\, p_i - L(\boldsymbol{q}, \dot{\boldsymbol{q}}, t)\,, \tag{3.3}$$

and the differential form dH is given by :

$$dH = \sum_i \left(\frac{\partial H}{\partial q_i} dq_i + \frac{\partial H}{\partial p_i} dp_i\right) + \frac{\partial H}{\partial t} dt\,, \tag{3.4}$$

$$dH = \sum_i \left(\dot{q}_i dp_i + p_i d\dot{q}_i - \frac{\partial L}{\partial q_i} dq_i - \frac{\partial L}{\partial \dot{q}_i} d\dot{q}_i\right) - \frac{\partial L}{\partial t} dt\,. \tag{3.5}$$

We insert equation (3.2) in equation (3.5) and we obtain:

$$dH = \sum_i \left(\dot{q}_i dp_i - \dot{p}_i dq_i\right) - \frac{\partial L}{\partial t} dt\,. \tag{3.6}$$

We compare this relation with equation (3.4) and we finally obtain the Hamilton equations of motion:

$$\dot{q}_i = \frac{\partial H}{\partial p_i}\,, \tag{3.7}$$

$$\dot{p}_i = -\frac{\partial H}{\partial q_i}\,, \tag{3.8}$$

$$\frac{\partial L}{\partial t} = -\frac{\partial H}{\partial t}\,. \tag{3.9}$$

If we consider a system composed of many degree of freedom, equations (3.7) and (3.8) are expressed in a more elegant form using the symplectic notation. For a system of N degrees of freedom, we define a $2N$ column matrix $\boldsymbol{\eta}$ whose elements are given:

$$\eta_i = q_i\,, \qquad \eta_{i+N} = p_i\,, \quad 1 \leq i \leq N\,. \tag{3.10}$$

$$\tag{3.11}$$

Similarly, the column matrix $\frac{\partial H}{\partial \eta}$ has elements:

$$\left(\frac{\partial H}{\partial \boldsymbol{\eta}}\right)_i = \frac{\partial H}{\partial q_i}\,, \qquad \left(\frac{\partial H}{\partial \boldsymbol{\eta}}\right)_{i+N} = \frac{\partial H}{\partial p_i}\,, \qquad 1 \leq i \leq N\,. \tag{3.12}$$

Finally, we define the antisymmetric matrix $\boldsymbol{J}$ as a $2N \times 2N$ square matrix according to:

$$\boldsymbol{J} = \begin{pmatrix} 0 & I_N \\ -I_N & 0 \end{pmatrix} , \tag{3.13}$$

where I_N is the unit matrix of dimension $N \times N$. With these notations, the Hamilton equations of motion are written in a compact form:

$$\dot{\boldsymbol{\eta}} = \boldsymbol{J} \frac{\partial H}{\partial \boldsymbol{\eta}} . \tag{3.14}$$

3.1.2 Canonical transformation and symplectic conditions

For some problems, it may be suitable to express equations of motion in a specific system of coordinates. Here, we introduce the concept of canonical transformation which expresses the new coordinates (Q, P) in terms of old coordinates and momenta (q, p). Only transformations that satisfied equations of motion are allowed and therefore, there is a function K which satisfies:

$$\dot{Q}_i = \frac{\partial K}{\partial P_i} , \tag{3.15}$$

$$\dot{P}_i = -\frac{\partial K}{\partial Q_i} . \tag{3.16}$$

By inspection, we notice that in these equations K corresponds to the Hamiltonian in the new set of coordinates. If P_i, p_i, Q_i and q_i are canonical variables, they must satisfied the *Hamilton's principle* which says that [129]: *The motion of the system from time t_1 to time t_2 is such that the variation of the line integral is zero:*

$$\delta \int_{t_1}^{t2} \left(P_i \dot{Q}_i - K \right) = 0 , \tag{3.17}$$

$$\delta \int_{t_1}^{t2} \left(p_i \dot{q}_i - H \right) = 0 . \tag{3.18}$$

Both equations are equal if the integrand are connected by a relation of form:

$$p_i \, \dot{q}_i - H = P_i \, \dot{Q}_i - K + \frac{dF}{dt} , \tag{3.19}$$

with F is any function of the phase space coordinates. F is called the *generating function* of the transformation. A canonical transformation changes the coordinates while preserving the Hamilton equations of motion [129].

We will see in section 3.2.2 that we must use a generating function that expresses the new momenta from the old coordinates. We may define a generating function F_3 of the old momenta p_i, the new coordinates Q_i and the time t as:

$$F = q \, p + F_3 \left(Q, p, t \right) . \tag{3.20}$$

This function is inserted in equation (3.19) and we use the properties that the old and the new coordinates are independent ($q = -\frac{\partial F_3}{\partial p}$ and $P = \frac{\partial F_3}{\partial Q}$) and we obtain the relation between H and K:

$$K = H + \frac{\partial F_3}{\partial t} . \tag{3.21}$$

As in the previous section, the canonical transformation can also be expressed in terms of symplectic formulation of Hamilton's equations. Let us define $\boldsymbol{\xi}$ a $2N$ columns matrix which contains a new set of coordinates (Q_i, P_i).

$$\boldsymbol{\xi} = \boldsymbol{\xi}(\boldsymbol{\eta}) \,. \tag{3.22}$$

The time derivative of this equation is written as:

$$\dot{\boldsymbol{\xi}} = \boldsymbol{M}\dot{\boldsymbol{\eta}} \,, \tag{3.23}$$

where $\boldsymbol{M}$ is the Jacobian matrix of the transformation, with elements $M_{ij} = \partial\xi_i/\partial\eta_j$. We can show that equation of motion for any set of variables $\boldsymbol{\xi}$ transforming from the canonical set $\boldsymbol{\eta}$ is given by:

$$\dot{\boldsymbol{\xi}} = \boldsymbol{M}\boldsymbol{J}\tilde{\boldsymbol{M}}\frac{\partial H}{\partial \boldsymbol{\xi}} \,, \tag{3.24}$$

where $\tilde{\boldsymbol{M}}$ is the inverse matrix of $\boldsymbol{M}$. Therefore, the transformation (3.22) is canonical only if:

$$\boldsymbol{M}\boldsymbol{J}\tilde{\boldsymbol{M}} = \boldsymbol{J} \,. \tag{3.25}$$

This condition is called the symplectic condition for a canonical transformation, and $\boldsymbol{M}$ is said to be symplectic if it satisfies the condition: *the square of the determinant of a symplectic matrix, and therefore the Jacobian matrix of a canonical transformation, is equal to unity* [130].

$$|\boldsymbol{M}|^2 = 1 \,. \tag{3.26}$$

From these properties, one deduces the *Liouville's theorem* which expresses that [130]: *In any system governed by a Hamiltonian, the density of system points surrounding a particular system point in phase space must remain constant as the independent variable evolves.* It means that if the boundary of the phase space is changing, the volume of the region is always the same because the determinant of the Jacobian matrix M is equal to one. A region in the phase space may twist or change shape but the volume of this region is preserved (see figure 3.1).

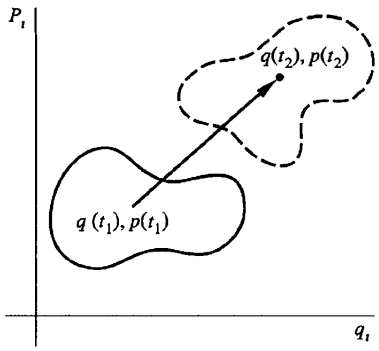

Figure 3.1: Motion of a volume in phase space. The shape of the region is changing but the volume is preserved. Reproduced from [129].

3.2 Fundamentals in particle beam dynamics

In this section, we present the different equations for the description of the motion of particles in an electromagnetic field. We develop in section 3.2.1 the Hamilton equations

of motion to derive the so-called Hill's equations. In section 3.2.3, we briefly explain the acceleration principle in a cyclotron. The betatronic equations for elements in a beam line are described in section 3.2.4. Finally, section 3.2.5 deals with the description of particles beams and the motion of the phase space.

3.2.1 Hamiltonian for charged particles in electromagnetic fields

Let us consider a charged particle with a velocity $\boldsymbol{v}$ inside an electromagnetic field characterized by $\boldsymbol{E}$ (the electric field) and $\boldsymbol{B}$ (the induction magnetic field). The motion of the particle is governed by the Lorentz force:

$$\frac{d\boldsymbol{P}}{dt} = \boldsymbol{F} = e\left(\boldsymbol{E} + \boldsymbol{v} \times \boldsymbol{B}\right) , \tag{3.27}$$

where $\boldsymbol{P} = \gamma m \boldsymbol{v}$ is the relativistic momentum, m is the particle mass, $\boldsymbol{v}$ is the velocity, e is the particle charge and γ is the relativistic Lorentz factor ($\gamma = 1/\sqrt{1 - v^2/c^2}$ with c, the speed of light). $\boldsymbol{E}$ and $\boldsymbol{B}$ are expressed as a function of the scalar and vector potential Φ and $\boldsymbol{A}$ that are given by:

$$\boldsymbol{E} = -\nabla\Phi - \frac{\partial \boldsymbol{A}}{\partial t} , \tag{3.28}$$

$$\boldsymbol{B} = \nabla \times \boldsymbol{A} . \tag{3.29}$$

We can show that the Lagrangian of the system is given by:

$$L = -mc^2\sqrt{1 - \frac{v^2}{c^2}} - e\Phi + e\boldsymbol{v} \cdot \boldsymbol{A} . \tag{3.30}$$

The canonical momentum $\boldsymbol{p}$ is determined using the relation (3.2):

$$\boldsymbol{p} = \frac{\partial L}{\partial \boldsymbol{v}} = \boldsymbol{P} + e\boldsymbol{A} , \tag{3.31}$$

where $\boldsymbol{P}$ is the mechanical momentum (relativistic momentum). Finally, we determine the Hamiltonian of the system with equation (3.3):

$$H_0 = \boldsymbol{p} \cdot \boldsymbol{v} - L , \tag{3.32}$$

$$= e\Phi + c\sqrt{m^2c^2 + (\boldsymbol{p} - q\boldsymbol{A})^2} . \tag{3.33}$$

Hamilton equations of motion are thus given by:

$$\dot{x_k} = \frac{dx_k}{dt} = \frac{\partial H_0}{\partial p_k}; \qquad \dot{p_k} = \frac{dp_k}{dt} = -\frac{\partial H_0}{\partial x_k}; \qquad k = x, y, z . \tag{3.34}$$

3.2.2 Hamiltonian in Frenet-Serret coordinates

In accelerator physics, it is more convenient to use a curvilinear system of coordinates whose origin follows the trajectory of the reference particle. This coordinate system is also called the *Frenet-Serret coordinates system*. The reference orbit of the particle is defined as the path of the particle having the central design momentum of the accelerator through idealised magnets [131].

Figure 3.2 shows the system of coordinates for the particle motion. The hat refers to the unit vector of the system. The global Cartesian ($\hat{X}$,$\hat{Y}$,$\hat{Z}$) (resp. Frenet-Serret) system of coordinates is shown in green (resp. in blue). In this thesis, we assume that the Frenet-Serret system has no torsion.

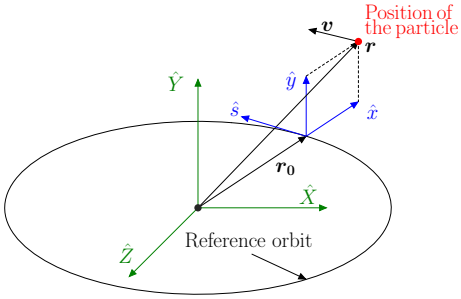

(a) In a circular accelerator.

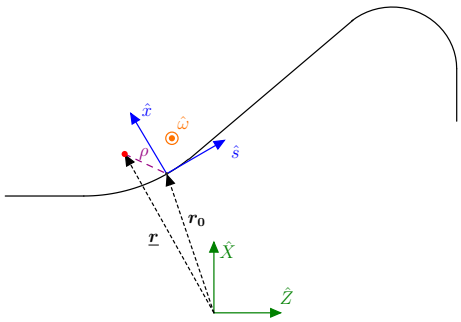

(b) In a beamline.

Figure 3.2: Global and curvilinear system of coordinates. Reproduced from [132].

The three vectors $\{\hat{x}, \hat{s}, \hat{y}\}$ form a right-handed system of unit vectors of the Frenet-Serret system of coordinates. $\hat{s}$ is tangential to the curve, $\hat{x}$ is radial to the curvature of the curve, $\hat{y}$ is given by the vectorial product $\hat{s} \times \hat{x}$.

We denote by $\boldsymbol{r_0}(s)$ the reference orbit, s the measured path length along the closed orbit from a reference initial point and $\rho(s)$ the local curvature radius. The unit vectors are given by:

$$\hat{s}(s) = \frac{d\boldsymbol{r_0}(s)}{ds}\,, \qquad \hat{x}(s) = -\rho(s)\frac{d\hat{s}(s)}{ds}\,, \qquad \hat{y}(s) = \hat{x}(s) \times \hat{s}(s)\,. \tag{3.35}$$

The derivation of the unit vector with respect to s is done using the Darboux vector with $h = 1/\rho$[133].

$$\frac{d\boldsymbol{r_0}(s)}{ds} = \hat{s}\,, \tag{3.36}$$

$$\frac{d\hat{x}(s)}{ds} = \hat{x}' = \hat{\omega} \times \hat{x} = h\boldsymbol{s}\,, \tag{3.37}$$

$$\frac{d\hat{y}(s)}{ds} = \hat{y}' = \hat{\omega} \times \hat{y} = 0\,, \tag{3.38}$$

$$\frac{d\hat{s}(s)}{ds} = \hat{s}' = \hat{\omega} \times \hat{s} = -h\boldsymbol{x}\,. \tag{3.39}$$

The trajectory of the particle around the reference orbit is given by:

$$\underline{\boldsymbol{r}}(s) = \boldsymbol{r_0}(s) + x\hat{x}(s) + y\hat{y}(s)\,. \tag{3.40}$$

The Hamiltonian in equation (3.33) is given in a Cartesian coordinates system, but we want to express it in the curvilinear coordinates system [134]. The transformation is done using a generating function F (see equation (3.21)). As we know the new coordinates and the old momentum, we use a generating function of the third type, F_3 (see section 3.1.2) expressing the new momentum ($\boldsymbol{p}$) from the old coordinates ($\underline{\boldsymbol{r}}$). A solution for F_3 is:

$$F_3(\boldsymbol{p}, \underline{\boldsymbol{r}}, t) = -\boldsymbol{p} \cdot \underline{\boldsymbol{r}}\,, \tag{3.41}$$

with $\underline{\boldsymbol{r}}$ given by equation (3.40). Thus, the new momentum is given by:

$$p_s = -\frac{\partial F_3}{\partial s} = \boldsymbol{p} \cdot \left(\frac{\partial \boldsymbol{r_0}(\boldsymbol{s})}{\partial s} + \frac{\partial \hat{x}(s)}{\partial s} \cdot x + \frac{\partial \hat{y}(s)}{\partial s} \cdot y \right). \tag{3.42}$$

As F_3 has no time dependence, we have $H_1 = H_0$ (see equation (3.21)). The next step is to replace the old momenta in H_0 by the new ones:

$$H_1 = c\sqrt{\left(\frac{p_s}{1+hx} - qA_s\right)^2 + (p_x - qA_x)^2 + (p_y - qA_y)^2 + m_0^2c^2} + e\Phi\,. \tag{3.43}$$

For the beam description, it is easier to use the coordinates s as the independent variable rather than the time t. The derivative of x (resp. p_x) with respect to s is given by:

$$x' = \frac{\partial p_s}{\partial x}; \qquad p_x' = \frac{\partial p_s}{\partial p_x}\,. \tag{3.44}$$

If we use s as independent variable, the quantity $-p_s$ corresponds to the new Hamiltonian H_2 with the new equations of motion:

$$x' = \frac{\partial H_2}{\partial p_x}, \qquad p_x' = -\frac{\partial H_2}{\partial x}\,, \tag{3.45}$$

$$H_1' = \frac{\partial H_2}{\partial t}, \qquad t' = \frac{\partial p_s}{\partial H_1}\,, \tag{3.46}$$

where H_2 is obtained by solving equation (3.43) for $-p_s$ and reads:

$$H_2 = -p_s = -(1+hx).\left\{\sqrt{\left(\frac{H_1 - e\Phi}{c}\right)^2 - m_0^2c^2 - (p_x - qA_x)^2 - (p_y - qA_y)^2} + qA_s\right\}. \tag{3.47}$$

This Hamiltonian is the standard Hamiltonian for beam dynamics in a Frenet-Serret system of coordinates with s as independent variable. Different approximations are made in order to further simplify this relation:

1. There is no acceleration of the particles, $\Phi = 0$, and so H_1 is equal to the total energy with the relation: $H_1^2 \equiv E^2 = c^2\left(p^2 + m_0c^2\right)$.
2. The magnetic fields are purely transverse and we have $A_x = A_y = 0$.
3. The particles have a small transverse momenta compared to the total momenta. This approximation is also called the paraxial approximation: $p_{x,y} \ll p$.

With these 3 approximations, and expanding H_2 to the second order, we obtain:

$$H_2 = -(1 + h\,x)\left(p\left(1 - \frac{p_x^2 + p_y^2}{2p^2}\right) + q\,A_s\right) . \tag{3.48}$$

A beam line is designed for a specific momentum p_0 but the particles may have deviations around this value. We inject the relative momentum deviation as:

$$\delta = \frac{p - p_0}{p_0} = \frac{\Delta p}{p_0} . \tag{3.49}$$

We introduce the relative momentum deviation in (3.48) and we use the notation $\tilde{p}_{x,y} = p_{x,y}/p_0$.

$$\tilde{H}_2 = -(1 + h\,x)\left(1 + \delta - \frac{\tilde{p}_x^2 + \tilde{p}_y^2}{2(1+\delta)} + \frac{q}{p_0}A_s\right) . \tag{3.50}$$

The last step of this development consists in introducing a practical expression for A_s. It is achieved using a multipolar expansion:

$$\frac{q}{p_0}A_s = -\,\mathrm{Re}\left(\sum_{n=1}^{\infty}\frac{ia_n + b_n}{n}\,(x + iy)^n\right) , \tag{3.51}$$

where i is the imaginary unit number, n is the order of the multipole (1 for dipole, 2 for quadrupole, ...). The coefficients b_n (resp. a_n) are for regular multipoles (resp. skew multipoles[1]).

In a typical beamline, there is no coupling and therefore no skew multipole ($a_n = 0$). The expressions of the magnetic field in the transverse plane expanded to the third order (sextupoles) are obtained with equation (3.29) [134]:

$$\begin{aligned} B_x &= -\frac{\partial A_s}{\partial y} = -\frac{p_0}{q}\,(b_2\,y + 2\,b_3\,x\,y) , \\ B_y &= \frac{\partial A_s}{\partial x} = -\frac{p_0}{q}\,\left(b_1 + b_2\,x + b_3(x^2 - y^2)\right) . \end{aligned} \tag{3.52}$$

Finally, we combine (3.50) in (3.51) and we obtain the expression of the Hamiltonian for a multipolar field. We also subtract the constant terms which are irrelevant for equations of motion.

$$\boxed{\tilde{H} = \frac{\tilde{p}_x^2 + \tilde{p}_y^2}{2(1+\delta)} - b_1 x\delta + \frac{b_1^2}{2}x^2 + \frac{b_2}{2}(x^2 - y^2) + \frac{b_3}{3}(x^3 - 3xy^2) + ...} \tag{3.53}$$

Equations of motion are now determined using $\tilde{H}$:

$$x' = \frac{\partial \tilde{H}}{\partial p_x} = \frac{\tilde{p}_x}{(1+\delta)} , \qquad p_x' = -\frac{\partial \tilde{H}}{\partial x} = b_1\delta - (b_1^2 + b_2)x - b_3(x^2 - y^2) , \tag{3.54}$$

$$y' = \frac{\partial \tilde{H}}{\partial p_y} = \frac{\tilde{p}_y}{(1+\delta)} , \qquad p_y' = -\frac{\partial \tilde{H}}{\partial y} = b_2 y + 2b_3 xy . \tag{3.55}$$

[1] Skew multipoles refers to a regular multipole with a rotation of an angle equal to $90°/n$.

If we differentiate again these equations, we find the *Generalized Hill's equation* of motion [135]:

$$\begin{aligned}(1+\delta)x'' - b_1\delta + (b_1^2 + b_2)x + b_3(x^2 - y^2) = 0\,,\\ (1+\delta)y'' - b_2 y - 2b_3 xy = 0\,.\end{aligned} \tag{3.56}$$

If we consider only linear fields, (3.52) becomes [132]:

$$\begin{aligned}B_x &= \frac{\partial B_y}{\partial x} y = B_{x;y}\, y\,,\\ B_y &= -B_0 + \frac{\partial B_y}{\partial x} x = -B_0 + B_{x;y}\, x\,,\end{aligned} \tag{3.57}$$

where B_0 is the dipole field defined for the design orbit. We insert equations (3.57) in (3.56) to obtain[2]:

$$\begin{aligned}x'' + \left(\frac{1}{\rho_0^2} - \frac{B_{x;y}}{B_0\rho_0}\right) x = \frac{\delta}{\rho_0}\,,\\ y'' + \frac{B_{x;y}}{B_0\rho_0}\frac{1}{1+\delta}\, y = 0\,.\end{aligned} \tag{3.58}$$

If the particle has a no momentum deviation ($\delta = 0$), equations (3.58) become the well-known Hill equations:

$$\begin{aligned}x'' + \left(\frac{1}{\rho_0^2} - \frac{B_{x;y}}{B_0\rho_0}\right) x = 0\,,\\ y'' + \frac{B_{x;y}}{B_0\rho_0} y = 0\,.\end{aligned} \tag{3.59}$$

Let us consider as an example, the Hill equation (equation (3.59)) for a quadrupole, we have $\rho = \infty$ and if we denote the ratio $B_{x;y}/B_0\rho_0$ by K, we obtain :

$$\begin{aligned}x'' - K\, x = 0\,,\\ y'' + K\, y = 0\,.\end{aligned} \tag{3.60}$$

These equations show that the focus is only possible in one direction at the time. Therefore, in a beamline, the gradient of the quadrupoles must be alternated to restore a global focusing system. The system is called *alternating gradient*.

3.2.3 Orbit and acceleration in a cyclotron

As mentioned before, the typical maximum proton energy for medical applications must be at least 230 MeV. Therefore, cyclotrons are typically used as proton therapy accelerator: they can produce the required current at those energies in a reduced footprint. To reach 230 MeV, the cyclotron design must take into account the relativity of the proton and we describe below two typical cyclotron designs. Despite the dose considerations, 70% of the beam is still lost in the cyclotron. Therefore, a detailed understanding of accelerators are of primary importance for radioprotection and shielding studies.

[2] Where we use the relation $p = qB\rho$ to further simplify the resulting expression (see section 3.2.4.2).

The trajectory of the particle is curved using a magnetic field and the radius of the trajectory increases with the energy. The acceleration of the particles is realized with the electric field induced by a Radio-wave Frequency (RF). Using Newton's second law and the Lorentz force, the revolution frequency of the particle is given by [132]:

$$f = \frac{qB}{2\pi\gamma m}\,, \tag{3.61}$$

with γ, the relativistic factor which increases with time. We define by *synchronous particle*, the particle which stays in synchronism with the RF turn after turn [136]. To provide a net acceleration, the RF frequency (f_{RF}) must be locked to the revolution frequency f_{rev}. There are two possibilities to maintain the synchronism between the particle and the pulsation of the RF:

1. B depends on the radius and therefore, f_{rev} is kept constant. This is an *isochronous cyclotron.*
2. B is independent of the radius, f_{rev} decreases with the radius and therefore, f_{RF} must decrease with the time. This is a *synchrocyclotron.*

Let us consider the motion of a charged particle inside a uniform magnetic field B_0. If the particle has a momentum along the z direction, the motion of the particle is helicoidal. To avoid this effect, we may use a field gradient and a radial component to focus the beam along the z direction. The B_r component is given by [137]:

$$B_r = -\frac{r}{2}\frac{dB_z(0,z)}{dz}\,. \tag{3.62}$$

Equation $\nabla \times \boldsymbol{B} = 0$ implies:

$$\frac{\partial B_z}{\partial r} = \frac{\partial B_r}{\partial z}\,. \tag{3.63}$$

The *field-index* (n) characterizes the change of the magnetic field as a function of the radius and is given by:

$$n(r) = -\frac{r}{B_z}\frac{\partial B_z}{\partial r}\,. \tag{3.64}$$

The vertical stability is ensured only if the field index is comprised between 0 and 1. We remark that there is a contradiction between the vertical stability (negative gradient) and the increase of the field with the radius (positive gradient).

The Azimuthal Varying Field (AVF) introduces an azimuthal dependence of the field using wedge-shaped inserts at periodic azimuthal position (see figure 3.3).

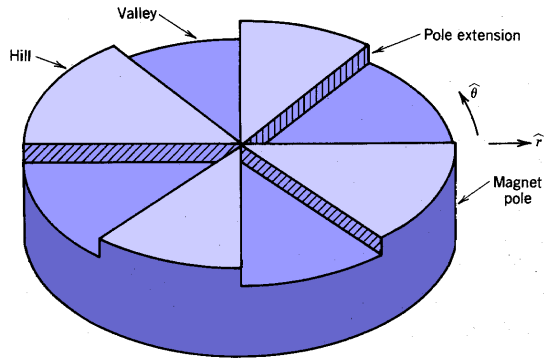

Figure 3.3: Magnetic poles of an AVF cyclotron. Reproduced from [137].

We define the *flutter* as the azimuthal variation of the magnetic field between hills and valleys. If we denote by $\langle B \rangle$, the average magnetic field, the expression of the flutter is given by:

$$F = \frac{\langle B_\theta^2 \rangle - \langle B \rangle^2}{\langle B \rangle^2} . \tag{3.65}$$

The acceleration of charged particles to high energies needs high magnetic fields. Unfortunately, the average field is limited to 2.5 T to avoid the iron saturation. Indeed, the shape of the magnetic field is given by the poles. If the magnetic field is above saturation, the iron is transparent to the magnetic field and the flutter becomes too small to provide focusing [138]. As example, we summarize in table 3.1 several values of the *flutter* as a function of the magnetic field [139].

$\langle B \rangle$(T)	F(%)
2.1	22.7
3.5	8.2
7	2

Table 3.1: Example of values of the flutter as a function of the average magnetic field. Data from [139].

We can see from table 3.1 that using superconducting coils does not allow to maintain the vertical focusing. To overcome this limitation, we can design an accelerator with an average magnetic field decreasing with the radius and a variable RF frequency: a synchrocylotron.

To decrease the size of the accelerator, one needs to use a strong magnetic field in the central region and thus need to use superconducting magnets. To keep the synchronism between the particles and the RF frequency, the latter is modulated. This modulation is only valid for a given energy for a given time and therefore, the beam at the exit will be pulsed. We show in figure 3.4 the two cyclotrons produced by *IBA* for proton therapy solutions. The beam energy at the exit of the accelerator is fixed at 230 MeV, which corresponds to a range of 32.95 cm in water.

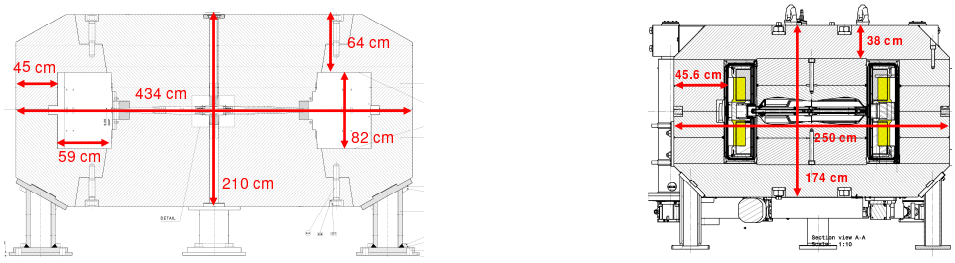

(a) Isochronous cyclotron (C230). *(b) Synchrocyclotron (S2C2).*

Figure 3.4: Schematic representation of the two IBA *cyclotrons. We remark the difference between the diameter of the C230 (434* cm*) and the S2C2 (250* cm*). Reproduced from [121].*

The aim of this work is to evaluate the concrete shielding activation of a Proteus® One system. The latter uses a S2C2 for beam production. We have obtained in chapter 2 that about 70% of the beam is lost before entering the beamline, *i.e* at high radius. The beam extraction is made using a passive system [140] which is mainly composed of three elements: a regenerator, an extraction channel and a gradient corrector (see figure 3.5).

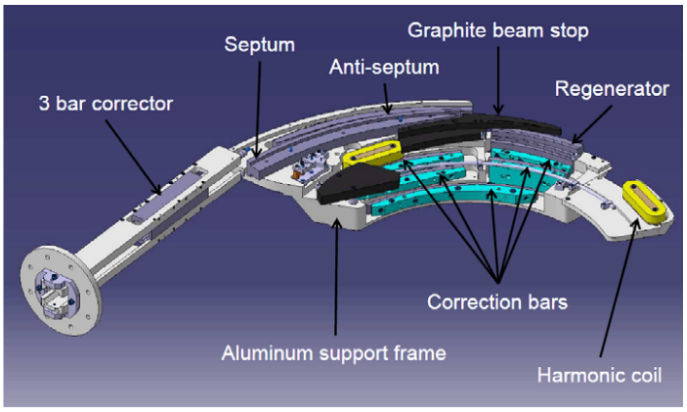

Figure 3.5: View of the S2C2 extraction system. Reproduced from [139].

At extraction these elements are used to properly separate the orbit at turn $N-1$ to the orbit at turn N. This extraction causes an important dispersion in the phase-space and results in losses at the level of the graphite beam stop. This protection is installed to reduce the activation of the metallic part of the extraction system. Finally, before exiting the accelerator, the beam passes through a permanent magnet quadrupole (PMQ) to match the beamline (not represented).

3.2.4 Betatronic equations for elements in a transport beamline

The general form of the solutions of equation (3.56) is the sum of the homogeneous solution and the particular solution. The homogeneous equations are just given by:

$$\begin{aligned} x'' + K_x(s)x = 0\,, \qquad & K_x(s) = \frac{1}{\rho^2} - \frac{B_{x;y}}{B\rho}\,, \\ y'' + K_y(s)y = 0\,, \qquad & K_y(s) = \frac{B_{x;y}}{B\rho}\,. \end{aligned} \tag{3.66}$$

Let z and z' represent either the horizontal or the vertical phase-space coordinates. Equation (3.66) becomes [132]:

$$z'' + K_z(s)z = 0\,, \tag{3.67}$$

The solution of this equation is given by:

$$z(s) = C(s)z(0) + S(z)z'(0)\,, \tag{3.68}$$

$$z'(s) = C'(s)z(0) + S'(z)z'(0)\,, \tag{3.69}$$

with $C(s)$, $S(s)$, $C'(s)$ and $S'(s)$ depending on the sign of K and summarized in table 3.2

	$K > 0$	$K < 0$
C(s)	$\cos\left(\sqrt{K}l\right)$	$\cosh\left(\sqrt{\lvert K\rvert}l\right)$
S(s)	$\frac{1}{\sqrt{K}}\sin\left(\sqrt{K}l\right)$	$\frac{1}{\sqrt{\lvert K\rvert}}\sinh\left(\lvert\sqrt{K}\rvert l\right)$
C'(s)	$-\sqrt{K}\sin\left(\sqrt{K}l\right)$	$\sqrt{\lvert K\rvert}\sinh\left(\sqrt{\lvert K\rvert}l\right)$
S'(s)	$\cos\left(\sqrt{K}l\right)$	$\cosh\left(\sqrt{K}l\right)$

Table 3.2: Definitions of C, S, C' and S' as function of the sign of K.

It is more convenient to use a matrix formalism to describe the propagation of the particle between $s = 0$ and any position s. We use the following notation:

$$\begin{pmatrix} z(s) \\ z'(s) \end{pmatrix} = M \begin{pmatrix} z(0) \\ z'(0) \end{pmatrix} = \begin{pmatrix} C(s) & C'(s) \\ S(s) & S'(s) \end{pmatrix} \begin{pmatrix} z(0) \\ z'(0) \end{pmatrix} . \tag{3.70}$$

Up to now, we have described the behaviour of a particle with a momentum p_0 whose trajectory describes a closed orbit. This closed orbit is called the *design orbit* and the particle is called a *synchronous* particle. However, at the extraction of an accelerator, the beam is composed of particles with momenta different from p_0. Let us remember equation (3.58) in term of x:

$$x'' + \left(\frac{1}{\rho_0^2} - \frac{B_{x;y}}{B_0 \rho_0} \right) x = \frac{\delta}{\rho_0} , \tag{3.71}$$

The solution of this general equation is thus the sum of the homogeneous equation and the particular solution:

$$x(s) = x_\beta(s) + D(s)\delta , \tag{3.72}$$

where x_β and D must satisfy the following relation:

$$x''_\beta + K_x(s) x_\beta = 0 , \tag{3.73}$$

$$D'' + K_x(s) D = \frac{1}{\rho} , \tag{3.74}$$

where D, the dispersion function, is the solution of the inhomogeneous equation. The physical meaning of the dispersion is that $D(s)\delta$ represents the offset of the reference trajectory from the ideal path for particle with a relative momentum deviation δ. The solution of the homogeneous equation for D is the same as equation (3.67). The general solution of the dispersion function is:

$$\begin{pmatrix} D(s) \\ D'(s) \end{pmatrix} = M(s|0) \begin{pmatrix} D(0) \\ D'(0) \end{pmatrix} + \begin{pmatrix} d \\ d' \end{pmatrix} . \tag{3.75}$$

Where $\bar{d}$ is called the two-component dispersion vector. Finally, we combine equation (3.75) and (3.70) to obtain the final transfer matrix of an element considering the off-momentum deviation.

$$M = \begin{pmatrix} C(s) & S(s) & D(s) \\ C'(s) & S'(s) & D'(s) \\ 0 & 0 & 1 \end{pmatrix} . \tag{3.76}$$

In this work, we mainly use drifts, sector dipoles and quadrupoles as lattice element in the beamline. If we neglect the coupling between the horizontal and the vertical plane, the relation between the phase space at the entrance and the exit is given by:

$$\begin{pmatrix} x_1 \\ x'_1 \\ y_1 \\ y'_1 \\ \delta_1 \end{pmatrix} = \begin{pmatrix} C_x(s) & S_x(s) & 0 & 0 & D_x(s) \\ C'_x(s) & S'_x(s) & 0 & 0 & D'_x(s) \\ 0 & 0 & C_y(s) & S_y(s) & D_y(s) \\ 0 & 0 & C'_y(s) & S'_y(s) & D'_y(s) \\ 0 & 0 & 0 & 0 & 1 \end{pmatrix} \begin{pmatrix} x_0 \\ x'_0 \\ y_0 \\ y'_0 \\ \delta_0 \end{pmatrix} . \tag{3.77}$$

We present in the following section, the transfer matrix of the most common elements in an accelerator: drifts, sector dipoles and quadrupole.

3.2.4.1 Drift

A drift is the most simple element, it is simply a straight line section without field. Thus, equations (3.66) become:

$$x'' = 0\,, \tag{3.78}$$

$$y'' = 0\,. \tag{3.79}$$

If the drift has a length l, the 5-dimension matrix transfer is given by:

$$M = \begin{pmatrix} 1 & l & 0 & 0 & 0 \\ 0 & 1 & 0 & 0 & 0 \\ 0 & 0 & 1 & l & 0 \\ 0 & 0 & 0 & 1 & 0 \\ 0 & 0 & 0 & 0 & 1 \end{pmatrix}\,. \tag{3.80}$$

3.2.4.2 Sector dipole

The dipoles are used to change the direction of the particles along the desired orbit. We consider a uniform B field along the y direction, the equilibrium between the centripetal force and the Lorentz force gives us:

$$q\,v\,B = m\frac{v^2}{\rho}\,, \tag{3.81}$$

$$p = q\,B\,\rho\,. \tag{3.82}$$

With this relation, the bending angle is thus given by:

$$\theta = \frac{q}{p}\int_{s_1}^{s_2} B\,. \tag{3.83}$$

To describe the behaviour of a particle in an electromagnetic field, we have introduced the curvilinear system of coordinates. Wiedemann [141] defines the *natural bending magnet* as one, where the ideal path of the particle enters and exits the normal to the magnet pole face. We illustrate in figure 3.6 the behaviour of a dipole for particles with different energies ($E_a < E_0 < E_b$). For the design orbit, the particle with the correct energy (E_0) is transmitted normally to the exit face, and the particles without the correct energy are deviated differently from the design orbit with the relation:

$$\Delta\theta = \delta\theta\,. \tag{3.84}$$

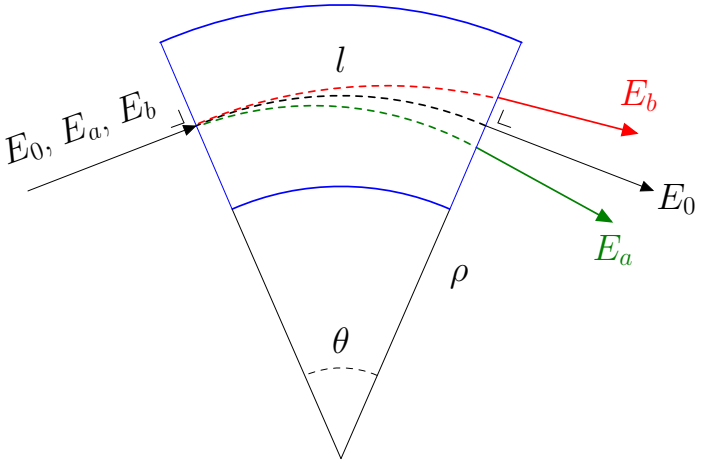

Figure 3.6: Deviation of the particles in a sector bend. Adapted from [132].

In absence of a quadrupolar field in the dipole, we have $K_x = \frac{1}{\rho^2}$ and $K_y = 0$ and the matrix transfer (3.75) for a sector bend is:

$$M = \begin{pmatrix} \cos(\theta) & \rho\sin(\theta) & 0 & 0 & \rho(1-\cos(\theta)) \\ -\frac{1}{\rho}\sin(\theta) & \cos(\theta) & 0 & 0 & \sin(\theta) \\ 0 & 0 & 1 & l & 0 \\ 0 & 0 & 0 & 1 & 0 \\ 0 & 0 & 0 & 0 & 1 \end{pmatrix}. \tag{3.85}$$

We note that the motion along the y direction corresponds to a drift.

The previous relation may be generalized in cases where the path of the particle enters and exits the magnet at an arbitrary pole face (see figure 3.7).

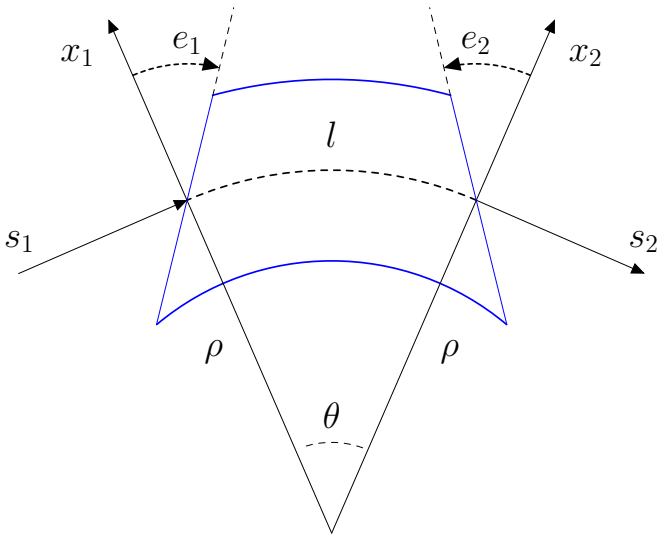

Figure 3.7: Definition of the pole face angle for a sector bend. Reproduced from [131].

In this case, the transfer matrix is given by [141]:

$$\begin{pmatrix} 1 & 0 & 0 & 0 & 0 \\ \frac{1}{\rho}\tan(e_1) & 1 & 0 & 0 & 0 \\ 0 & 0 & 1 & 0 & 0 \\ 0 & 0 & -\frac{1}{\rho}\tan(e_1) & 1 & 0 \\ 0 & 0 & 0 & 0 & 1 \end{pmatrix} \times \begin{pmatrix} \cos(\theta) & \rho\sin(\theta) & 0 & 0 & \rho(1-\cos(\theta)) \\ -\frac{1}{\rho}\sin(\theta) & \cos(\theta) & 0 & 0 & \sin(\theta) \\ 0 & 0 & 1 & l & 0 \\ 0 & 0 & 0 & 1 & 0 \\ 0 & 0 & 0 & 0 & 1 \end{pmatrix} \times \begin{pmatrix} 1 & 0 & 0 & 0 & 0 \\ \frac{1}{\rho}\tan(e_2) & 1 & 0 & 0 & 0 \\ 0 & 0 & 1 & 0 & 0 \\ 0 & 0 & -\frac{1}{\rho}\tan(e_2) & 1 & 0 \\ 0 & 0 & 0 & 0 & 1 \end{pmatrix}. \tag{3.86}$$

In this case, both planes are impacted and depending on the values of e_1 and e_2, one could design a dipole which focuses in the vertical plane.

3.2.4.3 Quadrupole

A quadrupole is used to focus the beam along a specific direction (x or y). In figure 3.8, we show the field and the force exerted on the beam (in red). We confirm that if we focus along a specific direction, we defocus along the other. Thus, in a beam line, the quadrupole are alternated. By convention, a focusing quadrupole focuses along the horizontal plane.

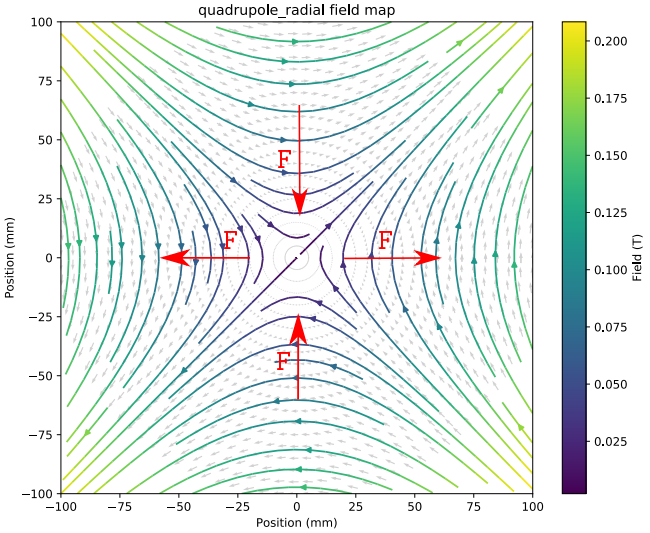

Figure 3.8: Induction magnetic field and force in a quadrupole. Reproduced from [142].

In a quadrupole, we have $1/\rho = 0$ which implies $K_x(s) = -K_y(s)$. With this relation, the matrix transfer of a quadrupole with a length l is given by:

$$M = \begin{cases} \begin{pmatrix} \cos\left(\sqrt{K}l\right) & \frac{1}{\sqrt{K}}\sin\left(\sqrt{K}l\right) & 0 & 0 & 0 \\ -\sqrt{K}\sin\left(\sqrt{K}l\right) & \cos\left(\sqrt{K}l\right) & 0 & 0 & 0 \\ 0 & 0 & \cos\left(\sqrt{K}l\right) & \frac{1}{\sqrt{K}}\sin\left(\sqrt{K}l\right) & 0 \\ 0 & 0 & -\sqrt{K}\sin\left(\sqrt{K}l\right) & \cos\left(\sqrt{K}l\right) & 0 \\ 0 & 0 & 0 & 0 & 1 \end{pmatrix} & K > 0\text{: focusing} \\ \begin{pmatrix} \cosh\left(\sqrt{|K|}l\right) & \frac{1}{\sqrt{|K|}}\sinh\left(\sqrt{|K|}l\right) & 0 & 0 & 0 \\ \sqrt{|K|}\sinh\left(\sqrt{|K|}l\right) & \cosh\left(\sqrt{|K|}l\right) & 0 & 0 & 0 \\ 0 & 0 & \cosh\left(\sqrt{|K|}l\right) & \frac{1}{\sqrt{|K|}}\sinh\left(\sqrt{|K|}l\right) & 0 \\ 0 & 0 & \sqrt{|K|}\sinh\left(\sqrt{|K|}l\right) & \cosh\left(\sqrt{|K|}l\right) & 0 \\ 0 & 0 & 0 & 0 & 1 \end{pmatrix} & K < 0\text{: defocusing} \end{cases} \tag{3.87}$$

For a quadrupole with $K = 0$, we recover the same transfer matrix as for a drift.

3.2.5 Particle beams and phase space

An accelerator or a beamline never transports one particle but many particles. In the following, we consider a particle beam of N particles without interactions between them (no space charge and collective effect) and without coupling between the horizontal and vertical plane. The resulting Hamiltonian of the system is the superposition of the Hamiltonian of each particle.

Each particle is represented by a point in a six-dimensional phase space with coor-

dinates (x, x', y, y', l, δ)[3] The dynamical evolution of the system is represented by the motion of the point in the phase-space. As we neglect the mutual interactions and coupling effects between particles, the 6^{th} dimensional phase-space can be split in 3 phase-space of 2 dimensions: horizontal (x,x'), vertical (y,y') and longitudinal (l,δ).

In the phase space, the trajectory of a unique particle can be described by an ellipse as shown in figure 3.9.

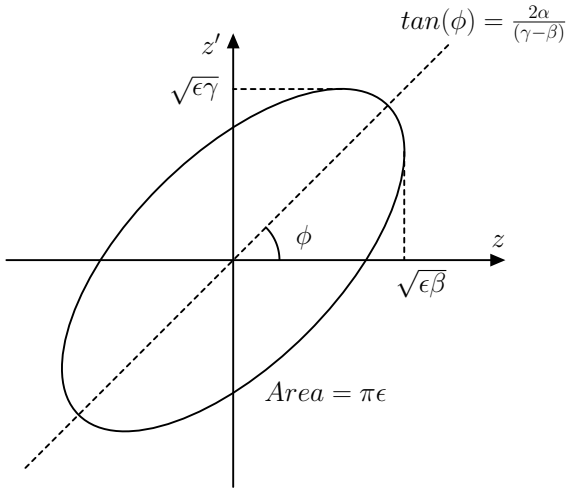

Figure 3.9: Beam particle distribution in the phase space and definition of the emittance. Reproduced from [132].

We denote by (z, z') the horizontal phase space as well as the vertical phase space. This ellipse is described by the following equation:

$$\gamma z^2 + 2\alpha z z' + \beta z'^2 = \epsilon\,, \tag{3.88}$$

where α, β, γ are called the Twiss parameters which determine the orientation and the shape of the ellipse in the phase space. ϵ is the beam emittance and is defined by:

$$\int_{ellipse} dz dz' = \pi\epsilon\,. \tag{3.89}$$

The beam emittance parameter ϵ represents the amplitude factor for an individual particle and defines the emittance of a part of the total beam whose trajectories satisfy [141]:

$$\gamma z^2 + 2\alpha z z' + \beta z'^2 < \epsilon\,, \tag{3.90}$$

To characterize the beam quality, the rms emittance is widely used [143] because it provides a useful meaning of the beam envelope. Moreover for the specific case where the beam is Gaussian, the emittance represents the occupied area by 68% of particles. Along the geometric properties of the ellipse, we have also the relation:

$$\beta\gamma - \alpha^2 = 1\,. \tag{3.91}$$

The particle beams may be also described with an unknown symmetric sigma matrix $\boldsymbol{\sigma}$. Equation of a n-dimensional ellipse is given by [141]:

$$u^T \boldsymbol{\sigma}^{-1} u = 1\,, \tag{3.92}$$

[3] l is the longitudinal separation from the reference particle.

with

$$u^T = (x, x', y, y', s, \delta)\,, \tag{3.93}$$

and the volume of this n-dimensional ellipse is given by:

$$V_n = \frac{\pi^{n/2}}{\Gamma\left(1 + n/2\right)} \sqrt{\det(\boldsymbol{\sigma})}\,, \tag{3.94}$$

where Γ is the Gamma-function.

Let us first consider the area in the 2 dimensional phase space (horizontal or vertical), denoted by z and z'. In absence of momentum deviation ($\delta = 0$), the ellipse equation (3.92) is given by:

$$\sigma_{22} z^2 + 2\sigma_{12} z z' + \sigma_{11} z'^2 = \epsilon_z^2\,. \tag{3.95}$$

The comparison of this relation with equation (3.88) gives us the relation between the σ-matrix and the Twiss parameter:

$$\begin{pmatrix} \sigma_{11} & \sigma_{12} \\ \sigma_{12} & \sigma_{22} \end{pmatrix} = \epsilon \begin{pmatrix} \beta & -\alpha \\ -\alpha & \gamma \end{pmatrix}\,. \tag{3.96}$$

In 2D, the area of the ellipse is given by:

$$V = \pi \sqrt{\sigma_{11}\sigma_{22} - \sigma_{12}^2} = \pi \epsilon_z\,, \tag{3.97}$$

which is consistent with the relation (3.91). Usually, a realistic beam is often Gaussian and we can show that the beam matrix elements are given by:

$$\begin{aligned} \sigma_{11} &= \left\langle z_i^2 \right\rangle = \epsilon_z \beta_z\,, \\ \sigma_{22} &= \left\langle z_i'^2 \right\rangle = \epsilon_z \gamma_z\,, \\ \sigma_{12} &= \left\langle z_i z_i' \right\rangle = -\epsilon_z \alpha_z\,, \end{aligned} \tag{3.98}$$

where i stands for the i^{th} particle. Finally, the beam emittance is expressed as:

$$\epsilon_z(s)^2 = \left\langle z_i^2 \right\rangle \left\langle z_i'^2 \right\rangle - \left\langle z_i z_i' \right\rangle\,. \tag{3.99}$$

Following [141], this relation is accepted for any arbitrary particle distribution. The beam half-width of this beam envelope is defined by:

$$\sigma_z(s) = \pm \sqrt{\beta_z(s)\epsilon_z(s)}\,. \tag{3.100}$$

This relation is a function of two notions:

1. $\beta_z(s)$ is related to the lattice and depends on the disposition of the elements in a lattice.

2. $\epsilon_z(s)$ is related to the beam properties and does not change in a lattice if there are no interactions.

If the beam has a momentum distribution ($\delta \neq 0$), characterized by a dispersion function $D(s)$, the beam size for Gaussian beams is thereby [141]:

$$\sigma_z(s) = \pm \sqrt{\beta_z(s)\epsilon_z(s) + D^2(s)\sigma_\delta^2}\,, \tag{3.101}$$

3.3 Beam transport and modeling codes

Equations of motions are generally not analytically solvable. Therefore, computers codes are necessary in accelerator physics to study the dynamics of the beam along a beamline or inside an accelerator. In this section, we present three softwares used in this thesis: MAD-X, Manzoni and BDSIM [144, 131, 145]. These codes have been interfaced in a single Python library developed by C.Hernalsteens: *Georges* [146].

These softwares contain a description of the main elements that form a beamline such as drifts, bending magnets and quadrupoles. MAD-X implements the Twiss formalism and allows to calculate both the Twiss parameters and the Σ matrix along a beamline. This description of Twiss, is particularly useful for the design and optimization of optics (beam size, divergence, dispersion, ...).

Nevertheless for our studies which is particularly interested in detailed beam properties (size, divergence, emittance) and beam losses, a more detailed description is needed. Therefore, we want a complete tracking of the beam in which each particle is propagated individually in the beamline and where the properties of the beam are statistical properties calculated over the whole distribution. Although MAD-X allows the tracking of a large number of particles, large-scale tracking is relatively expensive in computation time. Thus for our studies and also to allow an optimization of the beamline, we participated in the development of a new tracking code: Manzoni.

In the context of a complete study of the shielding activation, it is necessary to take into account the interactions between particles and the environment, which is not possible in MAD-X or Manzoni. BDSIM has been developed to answer this problem. This software considers the transport of particles in a beamline while being able to model, using *Geant4*, the interactions between particles and matter.

Each of these softwares is described below.

MAD-X

MAD-X is the most common software used in the field of beam accelerator. It has been developed at CERN for the preliminaries studies of the design of the Large Hadron Collider (LHC) and it is used for accelerators design and for testing beam behaviour. An important library, called PTC (Polymorphic Tracking Code) has been integrated in MAD-X, especially to describe all elements symplectic [147]. In the following, we called MAD-X, the software MAD-X using the PTC library.

Any element is defined by a block and described with a model which computes the motion of particles in an electromagnetic field, also called integrator. Knowing the particle phase-space coordinates at the entrance of the frame, MAD-X computes a relation f, generally non-linear, which is determined by the integration of the Hamiltonian (3.47) and gives the beam phase coordinates at the exit of the block:

$$z_{in} \longrightarrow z_{out} = f(z_{in}) \tag{3.102}$$

Then, the blocks are putted together in a global frame, as shown in figure 3.10. From the position of the element in the global frame, MAD-X determines geometric transformations that connect the exit frame of the i^{th} element to the entrance frame of the $i+1^{th}$ element in the local frame.

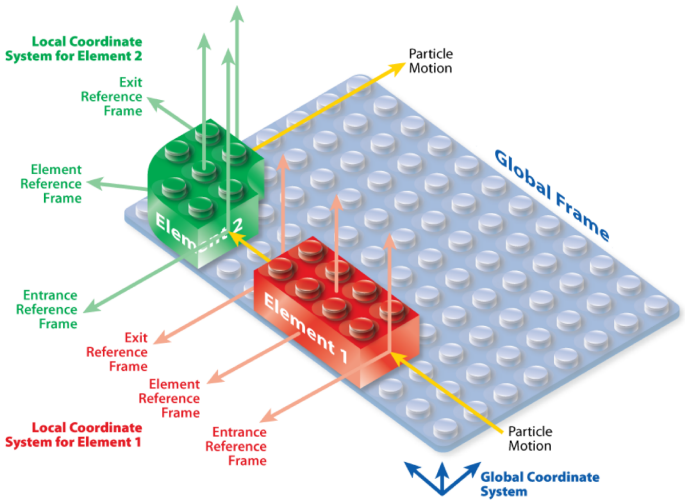

Figure 3.10: Representation of the global frame. Reproduced from [148].

The reduction of the beam energy due to an energy degrader is not implemented in MAD-X and to describe this behaviour, we need to use Manzoni or BDSIM.

Manzoni

Manzoni allows the tracking of a large number of particles through a beamline and implements all the elements commonly used in beamline proton therapy.

Thus Manzoni implements efficient methods for matrix multiplication but with fewer elements (only dipoles, drifts and quads) than MAD-X, essentially at the magnetic level. Moreover, we will see in chapter 4 that propagation of protons inside matter can be described by analytical models. Therefore, the formalism of Fermi-Eyges, based on the scattering power, has been implemented to include a simplified description of the degrader. In addition, based on fit over Monte Carlo data, the transmission of the degrader can be evaluated for an optimization of the beamline.

BDSIM

BDSIM is currently in development at the CERN and at the *Royal Holloway university of London* (RHUL). It is a C++ program which uses GEANT4 toolkit to model the propagation of the beam inside a beamline and simulate the interactions between the beam and the accelerator components [145].

The input file consists of a file with the placement of the different elements following the position in the beamline (along the curvilinear coordinates s). Then, BDSIM provides classes to transform the curvilinear coordinates into global coordinates. The field of each magnetic element is expressed in the global coordinates and is computed using the strength of each element (see equations (3.87) and figure 3.8 for a quadrupole).

The motion of the particle in an electromagnetic field is computed using the *Geant4* default integrator: a 4^{th} Runge-Kutta integrator. However, for some elements, there exist analytical solutions to the motion (see section 3.2.4) and these solutions are directly implemented to improve the efficiency of the simulation. This tracking is called thick-lens tracking.

The secondary particles that may be generated during the propagation of the beam can not be treated with the thick lens tracking and for these specific particles, a 4^{th} Runge-Kutta integrator is also used. Other integrators may be used for the resolution of equation of the motion but for these cases, we refer the readers to the manual.

The field outside the magnet is generated using a multipolar field which does not take into account the permeability of the iron. The field is described using current source along the curvilinear coordinates. The location of each wire and the field are given by:

$$c_i = \begin{bmatrix} x \\ y \end{bmatrix}_i = \begin{bmatrix} 0 \\ radius_{pole} \end{bmatrix} \begin{bmatrix} \cos(\theta_i) & -\sin(\theta_i) \\ \sin(\theta_i) & \cos(\theta_i) \end{bmatrix} \tag{3.103}$$

$$\theta_i = \left\{ \frac{i\,2\pi}{n_{poles}} \right\} \quad \text{for i} = 0, ..., \text{n}_{poles} \tag{3.104}$$

$$B(r) = \sum_{i=1}^{i=n_{poles}} (-1)^i \frac{r - c_i}{\|r - c_i\|} \tag{3.105}$$

As example, we show in figure 3.11 the field in the yoke of a dipole and a quadrupole.

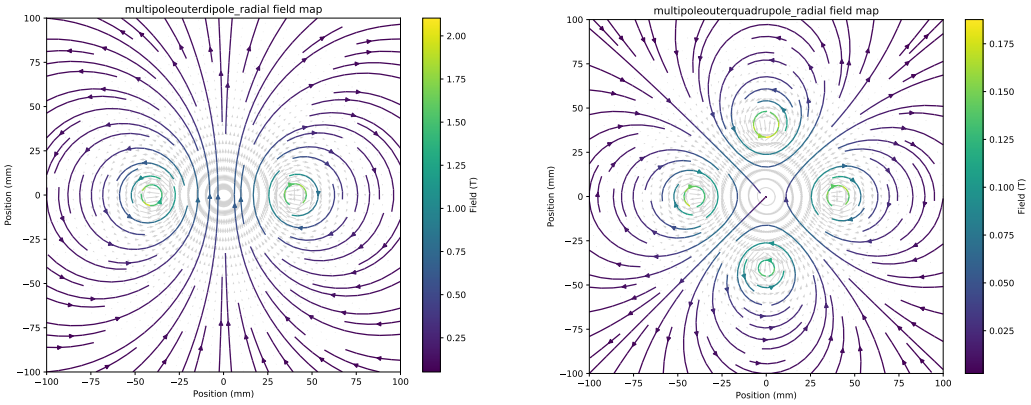

(a) Dipole. *(b) Quadrupole.*

Figure 3.11: Field inside the yoke. Reproduced from [142].

As BDSIM built an entire *Geant4* model, it is possible to simulate the interactions between particles and matter. We can therefore, simulate the beam losses along the beamline and determine the type of generated secondary particles which is not possible with Manzoni and MAD-X.

Georges: A python library as interface for our studies

The aim of this library is to unify the description and computation of particle accelerator beamlines for different softwares (Manzoni, MAD-X and BDSIM) in a unique Python library. A clear separation between the beamline data, the beamline computations and the computation context is achieved. Beamline data are immutable, the context (e.g. external parameters such as the energy, momentum offset, initial beam, etc.) is immutable and always passed explicitely as a parameter and the computational facilities are implemented following a modular and chainable functional approach, unifying the above mentioned aspects.

Beamlines are loaded, converted (if necessary) and then transformed using functions split in packages (one package per beam physics code, e.g. MAD-X or BDSIM).

Support tools are also provided, especially plotting capabilities for various optics computation (beam envelope, dispersion, etc.).

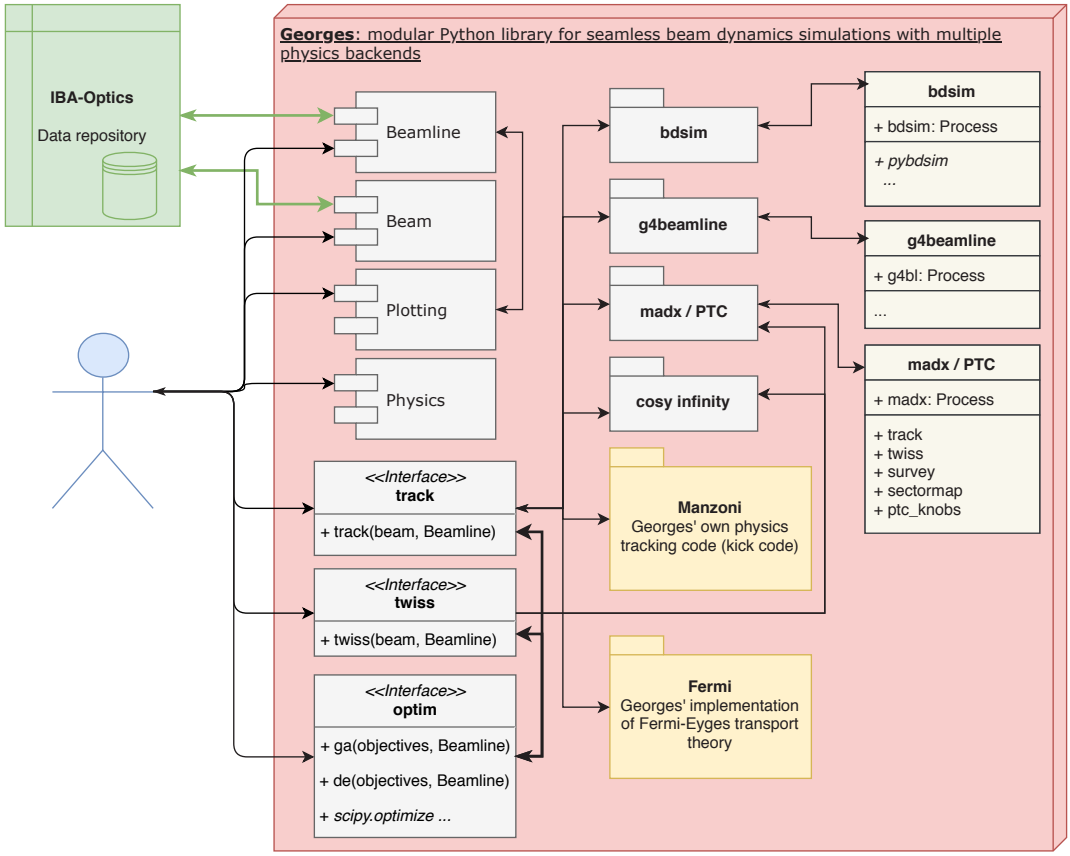

Figure 3.12: Georges interface.

We present in table 3.3, an example of a beamline input file for *georges*. Each element in this table is described by:

- Its name.
- Its physical properties: position, length, aperture.
- Its magnetic properties: type (dipole, quadrupole, ...) and depending on the type, the bending angle, the pole face angle or the strength of the quadrupole ($K1$).

This file is then used to form a model of the beamline and can be used independently with Manzoni, MAD-X or BDSIM.

NAME	TYPE	AT_CENTER	LENGTH	ANGLE	CHAMBER	APERTYPE	APERTURE	E1	E2	PLUG	CIRCUIT
ST	MARKER	0									
PMQ1	QUADRUPOLE	0.2	0.206		0.002	CIRCLE	0.02975			K1	IPMQ
PMQ2	QUADRUPOLE	0.44	0.206		0.002	CIRCLE	0.02975			K1	IPMQ
Q1C	QUADRUPOLE	1.092	0.29		0.002	CIRCLE	0.02975			K1	IQ1C
SL1E	SLITS	1.442	0.06			RECTANGLE				APERTURE	{wSL1EX,wSL1EY}
Q2C	QUADRUPOLE	1.7905	0.49		0.002	CIRCLE	0.02975			K1	IQ2C
P1E	SOLIDS	2.404									
COL	COLLIMATOR	2.528	0.055			CIRCLE	0.005				
ROT	SROTATION	2.55								ANGLE	ROT_ANGLE
T1GX	MARKER	2.72									
T2GY	MARKER	2.95									
Q1G	QUADRUPOLE	3.588	0.297		0.002	CIRCLE	0.02975			K1	IQ1G
Q2G	QUADRUPOLE	4.188	0.297		0.002	CIRCLE	0.02975			K1	IQ2G
P1G	MARKER	4.518									
SL1G	SLITS	4.568	0.06			RECTANGLE				APERTURE	{wSL1GX,wSL1GY}
SL2G	SLITS	4.638	0.06			RECTANGLE				APERTURE	{wSL2GX,wSL2GY}
B1G	SBEND	5.588	1.0472	0.6981	0.002	RECTANGLE	0.058, 0.0258	0.31415	0.31415		
Q3G	QUADRUPOLE	6.518	0.29		0.002	CIRCLE	0.02975			K1	IQ3G
P2G	MARKER	6.808									
Q4G	QUADRUPOLE	7.138	0.29		0.002	CIRCLE	0.02975			K1	IQ4G
T3G	MARKER	7.418									
Q5G	QUADRUPOLE	7.858	0.49		0.002	CIRCLE	0.02975			K1	IQ5G
Q6G	QUADRUPOLE	8.588	0.29		0.002	CIRCLE	0.02975			K1	IQ6G
T4G	MARKER	8.868									
Q7G	QUADRUPOLE	9.238	0.29		0.002	CIRCLE	0.02975			K1	IQ7G
P3G	MARKER	9.498									
SL3G	SLITS	9.578	0.06			RECTANGLE				APERTURE	{wSL3GX,wSL3GY}
B2G	SBEND	10.828	1.832	-1.2217	0.002	RECTANGLE	0.11, 0.0258	-0.1745	-0.2617		
P4G	MARKER	11.958									
SMX	HKICKER	12.14	0.159							KICK	SMX_SCAN
SMY	VKICKER	12.40	0.109							KICK	SMY_SCAN
B3G	SBEND	13.528	1.675	-1.0471	0.002	RECTANGLE	0.11, 0.09				
IC1	MARKER	14.419									
IC2	MARKER	14.767									
ISO	MARKER	15.370									

Table 3.3: Element by element model of the Proteus® One extraction beamline and gantry.

In figure 3.13, we illustrate the beamline generated by *Georges* based on the elements in table 3.3. The quadrupoles are illustrated in blue, the dipoles in red and the collimators in yellow. The aperture of the elements in each plane has also been taken into account.

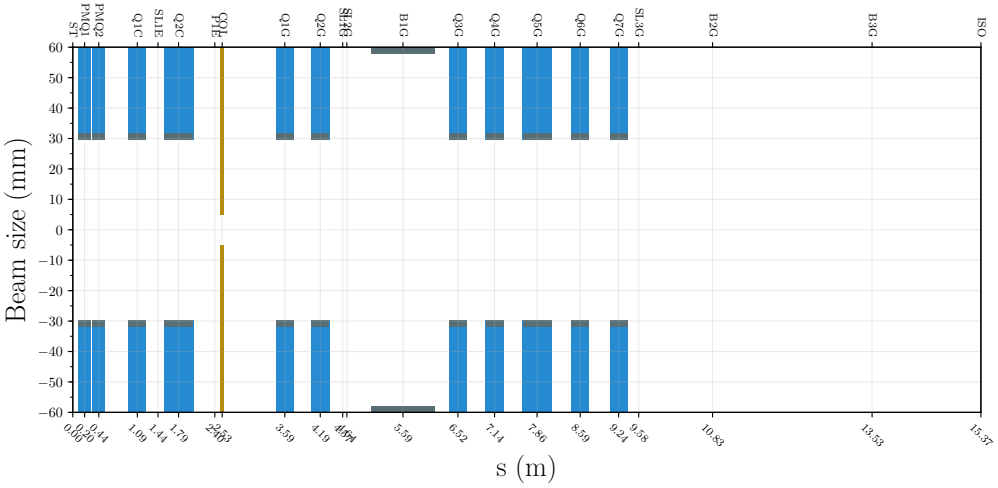

(a) Horizontal plane.

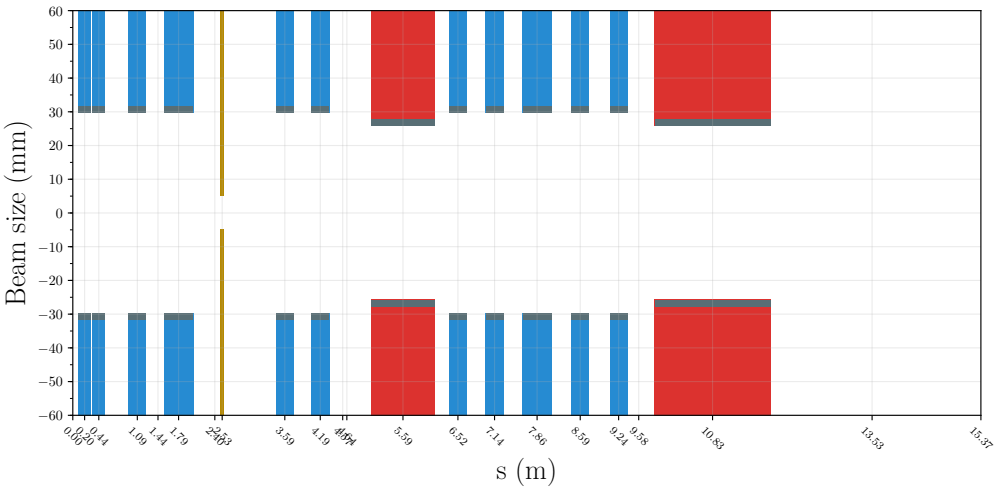

(b) Vertical plane.

Figure 3.13: Drawings of the beamline generated using Georges.

Chapter 4

Detailed study of energy degraders toward innovative design for therapeutic beams

Contents

4.1 Objectives

Cyclotron-based proton therapy installations often rely on a degrader system to modulate the beam energy from the cyclotron output energy to the energy necessary during the clinical treatment. However, the degrader also induces a growth in the beam transverse phase space and an increase of the energy spread. Both effects will negatively impact the transmission in the extraction beamline and through the gantry. They increase the beam losses, leading to shielding and building activation, and impact the beam properties at the isocenter (patient). The transverse properties of the beam are indeed crucial for a detailed understanding of installations in operation and for the design of future systems,

in particular with Pencil Beam Scanning (PBS) treatment modes where a small spot size at the isocenter is favored as well as other beam properties with tight tolerances [22]. Similarly, a precise knowledge of the beam loss pattern is important for the design of the shielding surrounding the installation, in particular for compact systems. Indeed, as we have seen in chapter 2, the degrader is one of the major contributors to the activation of concrete in a Proteus®One.

The actual degrader used at *IBA* consists of a rotating wheel with different blocks in different materials: beryllium, graphite and aluminium. We will see through this chapter that a performant material for energy degrader is characterized by a low atomic weight and a high density. Although beryllium appears to be an excellent material, it is toxic[1] and a major neutron emitter [149]. Graphite is a possible solution but is difficult to machine with tight tolerances at small thicknesses. It is for this reason that aluminium is used for small dimensions. Boron carbide and diamond are two excellent candidates for an energy degrader but due to their high density, they are also relatively difficult to manufacture.

During a medical treatment, especially in PBS mode, it is necessary to quickly modulate the beam energy while keeping a high beam transmission [150]. Various current studies focus on the improvement of the energy degrader [151, 152, 153]. Recently, *IBA* and the *Paul Scherrer Institute* have developed independently a new design for an energy degrader based on a multi-wedge scheme (see figure 4.1).

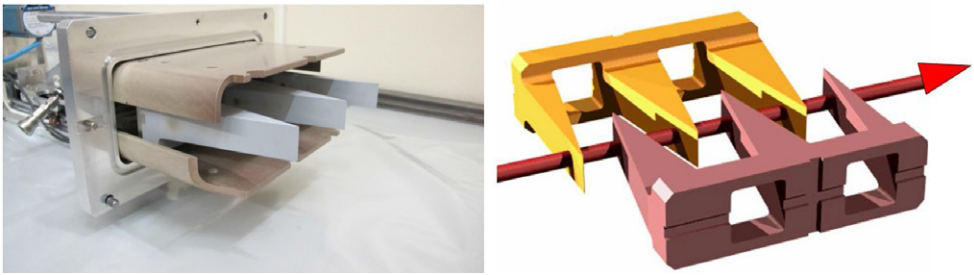

Figure 4.1: Degrader installed at Paul Scherrer Institute. Reproduced from [152].

This shape has been modelled by Liang *et al.* in 2018 in *Geant4* with a high-density graphite ($\rho = 1.95 g/cm^3$) [150]. They have shown that this design may increase the beam transmission and the energy modulation. However, an initial gap is necessary to avoid heat radiation. In this thesis, we propose a new design based on insertable cylinders with different thicknesses (called lollipops), made of diamond (see section 4.5).

Before analysing the performance of the real degrader, we compare the different materials in a synthetic geometry, *i.e* a semi-infinite block. The aim of this chapter is to predict with Monte Carlo simulations the properties of the beam at the exit of a block of matter as shown in figure 4.2. We evaluate the transmitted energy E, the scattering angle θ, the beam size, the emittance and the transmission at the exit of this slab of matter. The slab is irradiated by a proton beam with an energy E_0 and is characterized by a thickness t, a density ρ and a Stopping Power S/ρ.

[1] The exposition to Beryllium may cause Chronic Beryllium Disease (CBD) and lung complications.

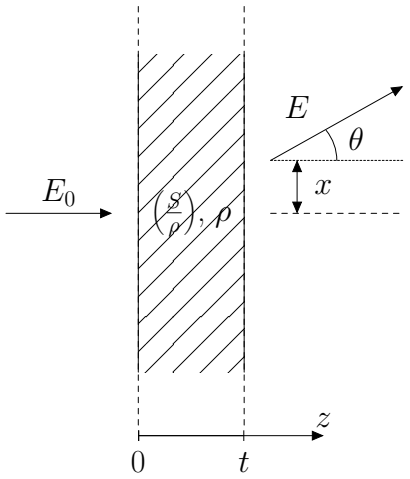

Figure 4.2: Model for comparison of different materials.

The thickness t is a function of the input energy (E_0), the energy at the exit (E), and the Range in the material ($\mathbb{R}$) as defined in section 1.2.2:

$$t = \mathbb{R}(E_0) - \mathbb{R}(E)\,. \tag{4.1}$$

For this chapter, the initial energy is fixed to 228.15 MeV which is the energy at the exit of the *IBA* accelerator. In table D.1 (see appendix), we summarized the thicknesses of the slab for different materials as function of the transmitted energy. They are graphically presented in figure 4.3.

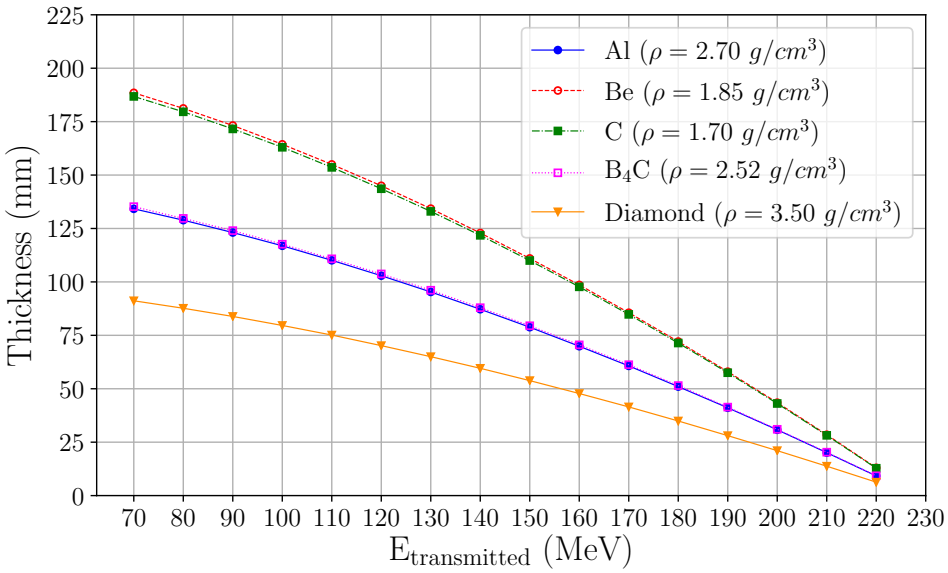

Figure 4.3: Degrader length as a function of the transmitted energy.

As the mass total stopping power S/ρ is almost equal for different materials down to MeV (see figure 1.6), materials with a similar density will have the same energy losses by unit of length and thus the same thickness. This is why the graphite block ($\rho = 1.7\ g/cm^3$) and the beryllium block ($\rho = 1.85\ g/cm^3$), as well as the the aluminium block ($\rho = 2.7\ g/cm^3$) and the boron carbide block ($\rho = 2.52\ g/cm^3$) have similar dimensions. Due to

the high density of diamond ($\rho = 3.5\ g/cm^3$), the required thickness is smaller than other materials and we would expect the scattering angle and the emittance improvements.

We structure this chapter as follows. We present the tools and methods for the computation of the beam characteristics in section 4.2. In section 4.3, a complete comparison between materials is made for an ideal case to select the material with the best properties. In section 4.4, the real design of the *IBA* degrader is considered to understand the current properties and identify possible improvements. Finally, in section 4.5, performances of a new type of degrader made of diamond is studied.

4.2 Tools and methods

In section 4.2.1, we introduce the formalism of Fermi-Eyges for beam propagation in matter. Used with the scattering power of protons, the beam spreading angle and the beam size at the exit of a slab will be computed. A comparison between two *Geant4* physic lists is performed in section 4.2.2 and a method to recover the Gaussian core of the angular distribution is developed in section 4.2.3. Differences between these analytical models and Monte Carlo simulations are also explained in section 4.2.4. All results obtained in this section are integrated in Manzoni code for further studies about an optimization of the beamline. These results have been presented during the *IPAC* conference in 2018 [154]

4.2.1 The Fermi-Eyges transport formalism

In 1948, Eyges generalized Fermi's theory to describe the evolution of spatial and angular distribution of particles going through matter [155]. The purpose of this theory is to compute the phase-space distribution and the related quantities at any depth z in the material. We suppose a pencil beam, *i.e* a punctual beam without spatial and angle extension, at the entrance of the slab and we denote by x (resp. θ) the transverse direction (resp. the scattering angle). In [155], Eyges showed that the probability of finding the proton at some z with x in dx and θ in $d\theta$ can be expressed as:

$$P(x,\theta)\,dx\,d\theta = \frac{1}{2\pi\sqrt{B}} e^{-\frac{1}{2}\frac{A_0 x^2 - 2A_1 x\theta + A_2\theta^2}{B}} dx d\theta\,, \tag{4.2}$$

where the A_n are expressed as the moments of the scattering power T as defined in section 1.2.3 and are written as:

$$A_0(z) \equiv \int_0^z T(u)du\,, \tag{4.3}$$

$$A_1(z) \equiv \int_0^z (z-u)T(u)du\,, \tag{4.4}$$

$$A_2(z) \equiv \int_0^z (z-u)^2 T(u)du\,, \tag{4.5}$$

$$B \text{ is given by: } B(z) \equiv A_0 A_2 - A_1^2\,. \tag{4.6}$$

The distribution of x (resp. θ) is obtained by integration of (4.2) over θ (resp. x). These two integrations could be related to the angular distribution and spatial distribution where the symbol $\langle\rangle$ corresponds to the variance.

$$A_0 = \langle\theta^2\rangle\,, \tag{4.7}$$

$$A_2 = \langle x^2\rangle\,, \tag{4.8}$$

$$A_1 = \langle x\theta\rangle\,. \tag{4.9}$$

The scattering power is thus the key quantity to compute the distribution of the scattering angle (θ) at the exit of the slab. The contour in the phase space is obtained when equation (4.2) equals $e^{-1/2}$. We find thus equation of an ellipse as defined in section 3.2.5:

$$A_0 x^2 - 2A_1 x\theta + A_2\theta^2 = B \tag{4.10}$$

The extrema of this ellipse are:

$$\hat{\theta} = \pm\sqrt{A_0} = \left\langle \theta^2 \right\rangle^{1/2} \quad \text{at } x = \pm A_1/\sqrt{A_0} \tag{4.11}$$

$$\hat{x} = \pm\sqrt{A_2} = \left\langle x^2 \right\rangle^{1/2} \quad \text{at } \theta = \pm A_1/\sqrt{A_2} \tag{4.12}$$

We can show that the area of the ellipse is given by $\pi\sqrt{B}$ and thus, the emittance of the beam after going through a slab of matter is given by:

$$\epsilon_{mat} = \sqrt{B}\,. \tag{4.13}$$

In this chapter, we consider a pencil beam as input and the scattering power of Farley and Gottschalk, introduced in section 1.2.3, to determine the beam properties (A_0, A_1, A_2, B) at the exit of any material. The formalism of Fermi-Eyges has been implemented in Manzoni to provide the properties of the beam after a slab of matter.

4.2.2 Difference between hadronic models and electromagnetic models in *Geant4* simulations

In this section, the Monte Carlo simulations are performed with *Geant4* with the QGSP_BIC_HP physics list (called hadronic in the rest of this thesis) for a complete description of the interactions and the PENELOPE model (called electromagnetic and referenced as *Geant4*EM) for the electromagnetic process (without nuclear interactions).

To have a correct statistic, we use 10^6 primary particles. By default, in this section, we specify the output energy of the beam at 70 MeV and we use beryllium as material. Other cases may be treated similarly.

We have explained in chapter 1 that protons interact with matter through electromagnetic interactions (energy losses and Coulomb scattering) or by nuclear reactions. A major effect of nuclear interactions is to create heavier tails in the phase space projected distributions than the Multiple Coulomb scattering (MCS) for which this effect is absent.

In the post processing, we distinguish the primary and secondary particles produced by inelastic nuclear interactions. We illustrate in figure 4.4a, the energy spectrum of particles at the exit of the block and in figure 4.4b, the angular distribution is shown. The total spectrum is the blue curve, the contribution of primaries (resp. secondary) are represented in red (resp. green).

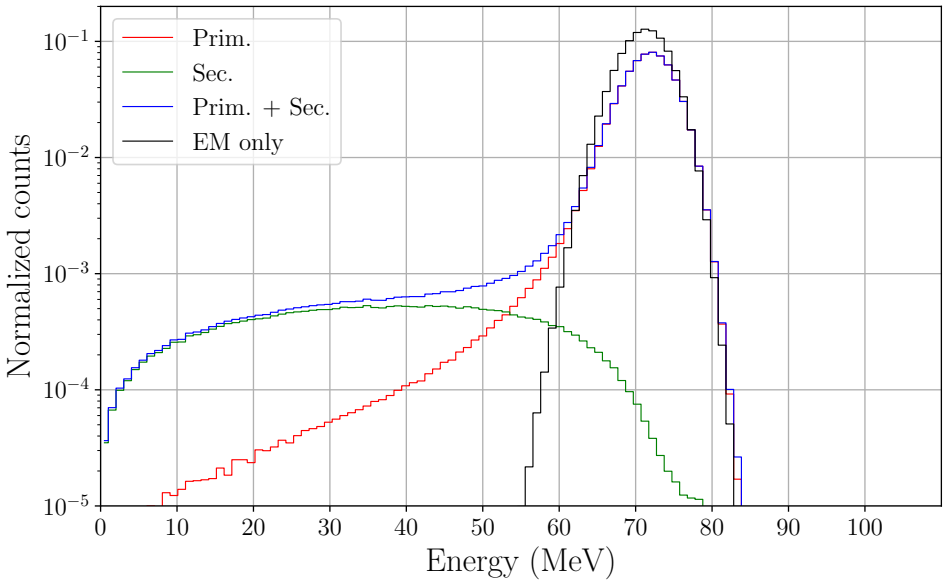

(a) Energy spectrum.

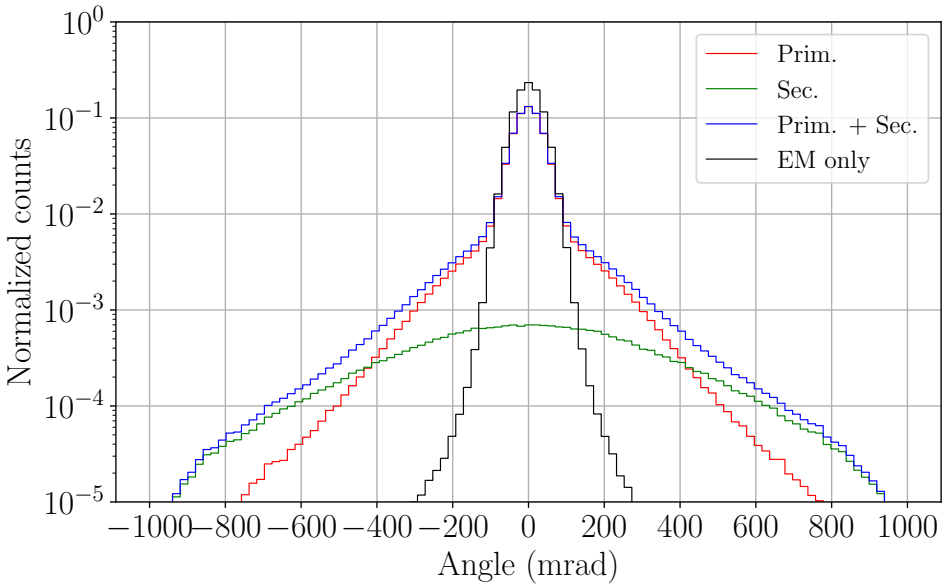

(b) Angular distribution.

Figure 4.4: Energy spectrum and angular distribution for beryllium degrading from 228.15 MeV *to 70* MeV*. The contribution of primaries is in red and the secondaries is in green.*

We note that two orders of magnitude separate the primaries and secondaries in the peaked region (median value) in the energy spectrum and in the angular distribution. Moreover, the contribution of the nuclear interactions is clearly visible on these figures (green curves) and corresponds to 35% of the total spectrum (blue curve). This proportion is in agreement with the results obtained by [34] (see chapter 1). In the rest of this thesis, except when explicitly specified, the contribution of secondary protons is always discarded.

4.2.3 The optimal Gaussian cuts method

In order to compare *Geant4* simulations with the analytical models, we need to separate the nuclear halo contribution from the Gaussian core. The particles which suffered large angular deviation, due to elastic and nuclear reactions, will be removed. Moreover, statistical variations appear at large angles due to the low probability to obtain these outputs in the Monte Carlo simulations. These values must also be eliminated to obtain the primary beam transmitted in the beamline.

The scattering angles θ_x and θ_y at the exit of the target are assumed to be constant, the particles move along the radial axis. As there is no preferential direction in the material, there cannot be a radial asymmetry in the output beam. This means that the angular distributions should follow the same Gaussian distribution along θ_x and θ_y.

To determine the Gaussian distribution of the angular spectrum, we use the properties of the chi-square distribution. A chi-square distribution of k degrees of freedom corresponds to the sum of the squares of k normally distributed independent variables. In our case we have $k = 2$. We defined the reduced transverse momentum $\tilde{\theta}$ as:

$$\tilde{\theta} = \left(\frac{\theta_x - \bar{\theta}_x}{\sigma_{\theta_x}}\right)^2 + \left(\frac{\theta_y - \bar{\theta}_y}{\sigma_{\theta_y}}\right)^2 , \tag{4.14}$$

where $\bar{\theta}_i$ is the mean value and σ_{θ_i} is the standard deviation of the corresponding distribution. When θ_x and θ_y are normally distributed, we have a χ^2 distribution.

The variance for a χ^2 distribution is equal to $\sigma^2 = 2k$. This implies that the standard deviation equal to 2 when θ_x and θ_y follow a Gaussian distribution. The values at large angles will be progressively cut until they reach the expected standard deviation. The remaining curves correspond to the central section of the beam where the proton angles are normally distributed. The successive cuts are illustrated in figure 4.5 with ξ the cut value corresponding to the percentage of protons eliminated starting with those at the extremities. We found that 14% of the protons need to be removed to obtain the expected χ^2 distribution, represented in black.

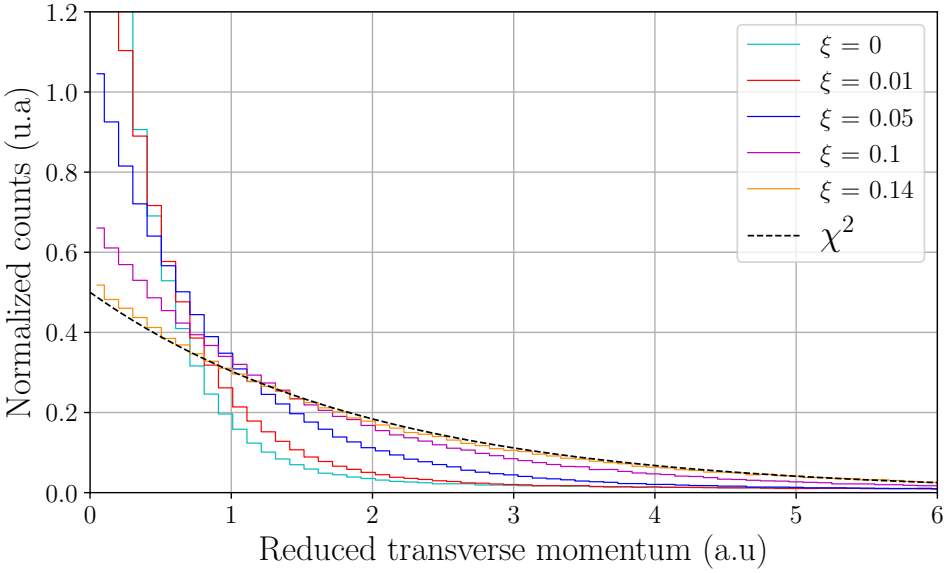

Figure 4.5: Reduced χ^2 distribution for different cut values.

The angular distributions in function of θ_x and θ_y are shown in figure 4.6 for different cut values. The original distributions with $\xi = 0$ in cyan are not Gaussian at larger angles due to the halo contribution of the single scattering effects. We remark also slight differences in these distributions between the two graphics due to statistical variations. Progressively, cut after cut, the distributions tend to a Gaussian distribution.

Physically, the nuclear reactions with an important angle are progressively removed to obtain the central part of the beam. The angular distribution due to the electromagnetic physic list implemented in *Geant4* EM for elastic and inelastic scattering is also shown in black. The difference between our results in orange and this curve corresponds to the elastic effects. However, this difference is minimal. Indeed, the additional cut between the two curves is equal to 0,85%.

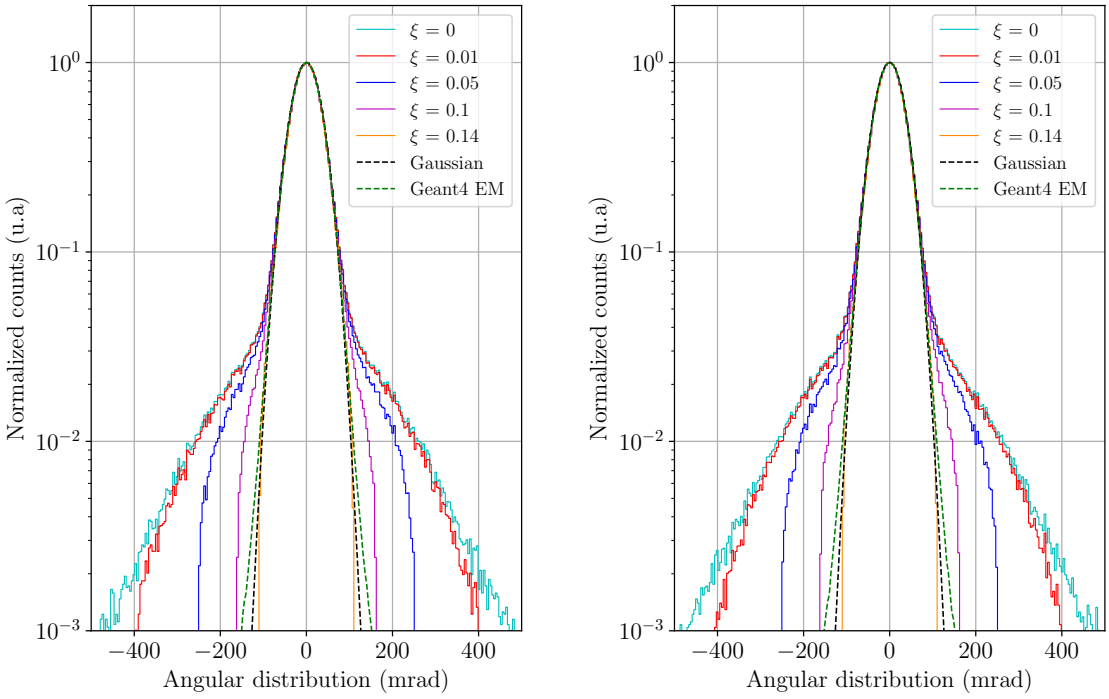

(a) Horizontal plane *(b) Vertical plane*

Figure 4.6: Reduced angular distribution for different cut values.

In figure 4.7, we observe the effects of our algorithm on the energy spectrum. For each value of the cut, we show the corresponding energy spectrum of protons. We observe that our method also gives the same energy distribution as the electromagnetic physic list (represented in black). With this algorithm, we are now able to characterize the Gaussian core of the beam which is then propagated in the beamline.

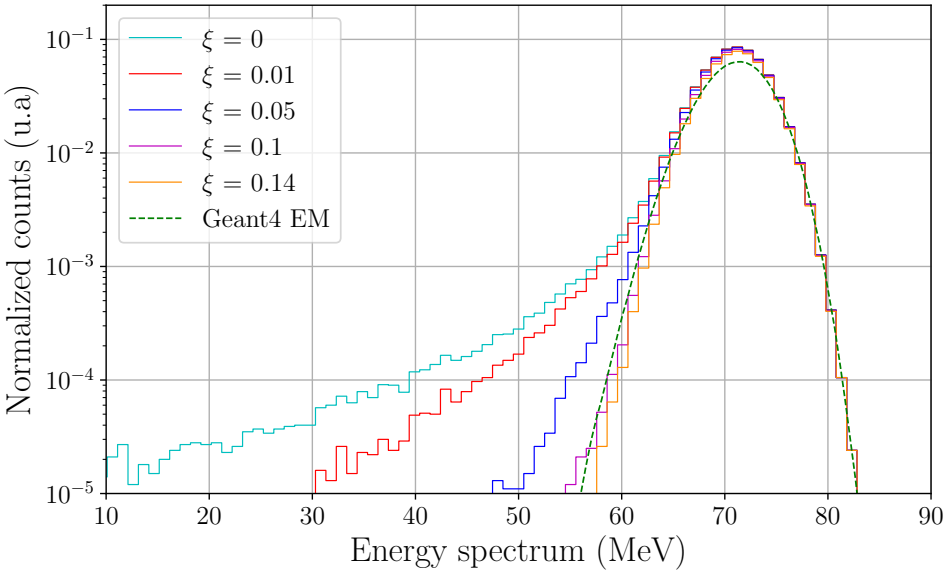

Figure 4.7: Energy spectrum for different cut values.

As the hadronic interactions and the single scattering depend on the materials and the thickness of the blocks, the algorithm must be applied for each transmitted energy and for each studied material. We present in figure 4.8 the value of ξ as a function of the transmitted energy for the common materials used as energy degrader in proton therapy.

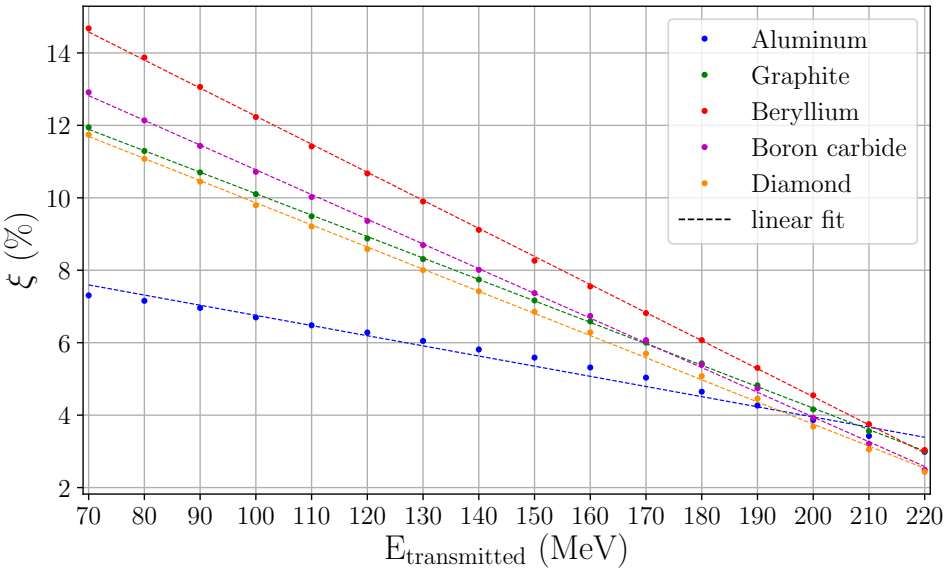

Figure 4.8: Cuts values for different materials studied in this chapter.

The greater transmitted energy, the minder there are nuclear reactions and therefore, lower is the cut. Based on these data, we decided to apply a linear regression on these results to determine a possible the between ξ and transmitted energy (E). For each material, a linear regression of type $\xi = aE + b$ is applied, where a and b are functions of the atomic weight (Z) (see figure 4.9).

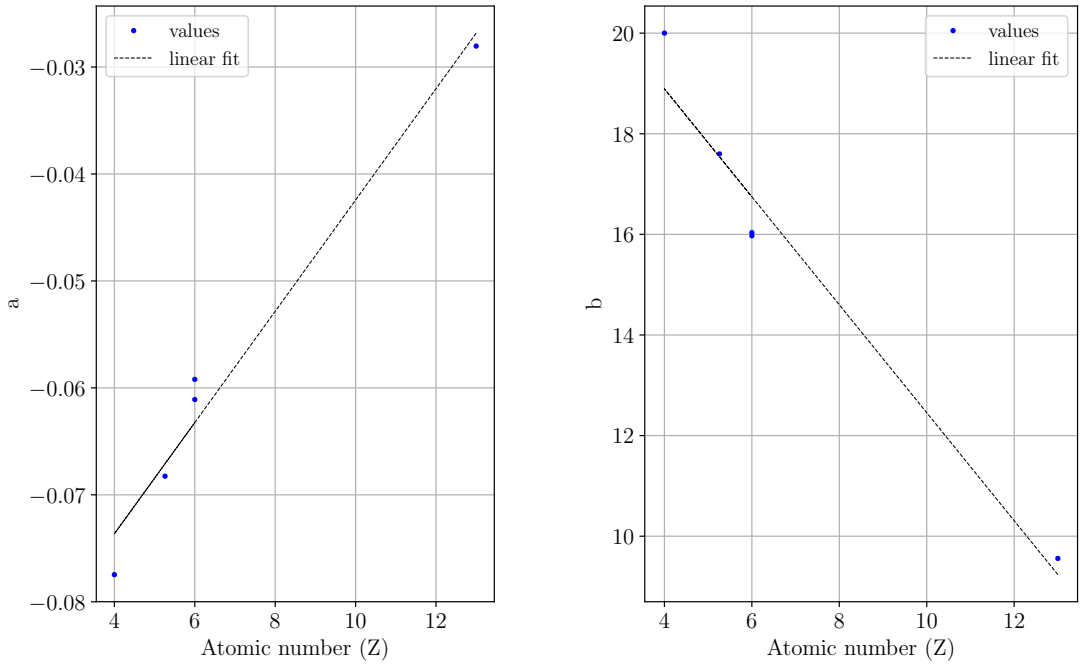

(a) Slope *(b) Independent term*

Figure 4.9: Values of a and b as a function of the atomic number Z.

These results lead us to propose the following regression law to determine the quantile as a function of the transmitted energy and the material:

$$\xi\,(Z, E) = (0.005\,Z - 0.09)\;E - (1.07\,Z - 23.17) \tag{4.15}$$

This law is valuable for transmitted energy between 70 and 220 MeV.

With this law, we are able to recover the Gaussian core of the distribution for any material and we can compute the beam Σ matrix (equation (3.96)) which serves as input for beam transport code like MAD-X or Manzoni. We now compare the Monte Carlo results with the analytical models of Gottschalk and Farley.

4.2.4 Comparison between Monte Carlo results and semi-analytical models

Geant4 and *Phits* are compared to the analytical models of Gottschalk (also called differential Molière) and Farley which have been introduced in section 1.2.3 (equations (1.24) and (1.25)) and for which we have the following scattering powers:

$$T_{dM} = f_{dM}(p_1 v_1, pv)\left(\frac{E_s}{pv}\right)^2 \frac{1}{X_S} \tag{4.16}$$

$$T_F = \frac{200 Z^2}{X_0 (p\beta)^2} \tag{4.17}$$

In this section, the results obtained for beryllium based on *Geant4* and the hadronic model (with applied cuts), on *Geant4* with the electromagnetic model and *Phits* (Data courtesy of F.Stichelbaut) are compared with the Gottschalk and Farley analytical models.

We successively compare the standard deviation of the beam size, the beam divergence and the emittance for different transmitted energy. The results for each quantities are summarized in figure 4.10.

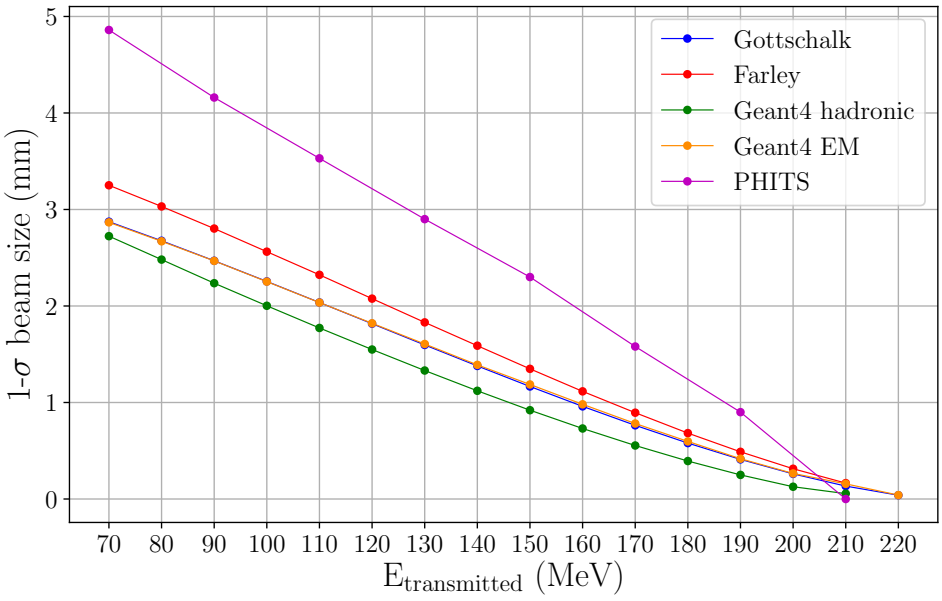

(a) Beam size.

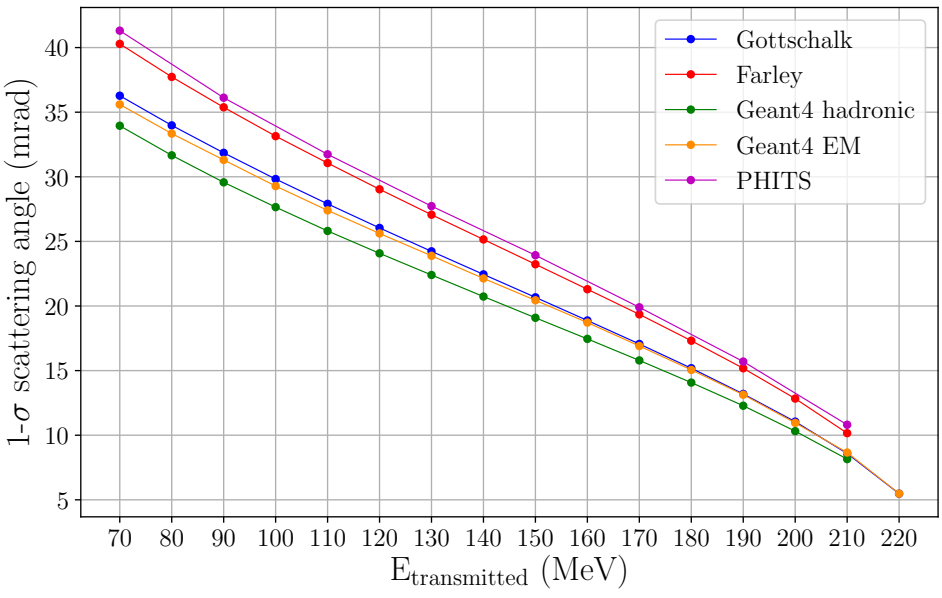

(b) Angular deviation.

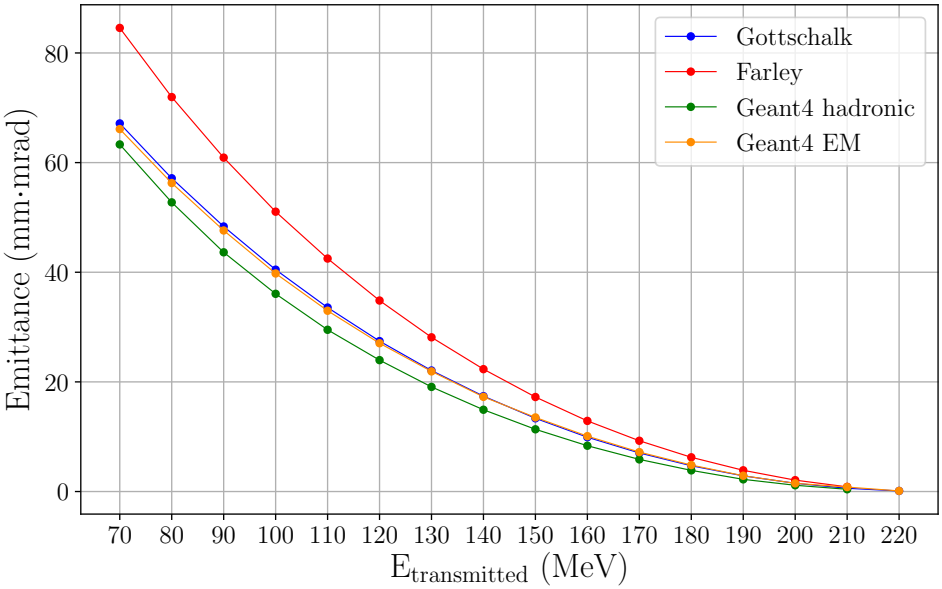

(c) Emittance

Figure 4.10: Beam parameters for beryllium as a function of the transmitted energy. Different analytical and numerical models are compared.

Geant4 with the electromagnetic processes and the differential Molière model proposed by Gottschalk are in excellent agreement.

We obtain similar results with the hadronic model (with cuts), the differences arise from the fact that our algorithm removes also the tails due to the single scattering (large angles).

The Farley model uses an approximation which is close to the Fermi-Rossi approximation known to be less accurate than the differential Molière model [47]. The overestimation obtained with *Phits* is probably due to another cut methodology.

In the rest of this chapter, we use the *Geant4* with the hadronic model and we compute the cuts to be closer to the analytical results obtained using the scattering power as modelled by Gottschalk.

4.3 Comparison of materials for degrader using synthetic geometry

In this section, we successively simulate the beam properties for each material and thickness (t) summarized in table D.1. We compare the transmission, the energy spread and the emittance. For each quantity, the secondary protons are removed and the cuts as explained in the last section, are applied to keep the useful part of the beam.

4.3.1 Transmission

The transmission represents the number of protons crossing the material which finally reach the patient. The losses are due to nuclear reactions that occur in the material. As we have seen in chapter 2, these reactions generate problems of radiation protections. The

objectives is to maximise the efficiency of the system and thereby to limit the activation of the shielding.

The transmission for each material is shown in figure 4.11 as a function of the transmitted energy (in 4.11a) and as a function of the thickness of the target (in 4.11b), the lines are a guide for the eyes.

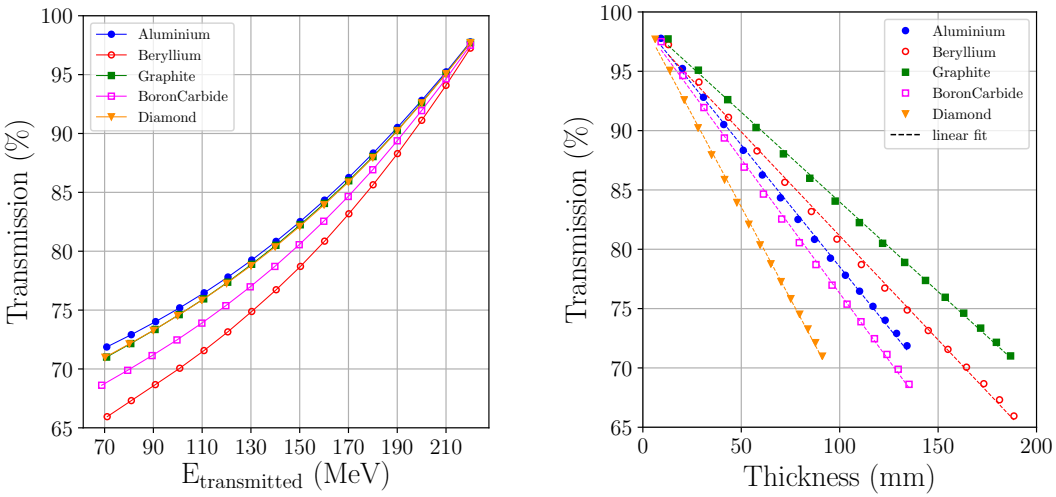

(a) *(b)*

Figure 4.11: Degrader transmission for protons as a function of the energy (a) and the thickness of the target (b). Materials are compared without transverse cuts.

In this case, we obtain the same transmission as the one defined in table 2.9. If we apply our algorithm to the data, we multiply the transmission (without cut) by the value of cuts for each material and we obtain the following transmission (see figure 4.12) as function of the thickness of the beam core.

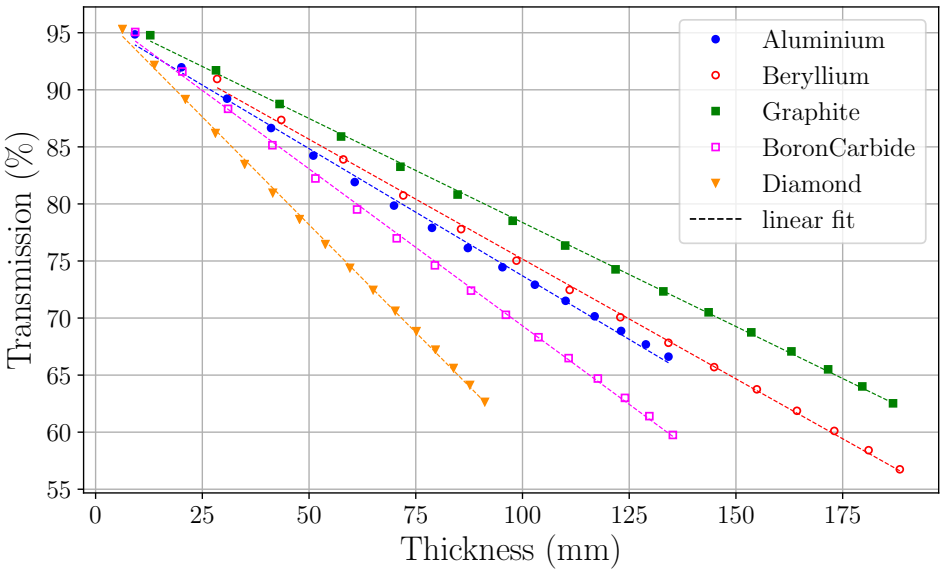

Figure 4.12: Degrader transmission for protons as a function of the thickness of the target. Materials are compared and transverse cuts are applied.

We apply a linear regression of the type $W = at + b$ to these data (represented by the dashed lines in figure 4.12). The values of a and b for the linear regression between the transmission and the thickness are summarized in table 4.1 for the different materials.

Material	a	b
Aluminium	-0.22	95.99
Beryllium	-0.21	96.16
Graphite	-0.18	96.60
Boron carbide	-0.27	96.83
Diamond	-0.38	97.07

Table 4.1: Values of a and b as a function of the material.

These values can be directly implemented in Manzoni to compute the beam transmission from the accelerator up to the isocenter (patient) for different energies.

We observe that diamond indeed improves the transmission for a given energy compared to beryllium. However, it is important to specify that if we change the design of the energy degrader, the transmission efficiency must be evaluated globally up to the isocenter because some other elements as slits or quadrupoles are present in the beam line and interact also with the beam.

4.3.2 Energy spread

As we have explained, after going through a slab of matter, the transmitted beam has a distribution in energy (see figure 4.4a). This spectrum is an important consideration in proton therapy because the deposit dose in the tumor is a direct function of the energy spread [156]. In function of the energy, particles will be stopped more or less deeply. This distribution is quantified using the energy spread which is the standard deviation of the spectrum. The energy spread for protons is shown in figure 4.13. From these results, we conclude that there are no major differences between materials.

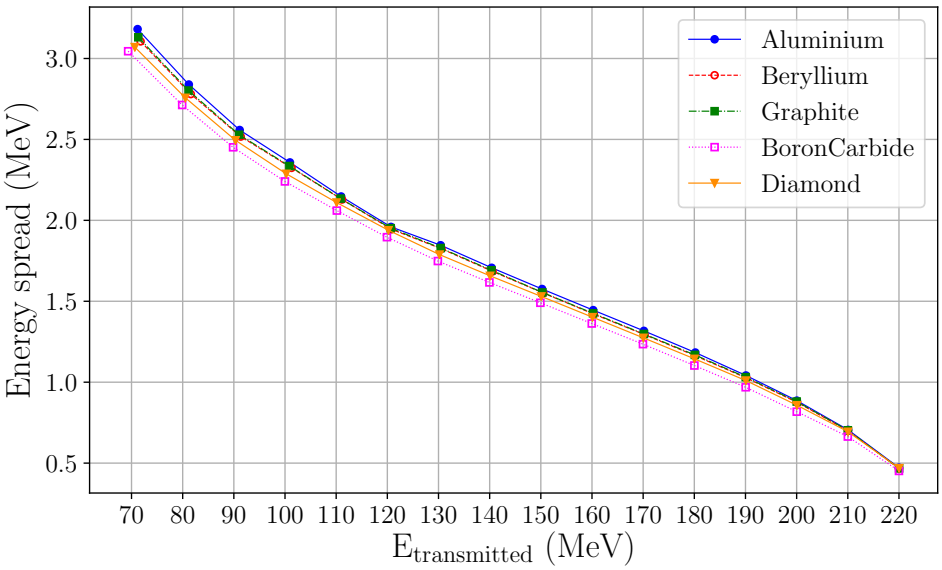

Figure 4.13: Energy spread for protons as a function of the transmitted energy.

4.3.3 Emittance

When comparing different degrader solutions of various lengths, it is key to consider a transverse beam transport invariant such as the emittance. Indeed, if we represent the beam size (figure 4.14a) and the scattering angle at the exit of the slab (figure 4.14b), we can not conclude which material is the most effective. In the first case, the beryllium seems to be better as it has a lower scattering angle but in the second case, the diamond has a lower beam size. Thus it is not possible, with only these informations, to choose the correct material, we need to consider the emittance for the comparison.

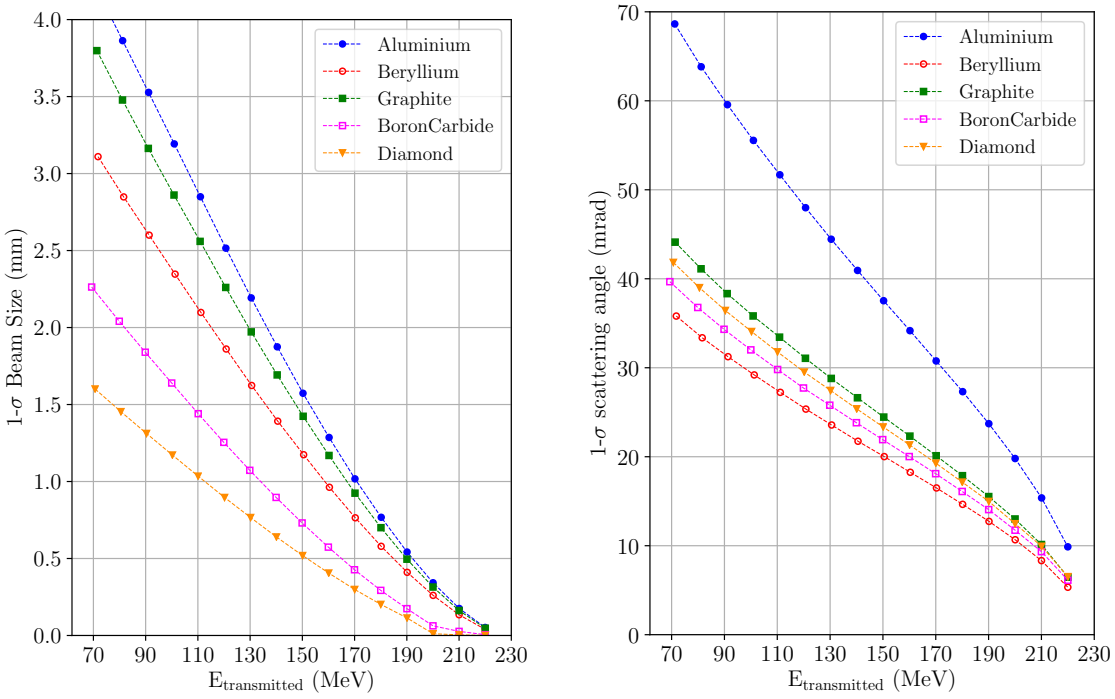

(a) Beam size. *(b) Scattering angle.*

Figure 4.14: Scattering angle and beam size as a function of the transmitted energy for each material.

As the emittance is directly related to the beam size and the beam divergence (see equation (3.97)), it must be as low as possible to avoid interactions with the different elements in the beamline. The emittance of each material is presented in figure 4.15.

The differences in emittance decrease as function of the output energy. In particular, the behaviours of aluminium, graphite and beryllium follow the expected order: the emittance increase is minimized by a high material density and by a low atomic number Z. This explains why beryllium is a material of choice and why it is used in the *IBA* degrader at low energy. We find the same behaviour between the boron carbide and the graphite as described in [152].

Based on these results, we propose to use diamond as new material for the degrader. Diamond will be integrated to a new degrader design that will be described in section 4.5. We first analyse the degrader used currently at *IBA* with the collimator considering a pencil beam to characterize the emittance variations with this section.

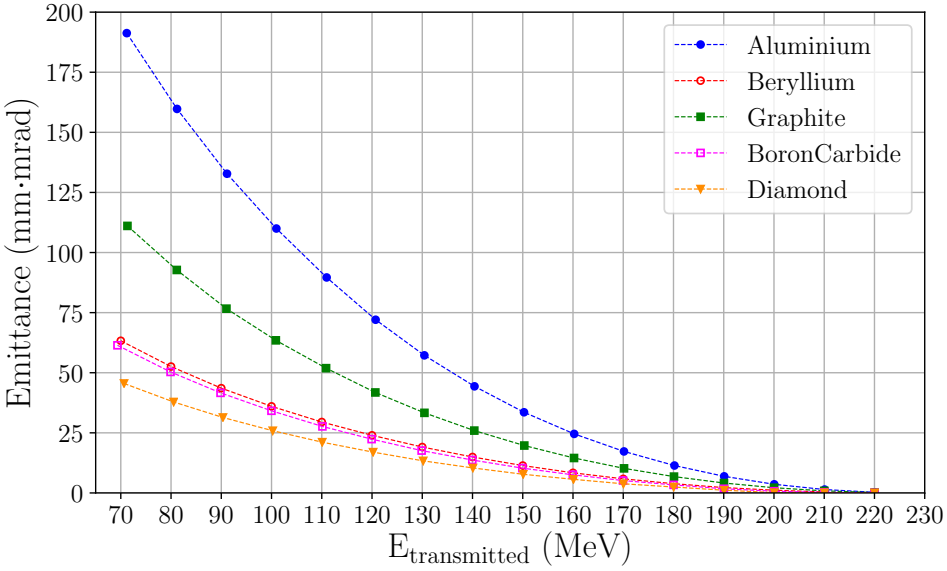

Figure 4.15: Emittance comparison for aluminium, beryllium, graphite, boron carbide and diamond as a function of the output energy.

4.4 Realistic simulation of the *IBA* degrader and collimator

In this section, the actual *IBA* energy degrader, illustrated in figure 4.16a, is studied. In function of the required energy, the material of the block is different:

- Beryllium for transmitted energy lower than 120 MeV
- Graphite for transmitted energy between 120 and 220 MeV
- Aluminium for transmitted energy higher than 220 MeV

This real and complex geometry is directly imported in *Geant4* for a better representation of the reality. The real design is coming from a *Computer-Aided Design* (CAD) software (figure 4.16b) and the resulting file is converted to a GDML (Geometry Description Markup Language) format [98]. The main advantage of this format is that we can take into account all the details of the geometry, specify the material of each element and directly import this model in *Geant4*.

The *Geant4* model of the degrader is shown in figure 4.16c where the beryllium is represented in purple, the graphite in gray and the aluminium in cyan. The collimator is also represented in yellow. It consists of a tantalum cylinder with a 10 mm diameter hole in the centre. It is used to remove particles with a large angle/position before entering the beamline.

(a) Picture of the degrader.

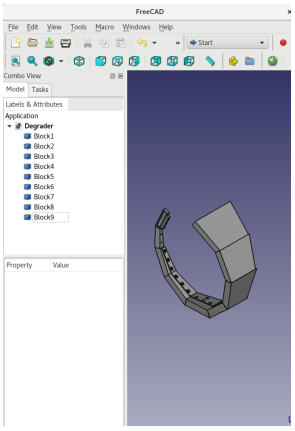

(b) CAD model.

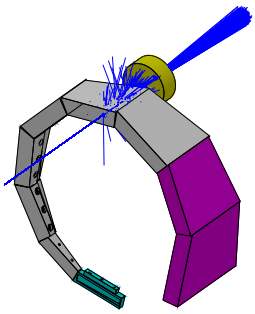

(c) Geant4 *model.*

Figure 4.16: Representations of the IBA *degrader system. From the real design (in a), simplified with a CAD software (in b) and model in* Geant4 *(in c).*

We first perform a simulation to determine the relation between the rotation angle of the degrader and the transmitted energy. A pencil beam is used. The energy spectrum and the corresponding range at the exit of the degrader for a given angle of the wheel are represented in figure 4.17a. A Gaussian fit is made over the histogram of this energy spectrum and the energy for a specific rotation angle corresponds to the mean value of the Gaussian distribution. The entire calibration is represented in figure 4.17b. The discontinuities result from the change of the blocks used for the energy degradation. We also compare our calibration made by *Geant4* with the real calibration of a Proteus®One system (figure 4.17b in red). Both calibrations are in excellent agreement.

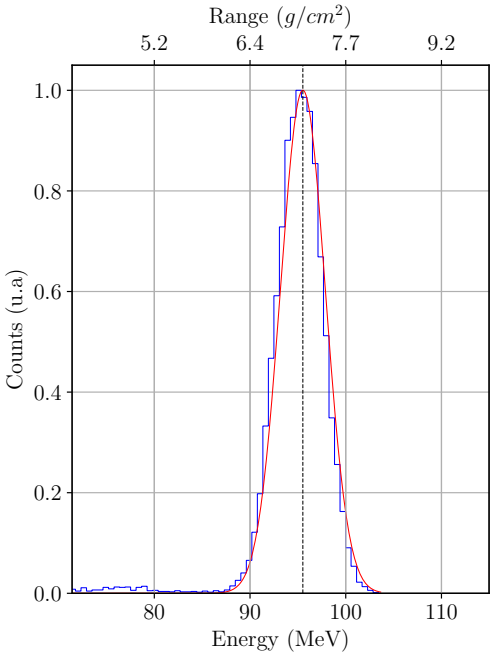

(a) Energy spectrum at the exit of the degrader for one specific angle.

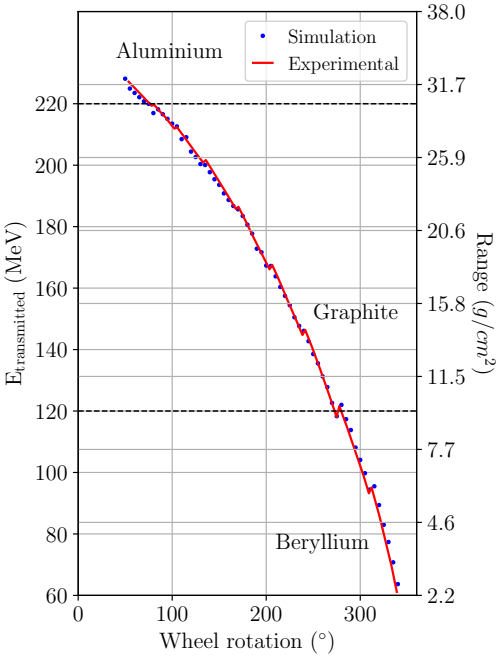

(b) Results for all energies

Figure 4.17: Wheel calibration obtained by simulation.

4.4.1 Beam properties at the exit of the degrader

In this section, we analyse the energy spectrum and the emittance at the exit of a synthetic geometry and at the exit of the *IBA* degrader.

4.4.1.1 Energy spectrum

In this section, we compare the differences between the energy spectrum at the output of the synthetic geometry and at the exit of the real geometry of the degrader for two transmitted energy, namely 70 MeV (beryllium) and 160 MeV (graphite).

The results for the energy spectrum are presented in figure 4.18. For both cases, we observe that protons at high energies are still present in the energy spectrum of the real geometry. This effect is due to the specific geometry of the degrader where protons can leave through the lateral sides (see figure 4.16c)

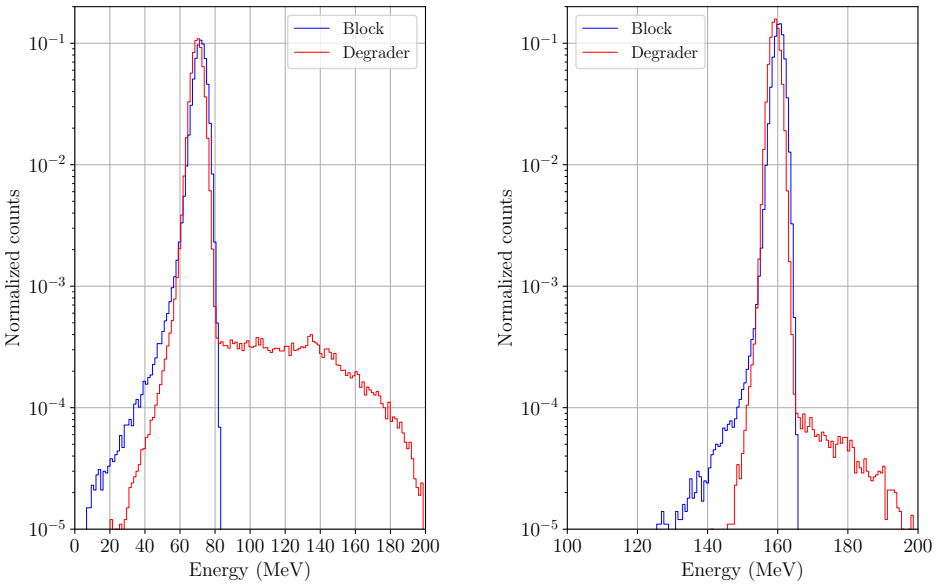

(a) 70 MeV. *(b) 160* MeV.

Figure 4.18: Energy spectrum of protons at the exit of the degrader for the synthetic geometry (in blue) and for the IBA *degrader (in red).*

In figure 4.19, we show the energy as a function of the horizontal and vertical position for the synthetic geometry (figure 4.19a) and for the real *IBA* degrader (figure 4.19b). This corresponds to the transverse plane at the exit of the degrader. The color scale represents the mean energy of the beam shifted from the average energy at the output of the degrader.

The dark circle represents the opening of the collimator. We notice that the energy spectrum is uniform in case (*a*) while for the *IBA* degrader, we observe that the transmitted energy is dependent on the geometry of the block. The protons leaving the degrader by the lateral sides have higher energy and correspond to the red area in figure 4.16c.

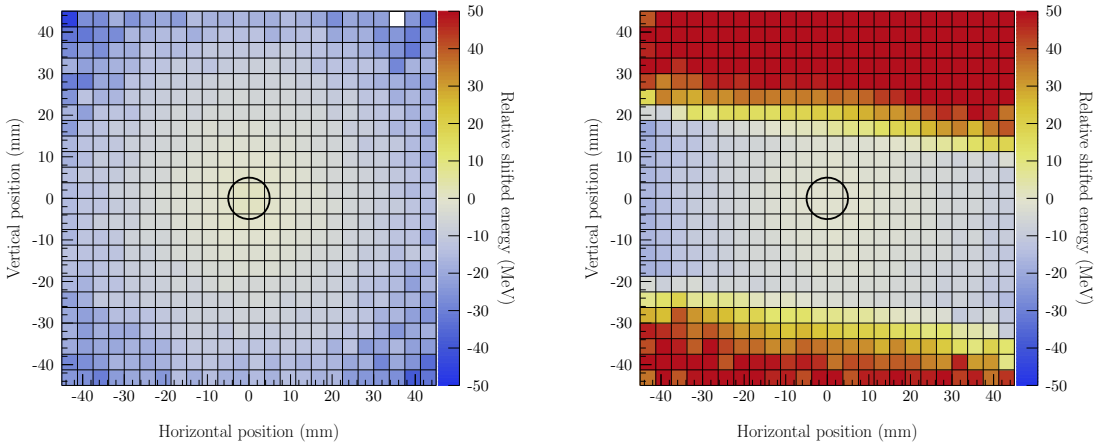

(a) Synthetic geometry *(b)* IBA *degrader*

Figure 4.19: 2D energy spectrum as function of the horizontal and vertical positions for the synthetic geometry (a) and the real geometry (b) of the degrader. The opening of the collimator is represented by the dark circle.

4.4.1.2 Emittance

We perform simulations to evaluate the emittance to compare the results with the synthetic geometry. We also applied to the exact geometry of the degrader, the cuts obtained in section 4.2.3. The results are shown in figure 4.20.

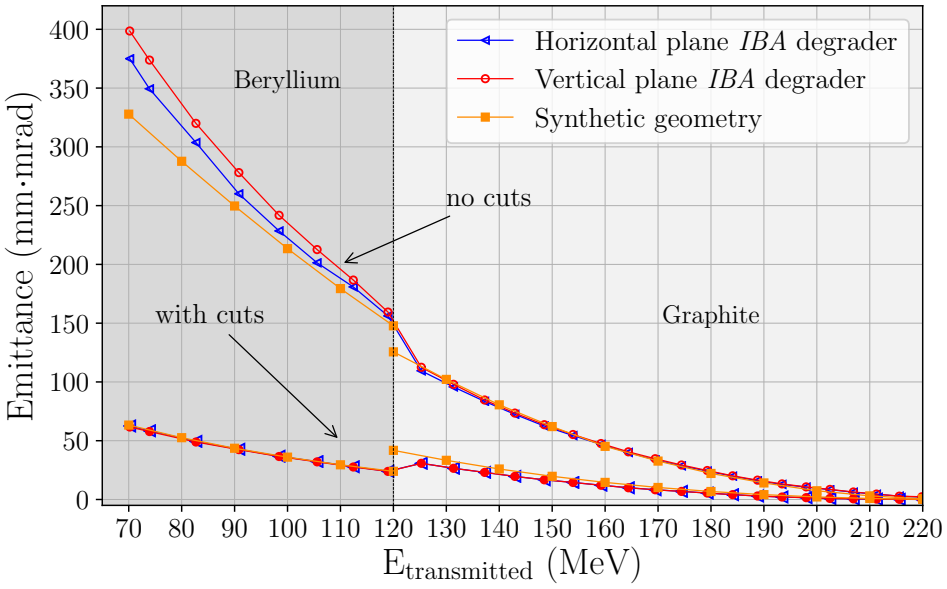

Figure 4.20: Beam emittance at the exit of the degrader. Comparison with semi-infinite blocks is also shown. Data with and without optimal Gaussian cuts are compared.

The difference between horizontal and vertical plane may be attributed to the asymmetric geometry of the block of the *IBA* degrader. Indeed, this effect disappears when cuts are applied. We also note the step in emittance at 120 MeV due to the change of material on the degrader wheel. When the cuts are applied, the emittance for the exact geometry matches well the ideal geometry.

4.4.2 Beam properties after the passage in the circular collimator

As said above, the collimator removes particles with a large angle before entering the beamline. However, interactions between beam and matter may occur also in the collimator. In this section, the effects of the collimator on the energy spectrum and on the emittance are studied.

4.4.2.1 Energy spectrum

In figure 4.21, we show the energy spectrum of primary protons for two transmitted energies at the entrance (in blue) and at the exit (in red) of the collimator. We observe that the high energy particles have been disappeared but a tail appears at low energy. This tail is due to interactions of protons inside the collimator. Indeed, if we adapt the collimator as an absorbing element (called ideal collimator in the rest of this section), we obtain the green curve which is symmetric around the desired energy.

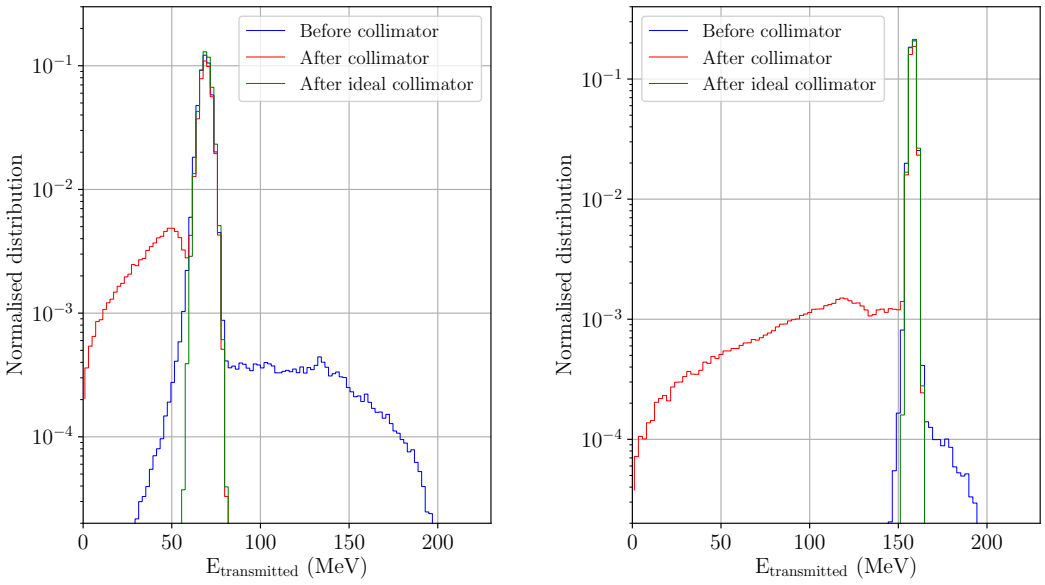

(a) 70 MeV *(b) 160 MeV*

Figure 4.21: Energy spectrum of protons before the collimator (in blue), behind the collimator (in red) and behind an ideal collimator without interactions (in green).

The proportion of protons interacting in the collimator is shown in figure 4.22. The proportion of interactions is greater at low transmitted energy because the emittance at the exit of the degrader is important. We observe a gap at the transition between beryllium and graphite. The material change allows reducing the number of interactions in the collimator.

In practice, these low energy protons will be removed by bending magnets (see section 3.2.4.2) present in the beamline. However, they contribute to losses of the system and generate radioprotection issues.

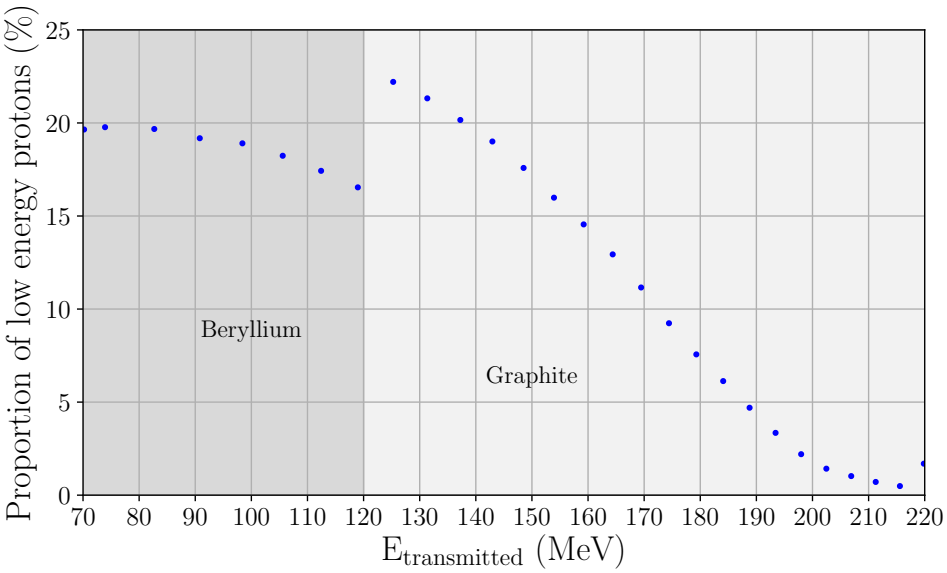

Figure 4.22: Proportion of low energy protons generated inside the collimator as a function of the transmitted energy.

4.4.2.2 Emittance

We now analyse the effect of the collimator over the beam emittance. We present in figure 4.23, the emittance before the collimator (blue and red curve), the emittance behind the collimator (in magenta and green) and behind the ideal collimator (in cyan and orange).

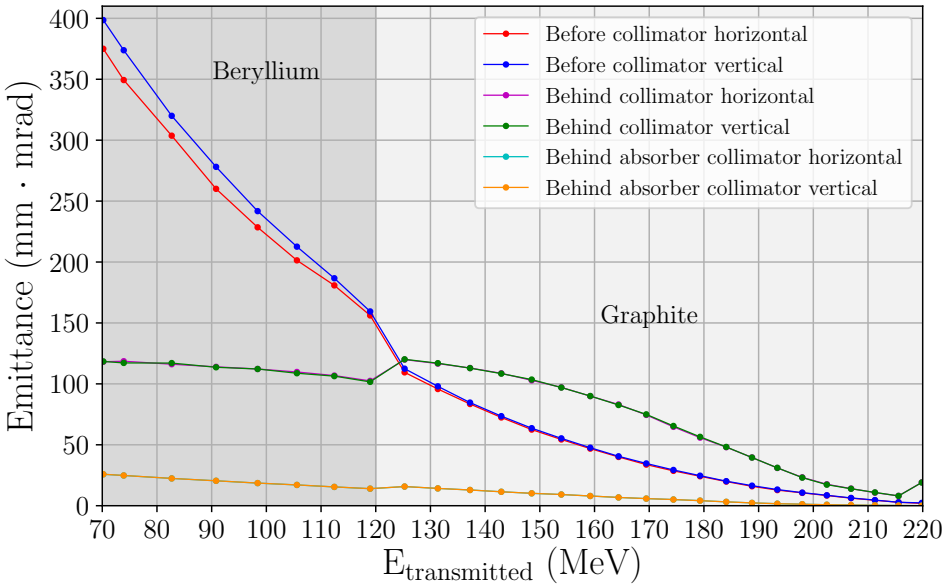

Figure 4.23: Emittance before and behind the collimator. The emittance behind an ideal one is also shown.

Three main conclusions can be deduced from these results:

1. The collimator symmetrizes the emittance in both planes (superposition of the curves in the transversal plane).

2. The real collimator induces an increase of the emittance compared to an ideal collimator.

3. For transmitted energies higher than 120 MeV, which correspond to the graphite blocks, the emittances are lower at the entrance than at the output of the collimator. The differences are explained by the interactions occurring in the collimator.

The emittance at the exit of the collimator is composed of particles having a large energy distribution (see figure 4.21). However, before reaching the patient, the beam goes into an energy selection system to keep only protons with the correct energy. Therefore, there will be losses along the beamline and the beam emittance that will finally reach the patient is represented by the yellow curve (in figure 4.23)

4.5 Study and performance reach for a diamond-based degrader

An energy degrader for medical facilities needs to have several specifications, the most important are [157]:

1. Material
2. Speed, especially for PBS treatment mode
3. Accuracy of positioning
4. Minimum energy to be reached
5. Transversal size of the beam at the exit of the degrader

We observed in the previous sections that the diamond has excellent properties for beam emittance minimization and transmission. Therefore, we propose a new degrader design based on insertable cylinders, also called lollipops. We investigate a realistic geometry for a diamond degrader made of discrete range shifting lollipops. The minimum thickness is computed in order to have a range variation of 0.1 g/cm^2 for the transmitted beam. To ensure reaching energies between 70 and 230 MeV, we use 9 cylinders whose thickness and the induced range reduction ($\Delta\mathbb{R}$) for an input beam of 230 MeV are summarized in table 4.2:

Lollipops	Thickness (mm)	$\Delta\mathbb{R}$
L0	64	20.34
L1	32	10.38
L2	16	5.42
L3	8	2.93
L4	4	1.52
L5	2	0.76
L6	1	0.38
L7	0.5	0.19
L8	0.25	0.09

Table 4.2: Thicknesses of the different lollipops.

Due to the delta range for L_0 and L_1, these two blocks are never placed together. To increase the compactness of the device, a maximal distance between two inserted blocks is

fixed at 0.1mm. In figure 4.24, we illustrate three configurations of the system to obtain a transmitted range of 5.0 g/cm^2 (using 4 blocks), 5.1 g/cm^2 (using 6 blocks) and 2.5 g/cm^2 with all blocks inserted (except L1).

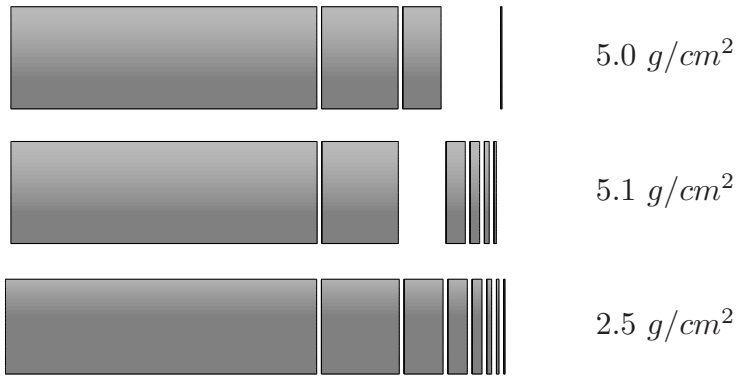

Figure 4.24: New energy degrader design based on diamond lollipops system.

Figure 4.25 represents the emittance computed using the new degrader design and these results are compared with a semi-infinite block of diamond (magenta line) and beryllium (dashed black line). The green line represents the emittance obtained with the *IBA* degrader (rotating wheel). The cuts determined in the previous section are applied to allow a comparison of the Gaussian core only.

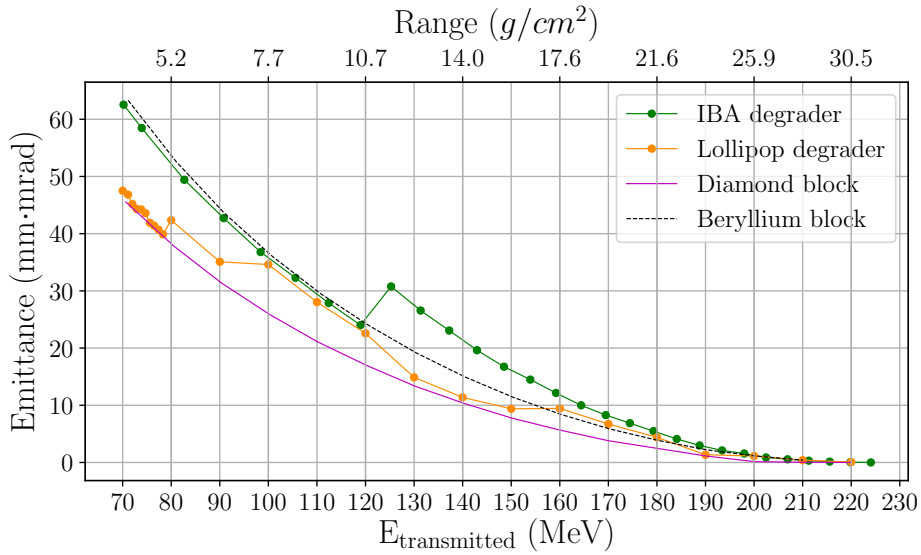

Figure 4.25: Emittance values obtained for the ideal and lollipop degrader models.

Depending on the position of the lollipops, the emittance is lower or equal to that obtained with a block of beryllium. For low transmitted energy, the majority of lollipops is inserted and the same behaviour as a diamond block is recovered. Indeed, the impact of the air gaps (distance between two inserted lollipops) is negligible. A disadvantage of this design is that the emittance jumps as function of the transmitted energy (mainly at 80 MeV). Indeed, the absence of some blocks implies a large amount of air between blocks. In this zone, the beam divergence is exacerbated causing the emittance jumps.

However, it is important to precise that this design is the first step of more complex studies. This kind of degrader has to be modelled in a real beamline with an optimization of the different magnetic elements. Finally, a study about the cost-benefit of this design must be done to evaluate more precisely its strengths and weaknesses.

4.6 Conclusion

In this chapter, we have introduced the analytical formalism to compute the rms beam properties at the exit of a slab using the scattering power. The contribution of the nuclear reactions to the energy and the angular spectrum have been compared to the electromagnetic process. We have developed a new method, based on cuts along the transverse momentum to quantify the nuclear losses and the halo effect from nuclear scattering. We proposed the following equation to compute the cuts as a function of the transmitted energy and the atomic number of the target:

$$\xi\left(Z,E\right)=\left(0.005\,Z-0.09\right)\,E-\left(1.07\,Z-23.17\right) \tag{4.18}$$

Based on these cuts, we are able to recover the Gaussian core of the distribution which is used as input for beam transport codes as Manzoni. Finally, the results obtained with Monte Carlo simulations have been compared with the analytical models of Farley and Gottschalk. The model proposed by Gottschalk is consistent with the results obtained with *Geant4* with an electromagnetic physics list. The Farley model uses an approximation which is less accurate than the Gottschalk model.

Different materials used in proton therapy have been compared in order to evaluate their performances. We have shown that the key notion to select a material is the emittance. The results obtained for diamond are particularly interesting, we observe a 30% reduction in emittance for the lowest energies compared to beryllium in a synthetic geometry.

The *IBA* degrader and collimator have been modelled in *Geant4*. The degrader consists of a rotating wheel composed of beryllium, graphite and aluminium blocks. Compared to a synthetic geometry, an asymmetry in the energy spectrum appears since higher energy protons leave the degrader through the lateral sides. The collimator is a tantalum cylinder with a hole in the centre. It symmetrizes the beam emittance in the transversal plane but produces low energy protons which decrease the efficiency of the system. We have determined that the collimator has an efficiency of about 80% for a transmitted energy of 70 MeV.

A new degrader design has been proposed to improve the beam transmission and minimize the beam emittance. It is based on insertable diamond cylinders and allows quick changes of the transmitted energy. We observe an improvement in the beam properties compared to the actual degrader. However, emittance jumps are observed due to the air gaps in the design.

Part III

Complete installation simulation using BDSIM

Chapter 5

Modelisation of the transport beamline

Contents

In chapter 3, we introduced the different equations useful for the determination of the beam propagation in a beamline as well as three softwares implementing these equations: Manzoni, MAD-X and BDSIM. The properties of the *IBA* degrader were studied in chapter 4 using a pencil beam. We have especially discussed the increasing emittance after the degrader and the collimator.

In this chapter, we develop a complete Monte-Carlo model of the Proteus® One with BDSIM (see figure 5.1). This model combines both the transport of the proton beam in magnetic elements as well as the interactions between particles and matter.

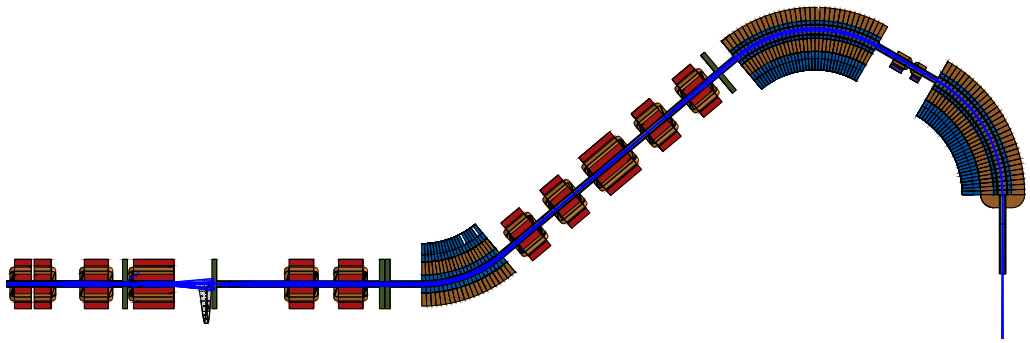

Figure 5.1: Complete model of the Proteus® One beam transport line made with BDSIM. The propagation of the proton beam is shown in blue. The secondary particles are not shown.

In section 5.1, we introduce the different elements constituting the Proteus®One system and the model obtained is validated and discussed in detail in section 5.2. In particular, we compare our simulations with experimental measurements collected along the beamline and at the isocenter of Proteus®One installations currently in operation in Royal Oak (USA) and Newport (UK).

5.1 Beam transport model for the Proteus One system

The Proteus®One layout is shown in figure 5.2, it is divided in three main parts:

1. The accelerator (S2C2) which produces the beam at a specific energy, namely 228.15MeV.
2. The extraction, which propagates the beam extracted from the accelerator up to the energy degrader.
3. The gantry, *i.e* the beamline from the degrader up to the isocenter which is called *Compact Gantry* (CGTR) (in blue in figure 5.2).

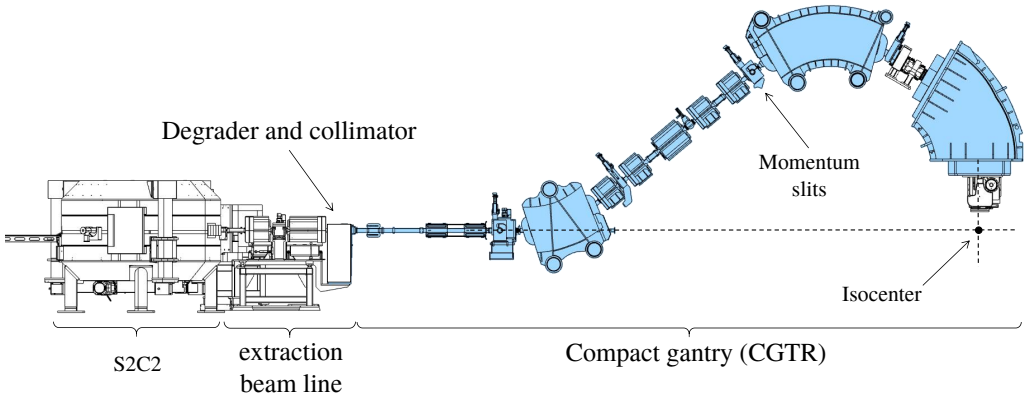

Figure 5.2: Layout of a Proteus®One. Reproduced from [119].

A *gantry* is a transport beamline which rotates around the isocenter. It is composed of different elements such as a mechanical support, magnets, beam diagnostics and other technical infrastructure [158]. As we have seen in section 3.2.4, dipoles and quadrupoles are used to bend or to focus the beam. The beam optics (beam size, divergence, dispersion, ...) of the gantry must be designed for any transmitted energy and rotation angle to ensure a correct treatment of the tumor. Therefore, the following requirements must be satisfied at the isocenter [159, 160]:

- Small and constant spot size at the tumor.
- Dispersion equal to 0 at the isocenter to minimize the beam size and suppress the energy-position dependence (see equation (3.100)).
- Independence of the beam optics in the gantry with the rotation angle.

The two first requirements are satisfied if we have:

1. Double waist at the degrader level to minimize the emittance at the entrance of the beamline (see section 5.1.3).

2. Maximal dispersion at the momentum slits to suppress the particles without the correct energies (see section 5.2).

The independence of the beam optics, is more complex to satisfy because it implies to have equal emittances in both planes [159]. However, as we will see in section 5.1.1, emittances (horizontal and vertical) at the exit of the accelerator are not equal. Therefore, for each proton therapy center, currents of quadrupoles in the gantry are adjusted as a function of the rotation angle. By convention, the zero degree rotation angle corresponds to the beam aligned along the vertical axis and points toward the floor (as represented in figure 5.2).

The design optic functions, namely β_x, β_y and D_x (see section 3.2.4), of the Proteus® One system are shown in figure 5.3. The requirements explained above are clearly visible on this figure: the double waist on the degrader, a small spot size at the isocenter and the dispersion function (in green) equal to zero at the isocenter.

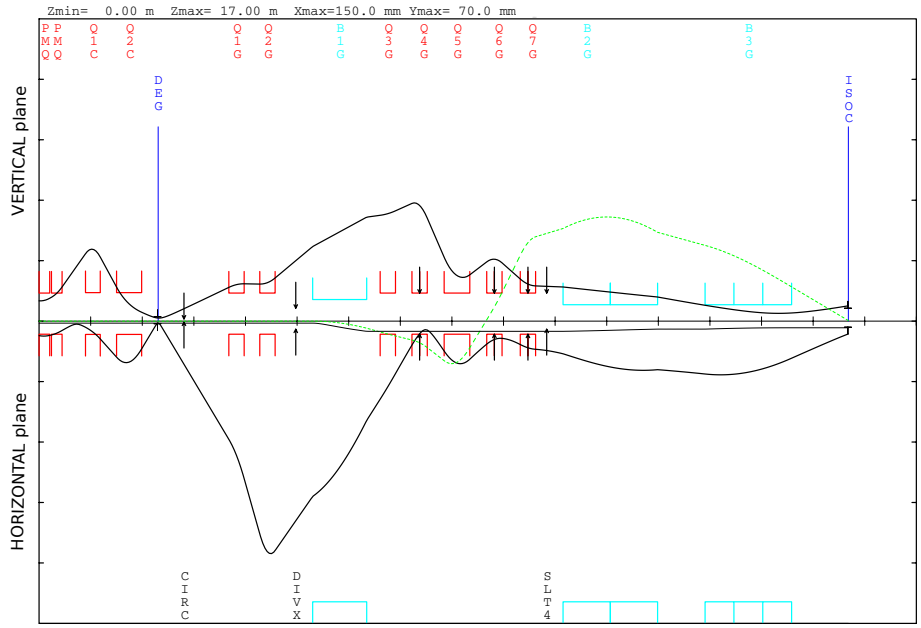

Figure 5.3: Design function of the Proteus® One system. Data courtesy of IBA.

We also notice that the envelope of the beam is important before the degrader (in Q1C and Q2C) resulting in interactions in the quadrupoles, as already mentioned in section 2.4.2.

The interactions with the different elements in the beamline induce losses. To precisely quantify the effect of these interactions on the beam, we have developed a complete Monte Carlo model of the Proteus® One system using BDSIM to take into account the beam propagation in the magnetic elements. Each element of the system is described in the following sections.

5.1.1 Properties of the beam at the output of the accelerator

The particle accelerator of a Proteus® One system consists of a supra-conducting synchro-cyclotron (usual abbreviation S2C2). The extraction of the beam out of an accelerator is a complex process. W. Kleeven *et al.* [161, 162] have made an entire *OPERA3D* model

of the S2C2 (see figure 5.4) and have simulated with Advanced Orbits Code (AOC) the particle distribution at the exit of the accelerator. All results presented in this section are courtesy of *IBA*.

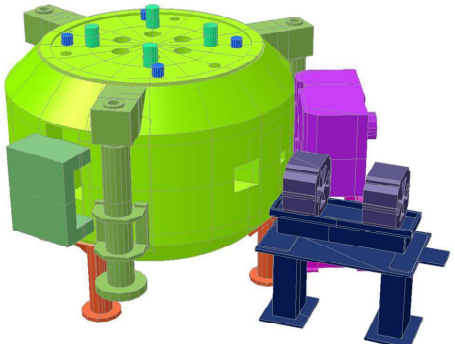

Figure 5.4: Model of the S2C2 and the extraction beamline in Opera 3D. Reproduced from [163]

OPERA3D is a software developed for the resolution of partial differential equations for the electromagnetic field calculations [164]. This software provides 3D maps of the electric and magnetic field. These maps are an input file for *AOC* software.

This software has been developed by *IBA* and tracks particles along a circular orbit under the combined action of magnetic and electric fields. A 5th order Rung-Kutta integrator is used to resolve equations of motion (equation (3.27)) from the ion source up to the extraction point. The beam losses are also computed in order to determine the efficiency of the accelerator.

Finally, after the extraction of the beam, different output files are available: the Twiss parameters of the beam, the locations of the losses, the RMS properties of the beam and the characteristics (position, momentum, energy) of each particle. To have correct statistics for the beam interacting with the elements of the beamline, an algorithm has been developed to resample this distribution [165]. The emittance, as defined in section 3.2.5, of the *S2C2* beam is shown for each plane in figure 5.5.

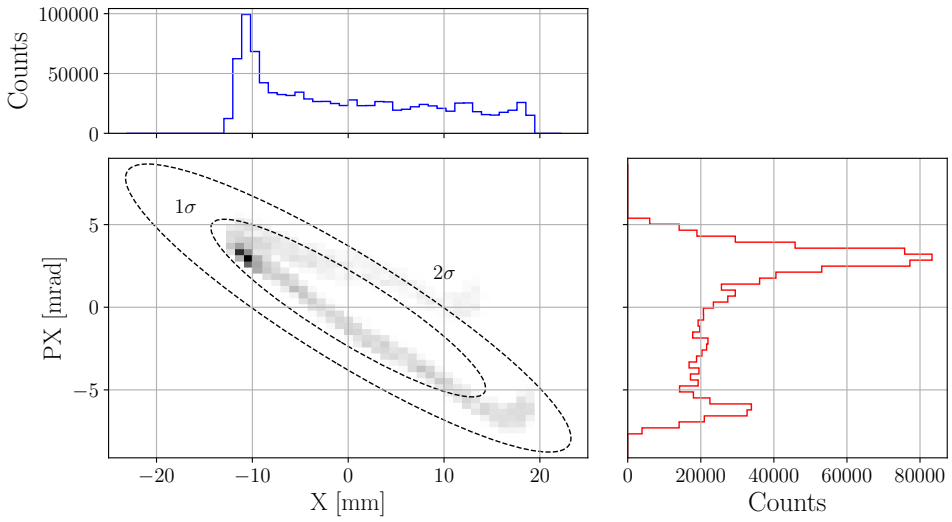

(a) Horizontal plane.

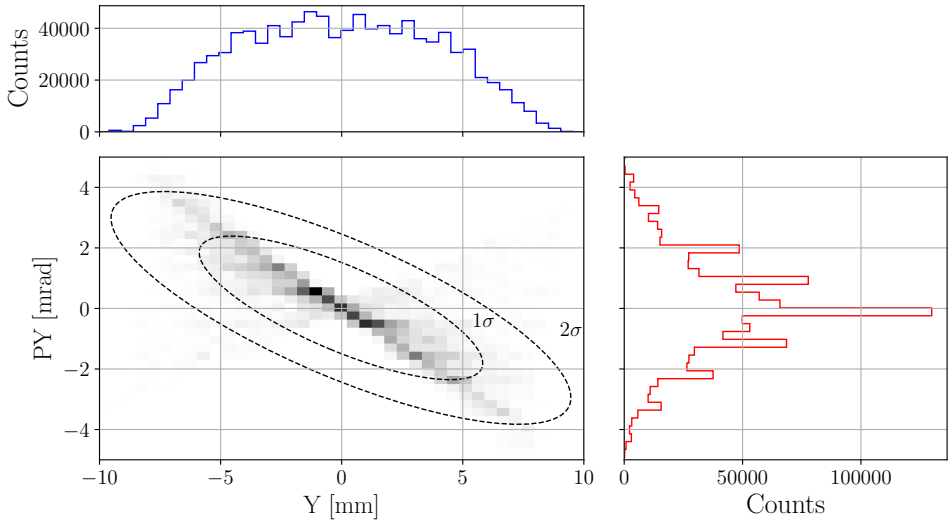

(b) Vertical plane.

Figure 5.5: Emittances of the beam in both planes. The projection over each axis is also shown. Data courtesy of IBA.

At the exit of the S2C2, the beam has a small energy deviation around the nominal energy. This deviation is characterized by the momentum deviation (δ). In figure 5.6, we show the distribution of the relative momentum deviation and the Gaussian fit over this distribution [166].

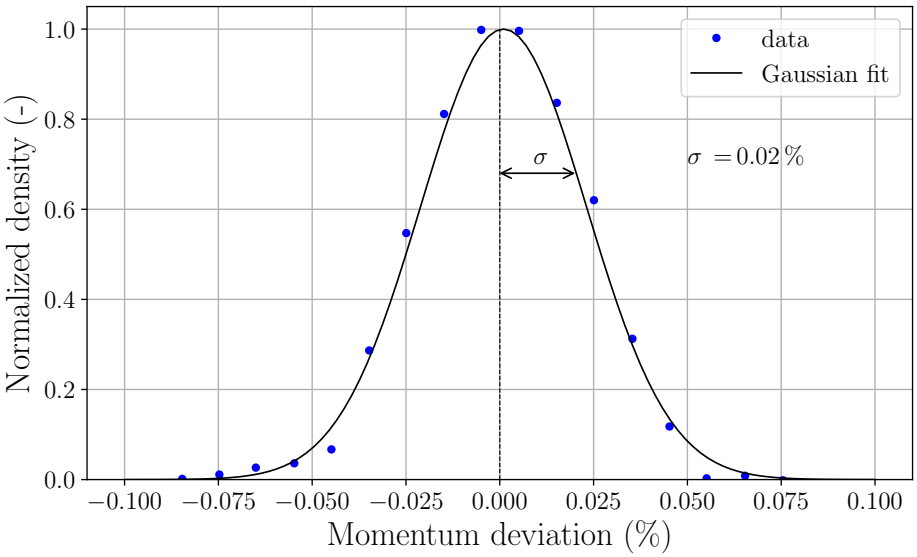

Figure 5.6: Distribution of the momentum deviation at the exit of the S2C2. Data extracted from [166]

The standard deviation of this distribution is about 0.02%, which represents an energy deviation of 150 keV. Table 5.1 summarizes the properties of the extracted beam (the bar stands for the mean value).

	Extracted beam (S2C2)
$\bar{x}$ (mm)	0.02
σ_x (mm)	9.5
$\bar{y}$ (mm)	-0.064
σ_y (mm)	3.88
$\bar{xp}$ (mrad)	0.034
σ_{xp} (mrad)	3.55
$\bar{yp}$ (mrad)	0.03
σ_{yp} (mrad)	1.57
σ_E (keV)	150

Table 5.1: Properties of the extracted beam.

This beam will serve as an input for the beam transport codes as Manzoni, MAD-X or BDSIM.

5.1.2 Description of the Proteus® One elements

In this section, the sequence of elements constituting the beamline is described. We show in figure 5.7 the schematic representation of the extraction (figure 5.7a) and the *CGTR* (figure 5.7b). The component characteristics are summarized in table 5.2. ST and ISO mean respectively the beginning of the beamline and the isocenter. The focus plane for quadrupoles and the pole face angle for bending magnet (e_1 and e_2) are also specified.

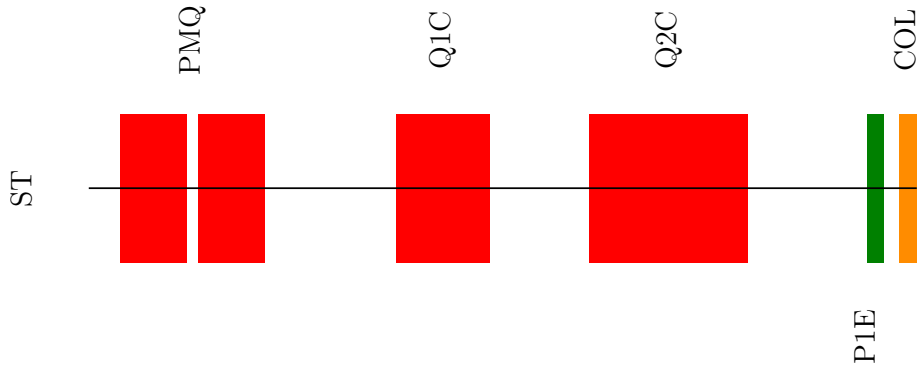

(a) Extraction.

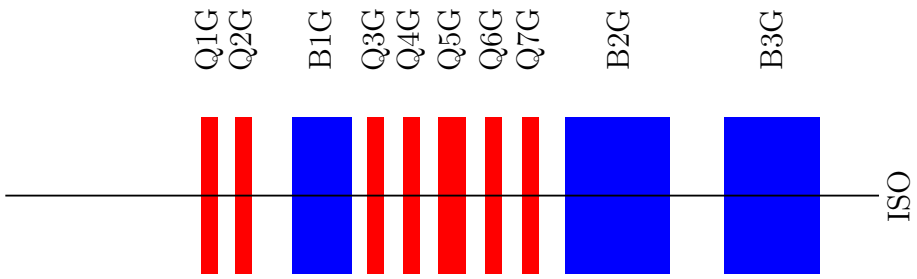

(b) CGTR.

Figure 5.7: Schematic representations of the extraction (a) and the CGTR (b) of a Proteus® One.

	Element	Type	Length (mm)	Focusing plane	$e1$ (rad)	$e2$ (rad)
Extraction	PMQ	Quadrupole	206	Horizontal	–	–
	Q1C	Quadrupole	290	Vertical	–	–
	Q2C	Quadrupole	490	Horizontal	–	–
Compact Gantry	Q1G	Quadrupole	297	Vertical	–	–
	Q2G	Quadrupole	297	Horizontal	–	–
	B1G	Sector dipole	1050	–	0.3142	0.3142
	Q3G	Quadrupole	290	Horizontal	–	–
	Q4G	Quadrupole	290	Vertical	–	–
	Q5G	Quadrupole	490	Horizontal	–	–
	Q6G	Quadrupole	290	Vertical	–	–
	Q7G	Quadrupole	290	Horizontal	–	–
	B2G	Sector dipole	1830	–	-0.175	-0.262
	B3G	Sector dipole	1680	–	0	0

Table 5.2: Properties of magnetic elements in the beamline.

5.1.3 Minimization of the emittance after the degrader

To minimize the losses in the beamline, the emittance at the exit of the energy degrader (P1E) must be as low as possible. We consider a degrader with a thickness t. Over that thickness t and in absence of interaction, the sigma matrix of the beam after the drift is given by [48]:

$$\Sigma_{beam}(t) = \begin{pmatrix} 1 & t \\ 0 & 1 \end{pmatrix} \begin{pmatrix} \sigma_{11} & \sigma_{12} \\ \sigma_{12} & \sigma_{22} \end{pmatrix} \begin{pmatrix} 1 & 0 \\ t & 1 \end{pmatrix} = \begin{pmatrix} \sigma_{11} + 2t\sigma_{12} + t^2\sigma_{22} & \sigma_{12} + t\sigma_{22} \\ \sigma_{12} + t\sigma_{22} & \sigma_{22} \end{pmatrix} \tag{5.1}$$

The Σ matrix of an energy degrader is given by equation (4.7):

$$\Sigma_{deg} = \begin{pmatrix} A_0 & A_1 \\ A_1 & A_2 \end{pmatrix} \tag{5.2}$$

The Σ matrix at the exit of the degrader is the sum of the Σ matrix of the beam and the Σ matrix of degrader.

$$\Sigma = \Sigma_{beam} + \Sigma_{deg} \tag{5.3}$$

The emittance at the exit of the degrader is given by the determinant of this matrix. When computing equations (5.1) and (5.2) and calculating the determinant of the resulting matrix, we obtain the emittance:

$$\epsilon^2 = \epsilon_{beam}^2 + \epsilon_{deg}^2 + \left(A_0\sigma_{22} + A_2\left(\sigma_{11} + 2t\sigma_{12} + t^2\sigma_{22}\right) - 2A_1\left(\sigma_{12} + t\sigma_{22}\right)\right) \tag{5.4}$$

The two first terms, ϵ_{beam} and ϵ_{deg}, depend on the input beam and the degrader, they are thus constant. As our objective is to minimize equation (5.4), we derive each term and we obtain:

$$A_2 d\sigma_{11} + A_0 d\sigma_{22} - 2A_1 d\sigma_{12} = 0\,. \tag{5.5}$$

Furthermore, the emittance of the beam is constant and therefore, if we derive equation (3.99), we can write:

$$\sigma_{22} d\sigma_{11} + \sigma_{11} d\sigma_{22} - 2\sigma_{12} d\sigma_{12} = 0\,. \tag{5.6}$$

From these equations, we obtain:

$$\frac{\sigma_{11}}{\sigma_{12}} = \frac{A_0}{A_1} \tag{5.7}$$

$$\frac{\sigma_{22}}{\sigma_{12}} = \frac{A_2}{A_1} \tag{5.8}$$

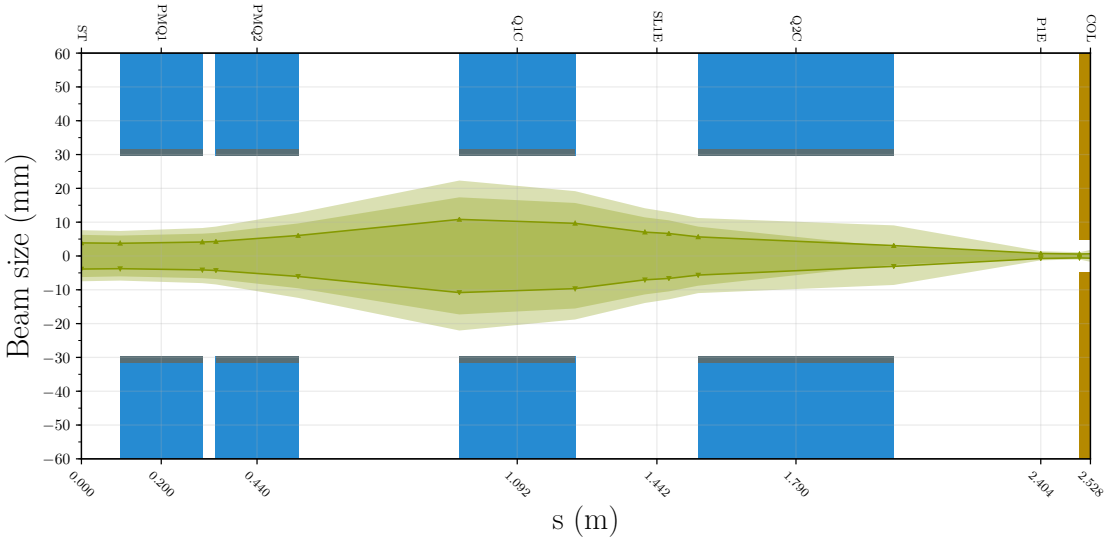

(b) Vertical.

Figure 5.8: Beam envelope along the extraction part of the Proteus® One system.

Finally, the optimum input beam matrix (which minimizes the emittance) is given by :

$$\Sigma_{beam}^{optim} = \frac{\epsilon_0}{\epsilon_{deg}} \begin{pmatrix} A_0 & A_1 \\ A_1 & A_2 \end{pmatrix} \tag{5.9}$$

If we transpose this matrix through a distance $-d$ to obtain an upright ellipse ($\sigma_{12} = 0$), we find that the beam must be focused in a distance $d = A_1/A_2$ before the end of the degrader to minimize the emittance at the exit of the degrader. This is why before entering the degrader (P1E), the beam is focused as we show in figure 5.8 (results obtained with our model). The lines represent the beam envelope at 1σ (rms standard deviation) and the degraded color corresponds respectively to 2 and 3 σ.

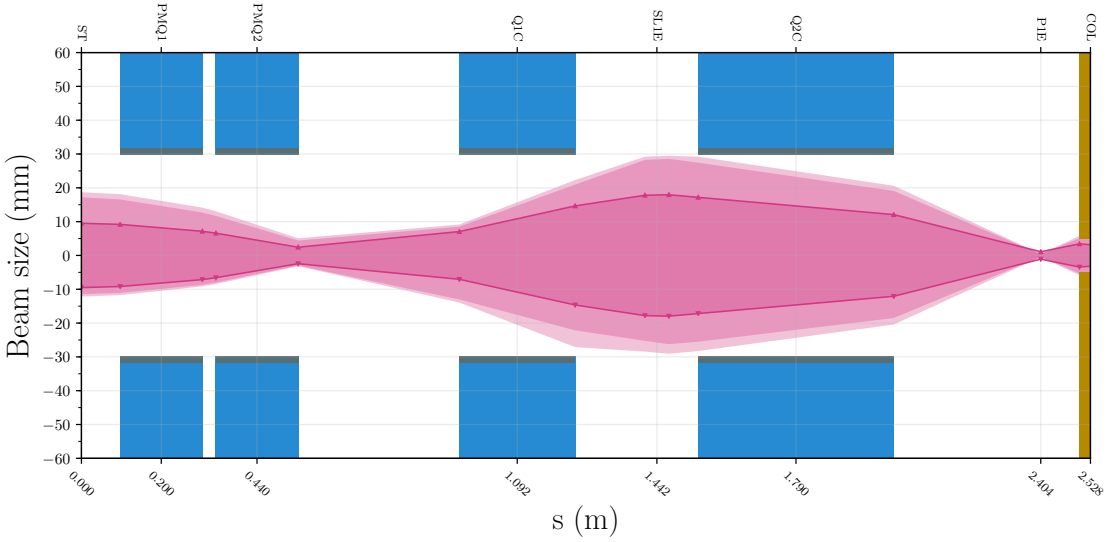

(a) Horizontal.

5.1.4 Propagation of the extracted beam in the beamline

In this section, we consider the propagation of the extracted beam in the beamline without degrader (in *pass through* position) with MAD-X, Manzoni and BDSIM. We compute the evolution of the beam size along the beamline. The results are shown in figure 5.9.

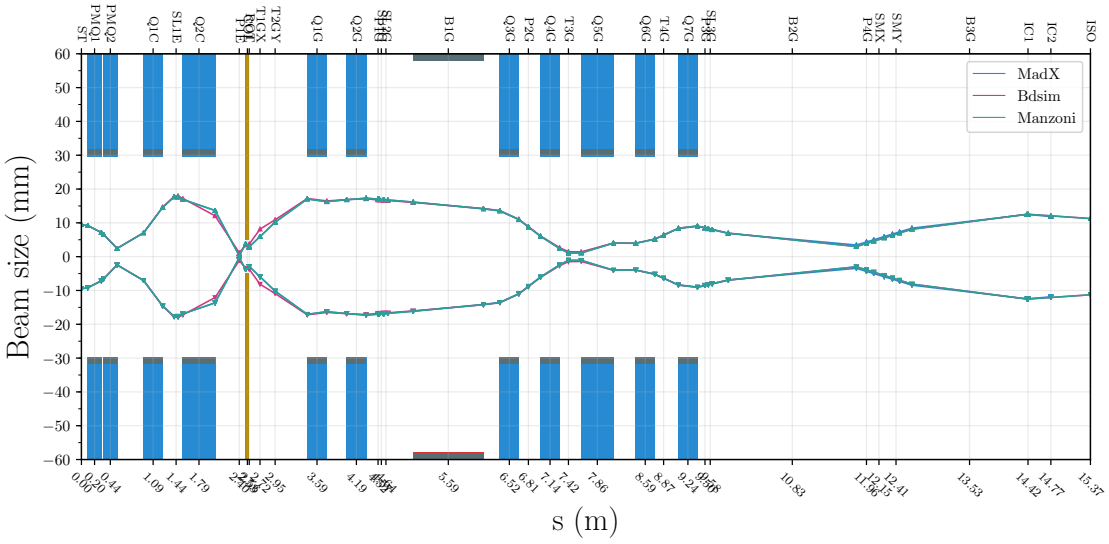

(a) Horizontal plane.

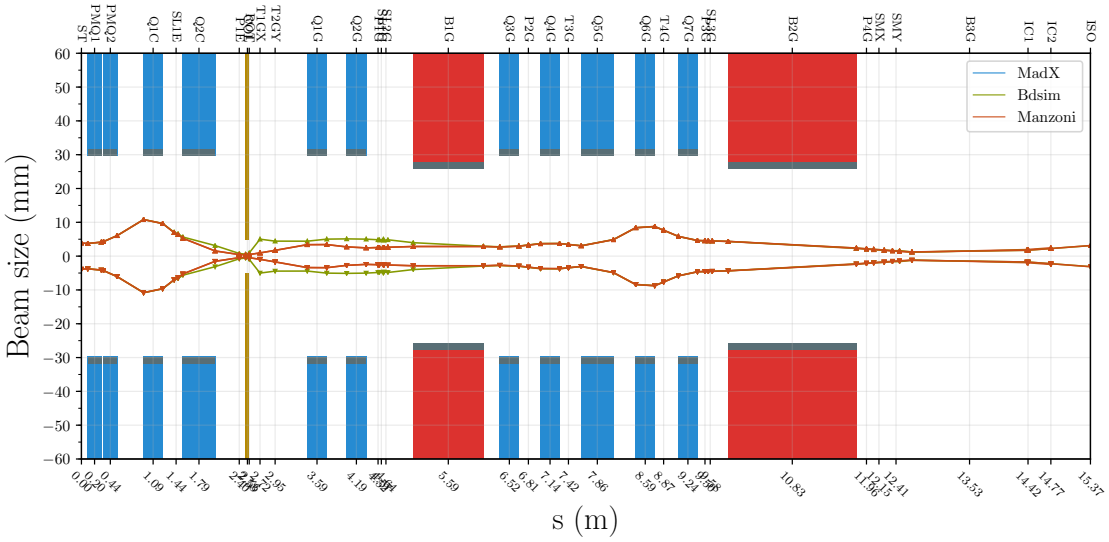

(b) Vertical plane.

Figure 5.9: Beam envelope inside a Proteus® One for Manzoni, MAD-X and BDSIM.

We notice that all softwares give the same envelope along the beamline in both planes. The differences that we observe with BDSIM are essentially due to the low energy protons generated inside the collimator because they are lost after the first bending magnet (B1G). The dispersion function is computed using MAD-X and is shown in figure 5.10.

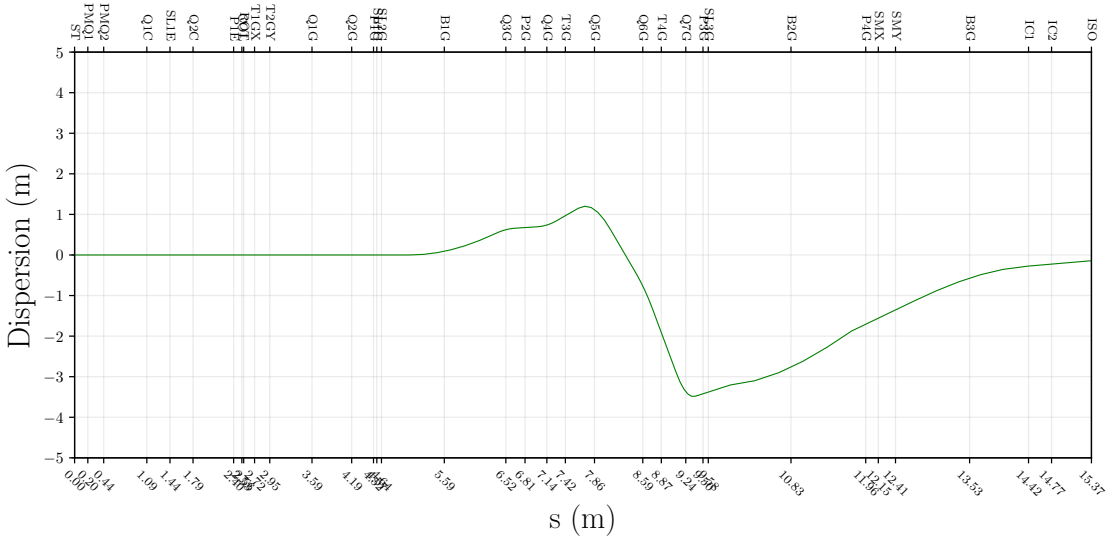

Figure 5.10: Dispersion function along the beamline.

The dispersion has the expected behaviour, namely, it is equal to zero at the isocenter and maximum at the level of the momentum slits. In the rest of this thesis, we use BDSIM to provide a complete Monte Carlo model of the Proteus®One system.

5.2 Experimental validation of the Monte Carlo Proteus One model.

In this section, we validate the Proteus®One model developed previously by comparison with experimental data. To ensure correct properties of the beam reaching the patient, different Beam Profile Monitors (BPMs) placed along the beamline are used (P1E, P1G, P2G, P3G). Each one consists of an assembly of horizontal and vertical electric wires as we can observe in figure 5.11. When the proton beam interacts with the BPMs, it produces an electric signal proportional to the number of protons passing through the detector.

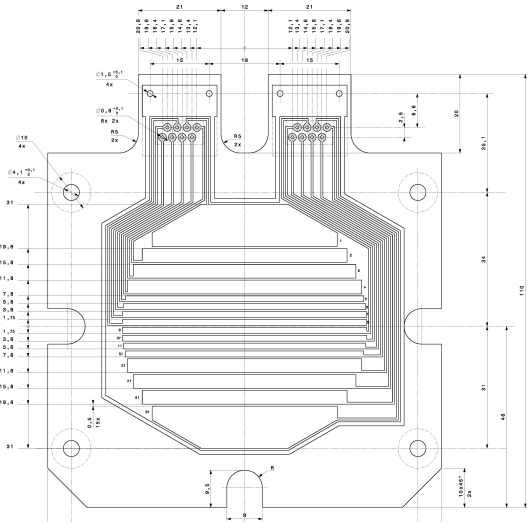

Figure 5.11: Technical drawing of a Beam Profile Monitor (BPM). Courtesy of IBA.

Along the beamline, five BPM (in green in figure 5.12) are available to monitor the beam. Four slits as well as the collimator (in orange in figure 5.12) control the spatial and energetic extension of the beam.

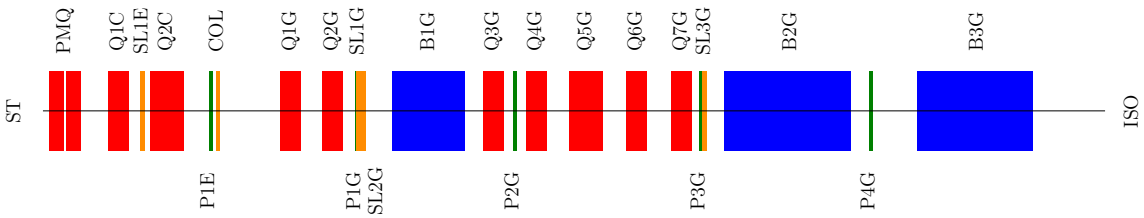

Figure 5.12: Position of the different BPM along the beamline. The quadrupoles are illustrated in red and the dipoles in blue.

Unlike the degrader, the slits do not interact with the entire beam but remove its halo. Two types of slits are used to control the behaviour of the beam:

1. Divergence slits (SL1E, SL1G, SL2G): These slits are positioned at locations where the beam size is important. Therefore, by inspecting figures 5.9a and 5.9b, we find these slits between quadrupoles Q1C and Q2C (SL1E for horizontal plane) and before the entrance of the bending magnet B1G (SL1G and SL2G for both planes).

2. Momentum slits (SL3G): We have seen in section 3.2.4.2 that the momentum spread of the beam induces a dependence between the bending angle and the energy of the particle. The momentum slits are used to remove protons with an incorrect energy. To maximize the effectiveness of the momentum slits, they are placed where the beam size is small and the dispersion function is maximum, *e.g* after Q7G (see figure 5.10).

The slits opening is a function of the energy at the isocenter and for each slit in the beamline, the relation between the aperture and the transmitted energy is shown in figure 5.13.

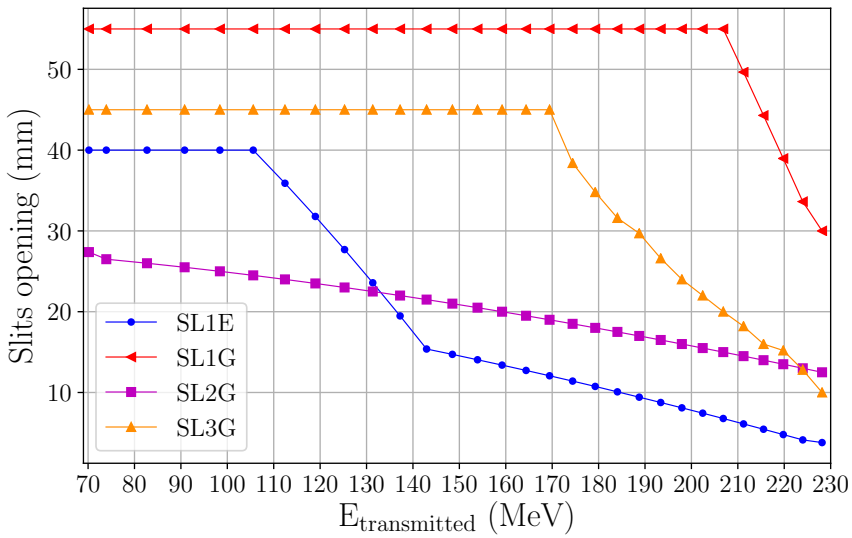

Figure 5.13: Opening of the slits as a function of the energy at the isocenter.

The experimental data have been taken in Proteus®One systems currently in operation. Two sets of data are available, the first one is a measurement on the BPMs for 6 different energies (70, 112, 148.5, 180, 200 and 226 MeV) and for 7 gantry rotation angles (0°, 30°, 60°, 90°, 120°, 150°, 180°). The second set of data is a measurement of the beamline efficiency.

BPM measurements

We present in this section, the results in P1G, P2G and P3G (see figure 5.12) for 112, 180 and 226 MeV and a gantry rotation of 0°. The results are similar for the other energies and rotation angles. For each BPM, the beam profile along the horizontal and the vertical directions is measured. The obtained results are presented in figure 5.14 for the horizontal plane and in figure 5.15 for the vertical plane. The red line corresponds to the experimental data and the blue line to the results obtained with our model.

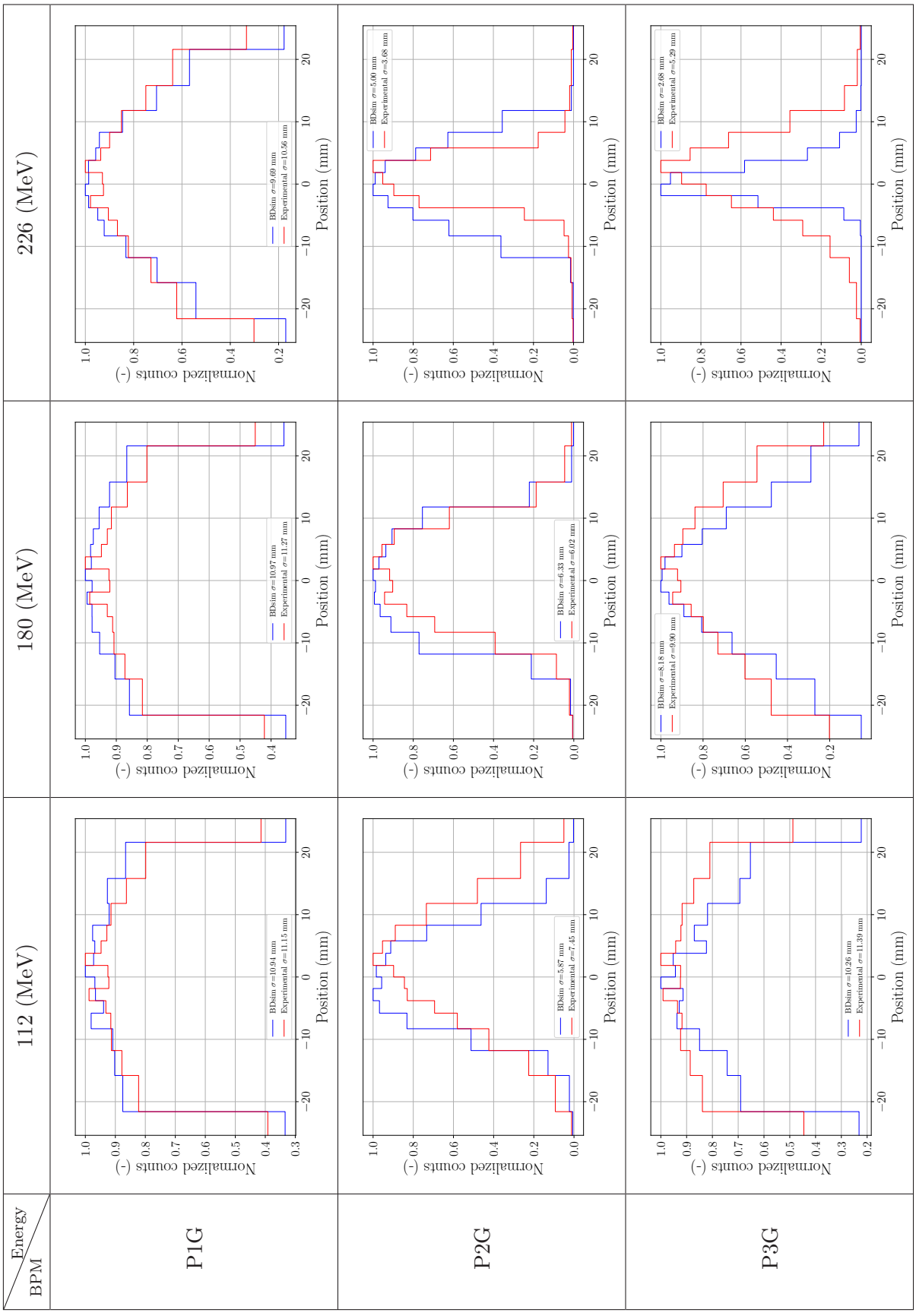

Figure 5.14: Comparison between the Proteus® One model made with BDSIM and experimental results for the horizontal plane.

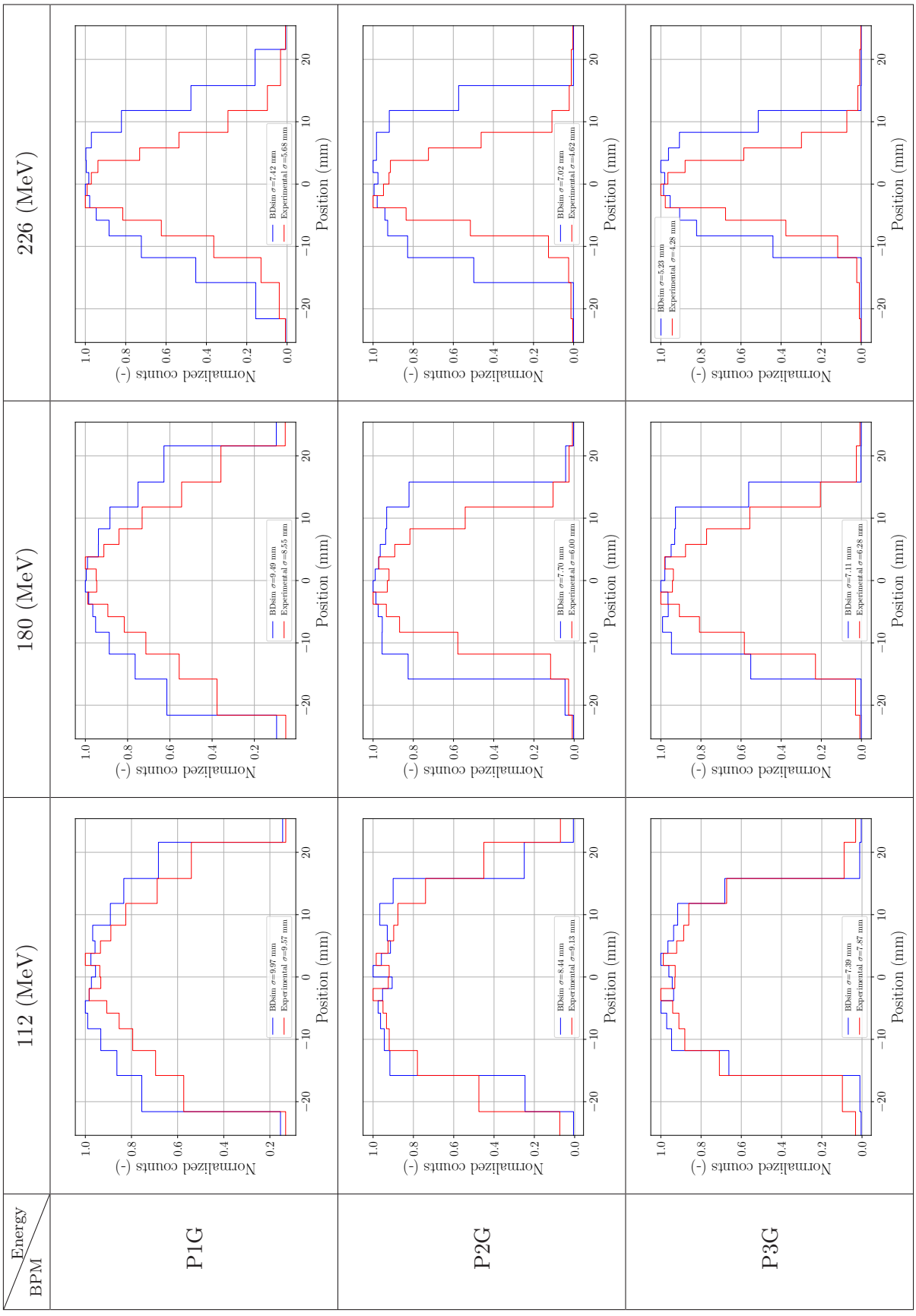

Figure 5.15: Comparison between the Proteus® One model made with BDSIM and experimental results for the vertical plane.

We observe an excellent agreement between our model and the experimental values. Table 5.3 summarizes the values of the experimental standard deviation as well as the one obtained with BDSIM.

BPM	Energy (MeV)	σ_x (exp.)	σ_x (BDSIM)	σ_y (exp.)	σ_y (BDSIM)
P1G	226	10.55	9.69	5.68	7.41
P1G	200	11.22	10.89	7.83	9.03
P1G	180	11.26	10.96	8.54	9.48
P1G	148.5	11.24	10.98	9.05	9.89
P1G	112	11.15	10.94	9.56	9.97
P1G	70	11.14	11.02	9.15	9.51
P2G	226	3.68	4.99	4.62	7.018
P2G	200	5.69	6.27	5.33	7.39
P2G	180	6.02	6.32	5.99	7.69
P2G	148.5	6.47	6.18	7.26	8.06
P2G	112	7.44	5.87	9.12	8.43
P2G	70	9.83	5.79	9.46	8.49
P3G	226	5.29	2.67	4.28	5.22
P3G	200	8.46	6.62	5.19	6.42
P3G	180	9.89	8.18	6.28	7.11
P3G	148.5	10.90	9.32	7.43	7.36
P3G	112	11.38	10.26	7.86	7.38
P3G	70	11.57	10.85	7.92	7.22

Table 5.3: Experimental values of the standard deviation and results obtained with BDSIM.

For each BPM and each gantry rotation angle, we compute the relative error over the standard deviation:

$$\eta = \frac{\sigma_{exp} - \sigma_{bdsim}}{\sigma_{exp}} \tag{5.10}$$

We show in figure 5.16, the histogram of η for the measurements along the horizontal plane and the vertical plane.

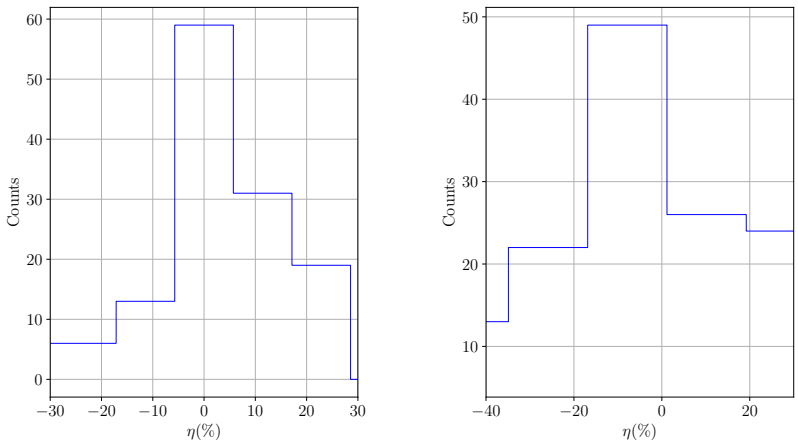

(a) Horizontal plane. *(b) Vertical plane.*

Figure 5.16: Histogram of the relative error for η.

Even though the number of experimental data is important, the histogram has a poor statistic. The average difference between sigma values is 6% for the horizontal plane and 1.2% for the vertical plane which is a relatively small error. Consequently, we consider that our model is valid. However, to obtain better statistics, experiments and simulations should be performed by varying the strength of quadrupoles to have a variation of the beam size in each BPM.

Beamline efficiency

For this second set of data, we compare the transmission of the beamline at the isocenter. In figure 5.17, we compare the beamline efficiency measured experimentally with our model results. We note that our model slightly underestimates the total transmission but shows a trend analogous to experimental results.

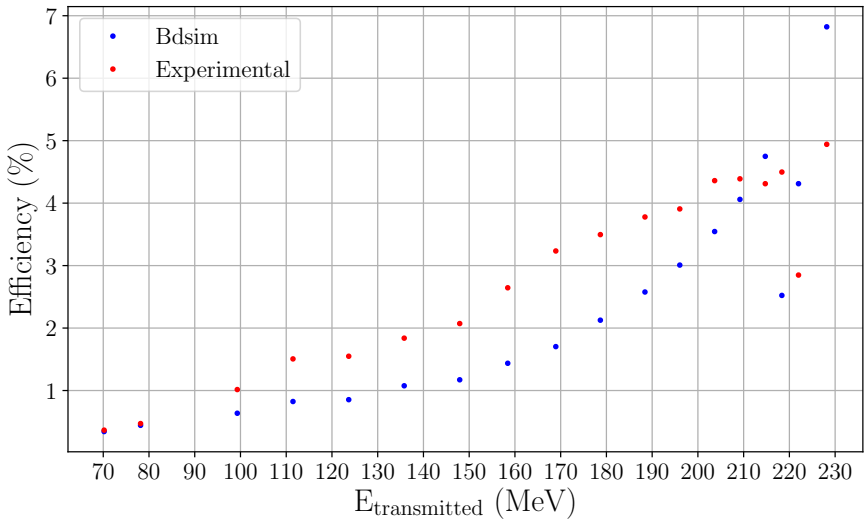

Figure 5.17: Comparison between the experimental efficiency and the efficiency computed with BDSIM for the beamline transmission.

5.3 Conclusion

In this chapter, we have developed a Monte Carlo model of a Proteus®One system. We first detailed the various components of this system. We also introduced the requirements for a medical gantry and we explained the importance of the double waist on the energy degrader to minimize the emittance. The beam size in the beamline has been computed using Manzoni, MAD-X and BDSIM and show similar results for the three softwares.

Finally, the obtained model was validated by comparison with experimental data, namely with measurements at the BPM and measurements of beamline transmission. This comparison showed that the developed model is suitable to characterize the properties of the beam at any location of the beamline. It is also possible to determine the types of secondary particles generated during interactions between protons and components of the beamline, especially the degrader, the slits, the quadrupoles and the dipoles.

Therefore, it is possible to conduct complete radiation protection studies, especially by generating ambient dose maps, or as we will see in the next chapter, to calculate the activation of concrete shielding.

Chapter 6

BDSIM model for the activation of a Proteus One system

Contents

In this last chapter, we use the model described in chapter 5 to first validate the neutron-equivalent source approximation (see section 2.2.1) and second to compare the results for the production of ^{152}Eu and ^{22}Na between this complete model and the simplified model discussed in chapter 2, hereinafter referred to as *Geant4*. Therefore, we add to the beamline described in the previous chapter, the different shielding walls (see section 2.4.1). Finally, we present 2D maps with the locations of the proton and neutron interactions. The final model of the Proteus®One system is shown in figure 6.1. The different elements used to guide and modulate the beam are in red and black. The patient is represented in blue. The accelerator is not modelled but the characteristics of the extracted beam (see section 5.1.1) are used as input.

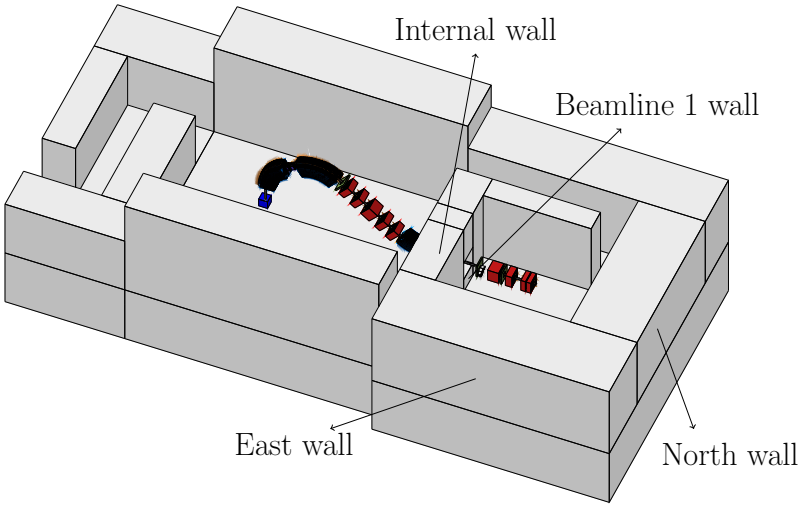

Figure 6.1: BDSIM model of the Proteus® One.

6.1 Validation of the neutron-equivalent source method

In chapter 2, we have assumed that protons were lost in some specific locations. In this section, we will compare these results with our model. We show, in figure 6.2, the beam losses and the transmission obtained along the beam line for a transmitted energy of 70 and 230MeV. The different elements refer to the dipoles (B), the quadrupoles (Q), the slits (SL), the degrader (P1E) and the BPMs (P). More details can be found in chapter 5. The major contributors to the activation are the extraction quadrupoles (Q1C and Q2C), the degrader (P1E) and the collimator (COL).

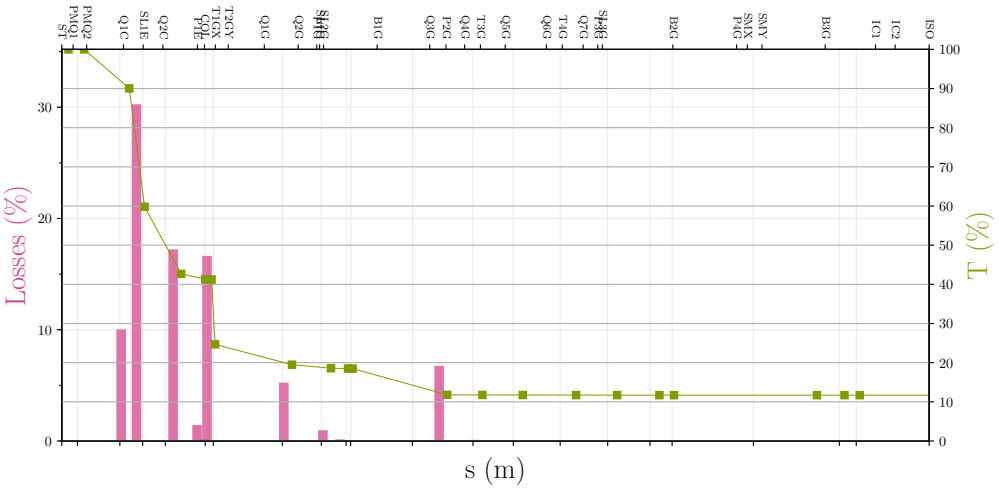

(a) 230 MeV

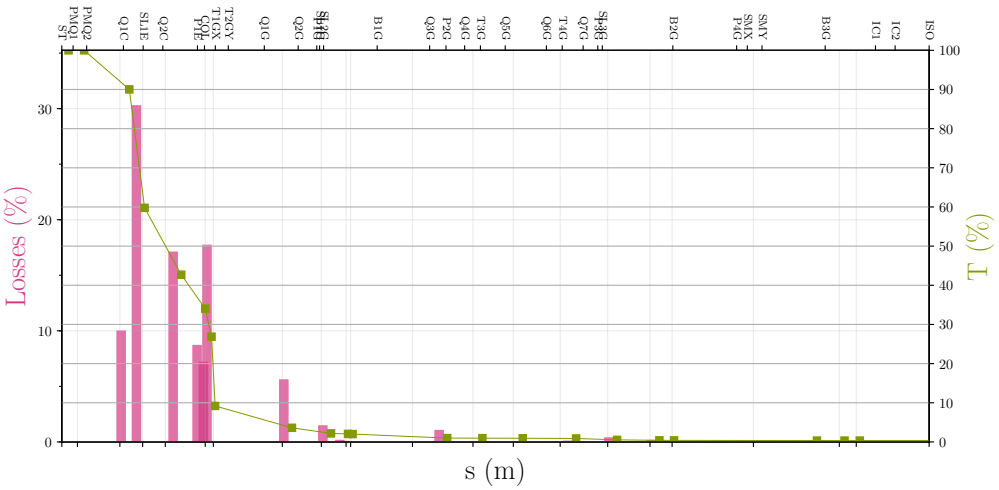

(b) 70 MeV

Figure 6.2: Beam losses along the beam line. The green curve shows the beamline transmission. The pink bars illustrate the loss locations.

We observe that the locations where the majority of the beam is lost correspond to the predictions made in section 2.4.2.

In table 6.1, we summarize the beam losses at different locations for different energies: the extraction quadrupoles (Q1C and Q2C), the degrader and the collimator. The values

between *Geant4* and BDSIM are compared for each element. The beamline efficiency is also specified for both models.

Energy (MeV)	Beam losses (%)								Efficiency (%)	
	Q1C		Q2C		Degrader		Collimator			
	Geant4	BDSIM	*Geant4*	BDSIM	*Geant4*	BDSIM	*Geant4*	BDSIM	*Geant4*	BDSIM
70	4.02	9.98	14.01	17.06	34.4	39.77	41.69	18.97	0.21	0.39
86	4.08	9.98	14.04	16.98	33.73	37.26	42.93	18.86	0.27	0.49
116	4.07	9.98	14.07	17.203	29.16	31.86	44.66	18.46	0.8	0.95
160	4.07	9.99	13.98	17.06	17.67	19.35	48.19	19.79	1.82	1.86
200	4.05	9.99	14.02	17.03	8.88	10.9	44.02	17.71	4.96	4.68
228.15	4.04	9.98	13.99	17.07	0	1.4	36.32	16.60	12.07	11.7

*Table 6.1: Beam loss comparison for different transmitted energies between the estimation of chapter 2.4.2 (*Geant4*) and the complete model (BDSIM).*

Except for the first quadrupole (Q1C) and the collimator, the results are in excellent agreement. Therefore, we can expect to obtain the same results as those presented in section 2.4.2, but with a different amplitude. We suspect that the beam emittance at the exit of the S2C2 and the beamline optics are different between both models which implies beam loss variations. Indeed, the values used in chapter 2 were obtained from estimation before knowing the extracted beam properties [121].

We also note that a significant part of the beam is lost in the drift between Q1C and SL1E (about 30%) but the thickness of the pipe is too small (3mm) to generate secondary neutrons and therefore do not contribute to the activation of the shielding. Indeed, the neutron production cross section of 230 MeV proton in iron is equal to 1.94 barn [52], which corresponds to a mean-free path (distance between two interactions) equal to 6 cm. However, it can be interesting to limit these losses in order to increase the total transmission efficiency.

6.2 Evaluation of the concrete shielding activation of a Proteus One using BDSIM

In this section, we use BDSIM in a single-pass simulation to evaluate the concrete shielding activation as we have done in chapter 2. The accelerator is not modelled with BDSIM but all other radiation sources are taken into account.

The geometry of the wall is discretised in cubes (see figure 6.3). The cells are defined by a unique number called below *Cell Id*. In each cell, we compute the relation for the reaction rate per proton (see equation (2.3)).

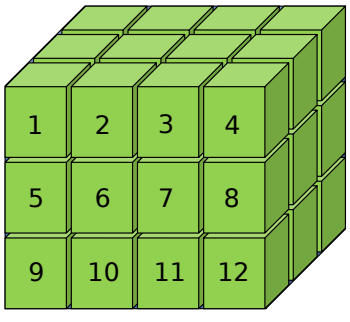

Figure 6.3: Position of detectors in the wall.

We show, in figure 6.4, 6.5, 6.6 and 6.7, the reaction rate per proton for ^{22}Na and ^{152}Eu for different shielding walls with BDSIM (in blue) and *Geant4* (in red). These results are obtained for a transmitted energy of 160 MeV. The trend is similar for the other energies. The horizontal axis corresponds to the *Cell Id* inside the wall.

As expected, we find the same trend for the reaction rate but with a different amplitude which is mainly explained by the fact that the collimator losses are lower with the complete model than with the neutron-equivalent method (see table 6.1). The discontinuities are due to the change of layer for the cubes inside the wall.

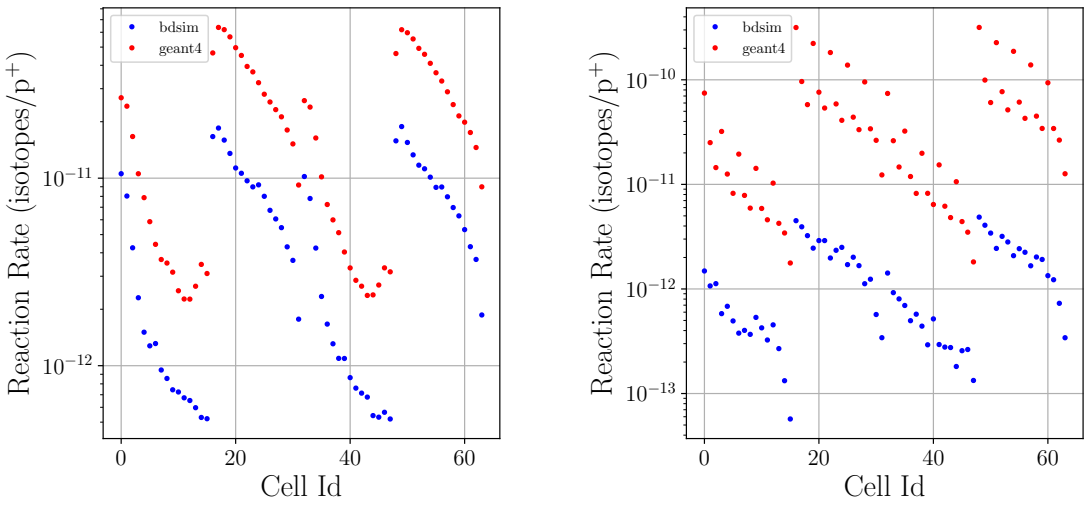

(a) ^{152}Eu (b) ^{22}Na

Figure 6.4: Results for the beamline1 wall

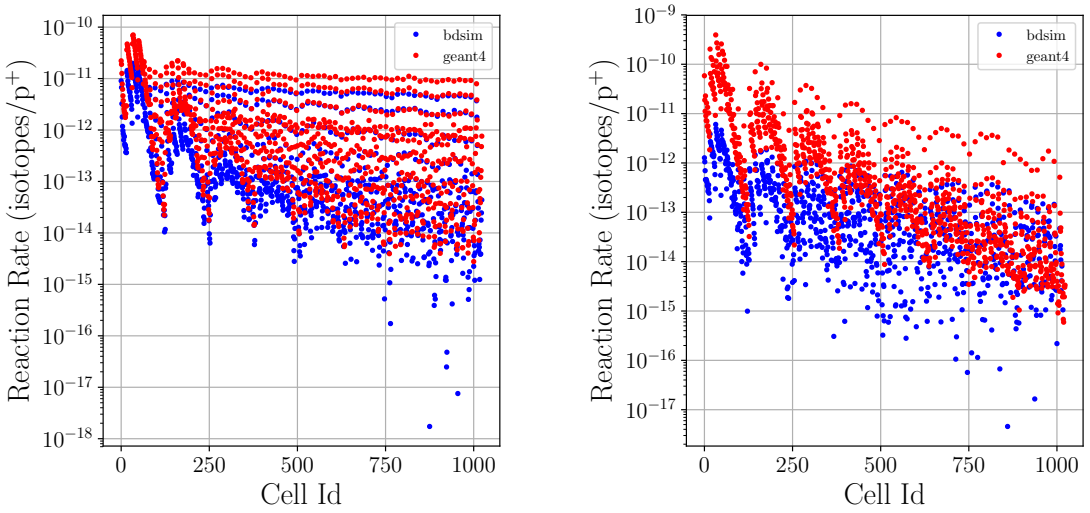

(a) ^{152}Eu (b) ^{22}Na

Figure 6.5: Results for the internal wall

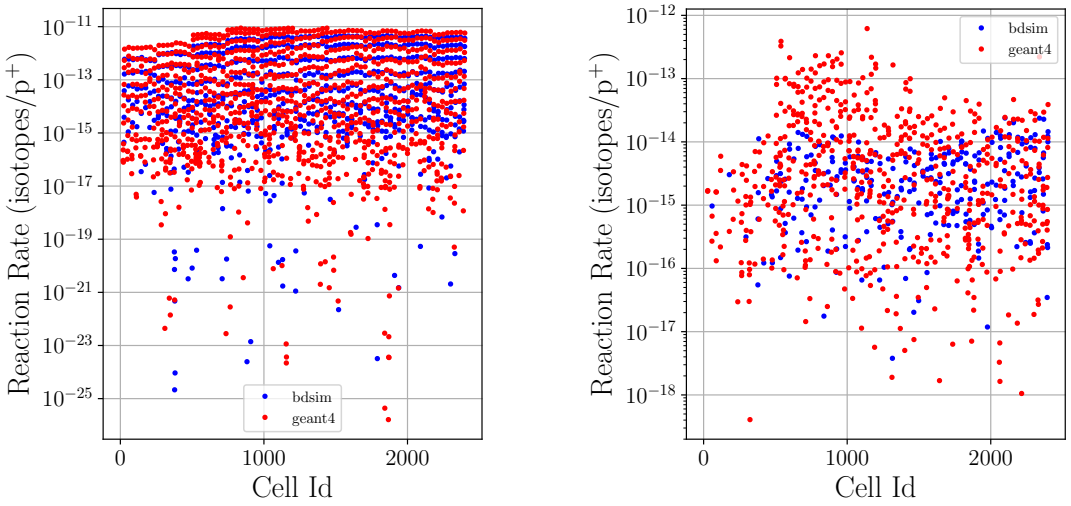

(a) ^{152}Eu (b) ^{22}Na

Figure 6.6: Results for the north wall

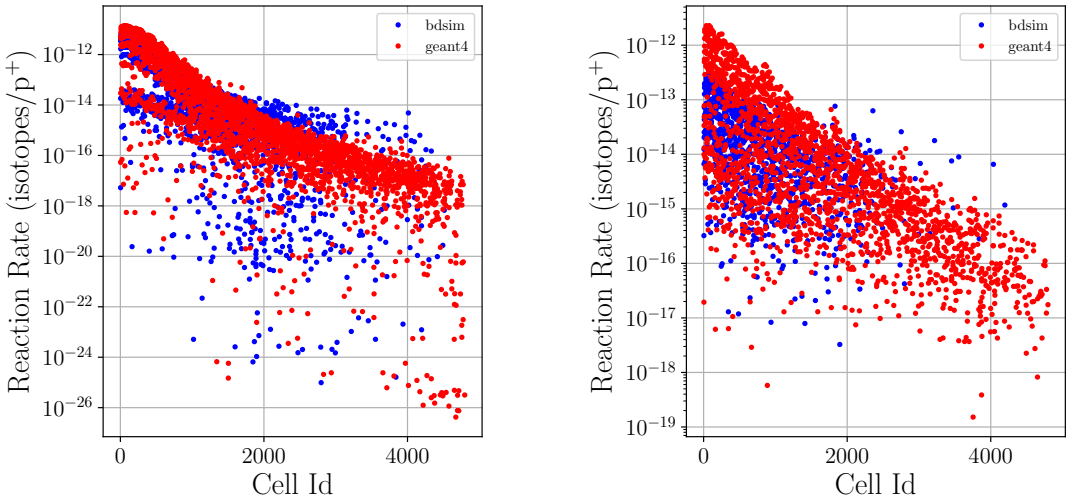

(a) ^{152}Eu (b) ^{22}Na

Figure 6.7: Results for the east wall

Results obtained for the north wall for the ^{22}Na must be put into perspective. Indeed, the ^{22}Na is created by high energy neutrons, which as we saw in chapter 1, are emitted mainly in the direction of the incident beam. As the north wall is located in the opposite direction to the beam propagation, the obtained results are essentially statistical fluctuations.

In figure 6.8, we show the histogram of the ratio between the reaction rates obtained with *Geant4* and BDSIM for each radionuclide.

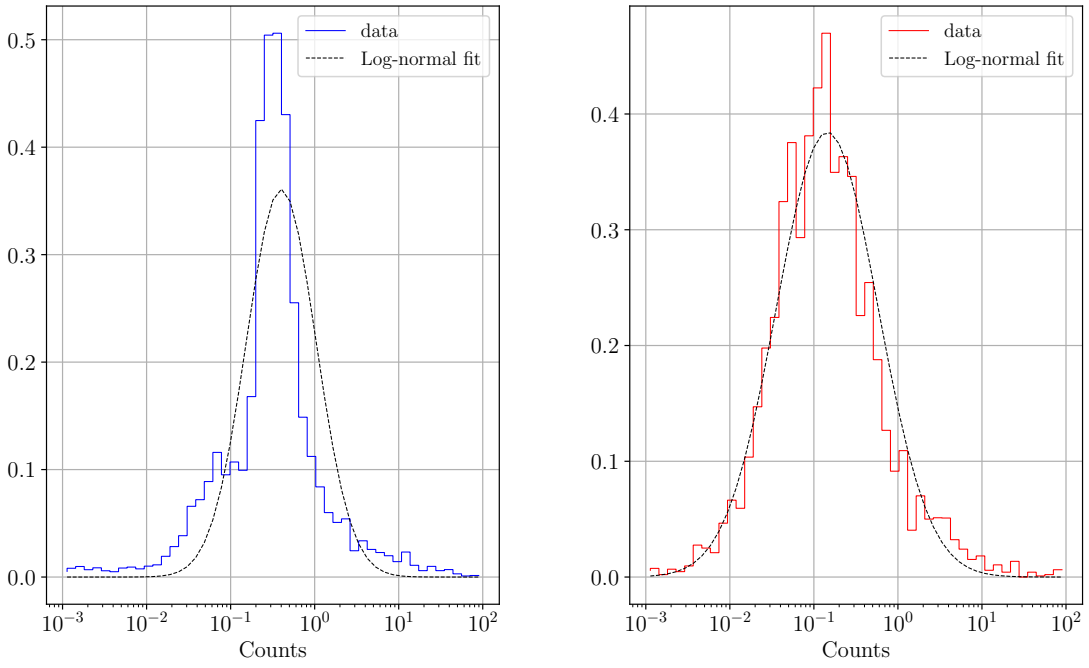

(a) ^{152}Eu. *(b)* ^{22}Na.

Figure 6.8: Histogram of the ratio of the reaction rate for both radionuclides. The dashed line is a log-normal fit over the data.

The behaviour of these curves corresponds to a log-normal distribution, represented by the black dashed lines. From this distribution, we compute the mode of, which represents the global maximum of the distribution. We find a value of 14% for the ^{22}Na and 40% for the ^{152}Eu. The value for both radionuclides is different due to the production method: spallation for ^{22}Na and neutronic capture for ^{152}Eu. These values of the mode are explained by the fact that the losses are different between *Geant4* and BDSIM.

Based on the results presented in this section, we confirm that the concept of a neutron-equivalent source presented in chapter 2 is valid. Indeed, we succeed in reproducing with the BDSIM model the results obtained with this concept. The greatest advantage of the BDSIM model is that we can take into account all the specifications of the beam and the real geometry of elements in the beamline.

In the next section, we present 2D maps of proton and neutron locations of interactions for further studies.

6.3 Neutron and proton maps in a Proteus One system

We use our model to irradiate the patient with a 160 MeV proton beam and we consider 10^6 protons as input beam. In figure 6.9, we illustrate the locations of proton interactions in a Proteus®One system. We use a color scale from yellow (few interactions) to red/dark (many interactions). We obviously have many interactions close to the quadrupoles, the degrader and the collimator. We notice few losses in the beam pipe and we observe the Bragg peak inside the patient (see zoom in figure 6.9).

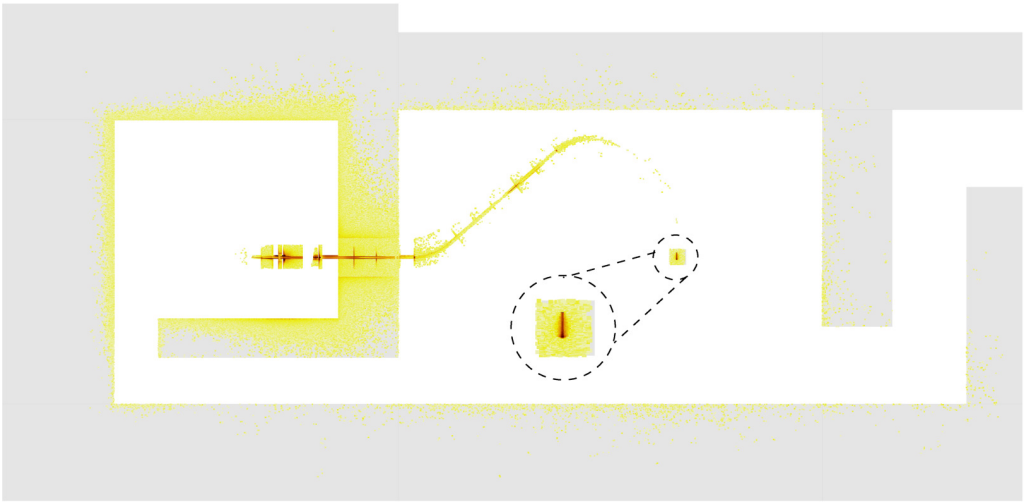

Figure 6.9: Locations of proton interactions. A lot of interactions is represented in red/-dark and few interactions in yellow.

In figure 6.10, we represent the 2D map for neutron interactions. The lighter colors represent the areas with a high number of interactions. This is an illustration of our concept of neutron-equivalent sources. The light places correspond to the location of the extraction quadrupoles, the degrader and the collimator. We also observe that the most irradiated walls are in the direction of the beam (see table 2.12).

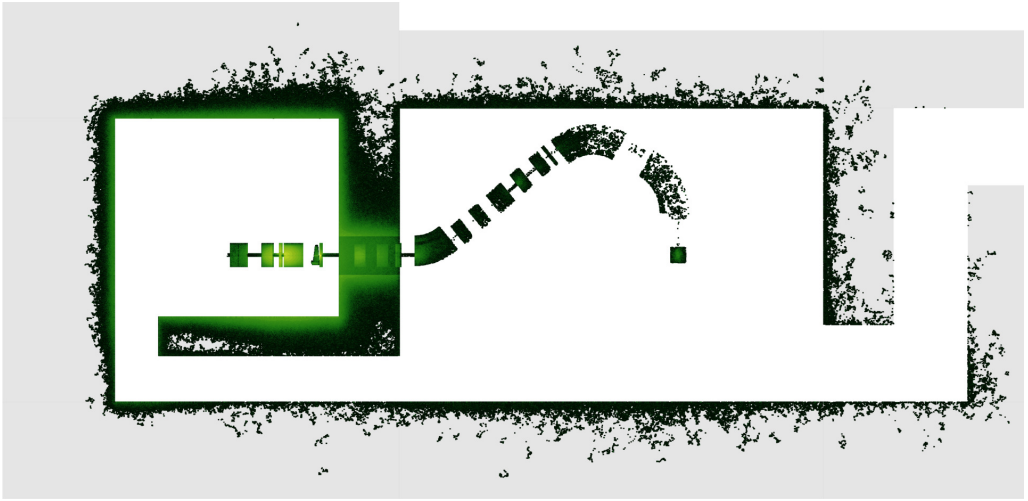

Figure 6.10: Locations of neutron interactions. A lot of interactions are represented in light green and a few interactions in black.

Finally, figures 6.9 and 6.10 are superimposed to obtain figure 6.11. This representation can be used to accurately determine the most irradiated areas and generate ambient dose maps. Moreover, we can use this figure to determinate the appropriate location for experimental measurements.

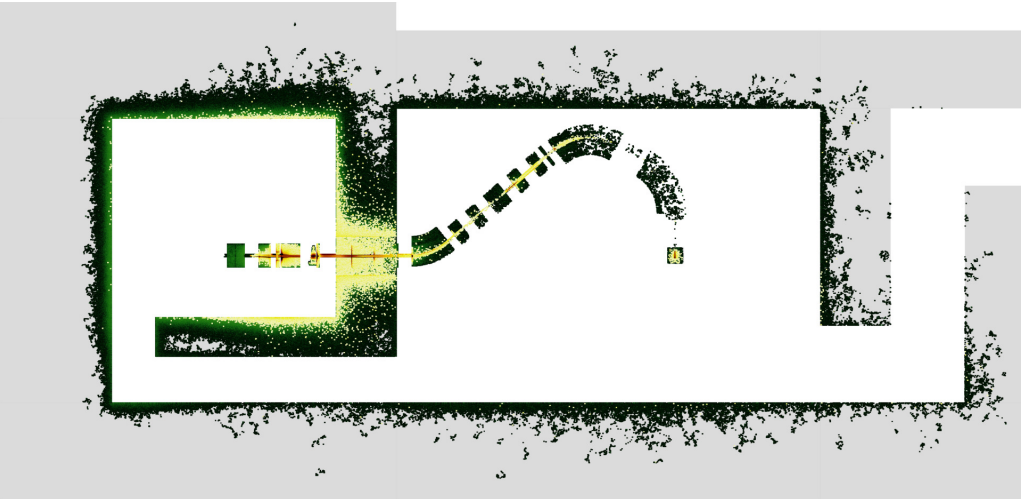

Figure 6.11: Locations of neutron and proton interactions.

6.4 Conclusion

The first section of this chapter constituted a validation of the neutron-equivalent sources introduced in chapter 2. We have shown that the locations of the losses and the beamline efficiency are consistent with those estimated previously. However, the amplitude of the losses are different for the collimator. Indeed, we have also shown that a non-negligible quantity of protons are lost in the drift between Q1C and Q2C (about 30%).

The concept of equivalent-neutron source being validated, we have evaluated the production of ^{22}Na and ^{152}Eu in the concrete shielding using the BDSIM model in a single-pass simulation. We have shown that the results obtained with the two models (*Geant4* and BDSIM) have the same trend, the differences being mainly explained by the losses in the collimator. There is no high energy neutrons incident on the north wall, which explains that ^{22}Na production is underestimated. The ratio between the reaction rate obtained with *Geant4* and BDSIM for each radionuclide can be described by a log-normal distribution with a mode of 40% for ^{152}Eu and 14% for ^{22}Na.

Finally, we have presented maps with the locations of proton and neutron interactions. These maps are useful to characterize the type of secondary radiations in the system or to determine the best locations for measurements of the ambient dose.

Conclusion

Proton therapy is increasingly used for cancer treatment. In the future, up to 20% of cancer patients could benefit from this efficient technique. The use of pencil beam scanning, a few millimeters thick beam with a high degree of precision limiting the exposure of healthy tissues, has shown encouraging clinical benefits. Therefore, the number of sites under construction is increasing. These new centers need an adequate concrete shielding to limit exposure of the surrounding people to the secondary radiations. A portion of this shielding will be activated and should be treated as a nuclear waste. Computational methods and Monte Carlo codes are essential to accurately estimate the impacts of the radiations on the system.

The aim of this thesis was threefold: first to quantitatively estimate the proportion of radioactive concrete created when operating a proton therapy center, second to investigate new possibilities to improve the system and last to develop a complete Monte Carlo model of the *IBA* compact proton therapy system (Proteus®One) taking into account the beam transport and its interactions with matter.

The interactions which produce radionuclides, resulting in the activation of the shielding, are the spallation reaction and the neutronic capture. The spallation induces the emission of high energy neutrons in the direction of the incident beam and the isotropic emission of low energy neutrons which will be captured in the shielding. High energy neutrons interact with the concrete by spallation. This chain reaction ends when all secondary particles are absorbed. Furthermore, during elastic and inelastic reactions, protons lose their energy and are deviated degrading the emittance of the beam. These phenomena are characterized by the Stopping and the Scattering Power. All these interactions are implemented in Monte Carlo software used in this work to determine the properties of the system.

To evaluate the quantity of nuclear wastes, the equivalent-neutron source method has been introduced to replace the proton beam/target model by a punctual neutron source with the same characteristics. This reduces the relative error on the activation rate while keeping the same computation time. The hadronic models of *Geant4* (Bertini, BIC and INCL) are validated for activation studies and compared with *MCNPX* and *Phits*. The results obtained for the neutronic capture are in good agreement for all softwares. We show that for the spallation reactions, the BIC model gives the largest values of activity concentration while Bertini underestimates the production of radionuclides due to its low cross section isotope production. To be conservative, the BIC model is used in this thesis. We model the Proteus®One system with *Geant4*. The major radiation sources in the beamline, i.e the accelerator, the degrader, the collimator, the extraction quadrupoles and the patient, are replaced by neutron-equivalent sources. We obtain that 30% of the concrete shielding is activated after 20 years of operation. The treatment

room is not activated at all contrarily to the vault where a part of each wall has to be removed. This corresponds approximately to 130 m^3 of nuclear waste, a significant quantity to manage during the decommissioning of the treatment center. This value is slightly higher than the value estimated by *IBA*, mainly due to the selected hadronic model which tends to overestimate the activity concentration. Two solutions are highlighted to reduce this quantity in the future: the utilization of concrete without impurities (low activation concrete) and the adaptation of the degrader design, which causes the majority of the losses. This modification implies a complete study of the beamline optics.

In this work, we focus our attention on the second solution. We propose a new degrader design with insertable diamond cylinders allowing rapid variations of the beam energy and giving better emittance and transmission properties. A complete study of the *IBA* degrader, made of wedge shaped slabs of materials wrapped around a rotating wheel, has been performed to determine the emittance as a function of the transmitted energy. The performances of different materials (beryllium, graphite, aluminium, boron carbide and diamond) as energy degrader have been evaluated with *Geant4*. The diamond improves the performance of a 30% decrease in emittance at low energy compared to beryllium. To obtain these results, a method to restore the Gaussian distribution of the beam, i.e separate the nuclear halo contribution from the core, is introduced to compare results obtained with *Geant4* and analytical models (Gottschalk and Farley).

As the degrader has an impact on the beam emittance, the beamline optics will be also impacted. Therefore a Monte Carlo model of the Proteus®One has been developed. The development of a single-pass simulation considering both the beam transport and the beam matter interactions allows the study of the complete Proteus®One center at the system level. The beam propagation along the beamline is performed using electromagnetic fields. The different elements present in the system (drifts, dipoles and quadrupoles) guide the beam to the patient. The impact of each of these elements is described by a transfer matrix in the beam transport and modelling codes. The codes MAD-X, Manzoni and BDSIM are compared in this thesis and give similar results. This 3D model contributes to the knowledge of the beam properties and losses inside the beamline. It is validated with experimental data and the concept of neutron-equivalent source is verified. The results show that the agreement is excellent, the overestimation of the losses is highlighted by the fact that BDSIM shows an activation lower than the results taking into account source terms, for the same current of protons. This model is also able to generate 2D maps showing the location of the proton and neutron interactions. These maps are essential to determine the type of radiations in the system and can be used to optimally position a detector or compute ambient dose maps. The capability of BDSIM for low energy machines have been demonstrated and can be used for many medical applications [167].

Among all possible future developments, the two main important ones are: the experimental validation of the diamond degrader and the shielding of superconducting magnets.

The performance of the diamond degrader has been shown but to ensure a medical utilization further feasibility studies must be performed. An experimental device should be developed to validate the predictions of chapter 4.

In order to make the proton therapy more affordable to a greater number of patients, it is necessary to reduce the cost of the gantry [168, 169]. A potential solution is the use of superconducting magnets. Indeed, they allow a size reduction due to a lower bend radius (higher magnetic field) and a weight reduction. However, protection systems are required

to avoid quenching, i.e a transition of the whole superconducting coil towards a normal conducting state due to temperature increase caused by particles losses [170]. For each magnet, the quenching limit, *i.e* the maximum amount of energy which can be deposited locally in the superconducting magnet has to be determined. Therefore, after designing and optimizing the beamline with Manzoni, the gantry can be modelled using BDSIM. This model allows to determine the locations of the interactions inside the magnet and some protections can be placed at the correct position.

References

[1] Institut Jules Bordet. Last consulation: 04/08/2018. URL: https://www.bordet.be/fr/radiotherapie.

[2] Ion Beam Applications. *Donner du sens à l'innovation*. 2016.

[3] O. Gencel et al. "An investigation on the concrete properties containing colemanite". In: *International Journal of Physical Sciences* 5.3 (2010), pp. 216–225.

[4] A. Samarin. "Use of Concrete as a Biological Shield from Ionising Radiation". In: *Energy and Environmental Engineering* 1.2 (2013), pp. 90–97. DOI: 10.13189/eee.2013.010208.

[5] K. Masaaki et al. "Activation Reduction Method for a Concrete Wall in a Cyclotron Vault". In: *J Radiat Prot Res* 42.3 (2017), pp. 141–145. DOI: 10.14407/jrpr.2017.42.3.141.

[6] *Application of the Concepts of Exclusion, Exemption and Clearance*. International Atomic Energy Agency. 2004.

[7] T. Vanhaudenhove. "Shielding Study against High-Energy Neutrons produced in a Proton Therapy Facility by means of Monte Carlo Codes and On-Site Measurements". PhD thesis. Université Libre de Bruxelles (ULB), 2014.

[8] D. Satoh et al. "Shielding study at the Fukui Prefectural Hospital Proton Therapy Center". In: *Journal of Nuclear Science and Technology* 49.11 (2012), pp. 1097–1109. DOI: 10.1080/00223131.2012.730900.

[9] S. Agosteo. "Radiation protection constraints for use of proton and ion accelerators in medicine". In: *Radiation Protection Dosimetry* 137.1-2 (2009), pp. 167–186. DOI: 10.1093/rpd/ncp187.

[10] S. Agosteo. "Radiation Protection at Medical Accelerators". In: *Radiation Protection Dosimetry* 96.4 (2001), pp. 393–406. DOI: 10.1093/oxfordjournals.rpd.a006627.

[11] S. Burnham. "Radiation resistant concrete for applications in nuclear power and radioactive waste industries". PhD thesis. University of Utah, 2014.

[12] J. Ahmedin et al. "Cancer Statistics". In: *A Cancer Journal for Clinicians* 58.2 (2008), pp. 71–96. DOI: 10.3322/CA.2007.0010.

[13] World Health Organization. *Cancer Country Profiles*. 2014. URL: http://www.who.int/cancer/country-profiles/en/.

[14] A. Allen et al. "An evidence based review of proton beam therapy: The report of ASTRO's emerging technology committee". In: *Radiotherapy and Oncology* 103.1 (2012), pp. 8 –11. DOI: 10.1016/j.radonc.2012.02.001.

[15] N. Mendenhall et al. "Early Outcomes From Three Prospective Trials of Image-Guided Proton Therapy for Prostate Cancer". In: *International Journal of Radiation Oncology*Biology*Physics* 82.1 (2012), pp. 213 –221. DOI: 10.1016/j.ijrobp.2010.09.024.

[16] B. Hoppe et al. "Involved-Node Proton Therapy in Combined Modality Therapy for Hodgkin Lymphoma: Results of a Phase 2 Study". In: *Int. J. Radiat. Oncol. Biol. Phys.* 89.5 (2014), pp. 1053 –1059. DOI: 10.1016/j.ijrobp.2014.04.029.

[17] G. Mondlane et al. "Comparative study of the calculated risk of radiation-induced cancer after photon- and proton-beam based radiosurgery of liver metastases". In: *Physica Medica* 42 (2017), pp. 263 –270. DOI: 10.1016/j.ejmp.2017.03.019.

[18] B. Eaton et al. "Secondary Malignancy Risk Following Proton Radiation Therapy". In: *Front. Oncol.* 5 (2015), p. 261. DOI: 10.3389/fonc.2015.00261.

[19] R. Srivastava et al. "Neutron Therapy-A Novel Approach To Radiotherapeutics: A Review". In: *International Journal of Contemporary Medical Research* 1.2 (2014), pp. 61–70.

[20] B. Marchand et al. "Iba Proton Pencil Beam Scanning: an Innovative Solution for Cancer Treatment". In: *European Particle Accelerator Conference (EPAC)*. 2000.

[21] Hanne M. Kooy et al. "A Case Study in Proton Pencil-Beam Scanning Delivery". In: *International Journal of Radiation Oncology*Biology*Physics* 76.2 (2010), pp. 624 –630. ISSN: 0360-3016. DOI: https://doi.org/10.1016/j.ijrobp.2009.06.065. URL: http://www.sciencedirect.com/science/article/pii/S0360301609010116.

[22] M. Moteabbed et al. "Impact of Spot Size and Beam-Shaping Devices on the Treatment Plan Quality for Pencil Beam Scanning Proton Therapy". In: *International Journal of Radiation Oncology* 95.1 (2016), pp. 190 –198. DOI: 10.1016/j.ijrobp.2015.12.368.

[23] F. Stichelbaut. *Development of Low-Activation Concrete for the Proteus® One System*. Tech. rep. 50897. Ion Beam Applications, 2016.

[24] J-C. David et al. "Benchmark of Spallation Models". In: *Progress in Nuclear Science and Technology* 2 (2011), pp. 942–947. DOI: 10.15669/pnst.2.942.

[25] C. Cohen-Tannoudji, B. Diu, and F. Laloë. *Mécanique quantique*. Vol. 2. Hermann, 2007. ISBN: 2705661212.

[26] M. Enferadi et al. "Nuclear reaction cross sections for proton therapy applications". In: *J. Radioanal. Nucl. Chem.* 314.2 (2017), pp. 1207–1235. DOI: 10.1007/s10967-017-5503-8.

[27] H. Barschall et al. "Nuclear Data for Neutron and Proton Radiotherapy and for Radiation Protection". In: *Journal of the International Commission on Radiation Units and Measurements* 32.2 (2000). DOI: 10.1093/jicru/os32.2.Report63.

[28] Nuclear Power. "Definition of Cross-section". Website. 2018. URL: https://www.nuclear-power.net/neutron-cross-section/.

[29] H. Nikjoo, S. Uehara, and D. Emfietzoglou. *Interaction of radiation with matter*. CRC Press, 2012. ISBN: 9781439853573.

[30] L. Landau and E. Lifshitz. "Mechanics". In: 3rd ed. Vol. 1. Elsevier Science, 1982. Chap. 4, p. 49. ISBN: 9780080503479.

[31] K. Snieder and S. John. "Time-reversed imaging as a diagnostic of wave and particle chaos". In: *Physical Review E* 58.5 (1998), pp. 5668–5675. DOI: 10.1103/physreve.58.5668.

[32] H. Paganetti, ed. *Proton Therapy Physics*. CRC Press, 2016. ISBN: 9781439836453.

[33] W. Newhauser and R. Zhang. "The physics of proton therapy". In: *Physics in Medicine & Biology* 60.8 (2015), R155–R209. DOI: 10.1088/0031-9155/60/8/r155.

[34] S.M Seltzer. *An Assessment of the Role of Charged Secondaries from Nonelastic Nuclear Interactions by Therapy Proton Beams in Water*. NIST, 1993.

[35] B. Gottschalk. *Passive Beam Spreading in Proton Radiation Therapy*. Tech. rep. Harvard High Energy Physics Laboratory, 2004. URL: https://gray.mgh.harvard.edu/attachments/article/212/pbs.pdf.

[36] F.H Attix. *Introduction to Radiological Physics and Radiation Dosimetry*. Wiley, 2008. ISBN: 9783527617142.

[37] M. Boschini et al. "Nuclear and Non-Ionizing Energy-Loss for Coulomb Scattered Particles from Low Energy up to Relativistic Regime in Space Radiation Environment". In: *Cosmic Rays for Particle and Astroparticle Physics*. World Scientific, 2011, pp. 9–23. DOI: 10.1142/9789814329033_0002.

[38] M. Berger et al. *Stopping Power and Range Tables for Electrons, Protons, and Helium Ions*. Tech. rep. National Institute of Standards and Technology - NIST, Physical Measurement Laboratory, 2011. URL: http://www.nist.gov.

[39] F. Padilla-Cabal, D. Georg, and H. Fuchs. "A pencil beam algorithm for magnetic resonance image-guided proton therapy". In: *Med. Phys.* 45.5 (2018), pp. 2195–2204. DOI: 10.1002/mp.12854. eprint: https://aapm.onlinelibrary.wiley.com/doi/pdf/10.1002/mp.12854.

[40] R. Zhang and W. Newhauser. "Calculation of water equivalent thickness of materials of arbitrary density, elemental composition and thickness in proton beam irradiation". In: *Physics in Medicine & Biology* 54.6 (2009), p. 1383.

[41] W. Newhauser and R. Zhang. "The physics of proton therapy". In: *Physics in Medicine & Biology* 60.8 (2015), pp. 155–209. DOI: 10.1088/0031-9155/60/8/r155.

[42] T. Bortfeld and W. Schlegel. "An analytical approximation of depth - dose distributions for therapeutic proton beams". In: *Physics in Medicine and Biology* 41.8 (1996), pp. 1331–1339.

[43] D. Jette and W. Chen. "Creating a spread-out Bragg peak in proton beams". In: *Phys. Med. Biol* 56.11 (2011), pp. 131–138. DOI: 10.1088/0031-9155/56/11/N01.

[44] Sh. Keshazare, SF. Masoudi, and FS. Rasouli. "Effects of Defining Realistic Compositions of the Ocular Melanoma on Proton Therapy". In: *Journal of biomedical physics & engineering* 4 (2014), pp. 141–50.

[45] H. Bethe. "Molière's Theory of Multiple Scattering". In: *Phys. Rev.* 89 (6 1953), pp. 1256–1266. DOI: 10.1103/PhysRev.89.1256.

[46] B. Gottschalk et al. "Multiple Coulomb scattering of 160 MeV protons". In: *Nucl. Instrum. Methods Phys. Res., Sect. B* 74.4 (1993), pp. 467 –490. DOI: 10.1016/0168-583X(93)95944-Z.

[47] N. Kanematsu. "Alternative scattering power for Gaussian beam model of heavy charged particles". In: *Nucl. Instrum. Methods Phys. Res., Sect. B* 266.23 (2008), pp. 5056 –5062. DOI: https://doi.org/10.1016/j.nimb.2008.09.004.

[48] F. Farley. "Optimum strategy for energy degraders and ionization cooling". In: *Nucl. Instrum. Methods Phys. Res., Sect. A* 540.2 (2005), pp. 235 –244. DOI: https://doi.org/10.1016/j.nima.2004.11.034.

[49] S. Tavernier. "Interactions of Particles in Matter". In: *Experimental Techniques in Nuclear and Particle Physics*. Springer, 2010. Chap. 2, pp. 23–53. ISBN: 978-3-642-00829-0. DOI: 10.1007/978-3-642-00829-0_2.

[50] V. Vsevolod and V.Balashov. *Interaction of Particles and Radiation with Matter*. Springer Berlin Heidelberg, 2011. ISBN: 9783642643835.

[51] "Passive Nondestructive Assay of Nuclear Materials". In: ed. by D. Reilly, N.Ensslin, and H.Smith. The Commission, 1991. Chap. 12, p. 357.

[52] M.B. Chadwick et al. "ENDF/B-VII.1 Nuclear Data for Science and Technology: Cross Sections, Covariances, Fission Product Yields and Decay Data". In: *Nuclear Data Sheets* 112.12 (2011), pp. 2887 –2996. DOI: 10.1016/j.nds.2011.11.002.

[53] I. Lux and L. Koblinger. *Monte Carlo Particle Transport Methods: Neutron and Photon Calculations*. CRC Press, 1991. ISBN: 9780849360749.

[54] E.E. Lewis and W.F. Miller. *Computational Methods of Neutron Transportation*. American Nuclear Society, 1984.

[55] A Letourneau et al. "Neutron production in bombardments of thin and thick W, Hg, Pb targets by 0.4, 0.8, 1.2, 1.8 and 2.5 GeV protons". In: *Nucl. Instrum. Methods Phys. Res., Sect. B* 170.3 (2000), pp. 299 –322. DOI: 10.1016/S0168-583X(00)00259-7.

[56] R. Serber. "Nuclear Reactions at High Energies". In: *Phys. Rev.* 72 (11 1947), pp. 1114–1115. DOI: 10.1103/PhysRev.72.1114.

[57] M.K. Hossain, M.A. Taher, and M.K.Das. "Understanding Accelerator Driven System (ADS) Based Green Nuclear Energy". In: *World Journal of Nuclear Science and Technology* 5 (2015), pp. 287–302. DOI: 10.4236/wjnst.2015.54028.

[58] M. M. Meier et al. "Differential Neutron Production Cross Sections and Neutron Yields from Stopping-Length Targets for 113-MeV Protons". In: *Nuclear Science and Engineering* 102.3 (1989), pp. 310–321. DOI: 10.13182/NSE89-A27480. eprint: https://doi.org/10.13182/NSE89-A27480.

[59] A. Heikkinen, N. Stepanov, and J.P. Wellisch. "Bertini intranuclear cascade implementation in GEANT4". In: *Computing in High Energy and Nuclear Physics* (2003). arXiv: nucl-th/0306008 [nucl-th].

[60] H.W Bertini. "Monte Carlo calculations on intranuclear cascades". PhD thesis. University of Michigan, 1963. URL: https://hdl.handle.net/2027/mdp.39015077306606.

[61] D.H. Wright and M.H. Kelsey. "The Geant4 Bertini Cascade". In: *Nucl. Instrum. Methods Phys. Res., Sect. A* 804.Supplement C (2015), pp. 175 –188. DOI: 10.1016/j.nima.2015.09.058.

[62] G. Folger, V. Ivanchenko, and J.P. Wellisch. "The Binary Cascade". In: *The European Physical Journal A - Hadrons and Nuclei* 21.3 (2004), pp. 407–417. DOI: 10.1140/epja/i2003-10219-7.

[63] A. Boudard et al. "Intranuclear cascade model for a comprehensive description of spallation reaction data". In: *Physical Review C* 66.4 (2002), p. 044615. DOI: 10.1103/physrevc.66.044615.

[64] P. Henrotte. "Extension du modèle de cascade intranucléaire pour les réactions de spallation". PhD thesis. Université de Liège, 2005.

[65] A. Iljinov, M. Kazarnovsky, and E. Paryev. *Intermediate-Energy Nuclear Physics*. CRC Press, 2017. ISBN: 9781315894706.

[66] J. Cugnon and P Henrotte. "The low-energy limit of validity of the intranuclear cascade model". In: *The European Physical Journal A - Hadrons and Nuclei* 16.3 (2003), pp. 393–407. DOI: 10.1140/epja/i2002-10096-6.

[67] J. Cugnon. "A Short Introduction to Spallation Reactions". In: *Few-Body Systems* 53.1 (2012), pp. 143–149. ISSN: 1432-5411. DOI: 10.1007/s00601-011-0249-2.

[68] C. Grégoire et al. "Semi-classical dynamics of heavy-ion reactions". In: *Nuclear Physics A* 465.2 (1987), pp. 317 –338. DOI: 10.1016/0375-9474(87)90437-4.

[69] A. Lejeune et al. "Hot nuclear matter in an extended Brueckner approach". In: *Nucl. Phys. A* 453.2 (1986), pp. 189 –219. DOI: 10.1016/0375-9474(86)90010-2.

[70] A. Bohnet et al. "Quantum molecular-dynamics approach to heavy-ion collisions with Brueckner G-matrix cross sections". In: *Nuclear Physics A* 494.2 (1989), pp. 349 –364. DOI: 10.1016/0375-9474(89)90028-6.

[71] M. Baldo et al. "Brueckner G matrix for a planar slab of nuclear matter". In: *Physics of Atomic Nuclei* 64.2 (2001), pp. 203–227. ISSN: 1562-692X. DOI: 10.1134/1.1349442.

[72] V. Bunakov and G. Matvejev. "The physical and mathematical foundations of the intranuclear cascade model algorithm". In: *Zeitschrift für Physik A Atoms and Nuclei* 322.3 (1985), pp. 511–521. DOI: 10.1007/bf01412089.

[73] D. Filges and F. Goldenbaum. "The Intranuclear Cascade Models". In: *Handbook of Spallation Research*. Wiley-Blackwell, 2010. Chap. 2, pp. 63–133. ISBN: 9783527628865. DOI: 10.1002/9783527628865.ch2. eprint: https://onlinelibrary.wiley.com/doi/pdf/10.1002/9783527628865.ch2.

[74] H. Bertini. "Low-Energy Intranuclear Cascade Calculation". In: *Phys. Rev.* 131 (4 1963), pp. 1801–1821. DOI: 10.1103/PhysRev.131.1801.

[75] J. Letaw, R. Silberberg, and C. Tsao. "Proton-nucleus total inelastic cross-sections: an empirical formula for E> 10 MeV". In: *The Astrophysical Journal* 51 (1983), pp. 271–275. DOI: 10.1086/190849.

[76] S. Pearlstein. "Medium-energy nuclear data libraries. A case study, neutron and proton induced reactions in Fe-56". In: *The Astrophysical Journal* 346 (1989), pp. 1049–1060. DOI: 10.1086/168089.

[77] V. Flaminio et al. *Compilation of cross-sections III: p and $\bar{p}$ induced reactions*. Research rep. 84-01. CERN-HERA, 1984.

[78] P.Ogden et al. "$\pi - p$ Elastic Scattering in the Energy Range 300-700 MeV". In: *Phys. Rev.* 137 (1965), B1115–B1125. DOI: 10.1103/PhysRev.137.B1115.

[79] M. Bleicher et al. "Relativistic hadron-hadron collisions in the ultra-relativistic quantum molecular dynamics model". In: *J. Phys. G: Nucl. Part. Phys.* 25.9 (1999), p. 1859.

[80] K. Niita et al. "Analysis of the (N,xN') reactions by quantum molecular dynamics plus statistical decay model". In: *Phys. Rev. C* 52 (5 1995), pp. 2620–2635. DOI: 10.1103/PhysRevC.52.2620.

[81] C. Patrignani and Particle Data Group. "Review of Particle Physics". In: *Chin. Phys. C* 40.10 (2016), p. 100001. DOI: 10.1088/1674-1137/40/10/100001.

[82] S. Pedoux. "Extension of the Liège Intranuclear Cascade Model to the 2-15 GeV Incident Energy Range". PhD thesis. Université de Liège, 2012.

[83] T. Gorbinet. "Etude des réactions de spallation $^{136}Xe + p$ et $^{136}Xe +^{12} C$ a $1GeV$ par nucléon auprès de l'accélérateur GSI". PhD thesis. Université Paris-Sud XI, 2011. URL: https://tel.archives-ouvertes.fr/tel-00660583.

[84] D. Mancusi et al. "Extension of the Liège intranuclear-cascade model to reactions induced by light nuclei". In: *Phys. Rev. C* 90 (5 2014), p. 054602. DOI: 10.1103/PhysRevC.90.054602.

[85] A. Boudard and J. Cugnon. "INCL4: Intra Nuclear Cascade of Liege". In: *Joint ICTP-IAEA Advanced Workshop on Model Codes for Spallation Reactions*. 2008, pp. 29–50. URL: https://www-nds.iaea.org/spallations/2008ws/boudard.pdf.

[86] J. Cugnon, C. Volant, and S. Vuillier. "Improved intranuclear cascade model for nucleon-nucleus interactions". In: *Nuclear Physics A* 620.4 (1997), pp. 475–509. DOI: 10.1016/s0375-9474(97)00186-3.

[87] R. Chasman. "Calculations in Nuclear Evaporation Theory". In: *Phys. Rev.* 122 (1961), pp. 902–907. DOI: 10.1103/PhysRev.122.902.

[88] J. Benlliure. "Spallation Reactions in Applied and Fundamental Research". In: *The Euroschool Lectures on Physics with Exotic Beams, Vol. II*. Ed. by Jim Al-Khalili and Ernst Roeckl. Berlin, Heidelberg: Springer Berlin Heidelberg, 2006. Chap. 5, pp. 191–238. ISBN: 978-3-540-33787-4. DOI: 10.1007/3-540-33787-3_5.

[89] H.Mitler. "Particle Evaporation from Excited Nuclei". In: *SAO Special Report* 204 (1966).

[90] N. Metropolis and S. Ulam. "The Monte Carlo Method". In: *Journal of the American Statistical Association* 44.247 (1949), pp. 335–341.

[91] T. Sato et al. "Particle and Heavy Ion Transport code System, PHITS, version 2.52". In: *Journal of Nuclear Science and Technology* 50.9 (2013), pp. 913–923. DOI: 10.1080/00223131.2013.814553.

[92] D. Pelowitz. MCNPX *2.6 manual*. Los Alamos National Laboratory. 2008.

[93] S. Agostinelli et al. "GEANT4: A Simulation toolkit". In: *Nucl. Instrum. Methods Phys. Res., Sect. A* 506.3 (2003), pp. 250–303. DOI: 10.1016/S0168-9002(03)01368-8.

[94] J. Allison et al. "Recent developments in Geant4". In: *Nucl. Instrum. Methods Phys. Res., Sect. A* 835.Supplement C (2016), pp. 186 –225. DOI: https://doi.org/10.1016/j.nima.2016.06.125.

[95] J. Allison et al. "Geant4 developments and applications". In: *IEEE Transactions on Nuclear Science* 53.1 (2006), pp. 270–278. DOI: 10.1109/TNS.2006.869826.

[96] E. Seravalli et al. "Monte Carlo calculations of positron emitter yields in proton radiotherapy". In: *Physics in Medicine & Biology* 57.6 (2012), 1659–1673. DOI: 10.1088/0031-9155/57/6/1659.

[97] A. Ferrari et al. *FLUKA: a multi-particle transport code*. CERN, 2005.

[98] R. Chytracek et al. "Geometry Description Markup Language for Physics Simulation and Analysis Applications". In: *IEEE Trans. Nucl. Sci.* 53.5 (2006), pp. 2892–2896. DOI: 10.1109/TNS.2006.881062.

[99] R. Brun and F. Rademakers. "ROOT — An object oriented data analysis framework". In: *Nucl. Instrum. Methods Phys. Res., Sect. A* 389.1 (1997). New Computing Techniques in Physics Research V, pp. 81 –86. DOI: doi.org/10.1016/S0168-9002(97)00048-X.

[100] M. Chadwick et al. "Cross-Section Evaluations to 150 MeV for Accelerator-Driven Systems and Implementation in MCNPX". In: *Nucl. Sci. Eng.* 131.131 (1999), pp. 293–328.

[101] H. Iwase, K. Niita, and T. Nakamura. "Development of General-Purpose Particle and Heavy Ion Transport Monte Carlo Code". In: *J. Nucl. Sci. Technol.* 39.11 (2002), pp. 1142–1151. DOI: 10.3327/jnst.39.1142.

[102] M. Uddin et al. "Measurements of neutron induced activation of concrete at 64.5MeV". In: *Ann. Nucl. Energy* 36.8 (2009), pp. 1133 –1137. DOI: 10.1016/j.anucene.2009.04.014.

[103] H. Patterson and R. Thomas. "Accelerator Health Physics". In: Academic Press, 1973. Chap. 6, p. 329. ISBN: 9780125471503.

[104] A. Ferrari, M. Ferrarini, and M. Pelliccioni. "Secondary particle yields from 400 MeV/u carbon ion and 250 MeV proton beams incident on thick targets". In: *Nuclear Instruments and Methods in Physics Research Section B: Beam Interactions with Materials and Atoms* 269.13 (2011), pp. 1474 –1481. DOI: 10.1016/j.nimb.2011.04.003.

[105] International Atomic Energy Agency. *The Statute of the IAEA*. https://www.iaea.org/about/statute. Last consultation 29/07/2018.

[106] R. Williams, C. Gesh, and R. Pagh. *Compendium of Material Composition Data for Radiation Transport Modeling*. Tech. rep. PNNL-15870. Pacific Northwest National Laboratory, 2006. DOI: 10.2172/902408.

[107] A. Suzuki et al. "Trace Elements with Large Activation Cross Section in Concrete Materials in Japan". In: *J. Nucl. Sci. Technol.* 38.7 (2001), pp. 542–550. DOI: 10.1080/18811248.2001.9715065.

[108] L.R Carroll. "Predicting long-lived, Neutron-induced activation of concrete in a cyclotron vault". In: *AIP Conference Proceedings* 576.1 (2001), pp. 301–304. DOI: 10.1063/1.1395309.

[109] ICRP. "The 2007 Recommendations of the International Commission on Radiological Protection". In: *Ann. ICRP* (2007).

[110] W. Dunn and J. Shultis. "The Fundamentals of Neutral Particle Transport". In: *Exploring Monte Carlo Methods*. Elsevier, 2012. Chap. 9, pp. 235 –267. ISBN: 978-0-444-51575-9. DOI: 10.1016/B978-0-444-51575-9.00009-9.

[111] V. Balashov. *Interaction of Particles and Radiation with Matter*. Springer, 1997. ISBN: 978-3-642-64383-5.

[112] A.J. Koning and D. Rochman. "Modern Nuclear Data Evaluation with the TALYS Code System". In: *Nuclear Data Sheets* 113.12 (2012), pp. 2841 –2934. DOI: 10.1016/j.nds.2012.11.002.

[113] J-C. David. "Spallation reactions: A successful interplay between modeling and applications". In: *The European Physical Journal A* 51.6 (2015), p. 68. DOI: 10.1140/epja/i2015-15068-1.

[114] F. Stichelbaut. *Rhodotron TT300-HE Tests in CM8*. Tech. rep. 72654. Ion Beam Applications, 2018.

[115] L. Jägerhofer et al. "A Shielding Concept for the MedAustron Facility". In: *EPJ Web Conf.* 153 (2017), p. 04006. DOI: 10.1051/epjconf/201715304006.

[116] T. Vanaudenhove et al. "Monte Carlo calculations with MCNPX and GEANT4 for general shielding study : Application to a proton therapy center". In: *Progress in Nuclear Science and Technology* 4 (2014), pp. 422–426. DOI: 10.15669/pnst.4.422.

[117] R. Tesse et al. "GEANT4 benchmark with MCNPX and PHITS for activation of concrete". In: *Nucl. Instrum. Methods Phys. Res., Sect. B* 416 (2018), pp. 68 –72. DOI: 10.1016/j.nimb.2017.12.006.

[118] F. Paolo La Torre. "Study of induced radioactivity in proton accelerator facilities". PhD thesis. Universität Bern, 2014.

[119] B. Cassart. *Introduction to ESBTS*. Tech. rep. 33634. Ion Beam Applications, 2012.

[120] F.Stichelbaut. Private communication. 2015.

[121] F. Stichelbaut. *Radiation Sources in the Proteus® One System*. Tech. rep. 36694. Ion Beam Applications, 2014.

[122] F. Stichelbaut. *Concrete Activation in Proteus® Plus System*. Tech. rep. 39132. Ion Beam Applications, 2013.

[123] R. Doyen. *CGTR: Beam losses*. Tech. rep. 29358. Ion Beam Applications, 2011.

[124] *Quatrième rapport d'inventaire des passifs nucléaires de l'ONDRAF à sa tutelle (période 2013–2017)*. NIROND 2017-01 F. 2018. URL: https://www.ondraf.be/.

[125] Præstegaard et al. "Low-activation concrete design of the Danish Center for Particle Therapy". In: *Particle Therapy Co-operative Group*. 2016.

[126] F. Stichelbaut. "Development of low-activation concrete for medical accelerators". In: *ARIA-17 Workshop*. 2017.

[127] M. Kumagai et al. "Activation Reduction Method for a Concrete Wall in a Cyclotron Vault". In: *Journal of Radiation Protection and Research* 42.3 (2017), pp. 141–145. DOI: 10.14407/jrpr.2017.42.3.141.

[128] S. Bumham. "Radiation Resistant Concrete for Applications in Nuclear Power and Radioactive Waste Industries". MA thesis. University of Utah, 2014.

[129] H. Goldstein. *Classical Mechanic*. Addison Wesley, 1980. ISBN: 9780201029697.

[130] J. Rees. *Symplecticity in Beam Dynamics: An Introduction*. Tech. rep. 9939. Standford Linear Accelerator, 2003.

[131] H. Grote et al. *The MAD-X program*. CERN.

[132] S.Y. Lee. *Accelerator Physics*. World Scientific, 2012. ISBN: 9789814374941.

[133] C. Pozrikidis. *Introduction to Theoretical and Computational Fluid Dynamics*. Oxford University Press, 2011. ISBN: 9780199909124.

[134] A. Streun. *The simplified Hamiltonian for transverse beam dynamics*. Paul Scherrer Institute. Oct. 2010. URL: https://ados.web.psi.ch/empp-streun/hamilton.pdf.

[135] J. Bengstsson. *The sextupole scheme for the Swiss Light Source (SLS) : An analytical approach*. Tech. rep. SLS Note 9/97. Paul Scherrer Institut, 1997. URL: https://ados.web.psi.ch/slsnotes/sls0997.pdf.

[136] P. Baudrenghien. "Low-level RF - Part I: Longitudinal dynamics and beam-based loops in synchrotrons". In: *CERN Yellow Report* 007 (2011), pp. 341–367.

[137] S. Humphries. *Principles of charged particle acceleration*. Wiley-interscience publications. J. Wiley, 1986. ISBN: 9780471878780.

[138] S. Sgobba. "Physics and measurements of magnetic materials". In: *CERN* 004 (2010), pp. 39–63.

[139] E. Poncelet. *S2C2 Synchrocyclotron: Training manual*. Tech. rep. 35979. Ion Beam Applications, 2014.

[140] A. Guyette. *FMECA S2C2 Extraction System*. Tech. rep. 39938. Ion Beam Applications, 2014.

[141] Helmut Wiedemann. *Particle Accelerator Physics*. eng. Springer Berlin Heidelberg, 2007. ISBN: 3540490434.

[142] BDSIM Collaboration. *BDSIM Documentation*. 2018.

[143] M. Rhee and R. Schneider. "The root-mean-square emittance of an axisymmetric beam with a Maxwellian velocity distribution." In: *Particle Accelerators* 20 (1986), pp. 133–141.

[144] C. Hernalsteens et al. "A fast tracking code for beam transport and simulation of beam-matter interactions in hadron therapy beamlines". In: *International Computational Accelerator Physics Conference*. In preparation. 2018.

[145] I. Agapov et al. "BDSIM: A particle tracking code for accelerator beam-line simulations including particle–matter interactions". In: *Nucl. Instrum. Methods Phys. Res., Sect. A* 606.3 (2009), pp. 708 –712. DOI: 10.1016/j.nima.2009.04.040.

[146] C. Hernalsteens, R. Tesse, and K. André. "Georges". In: *Software X* (2018). In preparation.

[147] F. Schmidt. "Mad-X PTC integration". In: *Particle Accelerator Conference*. 2005.

[148] D. Abell. *PTC : Library User Guide*. Tech-X Corporation. 2011. URL: https://www.txcorp.com/images/pdf/PTC-LibUG.pdf.

[149] R. Cooper and A. Harrison. "The uses and adverse effects of beryllium on health". In: *Indian J Occup Environ Med* 13.2 (2009), pp. 65–76. DOI: 10.4103/0019-5278.55122.

[150] Z. Liang et al. "Design and optimization of an energy degrader with a multi-wedge scheme based on Geant4". In: *Nucl. Instrum. Methods Phys. Res., Sect. A* 890 (2018), pp. 112 –118. DOI: 10.1016/j.nima.2018.01.073.

[151] M. van Goethem et al. "Geant4 simulations of proton beam transport through a carbon or beryllium degrader and following a beam line". In: *Phys.Med.Biol* 54.19 (2009). DOI: 10.1088/0031-9155/54/19/011.

[152] A. Gerbershagen et al. "Measurements and simulations of boron carbide as degrader material for proton therapy". In: *Phys.Med.Biol* 61.14 (2016). DOI: 10.1088/0031-9155/61/14/N337.

[153] W. Kleeven. *Innovative degrader studies: A comparisson for different degrader materials for protons and alpha*. Research rep. 61257. Ion Beam Applications, 2017.

[154] R. Tesse et al. "Numerical Simulations to Evaluate and Compare the Performances of Existing and Novel Degrader Materials for Proton Therapy". In: *International Particle Accelerator Conference*. 2018.

[155] L. Eyges. "Multiple scattering with energy loss". In: *Physical Review* 74.10 (1948), pp. 1534–1535. DOI: 10.1103/physrev.74.1534.

[156] W. Hsi et al. "Energy spectrum control for modulated proton beams". In: *Med. Phys.* 36.6 (2009), pp. 2297–2308. DOI: 10.1118/1.3132422.

[157] C. Ma and T. Lomax, eds. *Proton and Carbon Ion Therapy*. CRC Press, 2012. ISBN: 9781439816080.

[158] H. Owen et al. "Technologies for delivery of proton and ion beams for radiotherapy". In: *International Journal of Modern Physics A* 29.14 (2014), p. 1441002. DOI: 10.1142/s0217751x14410024.

[159] M. Benedikt and C. Carli. "Matching to gantries for medical synchrotrons". In: *Proceedings of the 1997 Particle Accelerator Conference*. Vol. 2. 1997, pp. 1379–1381. DOI: 10.1109/pac.1997.750699.

[160] U. Masood et al. "A light-weight compact proton gantry design with a novel dose delivery system for broad-energetic laser-accelerated beams". In: *Phys. Med. Biol.* 62.13 (2017), pp. 5531–5555. DOI: 10.1088/1361-6560/aa7124.

[161] W. Kleeven et al. "AOC, A beam dynamics design code for medical and industrial accelerators at IBA". In: *IPAC*. 2016.

[162] W. Kleeven. *AOC Version 5.23 user manual*. Ion Beam Applications. 2018.

[163] W. Kleeven and S. Zaremba. *Study of the S2C2 extracted beam optics*. Tech. rep. 34251. Ion Beam Applications, 2012.

[164] *Opera-3D Reference Manual*. Vector Fields Limited.

[165] K. André, C. Hernalsteens, and R. Tesse. *Beam dynamics studies for the IBA compact gantry: end-to-end cyclotron to isocenter simulations*. Tech. rep. 69582. Ion Beam Applications, 2018.

[166] J. van de Walle et al. "The S2C2: From source to extraction". In: *Proceedings of Cyclotrons*. 2016.

[167] W. Shields, S. Boogert, and L. Nevay. "Hadron Therapy Machine Simulations using BDSIM". In: *Proceedings of the 9th International Particle Accelerator Conference*. 2018. DOI: 10.18429/jacow-ipac2018-mopml061.

[168] A. Gerbershagen et al. "A novel beam optics concept in a particle therapy gantry utilizing the advantages of superconducting magnets". In: *Zeitschrift für Medizinische Physik* 26.3 (2016), pp. 224 –237. DOI: 10.1016/j.zemedi.2016.03.006.

[169] S. Sanfilippo et al. "Conceptual design of superconducting combined-function magnets for the next generation of beam cancer therapy gantry". In: *RuPAC*. 2016, pp. 139–141.

[170] M. Sapinski. "Quench Limits". In: *Proceedings of Chamonix 2012 workshop on LHC Performance*. 2012, pp. 121–127.

Part IV

Appendix

Appendix A

Cross section production in concrete

In this appendix, we present the cross section production of radionuclides summarized in table 2.2. The cross section is shown for each model: G4_BERT, G4_BIC and G4_INCL.

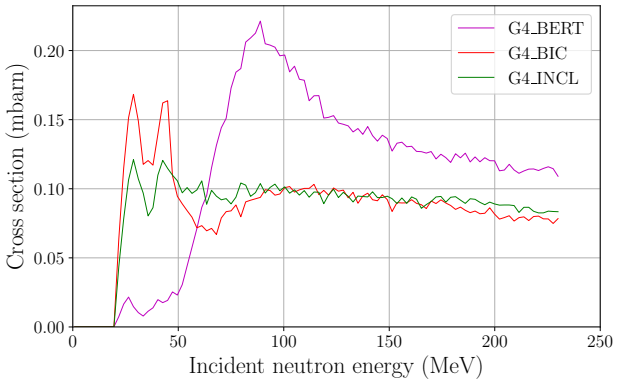

Figure A.1: Cross section production of ^{35}S

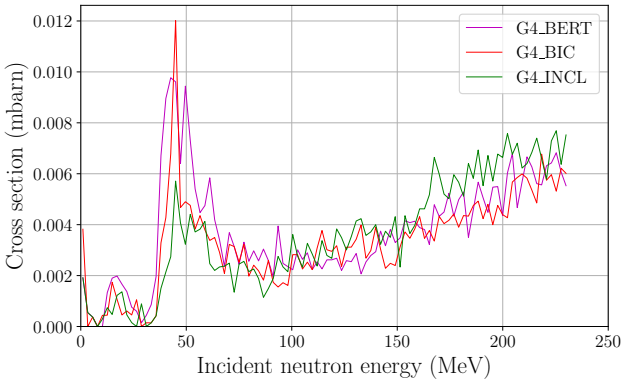

Figure A.2: Cross section production of ^{45}Ca

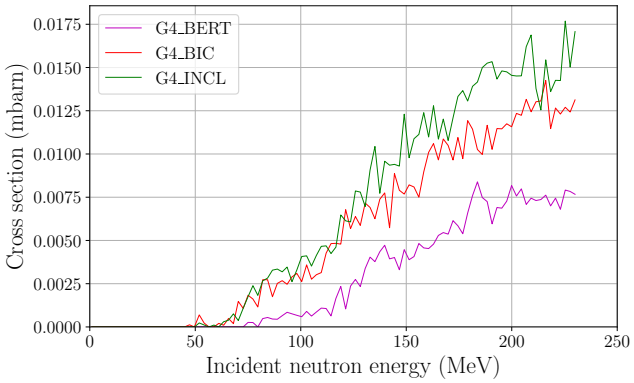

Figure A.3: Cross section production of ^{46}Sc

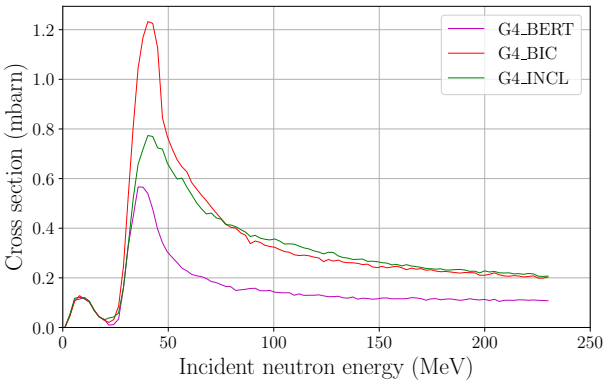

Figure A.4: Cross section production of ^{54}Mn

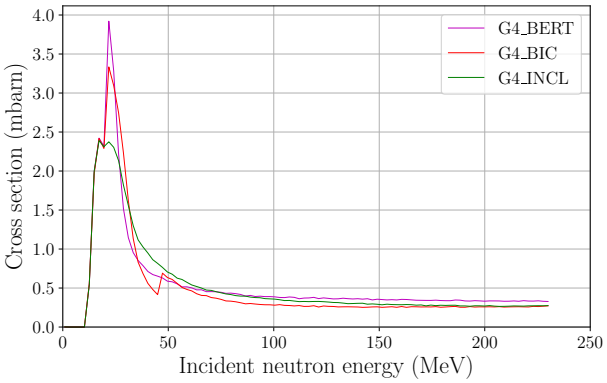

Figure A.5: Cross section production of ^{55}Fe

Appendix B

PSIsotopeProduction

```
#include "PSIsotopeProduction.hh"
#include "G4SystemOfUnits.hh"
#include "G4Track.hh"
#include "G4VSolid.hh"
#include "G4VPhysicalVolume.hh"
#include "G4VPVParameterisation.hh"
#include "G4UnitsTable.hh"
#include "Data.hh"
// Load one time table for each cpu
G4ThreadLocal G4bool PSIsotopeProduction::fLoadSpallationTable = false;
PSIsotopeProduction::PSIsotopeProduction(G4String name, G4String isotope, G4String modele ,G4int depth)
    :G4VPrimitiveScorer(name,depth),HCID(-1),EvtMap(0),weighted(true)
{
    /// Load cross section table
    G4cout << "PSIsotopeProduction::LoadTable()" <<  G4endl;
    flag_isotope = 1;
    char  spallationFilename[500];
    if(isotope == "Eu151") // Capture
    {
        CrsTable = Data::Instance()->LoadTable("CrossSection/CrossSection_Eu151.txt");
    }
    else if (isotope == "Na22") // Spallation
    {
        sprintf(spallationFilename,"CrossSection/SpallationCrossSection_Concrete_%s.txt",modele.c_str());
        CrsTable = Data::Instance()->LoadTable(spallationFilename);
        flag_isotope = 1;
    }
    else
    {
        G4String msg = "Pas d'isotope "+ isotope;
        G4Exception("PSIsotopeProduction::PSIsotopeProduction()","", FatalException,msg);
    }
    E_min = CrsTable[0][0]*MeV;
    E_max = CrsTable[CrsTable.size()-1][0]*MeV;
}
PSIsotopeProduction::~PSIsotopeProduction()
{}
/// Process the hit, get the energy, the fluence and compute cross-section
G4bool PSIsotopeProduction::ProcessHits(G4Step* aStep,G4TouchableHistory*)
{
    G4double stepLength = aStep->GetStepLength();
    G4double crs_production;
    G4double ProdRate = 0.;

    // Fluence
    if ( stepLength == 0. ) return FALSE;

    G4int idx = ((G4TouchableHistory*)(aStep->GetPreStepPoint()->GetTouchable()))->GetReplicaNumber(indexDepth);
    G4double cubicVolume = ComputeVolume(aStep, idx);
    G4double CellFlux = (stepLength / cubicVolume)*cm2;
    if (weighted) CellFlux *= aStep->GetPreStepPoint()->GetWeight();

    /// Cross section
    G4double energy = (aStep->GetPreStepPoint()->GetKineticEnergy())/MeV;
    if(energy >= E_min && energy <= E_max)
    {
        crs_production = (GetInterpCrossSection(energy))*1e-24; // barn -> cm2
    }
    else
    {
        crs_production = 0.;
    }
    ProdRate = crs_production*CellFlux;
    G4int index = GetIndex(aStep);
    EvtMap->add(index,ProdRate);
    return TRUE;
}
```

```
69 void PSIsotopeProduction::Initialize(G4HCofThisEvent* HCE)
   {
71     EvtMap = new G4THitsMap<G4double>(detector->GetName(),GetName());
       if ( HCID < 0 ) HCID = GetCollectionID(0);
73     HCE->AddHitsCollection(HCID,EvtMap);
   }
75 void PSIsotopeProduction::EndOfEvent(G4HCofThisEvent*)
   {;}
77 void PSIsotopeProduction::clear()
   { EvtMap->clear();}
79 G4double PSIsotopeProduction::ComputeVolume(G4Step* aStep, G4int idx)
   {
81     G4VPhysicalVolume* physVol = aStep->GetPreStepPoint()->GetPhysicalVolume();
       G4VPVParameterisation* physParam = physVol->GetParameterisation();
83     G4VSolid* solid = 0;
       if(physParam)
85     {
           // for parameterized volume
87         if(idx<0)
           {
89             G4ExceptionDescription ED;
               ED << "Incorrect replica number --- GetReplicaNumber : " << idx << G4endl;
91             G4Exception("G4PSCellFlux::ComputeVolume","DetPS0001",JustWarning,ED);
           }
93         solid = physParam->ComputeSolid(idx, physVol);
           solid->ComputeDimensions(physParam,idx,physVol);
95     }
       else
97     {
           // for ordinary volume
99         solid = physVol->GetLogicalVolume()->GetSolid();
       }
101    return solid->GetCubicVolume();
   }
103 G4double PSIsotopeProduction::GetInterpCrossSection(G4double E_x)
   {
105    /// Linear interpolation between energies
       int flag = 0;
107    while(CrsTable[flag][0] < E_x)
       {
109        flag ++;
       }
111    double E_a = CrsTable[flag-1][0];
       double E_b = CrsTable[flag][0];
113    double Crs_a = CrsTable[flag-1][flag_isotope];
       double Crs_b = CrsTable[flag][flag_isotope];
115    double Crs_x;
       double pente = (Crs_b-Crs_a)/(E_b-E_a);
117    Crs_x = pente*(E_x-E_a)+Crs_a;
       return Crs_x;
119 }
```

PSIsotopeProduction.cc

Appendix C

D'Alembert principle and Lagrangian equations

We consider a particle with a vector velocity $\boldsymbol{v}$ with a radius $\boldsymbol{r}$ from some given origin.

$$\boldsymbol{v} = \frac{d\boldsymbol{r}}{dt}\,. \tag{C.1}$$

We define the linear momentum $\boldsymbol{p}$ as the product of the particle mass m and its velocity.

$$\boldsymbol{p} = m\boldsymbol{v}\,. \tag{C.2}$$

The particle may suffer different external forces of various types, e.g gravitational or electrodynamics. We note $\boldsymbol{F}^{(t)}$, the total force, as the vector sum of the force exerted on the particle. The mechanics of the particle is entirely described by *Newton's second law of motion* :

$$\boldsymbol{F}^{(t)} = \frac{d\boldsymbol{p}}{dt} = \dot{\boldsymbol{p}}\,. \tag{C.3}$$

This relation can be generalized for a system with many particles and the total force can be decomposed into an external force $\boldsymbol{F}^{(e)}$ and an internal force $\boldsymbol{F}$ due to other particles in the system. Equation (C.3) for the i^{th} particle is to be written :

$$\sum_j \boldsymbol{F}_{ji} + \boldsymbol{F}_i^e = \dot{\boldsymbol{p}}_i\,, \tag{C.4}$$

where $\boldsymbol{F}_{ji}$ is the internal force on the i^{th} particle due to the j^{th} particle (we have obviously $\boldsymbol{F}_{ii} = 0$). The system motion is always limited and it is necessary to take into account the constraints which can be of different forms. However, if the condition of constraints has the form:

$$f(\boldsymbol{r_1}, \boldsymbol{r_2}, \boldsymbol{r_N}, t) = 0\,, \tag{C.5}$$

the constraints are said to be holonomic. Unfortunately, due to these constraints, the coordinates $\boldsymbol{r_i}$ are no longer independent. This problem is solved by introducing the *generalized coordinates*. In Cartesian coordinates, a system of N particles has $3N$ independent degrees of freedom. In the case of holonomic constraints, expressed in k equation of the form (C.5), we can eliminate k of the $3N$ equations to obtain $3N - k$ independent coordinates q_i. Therefore, the transformation equations that express the old coordinates $\boldsymbol{r_i}$ as a function of the new ones are of the form :

$$\boldsymbol{r_i} = \boldsymbol{r_i}\left(q_1, q_2, ..., q_{3N-k}, t\right)\,. \tag{C.6}$$

If the system is in an equilibrium state, there is no total force exerted on the i^{th} particle ($\boldsymbol{F_i^{(t)}} = 0$). Therefore, any infinitesimal displacement $\delta\boldsymbol{r_i}$ of the system gives a virtual work equal to 0.

$$\sum_i \boldsymbol{F_i^{(t)}}\,\delta\boldsymbol{r_i} = 0\,. \tag{C.7}$$

We combine equation (C.3) and (C.7) to write a condition involving the general motion of the system.

$$\sum_i \left(\boldsymbol{F_i^{(t)}} - \boldsymbol{p_i}\right)\,\delta\boldsymbol{r_i} = 0\,. \tag{C.8}$$

The force $\boldsymbol{F_i^{(t)}}$ may be decomposed into an applied force $\boldsymbol{F_i^{(a)}}$ and a force of constraints $\boldsymbol{f_i}$. Equation (C.8) becomes :

$$\sum_i \left(\boldsymbol{F_i^{(a)}} - \boldsymbol{p_i}\right)\,\delta\boldsymbol{r_i} + \sum_i \boldsymbol{f_i}\,\delta\boldsymbol{r_i} = 0\,. \tag{C.9}$$

For a system without sliding friction, which is the case in this thesis, the second term of equation (C.9) vanishes. We have thus a condition for the equilibrium of a system, also called *D'Alembert Principle* :

$$\sum_i \left(\boldsymbol{F_i^{(a)}} - \boldsymbol{p_i}\right)\,\delta\boldsymbol{r_i} = 0\,. \tag{C.10}$$

Unfortunately, this equation is not useful to furnish equations of motion for the system. To resolve this difficulty, we use the generalized coordinates introduced in equation (C.6) to differentiate equations of motion. If we assume n independent coordinates, equation (C.10) is written as[1]:

$$\sum_i \boldsymbol{F_i}\,\delta\boldsymbol{r_i} = \sum_{j,i} \boldsymbol{F_i}\frac{\partial\boldsymbol{r_i}}{\partial q_j}\partial q_j = \sum_j Q_j \partial q_j\,, \tag{C.11}$$

$$\sum_i \boldsymbol{p_i}\,\delta\boldsymbol{r_i} = \sum_i m_i\,\ddot{\boldsymbol{r}}_{\boldsymbol{i}}\frac{\partial\boldsymbol{r_i}}{\partial q_j}\partial q_j\,, \tag{C.12}$$

where Q_j is called the *generalized force*. If we note T, the system kinetic energy, we can show that the D'Alembert principle is of the form :

$$\sum_j \left[\left\{\frac{d}{dt}\left(\frac{\partial T}{\partial \dot{q_j}}\right) - \frac{\partial T}{\partial q_j}\right\} - Q_j\right]\delta q_j = 0\,. \tag{C.13}$$

As the variable q is independent, the only possibilities to satisfy equation (C.13) is to have n equations of the form:

$$\frac{d}{dt}\left(\frac{\partial T}{\partial \dot{q_j}}\right) - \frac{\partial T}{\partial q_j} = Q_j\,. \tag{C.14}$$

If the forces are derivable from a scalar potential function, we have $\boldsymbol{F_i} = -\nabla_i V$ and introducing the Lagrangian of the system $L = T - V$, we obtain the Lagrangian equations of the system

$$\boxed{\frac{d}{dt}\left(\frac{\partial L}{\partial \dot{q_j}}\right) - \frac{\partial L}{\partial q_j} = 0\,.} \tag{C.15}$$

[1]For the rest of this section, we removed the superscript $^{(a)}$

Appendix D

Thickness of the materials as function of the transmitted energy

Energy (MeV)	Thickness (mm)				
	Aluminium	Graphite	Beryllium	Boron Carbide	Diamond
70	134.24	186.63	188.39	135.22	91.17
80	128.98	179.38	181.08	129.72	87.67
90	123.19	171.4	173.04	124.00	83.84
100	116.91	162.73	164.29	117.65	79.62
110	110.18	153.42	159.9	110.81	75.13
120	103.02	143.5	144.89	103.74	70.18
130	95.38	132.91	134.19	96.11	65.01
140	87.33	121.75	122.92	87.94	59.57
150	78.86	109.99	111.05	79.48	53.81
160	70.00	97.66	98.59	70.54	47.77
170	60.76	84.80	85.61	61.25	41.5
180	51.13	71.39	72.07	51.49	34.92
190	41.16	57.49	58.03	41.41	28.06
200	30.84	43.08	43.49	31.03	21.03
210	20.18	28.2	28.46	20.32	13.76
220	9.2	12.8	13.0	9.27	6.28

Table D.1: Thickness of different slab as function of the transmitted energy